2009-06-01

Development of Renal Phantoms for the Evaluation of Current and Emerging Ultrasound Technology

Deirdre King
Technological University Dublin

DEVELOPMENT OF RENAL PHANTOMS FOR THE EVALUATION OF CURRENT AND EMERGING ULTRASOUND TECHNOLOGY

Deirdre King,
B.Sc.

A thesis submitted to the Dublin Institute of Technology for the degree of Doctor of Philosophy

Supervisors: Dr. Jacinta Browne, Dr. Carmel Moran,
Prof. Matthew Hussey

School of Physics,
Dublin Institute of Technology,
Kevin Street, Dublin 8.

June 2009

To my parents

ABSTRACT

The primary aim of this project was to develop novel anatomically realistic renal phantoms for the evaluation of current and emerging ultrasound techniques capable of diagnosing all grades of renal artery stenosis. Renal artery stenosis is considered the most common cause of potentially curable secondary hypertension which if left untreated can lead to renal failure. Its early detection is very important as it offers the possibility of various drug treatments, which are considerably less invasive and poses less risk to the patient. Computer-aided modelling techniques were used to generate a range of anatomically realistic phantoms of the renal artery from medical images of a 64-slice CT scan which was acquired from a healthy volunteer with normal renal vasculature. These phantoms comprised of a normal healthy vessel and vessels with increasing stenosis (30%, 50% 70% and 85%). Using these novel phantoms a comparative study between four of the imaging techniques currently used to detect renal artery stenosis (ultrasound, magnetic resonance imaging, computed tomography and digital subtraction angiography (DSA)) was carried out. A novel kidney perfusion phantom was also developed with the ability to achieve flow velocities comparable with those found in the blood vessels of the renal macrocirculation (renal artery and renal vein) and microcirculation (kidney). By developing an understanding of disease progression in the renal artery and kidney through experimentation, it is possible to improve the outcome of various treatment regimes by early detection of the disease. Recent and ongoing ultrasound technological developments such as ultrasound contrast agents should render accessible the technically more challenging imaging of the renal artery and kidneys and potentially replace invasive intra-arterial DSA technique.

DECLARATION

I certify that this thesis which I now submit for examination for the award of Doctor of Philosophy, is entirely my own work and has not been taken from the work of others save and to the extent that such work has been cited and acknowledged within the text of my work.

This thesis was prepared according to the regulations for postgraduate study by research of the Dublin Institute of Technology and has not been submitted in whole or in part for an award in any other Institute or University.

The work reported on in this thesis conforms to the principles and requirements of the Institute's guidelines for ethics in research.

The Institute has permission to keep, to lend or to copy this thesis in whole or in part, on condition that any such use of the material of the thesis by duly acknowledged.

Signature Deiedee King Date June 2009

Candidate

ACKNOWLEDGEMENTS

First of all I would like to thank my supervisors, Dr. Jacinta Browne, Dr. Carmel Moran and Prof. Matthew Hussey, for all their valuable advice and guidance during my studies. In particular I would like to extend a special thanks to Jacinta for the constant words of encouragement and day to day support. Thank you to Carmel for the guidance throughout with the contrast studies. Thank you to both Carmel and Matt for all the comments, suggestions and encouragements throughout the project, particularly in the final stages.

Thank you to Ann O'Shaughnessy and the members of the Vascular Department in Connolly Hospital for the helpful discussions on the design of the renal artery stenosis models. I am very grateful to Dr. Andrew Fagan, for arranging access to the scanning equipment in St. James Hospital and Trinity College Dublin for the comparative study and also for help and advice over the course of the project.

I would like to thank Joe Keogh, Sandy Campbell, Noel Murphy, John McNamara and Mark McGrath for all the help with the pump assembly. It took a few goes but it got there in the end. To Michael Ring, Sean Keane and Niall Brogan thank you for the assistance and guidance with the renal models and mechanical testing. Thank you to all in the School of Physics and Focus who have helped me over the past few years.

Thank you to the University of Edinburgh for facilitating access to equipment in the Medical Physics Unit. In particular to Dr. Pete Hoskins for the use of the Scanning Acoustic Marcosope for the acoustic characterisation study. Thank you to Mairead,

James, Kate, Michael, Adele, David and Ben for all the advice and helped make my visits enjoyable and my hours on the SAM system bearable.

To my fellow MUG members, Louise and Deepa, thank you for all the laughs and help, especially in the final stages of my experiments and thesis writing. Special thank you to my friends and extended family that I've neglected so much as the workload increased but have always been there for me. To Tony who encouraged me apply for this PhD in the first place, thank you so much for your unending support. Thank you for always being there for me, your positive words of encouragement got me through those times when another phantom burst or my pump broke down again.

Finally to my family, Mam, Dad, Diarmaid and Ciarán, I am eternally grateful for your love, support, advice, encouragement and belief in me through my many years of study, without you I could not have completed this work.

ABBREVIATIONS

2D	Two dimensional
3D	Three dimensional
α	Attenuation coefficient
γ	Ideal gas constant
η	Fluid viscosity
θ	Angle of insonation
θ_i	Angle of incidence
θ_r	Angle of refraction
μ	Relative backscatter
ρ	Density
ADC	Analogue to digital convertor
Al_2O_3	Aluminium oxide
AUC	Area under the curve
$A(x,y,f)$	Magnitude spectrum of freq f and position (x,y) through sample
$A_o(x,y,f)$	Magnitude spectrum of frequency f and position (x,y) of reference signal with no sample in the path
B	Bulk modulus
Bc	Benzalkoliumcholride
BMF	Blood mimicking material
c	Speed of sound
CAD	Computer aided design
CEUS	Contrast enhanced ultrasound
CSI	Contrast specific imaging
CT	Computed tomography
CTA	Computed tomography angiography
CTDI	Computed tomography dose index
c_w	Speed of sound through water
CW	Continuous wave
d	Diameter
D	Distance
DLP	Dose length product
DR	Dynamic range
d_s	Sample thickness
DSA	Digital subtraction angiography
EFSUMB	European Federation of Societies for Ultrasound in Medicine and Biology
EC	European Commission
f	Frequency
f_c	Centre frequency of the pulse
f_D	Doppler shift frequency
f_t	Transmitted frequency
f_r	Received frequency
f_R	Resonant frequency
FFT	Fast Fourier transforms
FMD	Fibromuscular disease
IA-DSA	Intra-arterial digital subtraction angiography
IEC	International Electrotechnical Commission

IPEM	Institute of Physicists and Engineers in Medicine
ISB	Intrinsic spectral broadening
L	Length
m	Total bubble mass
MI	Mechanical index
MRA	Magnetic resonance angiography
MRI	Magnetic resonance imaging
MTT	Mean transit time
n	Acoustic refractive index
NHO_3^{--}	Nitric acid
p-	Largest peak negative pressure
p	Pressure
PD	Power Doppler
PI	Pulse inversion
PRF	Pulse repetition frequency
PVA	Polyvinyl alcohol
PVA C	Polyvinyl alcohol cryogel
PSV	Peak systolic velocity
PW	Pulsed wave
Q	Volumetric flow
r	Radius
R	Reference site diameter
RAS	Renal artery stenosis
RBC	Red blood cells
RE	Reynolds number
$\mathbf{RE_{crit}}$	Critical Reynolds number
RF	Radio frequency
ROI	Renal aortic ratio
RP	Rapid prototyping
RVD	Renovascular disease
RVH	Renovascular hypertension
SAM	Scanning acoustic macroscope
SE	Standard error
S_{shell}	Stiffness of bubble shell
SiC	Silicon carbide
SNR	Signal-to-noise ratio
SV	Sample volume
$\mathbf{T_1}$	Longitudinal relaxation time
$\mathbf{T_2}$	Transverse relaxation time
T	Time
TGC	Time gain compensation
TE	Time to echo
TIC	Time intensity curve
TMM	Tissue mimicking material
TR	Time to repetition
t_r	Reference time
t_s	Time of flight through sample
TSE	Turbo spin echo
UCA	Ultrasound contrast agent
$\mathbf{U_O}$	Overall uncertainty

U_R	Random uncertainty
U_S	Systematic uncertainty
US	Ultrasound
v	Velocity
V	Volume
V_{error}	Maximum velocity error
V_{max}	Maximum velocity
V_{min}	Minimum velocity
V_{mean}	Mean velocity
VMM	Vessel mimicking material
V_{set}	Set maximum velocity
V_{spread}	Spread of the velocity spectrum
z	Impedance

TABLE OF CONTENTS

LIST OF FIGURES

LIST OF TABLES

CHAPTER 1 THEORY AND BACKGROUND

1.1 INTRODUCTION

This chapter provides a background and introduction to the work carried out in this thesis in addition to placing the work in the context of previous studies. The first section 1.2 provides an introduction to renal artery stenosis and in sections 1.3 and 1.4 the imaging techniques used to detect renal artery stenosis are discussed. Section 1.5 provides a background review of diagnostic ultrasound and advancements in ultrasound such as ultrasound contrast agents and contrast specific imaging. Section 1.6 provides a review of the limitations of the studies published on the diagnostic performance of the imaging techniques used to detect renal artery stenosis. Section 1.7 discusses *in-vitro* phantom experimentation and the potential that anatomically realistic phantoms have as tools for calibration, testing and training. The principal aims and objectives of the thesis are set out in section 1.8.

1.2 RENAL ARTERY STENOSIS

Renal artery stenosis (RAS) is a blockage or narrowing of the major arteries that supply blood to the kidney. Presented in Figure 1.1 is the location of the renal arteries and the kidneys in the abdomen. It is considered the most common cause of potentially curable renovascular hypertension (RVH), a form of secondary hypertension. RAS is present in 1% - 5% of all cases of hypertension and which increases to 16% - 32% in populations selected in a clinical approach who show specific history and clinical signs supporting the suspicion of renovascular hypertension (Olin et al., 1995; Radermacher and Brunkhorst 1998). There are two

main causes of RAS, atherosclerosis and fibromuscular dysplasia (FMD). Atherosclerosis accounts for 70% - 90% of cases of RAS, usually involving the ostium and proximal 2 cm of the renal artery (Beattie et al., 1997; Rabbia and Valpreda 2003). This is a chronic disease characterised by the deposition of atheromatous plaques containing cholesterol and lipids on the innermost layer of the artery wall. FMD causes growth of fibrous tissues on the arterial wall and mainly affects the middle and distal third of the renal arteries (Fenchel et al., 2006).

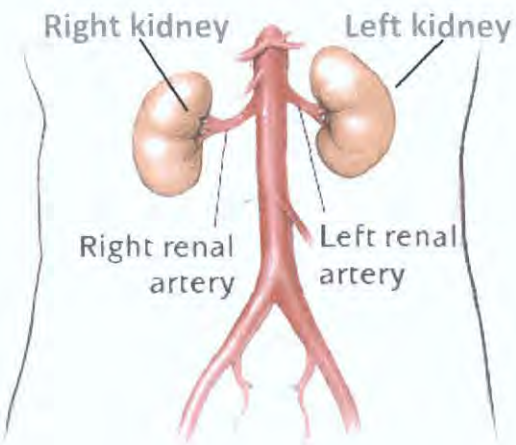

Figure 1.1 Anterior view of the renal arteries and kidneys (adapted from http://www.healthsystem.virginia.edu/internet/vascular/images/il_sa2_ras_renal_arteries.gif)

1.3 DETECTION OF RENAL ARTERY STENOSIS

Since secondary hypertension is potentially curable the early detection of RAS is important as it offers the possibility of various drug treatments, which are considerably less invasive and pose less risk to the patient than revascularisation (percutaneous angioplasty or surgery). If left untreated this progressive disease has many associated morbidities including progressive renal insufficiency, myocardial

infarction, congestive heart failure, stroke and death. Despite technological advances in non invasive methods for detecting RAS intra-arterial digital subtraction angiography (IA-DSA) still remains the gold standard technique for anatomical diagnosis of RAS; a sample image is shown in Figure 1.2 (Drieghe et al., 2008; Fraioli et al., 2006; Stacul et al., 2008). Possible reasons for this are that if carried out properly DSA does provide excellent resolution to show the presence, degree and extent of stenosis (Grenier et al., 2006). Also it offers the option of simultaneous therapeutic interventions such percutaneous revascularisation by balloon angioplasty and or stenting (Rountas et al. 2007). Most commonly, angiographic diameter reductions of $\geq$ 50% to $\geq$ 70% are used to define hemodynamically significant stenosis (Staub et al. 2007). However, this technique has not found widespread use for the diagnosis of blockages less than 70% due to severe difficulties in their accurate detection and characterisation. Furthermore, DSA is an invasive and expensive procedure and carries the risk of complications such as bleeding, anaphylaxis and contrast induced nephropathy (Williams et al., 2007). These factors render DSA unsuitable as a screening test for RAS. Currently there is no universally accepted screening test for RAS. The ideal test to diagnose this condition should be an imaging modality which is non-invasive, has high sensitivity and high specificity (> 90%), and is widely available at low cost.

Figure 1.2 Intra-arterial digital subtraction angiography image showing unilateral renal artery stenosis (RAS) in left main renal artery (Sung et al., 2006)

1.4 NON-INVASIVE IMAGING TECHNIQUES FOR DETECTION OF RENAL ARTERY STENOSIS

The non-invasive medical imaging techniques currently available are duplex ultrasound (US), helical computed tomography angiography (CTA) and magnetic resonance angiography (MRA). The choice of imaging procedure will depend on; the availability of the diagnostic tool, the experience and local accuracy of the chosen modality, as well as patient characteristics (e.g. body size, renal function, contrast allergy, and presence of prior stents or metallic objects that may serve as contraindications to MRA techniques). Table 1.1 provides a broad comparison of the imaging techniques currently used to detect RAS.

Table 1.1 Comparison of imaging modalities currently used to detect RAS

Modality	**US**	**MRI**	**CT**	**DSA**
Procedure	Non-invasive	Non-invasive	Non-invasive	Invasive
Safety (radiation)	Non-ionising	Non-ionising	Ionising	Ionising
Spatial resolution[a]	0. 3 - 3 mm	~ 1 mm	~ 1 mm	~ 1 mm
Portability	Excellent	Poor	Poor	Intermediate
Cost of diagnostic work-up[b]	€80	€250	€120	€730

[a](Szabo, 2004), [b]Approximate costing for St. James's Hospital, Dublin, May 2009

1.4.1 Magnetic resonance angiography

Contrast enhanced MRA is performed with gadolinium to obtain visualization of the renal arteries and abdominal vasculature. Figure 1.3(a) presents a sample MRA image of a normal renal artery and kidney. Comparisons with IA-DSA have indicated a range of sensitivities from 62% to 100% and specificities of 70% to 100% for detection of RAS (as shown in Table 1.2). Adverse reactions to gadolinium have been reported and its possible association with nephrogenic systemic fibrosis (Marckmann et al., 2006). Therefore, there is growing interest in non-contrast MRA which has demonstrated a sensitivity of 78% and a high specificity of 91% (Utsunomiya et al., 2008). However, it still has limitations and these include overestimation of stenosis, inability to image patients with metal implants, patient claustrophobia and the expense of the technique.

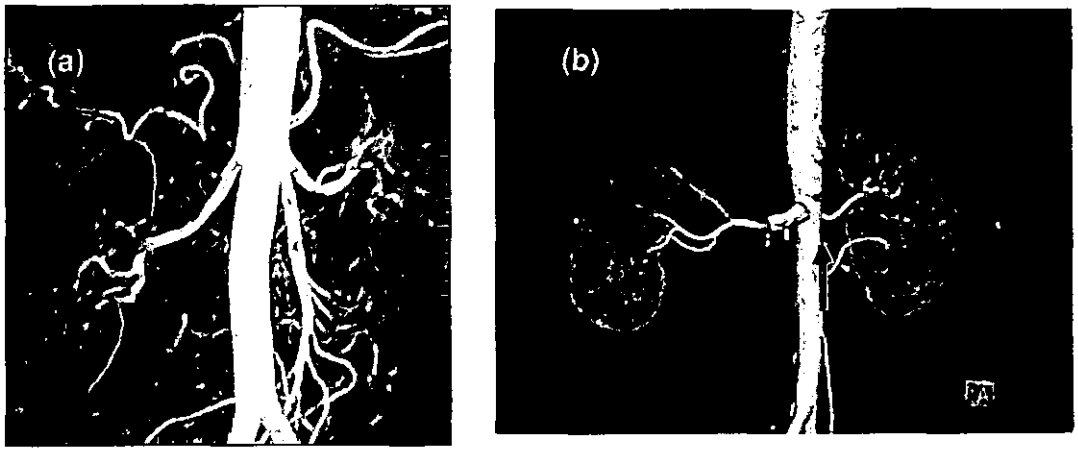

Figure 1.3 (a) Contrast enhanced MRA showing normal renal arteries, (b) CTA showing RAS in right renal artery located distally to a stent (Images adapted from http://www3.americanradiology.com/imggallery/RADIOLOGY/mri/renalmra1.JPG)

1.4.2 Computed tomography angiography

Computed tomography angiography (CTA) produces excellent 3D images of the aorta and renal arteries, an example of which is shown in Figure 1.3(b). CTA has a sensitivity and specificity for detecting significant RAS of 62% to 100% and 56% to 99%, respectively, compared with IA-DSA (Table 1.3). The major disadvantage of this technique is that CT involves the use of ionising radiation. Also, it requires the administration of iodinated contrast and is therefore not an ideal screening method for patients with renal insufficiency because of the risk of inducing contrast nephropathy. Other disadvantages include long processing times (30 - 90 minutes) and its inability to image persons who weigh more than 125 kg.

Table 1.2 Diagnostic performance of MRA studies for the detection of RAS in patients suspected of RVH, where NG = not given, PPV = positive predictive value, NPV = negative predictive value

First Author and Year	No. of patients	No. of arteries	Sensitivity (%)	Specificity (%)	PPV (%)	NPV (%)	Stenosis (%)	Contrast	Study type
Shetty et al., (2000)	51	NG	96	92	NG	NG	NG	yes	Prospective
De Cobelli et al., (2000)	45	90	100	93	86	100	50	yes	Prospective
Vasbinder et al., (2001)	288	NG	88-100	75-100	NG	NG	50-70	yes	Meta analysis
Willmann et al., (2003)	46	NG	93	100	96	100	50	yes	Prospective
Vasbinder et al., (2004)	356	NG	62	84	49	90	50	yes	Prospective
Patel et al., (2005)	NG	NG	90-100	76-94	NG	NG	50/60	yes	Meta analysis
Eklöf et al., (2006)	58	NG	98	70	NG	NG	60	yes	Retrospective
Hirsch et al., (2006)	34	68	84	74	57	92	50	yes	Retrospectively
Rountas et al., (2007)	129	132	90	94	75	98	50	yes	Prospective
Stacul et al., (2008)	26	57	83	76	63	91	50	yes	Prospective
Utsunomiya et al., (2008)	26	56	78	91	64	96	NG	no	Retrospectively

Table 1.3 Diagnostic performance of CTA studies for the detection of RAS in patients suspected of RVH, NG = not given

First Author and Year	No. of patients	No. of arteries	Sensitivity (%)	Specificity (%)	PPV (%)	NPV (%)	Stenosis (%)	Contrast	Study type
Kaatee et al., (1997)	71	166	96	96	96	96	50	nonionic	Prospective
Wittenburg et al., (1999)	82	197	96	99	NG	NG	NG	ioninated	Prospective
Vasbinder et al., (2001)	317	NG	94-100	65-97	NG	NG	50-70	NG	Meta analysis
Willmann et al., (2003)	46		92	99	87	100	50	ioninated	Prospective
Vasbinder et al., (2004)	356	NG	64	92	68	91	50	NG	Prospective
Hirsch et al., (2006)	NG	NG	59-96	82-99	NG	NG	50/60	NG	Meta analysis
Eklöf et al., (2006)	58	NG	100	56	NG	NG	60	Non ionic	Retrospective
Fraioli et al., (2006)	50	99	100	97	98	98	50	iodinated	Prospective
Rountas et al., (2007)	129	132	94	93	71	99	50	non ionic	Prospective

1.4.3 Ultrasound

Duplex ultrasound (US) combines the direct visualisation of the renal arteries and kidneys via B-mode imaging, with Doppler measurement of the velocity of blood flow in the main renal artery and within the kidney. In Figure 1.4 an example of a colour duplex ultrasound image of right-sided ostial RAS is shown. This combination allows anatomical evaluation and hemodynamic assessment. Different Doppler parameters have been used to diagnose RAS; direct parameters are obtained from the main renal artery and indirect parameters from the intrarenal branches within the kidney. The direct parameters are considered the more important and the indirect parameters are viewed as only contributing additional supplementary information (Jaeger, 2007). Typically, the maximum velocity through the neck of the stenosis is used to classify the severity of the stenosis based on the fact that, for a constant flow rate, a tighter constriction leads to higher velocities through the stenosis. The most generally accepted criteria for the identification of a hemodynamically significant RAS (generally 50% or 60% stenosis) is a peak systolic velocity (PSV) in the renal artery greater than 180 - 200 cm s^{-1} at the site of the lesion or a renal-aortic PSV ratio (RAR) of 3.5 (Eklöf et al., 2006; Soares et al., 2006; Staub et al., 2007). In a recent meta-analysis, Williams et al., (2007) found the PSV to be the most accurate test parameter with sensitivity and specificity of 85% and 92%, respectively.

Overall US, compared with IA-DSA, has a sensitivity of 67% to 98% and a specificity of 54% to 99% for detecting RAS (Table 1.4). It has several advantages over MRA and CTA in that it is widely available, non-invasive and inexpensive. It is an excellent test to monitor renal artery patency after endovascular treatment or surgical revascularization of RAS (Blum et al., 1997; Krumme et al., 1996). Unlike MRA, in

which most stents currently cause artefacts, ultrasound transmission through a stent is not a problem. Limitations of ultrasound examinations include its dependence on operator skill, the diminished ability to visualise accessory renal arteries, and the difficulty in imaging obese patients or patients with intervening bowel gas (Paven et al., 2006).

Despite these limitations, non-invasive US methods are now considered first-line methods for evaluation of renovascular diseases (RVDs) (Grenier et al., 2006). The most recent published guidelines have emphasised the leading position of US, followed by CTA (except in cases of renal failure) and MRA for the screening of RAS (Hirsch et al., 2006). This shows a shift from the previously recommended tests of MRA and DSA. Duplex US is the most widely utilized method for non-invasive imaging of the renal arteries as it is the most widely available equipment and is not as expensive as MRI, CT or DSA techniques (Staub et al., 2007).

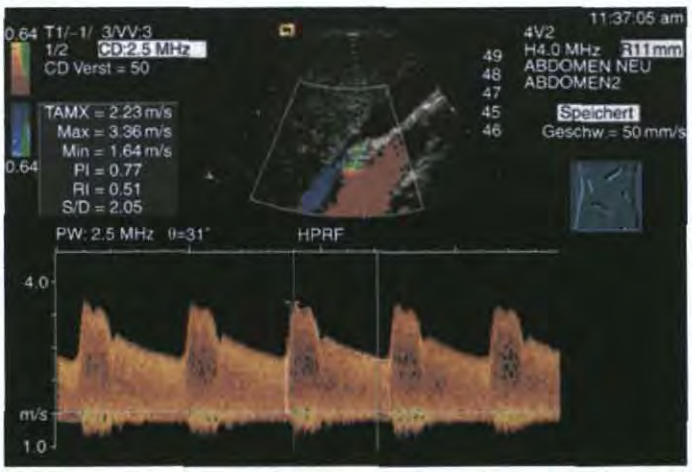

Figure 1.4 Colour duplex ultrasound of right-sided ostial renal artery stenosis

Table 1.4 Diagnostic performance of Duplex Ultrasound studies for the detection of RAS in patients suspected of RVH, where NG = not given, PPV = positive predictive value, NPV = negative predictive value

First Author and Year	No. of patients	No. of arteries	Sensitivity (%)	Specificity (%)	PPV (%)	NPV (%)	Stenosis (%)	Doppler criteria	Study type
Olin et al., (1995)	102	187	98	98	99	97	60	>200 cm s^{-1}	Prospective
De Cobelli et al., (2000)	45	91	79	93	85	90	50	>200 cm s^{-1}	Prospective
Souza et al., (2000)	50	96	67	98	NG	NG	50	>180 cm s^{-1}	Prospective
Vasbinder et al., (2001)	1592	NG	79	96	NG	NG	50-70	NG	Meta analysis
Nchimi et al., (2003)	91	178	91	97	88	94	60	>180 cm s^{-1}	Prospective
Hirsch et al., (2006)	NG	NG	84-98	62-99	NG	NG	50/60	>180 cm s^{-1}	Meta analysis
Eklöf et al., (2006)	58	NG	80	54	NG	NG	60	>180 cm s^{-1}	Retrospective
Li et al., (2006)	91	187	81	NG	NG	NG	50	>150 cm s^{-1}	Prospective
Soares et al., (2006)	67	67	97	79	NG	NG	60	>200 cm s^{-1}	Retrospective
Staub et al., (2006)	49	93	92	80	87	88	50	>200 cm s^{-1}	Retrospective
Rountas et al., (2007)	129	132	75	90	60	95	50	>200 cm s^{-1}	Prospective
Williams et al., (2007)	NG	2785	85	92	NG	NG	50/60	100-200 cm s^{-1}	Meta analysis

1.5 THEORY OF ULTRASOUND

Ultrasound is a mechanical wave, with a frequency higher than 20 kHz. Modern imaging systems use ultrasound with frequencies ranging from 2 MHz to 20 MHz. This ultrasound is produced by a transducer containing ceramic elements which exhibit the piezoelectric effect. A piezoelectric element expands and contracts rhythmically to generate ultrasound when subjected to a varying electrical stimulus as the transducer is in pulse receive mode. Ultrasound incident on a piezoelectric element induces an electrical signal across the element. To obtain an image a transducer is acoustically coupled to the body using coupling gel to eliminate air bubbles and the piezoelectric elements are stimulated electrically resulting in the transmission of a beam of ultrasound into the body. The ultrasound wave travels at different speeds through different tissues and undergoes a number of interactions with the tissues in accordance with their physical characteristics. A portion of the transmitted ultrasound beam is reflected back to the transducer as a result of these interactions. The returned portion is detected by the piezoelectric elements and converted into electric signals. These electrical signals undergo signal processing and are used to construct a two dimensional (2D) image.

The renal vessels and kidneys are visualised directly using B-mode (brightness mode) which yields cross-sectional images representing tissues and organ boundaries within the body. It is constructed from echoes which are generated by reflections of ultrasound at tissue boundaries and by scattering irregularities within the tissue. Images are formed using a pulse-echo technique, where a single pulse of ultrasound is transmitted into the patient, and the echoes returning from reflectors within the patient

are detected by the transducer. Each echo is displayed at a point in the image, which corresponds to the relative position of its reflector within the body cross-section. The brightness of the image at each point is related to the strength or amplitude of the detected returning echo. An image may be built up by sweeping a beam through a plane of tissue to build up a single 'frame' of an image.

1.5.1 Doppler ultrasound

Using Doppler ultrasound the hemodynamic information about the renal vessels and the kidneys is obtained. The Doppler Effect is the change in frequency observed as a sound source moves towards or away from an observer/detector. Ultrasound can be used to assess blood flow by measuring the change in frequency of the ultrasound scattered from moving blood. In Doppler ultrasound, both the source (transducer) and observer (transducer) of the ultrasound source are at rest, while the waves of ultrasound are reflected from the red blood cells (RBCs) which are moving in the blood with respect to both the source and the observer. The ultrasound waves transmitted by the transducer strike the moving blood, so the frequency of ultrasound as experienced by the blood is dependant on whether the blood is stationary, moving towards the transducer or moving away from the transducer. A modified Doppler equation is used to obtain the Doppler shift (f_D) which gives flow information about the blood,

$$f_D = f_t - f_r = (2vf_t \cos\vartheta)/c \qquad \textbf{Equation 1.1}$$

where f_t is the transmitted frequency, f_r is the received frequency, v is the velocity of the target, θ the angle between the ultrasound beam and the direction of the target's motion,

known as the angle of insonation, and c, the speed of sound of ultrasound in tissue. The Doppler blood flow information can be displayed in a number of formats: as a spectrum of the velocity profile with time (continuous wave (CW) or pulsed wave (PW) Spectral Doppler), as a colour overlay map of the mean Doppler frequency (Colour Doppler imaging) or amplitude map of Doppler signal (Power Doppler imaging).

1.5.2 Spectral Doppler

Spectral Doppler measurements are sampled sequentially at regular intervals along the renal artery and the kidney. In this mode, all the velocity information detected from a single location within the blood vessel is displayed in the form of a frequency shift *versus time plot*. The vertical distance from the baseline corresponds to the Doppler shift, while the greyscale indicates the amplitude of the detected ultrasound at that particular frequency. In CW systems, ultrasound is transmitted and received continuously and as a result they have no depth information or resolution. Also two transducers are required, one to transmit and the other to receive the ultrasound. In PW Doppler, the transducer transmits short bursts of ultrasound at regular intervals and receives only for a short period of time following an operator-adjustable delay. The location of the Doppler gate defines the range of depths from which the Doppler signal arises. PW Doppler suffers from a fundamental limitation of a maximum velocity limit and if the Nyquist limit is exceeded aliasing occurs. The maximum Doppler frequency shift that can be measured is half the pulse repetition frequency (PRF). PW systems do not actually measure the 'classical Doppler shift', as in CW Doppler. Two distinct mechanisms affect the received PW signal, (1) classical Doppler shift, (2) time shift, where the received signals undergo a time shift with respect to the time of transmission.

Since the frequency shift detected due to the changing phase relationship is virtually identical to that detected by a classical CW system, the basic Doppler equation (Equation 1.1) applies in the case of both CW and PW Doppler systems.

1.5.3 Colour Doppler

In clinical practice, Colour Doppler is often used to guide the sonographer to the area of the stenosis in the renal artery and then Spectral Doppler is used to measure the local maximum velocity. In the Colour Doppler mode an overlay of a colour velocity map is registered upon the B-mode image. These Colour Doppler images are formed using between four and sixteen pulses directed to each line-of-sight. This requirement reduces the frame rate in comparison to the grey-scale image. Colour Doppler imaging is limited as it provides only an estimate of the mean velocity towards or away from the transducer and an increase in variance with the sample volume (SV) due to the limited number and length of transmitted pulses (Evans and McDicken, 2000; Ferrara and DeAngelis, 1997; Hoskins and McDicken, 1997).

1.5.4 Power Doppler

Power Doppler imaging has been employed for over a decade as a means of improving sensitivity of Doppler to flow in small vessels such as in the renal cortex and to provide an indication of the spatial distribution of blood volume (Rubin et al., 1994). The power of the Doppler signal backscattered from blood is displayed in colour. Power Doppler mode enhances the ability of ultrasound to detect flow in small vessels for several reasons. Firstly, the power signal from blood is added to a background of electronic noise, therefore enabling a higher level of signal amplification and thus

improved dynamic range. Given that there is already a loss in velocity information, aliasing is not an issue and the PRF can therefore be reduced, resulting in improved sensitivity to low velocity flow. Furthermore, frame-to-frame averaging is increased which effectively reduces frame rates and temporal resolution but improves small vessel detection. There is also no need to consider the Doppler angle since power, rather than frequency is angle independent, and so the angle dependency of Power Doppler is much reduced relative to the other Doppler modalities.

1.5.5 Ultrasound contrast agents

Advances in ultrasound such as ultrasound contrast agents and contrast specific imaging have the potential to detect RAS at an earlier stage, and so significantly improve patient prognosis. The use of ultrasound contrast agents (UCAs) enhances considerably both B-mode and Doppler ultrasound sensitivity, usually increasing the Doppler signal amplitude by up to 30 dB (Burns et al., 2000). To date there have only been a small number of reports suggesting the application of UCAs in renal artery imaging and the following authors have provided reviews of these studies, Correas et al., (2003), Correas et al., (2006), Drelich-Zbroja et al., (2004), and Robbin et al., (2003). These studies show that UCAs improve the visualisation of the main renal arteries and the intra-renal arteries. The European Federation of Societies for Ultrasound in Medicine and Biology (EFSUMB) study group published recommendations for the use of UCAs in the evaluation of the micro- and macro-vasculature of the kidneys (Correas et al., 2009). It is important to note that the use of contrast enhanced ultrasound (CEUS) for renal applications has not yet obtained regulatory approval. Therefore the use of off-label UCAs (which have regulatory

approval for liver applications) should be justified by an individual risk/benefit assessment for the respective patient, based on available scientific data.

These UCAs have the advantage over other contrast agents used in DSA, MRA and CTA as they are not nephrotoxic and therefore are suitable for patients with elevated creatinine and those allergic to iodine-based agents. In general UCAs are very safe and have shown a low incidence of side effects. Adverse effects such as premature ventricular contractions predominantly occur when a high mechanical index (MI) (term is defined further in this section) and end-systolic triggering have been used together (Blomley et al., 2007). The properties of UCAs licensed for clinical use are presented in Table 1.5. For the contrast enhanced renal studies the second generation UCA Luminity® (formerly known as Definity®) (Lantheus Medical Imaging, MA, USA) was chosen as members of the research team had experience of characterising it previously.

Table 1.5 Examples of ultrasound contrast agents licensed for clinical use

Contrast Agent	Manufacturer	Shell material	Gas	Diameter	Licensing and use
Imagify (AI 700)	Acusphere Inc	Copolymer	Decafluorobutane	Mean 2 μm	Awaiting approval in USA
Definity® (USA/Canada) Luminity® (EU)	Lantheus Medical Imaging	Lipid	Octafluoropropane	Mean 2.5 μm 98% < 10 μm	USA and EU To opacify the left ventricle and to improve the delineation of the left ventricular endocardial borders
Imavist®/AF0150	Imcor Pharmaceuticals Inc	Lipid	Perfluorohexane/ Nitrogen	99.8%<10 μm	USA approved, To opacify the left ventricle and to improve the delineation of the left ventricular endocardial borders
SonazoidTM/ NC100100	GE Healthcare	Lipid	Perfluorobutane	Median 2.6 μm 99.9% <7μm	Japan approved Focal liver lesions
SonoVueTM (BR1)	Bracco	Lipids	SF6	99% < 11μm	EU approved Imaging chambers in the heart and large blood vessels
OptisonTM/FS069	GE Healthcare /Amersham	Albumin	Octafluoropropane	93%<10μm	USA and EU To opacify the left ventricle and to improve the delineation of the left ventricular endocardial borders
Echovist	Bayer Health Care	Galactose	Air	Mean 3.3 μm	To enhance gynaecological ultrasound images and assess tubal patency

UCAs are gas-filled microbubbles which can be used to enhance the backscatter of ultrasound and therefore are useful in the enhancement of echogenicity for the assessment of blood flow provided they are evenly dispersed in the flowing blood. Microbubbles are more compressible than soft tissue which has a compressibility of ~ 4 x 10^{-10} Pa^{-1} and therefore when exposed to oscillating acoustic signals expansion and compression of the microbubble occurs. Commercial UCAs are resonant due to the relationship between frequency and bubble radius for diagnostic frequencies between 2 MHz and 15 MHz. The resonance frequency f_R of an encapsulated microbubble of radius r and total bubble mass m that is surrounded by a liquid with density ρ and ambient pressure p is

$$f_R = \frac{1}{2\pi r}\sqrt{\left(\frac{3\gamma p}{\rho} + \frac{S_{shell} r^2}{m}\right)} \qquad \textbf{Equation 1.2}$$

where γ is the ideal gas constant and S_{shell} is the stiffness of the bubble shell (Kollmann, 2007).

The acoustical behaviour of UCAs depends on the surrounding liquid properties, the applied acoustic pressure and the physical characteristics of the bubble (size, shell) (de Jong et al., 2002). The magnitude of the peak negative pressure wave incident on the contrast microbubble will determine its behaviour as shown in Figure 1.5. In diagnostic imaging the insonation power is usually expressed by the MI defined as,

$$p-/\sqrt{f_c} \qquad \textbf{Equation 1.3}$$

where p- is the largest peak negative pressure and fc is the centre frequency of the pulse (Quaia, 2005).

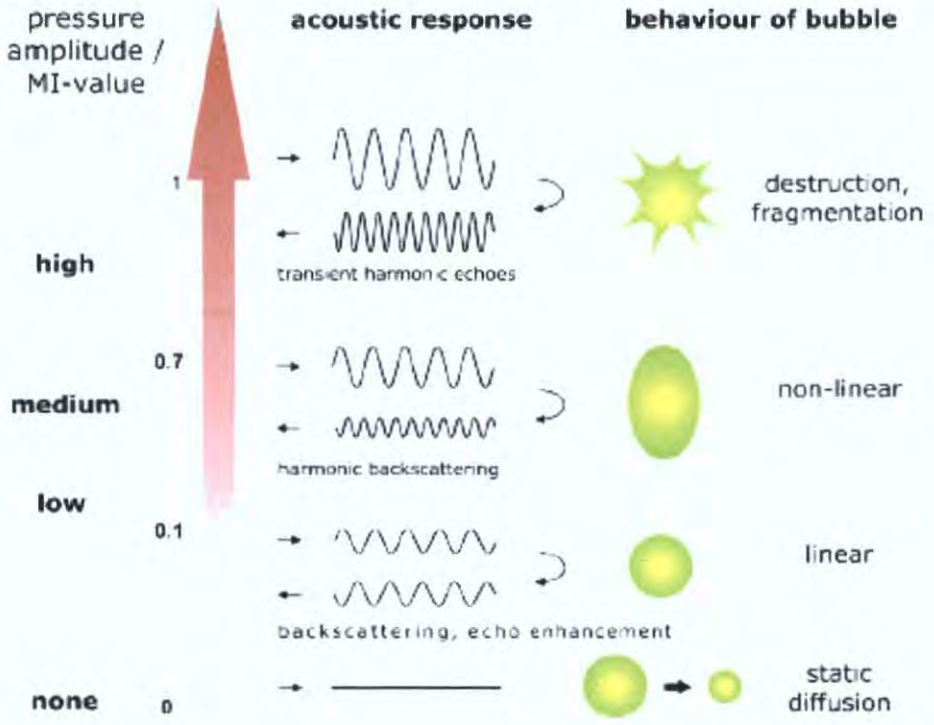

Figure 1.5 Schematic view of the behaviour of microbubbles (UCAs) at different ultrasonic amplitudes of the propagating pulse (MI values) (adapted from Kollmann, 2007)

Three ultrasound exposure modes are principally used with UCAs; 1) low MI techniques, 2) medium/normal MI techniques and 3) high MI techniques (Miller and Nanda, 2004). Low MI is considered around 0.1 and here the UCAs undergo linear oscillations. At low pressure, the peak-to-peak oscillatory change in the diameter of the bubble is in the order of a few percent (Miller and Nanda, 2004). The bubble oscillates at the same frequency as the applied ultrasound, expanding during the negative part of the cycle and contracting during the positive part of the cycle. As the pressure amplitude increases, the oscillatory changes in bubble diameter can be as much as 10% – 50% (Miller and Nanda, 2004). MI values most frequently used clinically are referred to as normal MI techniques are considered between 0.2 and 0.7 and here the UCAs undergo non-linear oscillations. This is due to the presence of the gas within the microbubble which cannot contract as much as it can expand in all directions and as a

result the oscillations are no longer in phase with or at the same frequency as the applied ultrasound. The resultant scattered ultrasound signal becomes non-linear and sub-harmonics, second harmonics and even higher harmonics may be generated. High MI is considered between 0.8 and 1.9, at these high pressures the vibrational amplitude is so large that the bubbles may be forced to collapse or burst.

Low MI imaging allows minimally disruptive contrast imaging and enables effective investigations over several minutes with the visualisation of the dynamic enhancement pattern in real time. Luminity® is a low solubility gas UCA and is characterised by the combination of improved stability with favourable resonant behaviour at low acoustic pressures. The EFSUMB study group recommend the use of low MI techniques rather than high MI techniques for the evaluation of the kidney. High MI techniques in which the microbubbles are deliberately destroyed are no longer recommended for imaging the kidney due to the difficult examination technique which results in unduly long exposure times increasing the risk of potential bioeffects from the interaction of diagnostic ultrasound and UCAs (Correas et al., 2009).

1.5.6 Contrast specific imaging

Conventional Doppler modalities are sensitive to the presence of microbubble artefacts such as colour blooming which reduces their benefit. Colour blooming is also known as colour bleeding describing how the colour spreads out from within the vessel and 'bleeds' beyond the wall into adjacent areas where flow is not possible (Rubens et al., 2006). An example of this artefact is shown in Figure 1.6. This artefact occurs immediately after the bolus injection of contrast agent arrives at the imaging site (Forsberg et al., 1994).

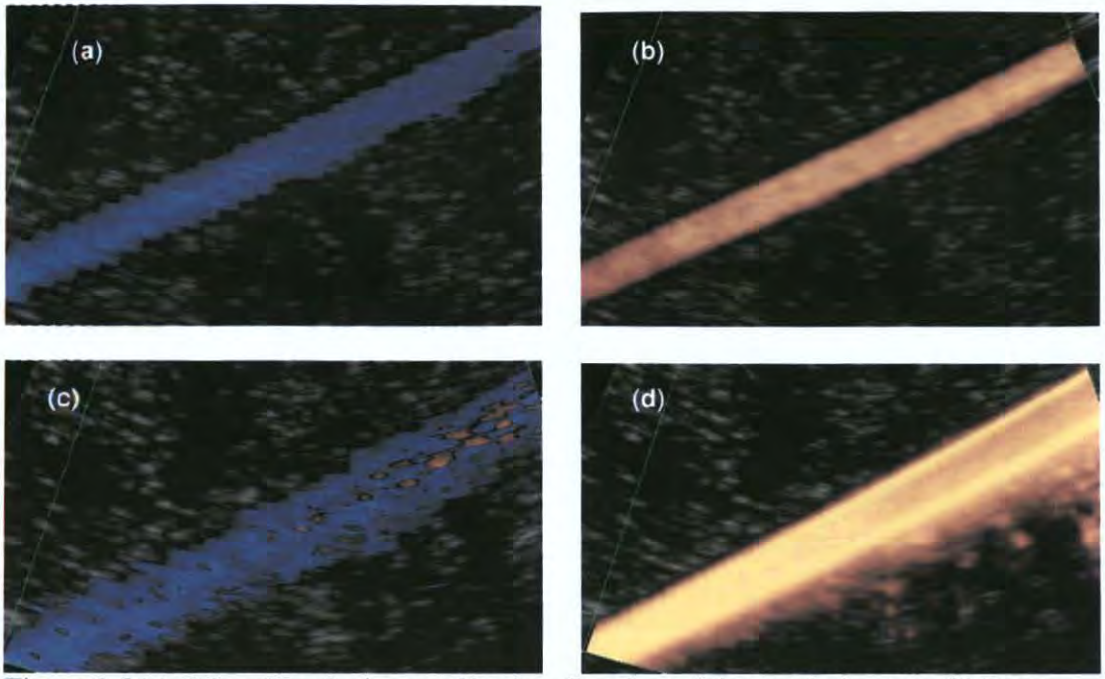

Figure 1.6 (a) Colour Doppler image of laminar flow in straight vessel phantom, (b) Power Doppler image of same vessel, (c) colour blooming of Colour Doppler due to bolus injection of UCA, (d) colour blooming of Power Doppler due to bolus injection of UCA

With developing understanding and knowledge of the UCA microbubbles and their interaction with ultrasound, new techniques have been developed based on the specific properties of UCAs. A range of specialized contrast specific imaging (CSI) techniques have been developed for ultrasound some of which have been listed by Quaia, (2007). Two of the most promising techniques are represented by phase and amplitude modulation. Both are low-transmit-power techniques which suppress or remove the tissue signal from non-linear microbubble signals to improve the contrast resolution and signal-to-noise ratio (SNR). Phase modulation involves the transmission of multiple US pulses per scan line followed by processing of the received radio frequency (RF) signals from each line (Quaia, 2007). Amplitude modulation uses alternating acoustic power to suppress the tissue signal. Here a train of three low power US pulses are transmitted per image line. The pulses are transmitted at 2 power levels where the first and the third pulse are half-height amplitude relative to the second pulse. The received echoes from the half-height transmitted pulses are subtracted from the full height signal which results

in effective removal of tissue clutter (Quaia, 2007). Only Pulse Inversion harmonic imaging (phase modulation technique) and Harmonic Power Doppler imaging will be discussed here.

Pulse Inversion Harmonic Imaging

Conventional contrast harmonic imaging is based on the fact that UCAs resonate in a non-linear fashion. This non-linear response generates additional frequencies at harmonics of the original frequency. Pulse Inversion (PI) harmonic imaging (Figure 1.7) is the most used phase modulation technique (Burns et al., 2000). In PI imaging a sequence of two ultrasound waves is transmitted in rapid succession into the tissue that contains a contrast agent. The second wave transmitted is an inverted replica of the first wave. Due to the presence of the contrast agent the response is non-linear, and therefore when the resulting backscatter signal from the two pulses is added, the fundamental signal is eliminated and the second harmonic and higher harmonics are enhanced. The advantage of this technique over harmonic techniques is that the overlap between fundamental and second harmonic spectra does not matter and there is no need to restrict the transmission spectra to the lower half of the frequency range (Quaia, 2007). This allows the use of broader bandwidths (shorter pulses) resulting in improved sensitivity for contrast detection. The disadvantage is the reduction in frame rate due to the need to interrogate each scan line twice.

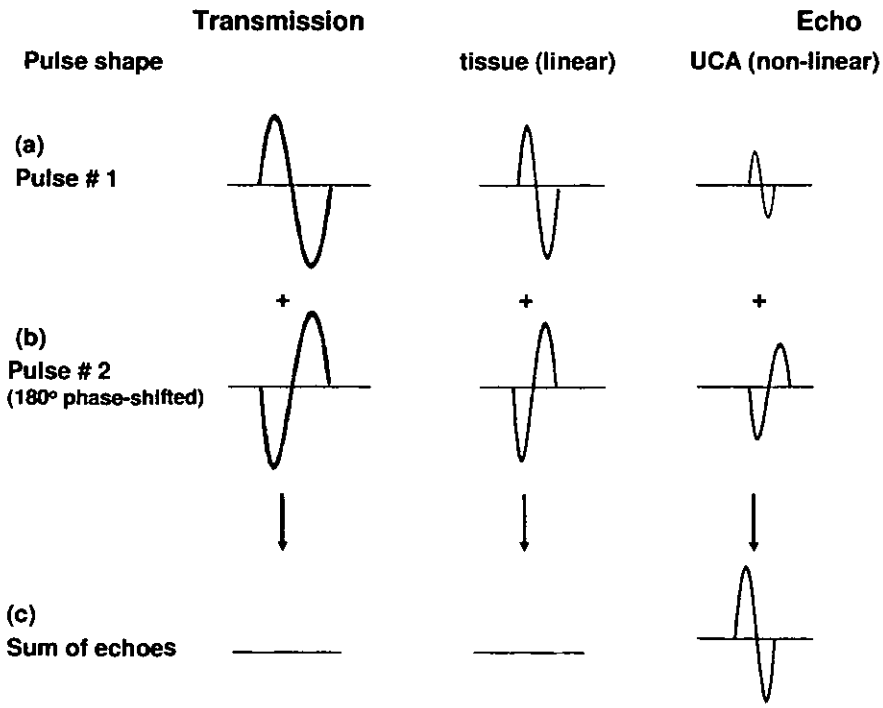

Figure 1.7 Method of pulse inversion

Harmonic Power Doppler Imaging

This technique uses the combination of harmonic imaging with Power Doppler to discriminate contrast agent and blood from tissue by detecting other characteristics of microbubble behaviour (enhancement and movement of microbubble) as well as its non-linear resonance. As discussed in section 1.5.4 above, Power Doppler has proven to be a very sensitive method in terms of SNR and flow detectability. With the addition of UCA, the signals received from the blood containing contrast are enhanced and the detectability of flow from small vessels is increased further. This technique reduces flash or motion artefacts from moving tissue by the combination with second harmonic filtering allowing sensitive visualization of the contrast agent. A high pass filter allows the cancelling of the signals produced by tissues and selective registration of that produced by the UCAs (Quaia, 2007).

1.6 LIMITATIONS OF CLINICAL STUDIES

There have been many clinical studies on the diagnostic performance of US, MRA, and CTA, with some of the most recent listed in Tables 1.2 - 1.4. There have been considerable conflicting and contradictory results regarding the accuracies of these imaging modalities. Meta-analyses carried out by Vasbinder et al., (2001, 2004) and Williams et al., (2007) have highlighted that diagnostic tests are poorly reported. From reviewing the literature, it has been found that many studies suffer from the following issues; difficulties recruiting a sufficiently large number of patients for statistical significance, poorly defined study samples, variation in the analysis of data and lack of standard criteria used to define a positive result (particularly in ultrasound). In the listed studies the imaging modality in question was compared to DSA, which was taken to be the gold standard with a presumed sensitivity and specificity of 100%. DSA is recognised to have substantial limitations such as inter-observer variability and its 2D nature only providing anatomical information (Leiner et al., 2005; Vasbinder et al., 2004). This may cause the results of that imaging modality to be worse than they actually need be. Also threshold values of 50% - 70% reductions in diameter have been considered as significant stenoses (Table 1.2 – 1.4). Currently the consensus is that a stenosis of 50% should be considered hemodynamically significant as it is at this level the pressure gradient measured invasively across the stenosis increases significantly (De Bruyne et al., 2006; Hirsch et al., 2006; Staub et al., 2007).

1.7 *IN-VITRO* VALIDATION OF IMAGING TECHNIQUES

There is a need to define the criteria whereby a technique is selected for screening patients with suspicion of RAS. As discussed in the previous section there are a number of problems associated with clinical trials which are expensive, lengthy and can have complicated ethical issues associated with them (Zalunardo and Tuttle, 2004). However, the validation procedures for new imaging techniques can also include *in-vitro* flow phantom experimentation (Smith et al., 1996; Zalunardo and Tuttle, 2004). With *in-vitro* phantom experiments the values of the flow parameters are established; hence it is possible to obtain accurate flow measurements allowing an estimation of mimicked disease progression and to directly compare each imaging technique using one reference standard. Ultrasound flow phantoms are used to test both the accuracy of ultrasound scanners (maximum velocity estimation) under standardised conditions that can be reproduced in many locations and to contribute to the understanding of normal and diseased states in the vascular system (flow profile of blood).

1.7.1 General features of flow phantoms

A flow phantom is designed to reproduce physically the flow of blood in a vessel (IPEM, 1994). Figure 1.8 shows the components of a basic flow phantom: a vessel contained within a tissue mimicking material through which a blood mimicking fluid is pumped using a computer-controlled system. This section gives an overview of the general features of a flow phantom. A more detailed review of Doppler flow phantoms and its components can be found in Hoskins, (2008).

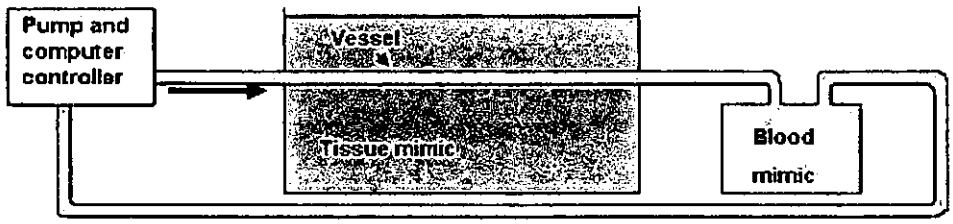

Figure 1.8 Components of a basic flow phantom

Pumps

A variety of pumps have been used in flow phantoms including gear, roller, piston and centrifugal (Boote and Zagzebski, 1988; Hoskins, 2008; Hoskins, Anderson, and McDicken, 1989; Law et al., 1989; McDicken, 1986). For experiments involving blood or particles that are easily damaged, roller or piston pumps are preferred. Gear and piston pumps allow rapid changes in flow rate, which make these pumps suited for the production of pulsatile flow. They also have sufficient output stability to provide steady flow. Piston pumps appear to offer the best in terms of temporal resolution, flow stability and minimum damage to particles of the blood mimicking fluid. Gear pumps also provide food temporal behaviour and stability and may be used for BMF particles that are not easily damaged, such as nylon particles (Hoskins, 2008).

Tissue mimicking materials

It is important that the material chosen to mimic tissue is equivalent in terms of its acoustical and mechanical properties. The International Electrotechnical Commission (IEC) Report 61685 has specified a set of acoustic parameters for a standard flow phantom which are discussed in section 2.1.2 (IEC, 2001). These specifications are based on normal healthy tissue and do not provide details about the properties of

diseased tissues. A compilation of data of the acoustic properties of healthy and diseased arteries is given by Hoskins, (2007). Table 1.6 lists the acoustic properties of some tissue mimicking materials (TMMs) which have been used to represent tissue in flow phantoms.

Table 1.6 Acoustic properties of some TMMs (Hoskins, 2008)

	Material	**Density** ($kg\ m^{-3}$)	**Speed of sound** ($m\ s^{-1}$)	**Attenaution coefficient** ($dB\ cm^{-1}\ MHz^{-1}$)
Hoskins (1994)	Foam 1	998	1488	1.2 (5 MHz)
Hoskins (1994)	Foam 2	998	1487	0.8 (5 MHz)
Madsen (1982)	Gelatin	980	1539	0.51
Burlew (1980)	Agar	1060	1539	0.85
Rickey (1995)	Agar	-	1535	0.8
Teirlinck (1998)	Agar	1049	1551	0.52
Meagher (2007)	Knojac-carrageenan	-	1550	0.56 (5 MHz)

Foam 1 is reticulated foam at 10 pores per inch and foam 2 is reticulated foam at 30 pores per inch, both immersed in water.

Blood mimicking fluids

The properties of the blood mimicking fluid (BMF) should be similar to those of blood *in-vivo*. Since the Doppler signal from blood arises from the moving red blood cells (RBCs), the BMF is prepared as a suspension of scattering particles. The approximate diameter of a RBC is 5 μm and so the particles used in the BMF are chosen to be approximately the same size. Rayleigh scattering is a phenomenon which is associated with the scattering by particles which are much smaller than the wavelength of the ultrasound wave. Many different recipes have been used and are reviewed in Law et al.,

(1989) and Hoskins, (2008). The IEC criteria emphases the creation of a BMF that more precisely matches the viscous and acoustic properties of blood, two examples of blood mimic which attempt this have been described by Boote and Zagzebski (1988) and Ramnarine et al., (1998, 1999). Table 1.7 shows the physical properties of these BMFs.

Table 1.7 Physical properties of 2 BMFs

Physical property	**Boote & Zagzebski (1988)**	**Ramnarine et al. (1989)**
Scatterer type	Polystyrene	Nylon
Scatter concentration (mm^{-3})	17	300000
Scatter size (μm)	30	5
Density ($kg\ m^{-3}$)	1043	1037
Viscosity (mPa s)	-	4.1
Backscatter ($f^4\ m^{-1}\ Sr^{-1}$)	Blood mimicking	Blood mimicking
Speed of sound ($m\ s^{-1}$)	1546	1548
Attenuation ($dB\ cm^{-1}\ MHz^{-1}$)	0.1 dB cm^{-1} at 1 MHz	0.05

Vessel mimicking materials

Various tubing materials have been employed in flow phantoms. Many were commercially available tubing which had the incorrect acoustic properties to mimic human vessels. These include glass, plastic, Teflon®, latex, C-flex®, heat shrink and neoprene (Law et al., 1989), the acoustic properties of some of these materials is shown in Table 1.8. C-flex® (Cole-Parmer, Walden, UK) is one of the more commonly used commercially available tubing materials in terms of acoustic properties, but even for a 0.8 mm inner diameter (i.d.) tube it gives significant distortion of the Doppler spectrum due to its very high attenuation coefficient (Teirlinck et al., 1998). C-flex® tubing has a reported speed of sound and attenuation of 1556 $m\ s^{-1}$ and 5.6 $dB\ cm^{-1}\ MHz^{-1}$,

respectively at 5 MHz and 22°C (Hoskins, 1994). In an attempt to reproduce realistic physical models of human vasculature, excised vessels or vessels from cadavers have been used (Dabrowski et al., 1997; Dabrowski et al., 2001). However, excised arteries are susceptible to geometric and acoustic changes if they are not stored properly (Wilhjelm et al., 1997). It is difficult to characterise excised vessels and especially to reproduce many copies of an exact specified geometry. Also, the use of excised vessels requires strict attention to issues of biological safety and to legislation regarding the use of human tissues. Therefore, it is desirable to use materials which can be well characterised and easily reproduced for *in-vitro* testing. One such material which has the ability to be moulded into different geometries and has suitable acoustic and mechanical properties similar to tissue is polyvinyl alcohol cryogel (PVA C). The characterisation of PVA C as a vessel mimicking material (VMM) for the anatomically realistic renal artery phantoms is discussed in section 2.1.3.

Table 1.8 Acoustic properties of materials used to mimic vessels (Hoskins, 2008)

	Material	**Density (kg m^{-3})**	**Speed of sound (m s^{-1})**	**Acoustic impedance 10^6 (Kg m^{-2} s^{-1})**	**Attenuation coefficient (5 MHz) (dB cm^{-1})**
Hoskins (2007)	Silicone rubber	1140	1005	1.15	23
Hoskins (1994)	C-flex	886	1556	1.38	28
Hoskins (1994)	Latex	921	1566	1.44	26
Hoskins (1994)	Norprene	975	1571	1.53	42
Selfridge (1985)	Polyethylene	900	1950	1.76	2.4
Hoskins (1994)	Heatshrink	960	1979	1.90	31.1
Hoskins (1994)	Perspex (acrylic)	1190	2756	3.28	4.4

1.7.2 Doppler flow phantoms

Many different types of flow phantoms have been developed and have been reviewed by Hoskins, (2008), IPEM, (1994) and Law et al., (1989). The simplest type of flow phantom to construct consists of a straight tube (rubber or plastic) embedded in a TMM through which BMF is pumped (Douville et al., 1983; Frayne et al., 1993; Law et al., 1989). These phantoms lack the complexity of human vessels, such as irregular lumens and the presence of stenosis. Wall-less phantoms overcame these problems and allowed for more complicated geometries to be produced by using lost core casting techniques (Poepping et al., 2002; Smith et al., 1999).

1.7.3 Anatomically realistic flow phantoms

To date the majority of work on anatomically realistic flow phantoms has concentrated on the development of realistic carotid flow phantoms (Frayne et al., 1993; Meagher et al., 2007; Poepping et al., 2002; Poepping et al., 2004; Smith et al., 1999; Watts et al., 2007). Frayne et al., (1993) described the manufacturer of a planar carotid bifurcation phantom. A wax core of the carotid artery was constructed from a mould created using a milling machine. Polyester resin was painted onto this wax model to create a vessel of the carotid artery with bifurcation. This phantom was used in a comparative study of x-ray, MRI and ultrasound. The disadvantage of this technique was that the wax had a tendency to be brittle and break at narrow points in the model. Using a low melting alloy instead of the wax overcame this problem as used by Smith et al., (1996, 1999) and allowed the creation of stensosed carotid vessels.

Poepping et al., (2002) overcame problems of leaking and TMM rupturing in the wall-less carotid phantoms by partially equalising the pressure in the vessels. This was achieved by using a polyethylene lid and two small holes between the TMM surface and the downstream vessels which allowed the BMF to flow into the space between the TMM and the lid. Poepping et al., (2004) further developed the carotid phantoms by using a thin silicone wall to provide mechanical stability.

The creation of wall-less nonplanar carotid bifurcation phantoms were described by Watts et al., (2007) and Meagher et al., (2007). A MRI data set from a healthy volunteer was used to generate of computer model of the carotid artery. A range of symmetrical stenosis was manually added to the computer model. Rapid prototyping was used to generate of core of low melting alloy. This was then mounted in a container and TMM poured in. When set the phantom was placed in a water bath to allow the metal core to melt out leaving an anatomically realistic wall-less carotid artery vessel.

7.1.4. Perfusion phantoms

A range of perfusion phantoms have been developed based on dialysis filters (Hindle and Perkins, 1994; Ugolini et al., 2000; Veltmann et al., 2002; Yeh et al., 2003). The majority of these studies were undertaken with the filter immersed in a tank containing either degassed water or castor oil instead of a TMM which is the first limitation of these phantoms. Another limitation of these previous studies is that the blood analogue used was non-degassed water without the presence of scatterers. Although capillary perfusion phantoms, based on dialysis filters offer a simple and economical method of investigating perfusion and have some of the correct dimensions, they lack some of the

characteristics which are essential for blood perfusion purposes. Primarily, the capillaries in these phantoms are parallel, with flow in one direction, and therefore, do not mimic the *in-vivo* situation of a complex fractal structure of the vessel tree of the kidney.

Other perfusion phantoms have consisted of a nest of vessels with an inner diameter of 0.28 mm to replicate the microcirculation (Eriksson et al., 1995). In the phantom described the vessels run randomly in between each other in an effort to obtain a flow that is both spatially and directionally evenly distributed. Although this phantom overcame the problem of the capillaries running parallel to each other, only one size of vessel was used. Realistically, there are arterioles, capillaries and venules with different diameters, lengths and flow speeds. Another earlier suggestion was to produce slow flow by diffusing blood analogue through reticulated foam in order to mimic perfusion (McDicken, 1986). The foam would have to be encased to prevent fluid from flowing outside the flow circuit and in order to obtain suitable flow rates. These phantoms have been designed to mimic microcirculation but not the microcirculation of a specific organ.

7.1.5 Validation of ultrasound techniques using flow phantoms

To date, the majority of such work has concentrated on the development of realistic carotid flow phantoms as discussed in above (Poepping et al., 2004; Smith et al., 1999). These phantoms have proved to be powerful research tools and have helped to improve the understanding of normal hemodynamic patterns and their correlation with the development of vascular stenosis at the bifurcation of the carotid artery. Duplex ultrasound has now replaced DSA as the technique most widely used to quantify

stenosis grade in the carotid arteries and to select patients for subsequent tests, or surgical or medical therapy (Grant et al., 2003; Netuka et al., 2006). Advancements in new applications in renal blood flow imaging such as the use of UCAs with CSI, offers promise of improvements in the detection of abnormal renal microvascular and macrovascular disorders (Correas et al., 2006). Comprehensive *in-vitro* experimentation is required to optimise the performance of UCAs for renal imaging. Currently there are no anatomically realistic renal artery phantoms available and current perfusion phantoms are not of sufficient sophistication to evaluate imaging techniques effectively in the area of complex renal artery and kidney geometry, or in the presence of different grades of stenosis (Yim et al., 2004).

1.8 THESIS AIMS

As discussed in section 1.3 the early diagnosis of a RAS offers the possibility of treatment using drugs, thereby improving the long-term prognosis for the patient. Furthermore, this would produce a substantial saving to the Irish healthcare system, considering the cost of a year's dialysis for one patient is approximately €50k. The objective of this project is to evaluate current and emerging ultrasound techniques capable of diagnosing all grades of blockages in the renal artery. As discussed in sections 1.4 and 1.6, clinical studies performed to date assessing the diagnostic performance of US, MRI and CT have been inconclusive in their findings.

The main aim of this thesis is to develop anatomically realistic renal artery flow phantoms with increasing degrees of stenosis and a contrast enhanced kidney perfusion phantom to enhance the performance evaluation of ultrasound scanners in kidney diagnosis, to improve training of technologists using these phantoms and facilitate improvement in the diagnosis of disease in the renal vasculature. These phantoms may act as standard reference phantoms which will allow evaluation of current and emerging ultrasound techniques such as CSI. UCAs offer considerable potential for renal imaging which has been validated with the recent publication of the EFSUMB Guidelines for CEUS (Correas et al., 2009). Also these phantoms will be primarily designed as ultrasound flow phantoms, using materials which are also compatible with DSA, MRI and CT. Using these multi-modality phantoms it should be possible to make direct quantitative comparisons of the phantom dimensions between the different imaging modalities using standard phantoms as references. The results obtained from this study could be invaluable both for performance evaluation of all imaging modalities used to

determine RAS and for future development of non-invasive techniques for detecting RAS.

The goal of this thesis is the development of anatomically realistic renal artery flow phantoms and a contrast enhanced kidney perfusion phantom. The following are the specific tasks that are addressed in the subsequent chapters to achieve this goal:

1. Characterisation of vessel mimicking material for anatomically realistic renal artery flow phantoms
2. Development of wall-less and walled anatomically realistic renal artery flow phantoms with increasing degrees of stenosis and capable of replicating flow velocities found *in-vivo*
3. Flow experimentation using anatomically realistic renal artery flow phantoms
4. Evaluation of the effect of fat mimicking layer on maximum velocity measurements
5. Implementing a comparative study between four of the imaging techniques used to detect renal artery stenosis (US, DSA, MRI and CT)
6. Development of a kidney perfusion phantom for contrast enhanced perfusion studies
7. Performing contrast enhanced renal phantom studies

1.9 THESIS OUTLINE

In Chapter 2, the acoustic and mechanical properties of the vessel mimicking material, polyvinyl alcohol cryogel (PVA C), for the anatomically realistic renal artery flow phantoms are characterised. The optimum number of freeze-thaw cycles required for PVA-C to exhibit similar acoustic and mechanical properties to the human artery walls is identified.

In Chapter 3, the development of a range of novel anatomically realistic renal artery flow phantoms with increasing degrees of stenosis is described. Three types of phantom were developed; wall-less and walled phantoms for flow experimentation and a wall-less multi-modality phantom which is used in the comparative study described in Chapter 6.

In Chapter 4, the flow experimentation using steady state velocities using the wall-less and walled anatomically realistic renal artery flow phantoms developed is described. In addition current ultrasound technology was evaluated to determine if it can distinguish changes in maximum velocity measurements due to the presence of a range of stenosis in the anatomically realistic renal arteries.

In Chapter 5, the effects of an overlying fat mimicking layer on maximum velocity measurements are reported as found in an investigation using a string phantom, a simple flow phantom and the anatomically realistic renal artery flow phantoms. By studying the effect of the fat mimicking layer using the Doppler test devices, the errors in maximum velocity measurements can be determined and their implications for measurements in patients with renal artery stenosis evaluated.

Chapter 6 reports on the use of the range of novel multi-modality anatomically realistic renal artery phantoms described in Chapter 3 to evaluate and compare current imaging techniques used to detect RAS (US, MRI, CT and DSA).

Chapter 7 presents the development of a perfusion phantom which attempts to mimic the vasculature of the kidney (diameter < 200 μm with velocity < 3 mm s^{-1}). This perfusion phantom is intended to be a significant tool for testing and validating ultrasound techniques to assess perfusion within organs such as the kidney.

In Chapter 8, an evaluation of an emerging technology in the area of RAS, namely CEUS using the newly developed anatomically realistic renal artery flow phantoms and kidney capillary perfusion phantom is described. The Doppler dynamic range of the ultrasound scanner was evaluated specifically for renal imaging.

Chapter 9 summarizes the major conclusions arising from this work and discusses future directions for the technical development of anatomically realistic flow and perfusion phantoms of the renal vasculature and their exploitation and application in evaluating current and emerging ultrasound technologies.

CHAPTER 2 PHANTOM MATERIAL CHARACTERISATION

2.1 INTRODUCTION

This chapter describes the characterisation of the acoustic properties of a tissue mimicking material (TMM) and vessel mimicking material (VMM) as well as the mechanical properties of the VMM. The acoustic properties of the blood mimicking fluid (BMF) were not evaluated in this study as the experimental set-up is very complex as the fluid is required to be flowing to obtain the even distribution of scatterers. Furthermore its production has previously been shown to be very reliable and reproducible (Ramnarine et al., 1998; Ramnarine et al., 1999).

To ensure the reproducibility of the TMM production the acoustic properties (speed of sound, attenuation coefficient and relative backscatter) were determined for three separate batches of an agar-based TMM. This study also investigated if PVA C exhibited similar acoustic and mechanical properties to human artery walls and therefore if it was a suitable VMM for the renal flow phantom. The effect of the number of freeze-thaw cycles on the speed of sound, attenuation coefficient, and relative backscatter were investigated. Furthermore, the effect of the addition of scatterers and the effect of an antibacterial agent Benzalkoniumchloride (Bc) on the acoustic properties of PVA C with increasing number of freeze-thaws cycles were studied. The variation in PVA C sample dimensions with increasing number of freeze-thaw cycles was also determined.

2.1.1 Acoustic properties of phantom components

It is very important to choose phantom materials whose acoustic characteristics match those of real tissues and blood. This section defines the acoustic properties which are important when developing phantoms which mimic tissue, vessels and blood.

Speed of sound

Speed of sound is the phase velocity of sound waves in the medium. The speed at which a sound wave travels is determined by the medium it is travelling. The material properties which determine the speed of sound are density and stiffness. Ultrasound travels at a high speed in materials of low density and high stiffness, whereas in materials of high density and low stiffness ultrasound travels at a low speed. This is expressed mathematically as,

$$c = \sqrt{k/\rho} \qquad \textbf{Equation 2.1}$$

where c is the speed of sound (m s^{-1}), k is the stiffness (Pa) and ρ the density (kg m^{-3}) of the material.

Acoustic impedance

Acoustic impedance is a measure of the response the particles in the medium, to a wave of a given pressure. The magnitude of the reflection is dependent on the acoustic impedance of the tissues on the two sides of the interface. It is defined as the product of the density and the speed of sound in the material and is denoted by Z.

$$Z = \rho c \qquad \textbf{Equation 2.2}$$

Scattering

Scattering may also occur when ultrasound is incident on an interface. The size of the interface, d, relative to the wavelength, λ, determines whether reflection or scattering occurs. When $d > \lambda$ reflection occurs, when $d \sim \lambda$ stochastic scattering occurs and when $d < \lambda$ Raleigh scattering occurs. Small interfaces ($d \sim \lambda$) scatter the ultrasound unequally in all directions, with preferential scattering back towards the transducer (anisotropic scattering). Interfaces smaller than the wavelength are referred to as Raleigh scatterers, scattering the wave uniformly in all directions (isotropic).

Absorption

As the ultrasound wave travels in a material, some of its mechanical wave energy is converted to heat energy through processes collectively called absorption. Absorption is strongly dependent on the material composition and structure. Absorption is also dependent on the frequency, being greater at higher frequencies.

Attenuation

As the ultrasound wave travels in a material its amplitude is reduced due to attenuation. Attenuation in biological tissues includes the effect of refraction, reflection, scattering and absorption. Attenuation in biological tissues includes the effect of refraction, reflection, scattering and absorption and is also described by an exponential function,

$$A = A_o \exp(-az) \qquad \textbf{Equation 2.3}$$

Where a is the attenuation coefficient, which is the sum of the scattering and absorption coefficients ($a = a_s + \alpha$)

Attenuation coefficient

Attenuation coefficient at a specified frequency is the fractional decrease in plane wave intensity per unit lath length due to scattering and absorption in the medium (units dB cm^{-1}).

Backscatter

Backscatter coefficient at a specified frequency is the mean acoustic power backscattered into a unit solid angle per incident intensity per unit volume. It is expressed in cm^{-1} sr^{-1}. Absolute backscatter coefficient measurements require a normalisation procedure to remove system-specific parameters. Relative backscatter measurements are made in dB relative to the signal from a flat reflector at the transducer focus.

2.1.2 Tissue mimicking components

It is very important to choose phantom materials whose speed of sound and attenuation characteristics matches those of real tissues and blood. Since a mismatch in the speed of sound between the vessel and the surrounding tissue and blood mimic, can produce non-clinical reflection and refraction of the ultrasound beam causing unrealistic distortion of the received Doppler signal. Similarly, unrealistic attenuation of the ultrasound beam in the different path lengths traversed in the mimicking materials can result in further Doppler signal distortion from the typical clinical range. The effects of these phenomena in terms of mean velocity estimations have been documented in the literature (Evans, 2000). The International Electrotechnical Commission (IEC) Report 61685 has specified a set of acoustic parameters for a standard flow phantom over a frequency range of 2 MHz – 10 MHz (IEC, 2001), as shown in Table 2.1. However, in

that specification no specific acoustic parameters were specified for a vessel mimicking material.

Table 2.1 IEC specifications for TMM and BMF, where f is the acoustic working frequency (Hz)

Material	Density ($kg\ m^{-3}$)	Speed of sound ($m\ s^{-1}$)	Attenuation ($dB\ cm^{-1}\ MHz^{-1}$)	Backscatter ($f^4\ m^{-1}\ sr^{-1}$)
TMM	1040 ± 100	1540 ± 15	0.5 ± 0.05	$(1 - 4) \times 10^{-28}$
BMF	1050 ± 100	1570 ± 30	<0.1	$(1 - 10) \times 10^{-31}$

Tissue mimicking material

The TMM used should mimic the speed of sound, attenuation coefficient and scattering coefficient of soft tissue. The TMM should have similar acoustic properties to those values presented in Table 2.1. The attenuation coefficient should be approximately proportional to the frequency. The IEC specifications recommended an attenuation coefficient variation with frequency for use in phantom mimicking materials ranging from $0.3 - 0.7\ dB\ cm^{-1}\ MHz^{-1}$. Very low backscatter is desirable in the range $(1 \text{ to } 4) \times 10^{-28} \times f^4\ m^{-1}\ sr^{-1}$, and it has been found that by adding appropriate scatterers one can control the backscatter coefficient (IEC, 2001).

For the anatomically realistic renal flow phantoms an agar-based TMM developed as part of the European Commission (EC) funded project was used (Teirlinck et al., 1998). This TMM is very well characterised and has good reproducibility (Brewin et al., 2008; Browne et al., 2003; Teirlinck et al., 1998). Table 2.2 shows the component materials and its manufacture is described elsewhere (Ramnarine et al., 2001).

Table 2.2 Weight composition of the TMM

Component	Weight composition (%)
Distilled water	82.97
Glycerol	11.21
Silicon carbide (400 grain)	0.53
Aluminium oxide (3 μm)	0.94
Aluminium oxide (0.3 μm)	0.88
Benzalkoniumchloride	0.46
Agar	3.0

The glycerol (Sigma Aldrich, MO, USA) is the main component used to modify the speed of sound in water. The benzalkoniumchloride (Bc) (Quatchem Ltd., Oldham, UK) prevents fungal growth. The aluminium oxide (Al_2O_3) powders (Logitech, Glasgow, UK) affect the attenuation and with the current concentration provide a linear dependence with frequency. The silicon carbide (SiC) (Logitech, Glasgow, UK) and Al_2O_3 powders modify the backscatter to more closely mimic human tissue. This TMM has a reported speed of sound of 1541 ± 3 m s^{-1} and attenuation coefficient of 0.52 ± 0.03 dB cm^{-1} MHz^{-1} (Teirlinck et al., 1998).

Blood mimicking fluid

The specifications for the basic BMF acoustical values are presented in Table 2.1. The BMF recommended in the IEC specifications was used in the anatomically realistic flow phantom developed in this work and its composition (in % weight) is presented in Table 2.3 (Ramnarine et al., 1998).

Table 2.3 Weight composition of the BMF

Component	Weight composition (%)
Distilled water	83.86
Glycerol	10.06
Dextran	3.36
Oragsol® (5 μm)	1.82
Synperonic A7	0.90

The water and glycerol solution is the main determinant of the speed of sound and the density of the BMF. Dextran (Sigma Aldrich, MO, USA) increases the viscosity and Synperonic A7 (Conservation Resources, Oxford, UK) is a low foaming surfactant which aids in the dispersion of the scattering particles.

Vessel mimicking material

For the development of an anatomically realistic renal phantom it is important to choose a VMM such that its speed of sound and attenuation coefficient values matches those of blood healthy vessels. Currently there are no IEC specifications for the acoustic parameters of VMMs other than that they should be the same as the TMM properties. A large number of tubing materials have been used to mimic vessels in flow phantoms as discussed in section 1.7.1. These materials are not suitable to mimic the vessel in the anatomical flow phantom as it is commercial tubing with fixed dimensions; it is not possible to create the geometrical features such as blockages and curvatures as are found in the renal artery. Anatomically realistic phantoms of the carotid arteries have been produced using clinical post-mortem arteries (Bale-Glickman et al., 2003). But

this method is not ideal as there are ethical issues associated with this and such vessels do not have long-term stability.

The acoustic properties of vessels within the body can vary greatly from the value for average soft tissues and thus, this should be a consideration when specifying the acoustic properties of a VMM (Duck, 1990). Alterations in the tissue-composition of arteries due to increasing age and disease progression are associated with alteration in both acoustic and mechanical properties (Hoskins, 2007). The reported speed of sound values found for healthy arteries vary from 1501 - 1534 m s^{-1} to 1568 - 1616 ± 23 m s^{-1} (Duck, 1990; Greenleaf et al., 1974; Hoskins, 2008). For diseased arteries speed of sound values of 1526 – 1760 m s^{-1} have been reported where 1760 m s^{-1} refers to the calcified region of the artery (Saijo et al., 2004; Saijo et al., 1998). Greenleaf et al., (1974) measured attenuation coefficients of 0.6 dB cm^{-1} MHz^{-1} at 10 MHz in healthy arteries. Hoskins et al., (2007) combined the data from Fraser et al., (2006) and Lockwood et al., (1991) to give a relationship of, $1.026f^{1.121}$, between attenuation and frequency describing the attenuation of healthy arteries from 5 to 56 MHz. The attenuation of diseased arteries is significantly higher than healthy arteries with a mean of 11 ± 4 dB cm^{-1} MHz^{-1} reaching 25 ± 1 dB cm^{-1} MHz^{-1} in the calcified regions of the artery (Saijo et al., 2004; Saijo et al., 1998).

In terms of the Doppler signal from blood, the vessel wall, the blood and the soft tissue surrounding the wall are the important features. Any mismatch between the curved vessel wall and the adjacent blood and soft tissues will cause partial focusing or defocusing of the incident beam, with alteration in the acoustic pressure field and, *via* the change in the beam direction, in the Doppler shift frequencies (Hoskins, 2008).

Hoskins, (1994) used a thin-walled model of healthy artery uniformly insonated by an incident beam to show that mismatch causes loss of low Doppler frequencies, and that for tissue-equivalence the loss of low-frequency data are negligible.

2.1.3 Polyvinyl Alcohol Cryogel

Polyvinyl alcohol cryogel (PVA C) was chosen as the material to replicate the renal artery in the anatomically realistic flow phantoms. Polyvinyl alcohol (PVA) is a non-toxic, industrial compound which when combined with water readily forms a gel. It is derived from the hydrolysis of poly(vinyl acetate), a process that does not go to completion, resulting in a final product that is a mixture of PVA and poly(vinyl acetate) (Surry et al., 2004). For this study 10% PVA powder (London Health Sciences Centre, London, Canada) was combined with water to form a PVA gel. The freeze-thaw cycles transform the PVA from an aqueous gel to a rigid material called PVA C by facilitating intermolecular cross-linking between the hydroxyl groups and thus forming crystallites. A temperature of -20°C is required to promote crystallite formation. The number and nature of the freeze-thaw cycles vary the acoustic and mechanical properties of the material produced.

PVA C has a wide variety of applications in the biomedical field. It was chosen as the VMM for the anatomically realistic renal artery phantoms as it has been successfully used in phantom designs for ultrasound and MRI in previous studies (Chu and Rutt, 1997; Dineley et al., 2006; Surry et al., 2004). Most importantly it has the ability to be produced in variable geometries although it has been reported that the dimensions of PVA C samples change with increasing freeze-thaw cycles (Chu and Rutt, 1997). Therefore, creating accurate PVA C vessels is only possible after characterising the

change in dimensions after the required number of freeze-thaw cycles. Furthermore, it has appropriate acoustic properties and elastic moduli to mimic those of vessels as shown in Table 2.4.

Table 2.4 Acoustic and mechanical properties of PVA C and *in-vivo* tissues

	Speed of sound ($m\ s^{-1}$)	**Attenuation Coefficient ($dB\ cm^{-1}\ MHz^{-1}$)**	**Young's Modulus (kPa)**
Soft tissue	1540[a]	0.3-0.6[a]	
Aorta (human)	1501-1534[b], 1616[a]	0.6 at 10 MHz[b]	70-100[c]
PVA C (10%)	1522-1545[d]	0.5-1.0[d]	24-135[e]
PVA C (15%)	1546 – 1584[f]	0.2 - 0.4[f]	190-1840[g]

[a](Duck, 1990), [b](Greenleaf et al., 1974), [c](Kawasaki et al., 1987), [d](Surry et al., 2004), [e](Duboeuf et al., 2007), [f](Dineley et al., 2006), [g](Chu, 1997)

The primary disadvantage of PVA C is the difficulty in preparing the material. The process is time-consuming as it takes a number of days to complete the required freeze-thaw cycles. Due to the many grades of PVA powder available the exact molecular structure, weight and impurities may vary between manufacturers and therefore it is recommended that the same type of PVA powder be used throughout a study.

Limitations of previous studies

A number of studies have investigated the effect of freeze-thaw cycles on the acoustic and mechanical properties of PVA C (Chu and Rutt, 1997; Fromageau et al., 2003; Fromageau et al., 2007; Surry et al., 2004; Dineley et al., 2006). In each of these studies different factors such as the concentration of PVA powder used to form the PVA C or

different freeze-thaw cycle times were employed. Therefore there is a need to carry out a more comprehensive study of both the acoustic and mechanical properties of PVA C for a range of freeze-thaw cycles.

Another feature of PVA C is that it is hydrophilic and if exposed to air there is a possibility that bacterial growth can occur. It is therefore advantageous to add an anti-bacterial agent to the PVA C which can help to increase the life of the sample. Chu, (1997) stated that the addition of an anti-bacterial agent changes the VMM properties slightly but no data were presented to support this statement. In this work the addition of an anti-bacterial agent, 10% benzalkoniumchloride solution (Bc), was investigated to determine if the acoustic properties of the PVA C samples were altered and if so to quantify and control for the magnitude of this change.

To date there are no published studies on the backscatter properties of PVA C. Chu, (1997) reported that increasing the number of freeze-thaw cycles resulted in an increase in the cross-linking and an associated increase in scattering occurred in the samples. Other studies have added scatterers to the liquid PVA in the preparation stages. These included the addition of 400-grain silicon carbide to 15% PVA and the addition of silica powder (1% by weight concentration) to 10% PVA (Dineley et al., 2006; Fromageau et al., 2003).

2.2 METHODOLOGY

2.2.1. Acoustic characterisation

To ensure reproducible production of the TMM, three separate batches of TMM samples (diameter 50 ± 0.1 mm, thickness 4.6 ± 0.7 mm) were prepared as described by Teirlinck et al., (1998). The acoustic properties of each of the three TMM samples were determined. Four different recipes of PVA C were prepared for the acoustic characterisation study, the composition of each batch and the number of freeze-thaw cycles they underwent are presented in Table 2.5.

Table 2.5 Composition and number of freeze-thaw cycles (f/t) for each batch

Batch No.	Composition	Freeze-thaw cycles
1	PVA C	1-6
2	PVA C + Bc1 (0.46%)	2, 4, 6
2	PVA C + Bc2 (0.92%)	2, 4, 6
2	PVA C + Bc3 (1.40%)	2, 4, 6
3	PVA C + SiC (0.75%) + Bc1	2, 4, 6
3	PVA C + SiC (0.75%) + Bc2	4, 6
3	PVA C + SiC (0.75%) + Bc3	4, 6
4	PVA C + SiC (0.75%)	2, 4, 6
4	PVA C + Al_2O_3 (0.75%)	4

The PVA C was prepared by heating a sealed container of 10% PVA gel in a water bath at 100 ± 1 °C for 60 minutes. The PVA gel was divided into 4 batches. The first batch contained PVA gel only. The second batch was further divided into 3 groups containing 3 different concentrations of Bc which were added to the liquefied PVA and slowly rotated to ensure even distribution. The third batch of PVA gel was divided into 3

groups, each containing one of the 3 concentrations of Bc and 0.75% per volume SiC. Care was taken when adding the scatterers to avoid clumping. The solution was continually stirred and slowly poured into moulds. For the fourth batch 0.75% per volume SiC was added to half of the batch and 0.75% Al_2O_3 (0.38% 0.3μm Al_2O_3 and 0.38% 3μm Al_2O_3) to the second half of the batch. From each batch 15 ml of liquefied PVA was injected into 6 Petri dishes (50 (diameter) × 15 (height) mm). The dishes were sealed with Parafilm® M (Pechiney Plastic Packaging, Il, USA) with 10% volume left for expansion during freezing. They were left to stand upright for up to 24 hours to allow for bubbles to rise and the material to settle. The samples containing additional scatterers were only left to stand for 8 hours as this ensured the material remained suspended in the PVA. Settling of the material on the bottom of the petri dishes was observed for longer periods.

For this study 1 freeze-thaw cycle consisted of 14 hours freezing (-20°C), and 10 hours thawing (room temperature ~ 22 ± 0.5°C). The moulds were placed in a freezer for 14 hours at -20°C after which time they were removed and allowed to thaw at room temperature for 10 hours. This step was counted as the first freeze-thaw cycle. The freeze-thaw cycles were repeated until the desired number of freeze-thaw cycles were completed (see Table 2.1). From previous studies it was decided that 1 - 6 freeze-thaw cycles were sufficient to obtain the desired range of acoustic properties similar to *in-vivo* arteries (Dineley et al., 2006; Surry et al., 2004). Once the required number of freeze-thaw cycles were completed the PVA C samples were removed from their moulds and stored in distilled water at 5°C to prevent evaporation and bacterial growth.

Acoustic measurements

The speed of sound (c), attenuation coefficient (α), and the relative backscatter (μ) of the TMM and PVA C samples were measured using the pulse-echo substitution method (Schwan and Carstensen, 1952). All measurements were performed using the scanning acoustic macroscope (SAM) system (Ultrasonic Sciences Limited, Fleet, UK) in the Medical Physics Unit at the University of Edinburgh. It allows for the collection and averaging of ultrasound data over a defined area of the sample which allows spatial averaging and thereby improves SNR. The SAM system consists of a Master System Controller which is a general purpose analogue and digital input/output board allowing software control of the system, a 1 - 20 MHz pulser receiver, an 8-bit 100 MSps analogue to digital convertor (ADC), a stepping motor control system, and a temperature monitored water tank. The whole system including the stepping motor which facilitated scanning was controlled by a personal computer (Dell model). A schematic diagram of the equipment is shown in Figure 2.1(a) and a photograph is shown in 2.1(b).

The two transducers used in this study were a 3.5 MHz (Ultrasonic Sciences Limited, Fleet, UK) and 7.0 MHz (Panametrics, Olympus, MA, USA) transducers each acted as both as a transmitter and a receiver with a frequency range of 2.65 - 5.12 MHz and 5.50 - 10.50 MHz, respectively. The technical parameters of each transducer used are given in Table 2.6. The acoustic properties of the TMM and VMM were tested at 20 ± 0.5 °C.

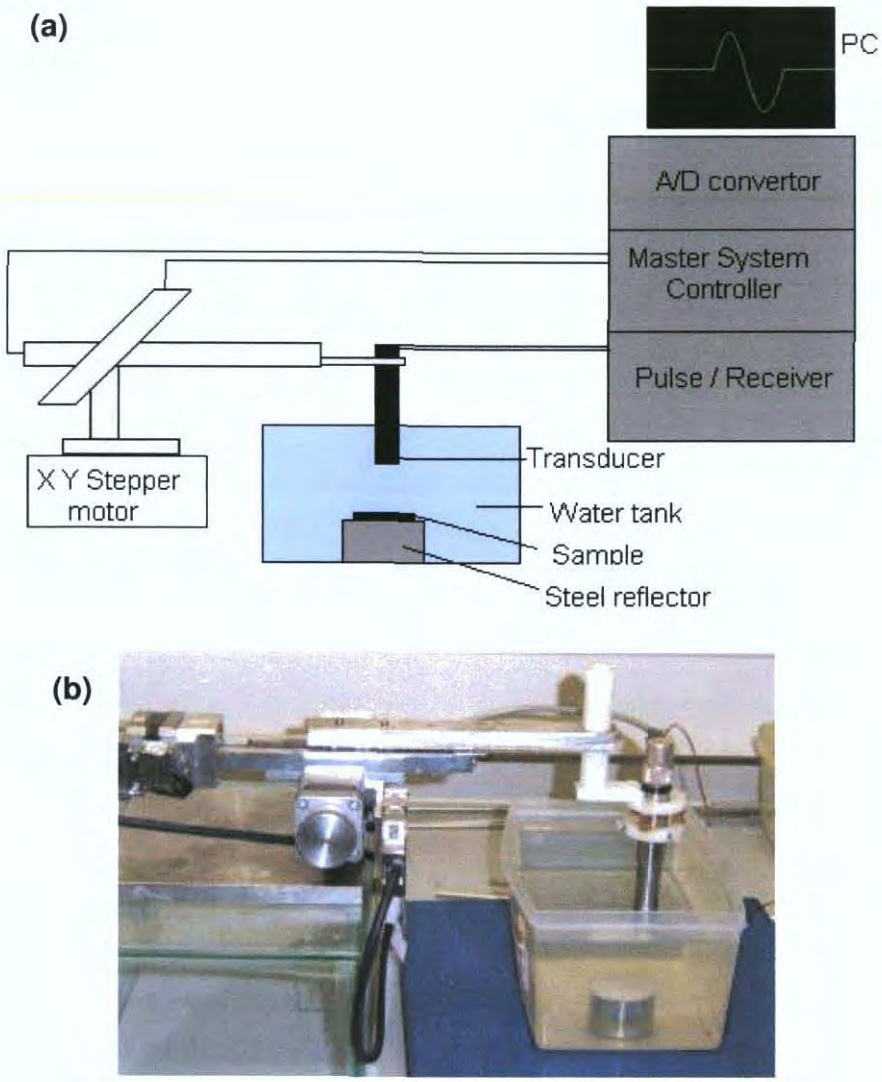

Figure 2.1 (a) Schematic diagram of the scanning acoustic macroscope (b) photograph showing the set-up for sample scan, transducer focused on surface of steel reflector

Table 2.6 Characteristics of the transducers used in the acoustic study

Frequency	**3.5 MHz**	**7.0 MHz**
Crystal diameter (mm)	9.9	11.8
Focal length (mm)	58	54
Centre frequency (MHz)	3.89	7
6 dB bandwidth (%)	63.4	71

Data acquisition

Measurements were carried out in a temperature monitored water tank. Degassed water was poured in to the tank at least 3 hours prior to measurement to allow the set-up to reach thermal equilibrium with its surroundings. Immediately prior to measurement, the submerged transducer face was inspected for air bubbles. If air bubbles were present they were removed by syringing water across the face of the transducer. The temperature of the water was recorded and monitored throughout the data acquisition. A highly polished steel reflector was placed in the focus of the transducer as shown in Figure 2.2. To ensure the ultrasound path length was uniform adjustments were made to ensure the target and transducer were coaxial. The transducer performed two raster scans with a set scan size (16 x 16 mm) and step size (1 x 1 mm increments), the first was a reference scan, which was of the steel reflector and the second, sample scan with the sample placed on top of the steel reflector. At each position of the transducer the reflected RF signal from the steel reflector was digitised at a sampling rate of 100 MHz and stored for offline analysis. For both transducers the driving voltage was set at a relatively low value of 100 V in order to minimise non-linearity effects (Duck, 2002; Zeqiri, 1992). For backscatter measurements the sample was positioned with the transducer focus just below the sample surface as shown in Figure 2.2. This was to minimise attenuation loss through the sample and to gate out the sample/water interface reflection. For the backscatter measurements the driving voltage was increased to 300 V to improve the SNR which allowed the much smaller backscatter signals to be located and measured.

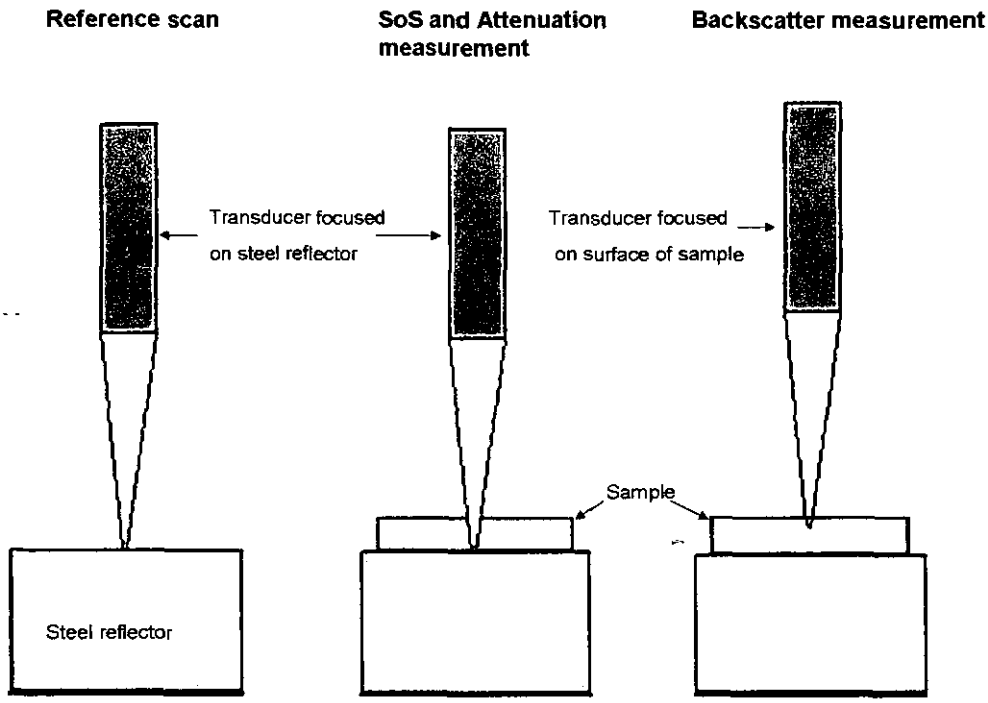

Figure 2.2 Schematic diagram of experimental set-up for speed of sound (sos), attenuation and relative backscatter measurements

Data analysis

Using an in-house MATLAB (MathWork Inc., MA, USA) program developed by the Medical Physics Unit in the University of Edinburgh the fast Fourier transform (FFT) of each of the RF signals was obtained. To improve the SNR averaging was performed using the 256 FFTs (one from each raster position). The acoustic properties of the PVA C samples were determined by comparing the resulting frequency spectra following measurements by the transducer without and with the sample in place. Figure 2.3 shows a plot of the reference and sample RF pulses from which a window size was chosen to encapsulate both the reference and sample pulse which were analysed.

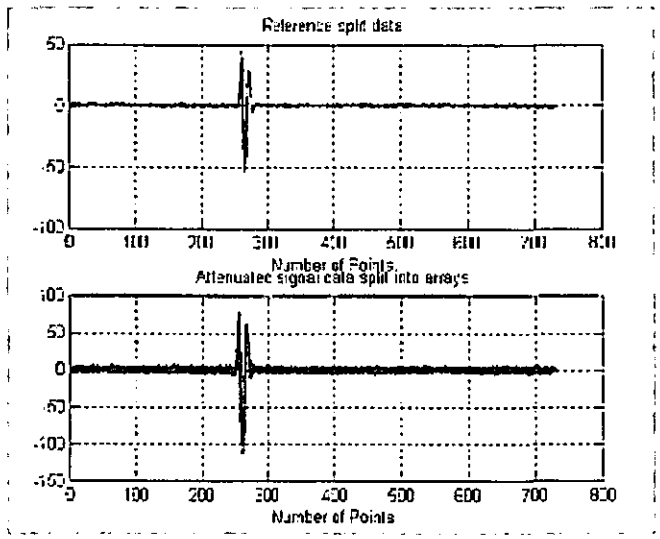

Figure 2.3 Plot of the reference and sample RF pulses

Speed of sound

Measurement of the speed of sound through the sample was achieved by calculating the difference between the peaks of the RF pulse from the steel reflector without and with the sample in the path (the time shift, ΔT). The reference time (t_r) of flight measured by the system with no sample in the path is given by:

$$t_r = \frac{2D}{c_w} \qquad \textbf{Equation 2.4}$$

where D is the distance between steel reflector and transducer (measured using ruler) and c_w, is the speed of sound through water. Mean speed of sound in water was 1486 m s^{-1} at 21.5°C (Kaye and Laby, 1995). The time of flight with the sample (t_s) in the path is given by the time of flight through the water path plus the time of flight through the sample,

$$t_s = \frac{2D - 2d_s}{c_w} + \frac{2d_s}{c_s} \qquad \textbf{Equation 2.5}$$

where c_s is the speed of sound through the sample and d_s is the sample thickness. The time shift (ΔT) in the position of the waveform peak from the steel reflector with and without the sample in the path is given by,

$$\Delta T = t_r - t_s = \frac{2d_s}{c_w} - \frac{2d_s}{c_s} \qquad \textbf{Equation 2.6}$$

The average speed of sound over the total sample path is thus calculated using the formula,

$$\frac{1}{c_s} = \frac{1}{c_w} - \frac{\Delta T}{2d_s} \qquad \textbf{Equation 2.7}$$

Attenuation coefficient

Frequency dependent attenuation was determined by performing a FFT on the RF signals from the steel reflector without and with the sample in the path. The attenuation in dB was calculated from the log difference between the spectra. The calculation was performed on each of the RF signals stored from the raster scan using Equation 2.8,

$$\alpha(x, y, f) = \frac{20}{2d_s} \log_{10} \frac{A(x, y, f)}{A_o(x.y.f)} \quad (\text{dB cm}^{-1}) \qquad \textbf{Equation 2.8}$$

where d_s is the sample thickness, $A(x,y,f)$ is the magnitude spectrum at frequency f and position (x,y) through the sample, $A_o(x,y,f)$ is the magnitude spectrum at frequency f and position (x,y) of the reference signal with no sample in the path. The average attenuation $\alpha(f)$ was obtained by averaging all the $\alpha(x_i,y_j,f)$ functions measured within the selected region of interest using Equation 2.9,

$$\alpha(x, y, f) = \frac{1}{nm} \sum_{i=1}^{n} \sum_{j=1}^{m} \alpha(x_i, y_i f) \quad (\text{dB cm}^{-1}) \qquad \textbf{Equation 2.9}$$

Relative backscatter

Measurement of the relative backscatter (μ) of the samples were made in dB relative to the signal from the flat steel reflector at the transducer focus. The sample was positioned with the transducer focus just beyond the sample surface to minimise attenuation loss through the sample and to gate out the sample/water interface reflection. The relative backscatter was calculated in dB from the log difference between the spectra of the flat steel reflector at the transducer focus and the spectra of the samples. The calculation was performed on each of the RF signals stored from the raster scan using the Equation 2.10,

$$\mu(x,y,f) = -\frac{20}{2d_s}\log_{10}\frac{A(x,y,f)}{A_o(x,y,f)} \quad \text{(dB)} \qquad \textbf{Equation 2.10}$$

where $A(x,y,f)$ is the magnitude of the spectrum at frequency f and position (x,y) through the sample, and $A_o(x,y,f)$ is the magnitude of the spectrum at frequency f and position (x,y) of the reference signal with no sample in the path.

Uncertainties in the measurements

There are a number of uncertainties to be taken into consideration in the determination of speed of sound, attenuation coefficient, and relative backscatter (Bamber, 1997). For speed of sound uncertainties the systematic errors are as a result of uncertainties in path length, sample thickness, definition of pulse arrival time, and the speed within the reference medium (water). The systematic error was estimated to be 0.8 m s^{-1}. The random uncertainty in the measurement of speed of sound was assessed from repeat measurements from a reference water path scan. It was calculated to be ± 0.5 m s^{-1}. The overall uncertainty was calculated using Equation 2.11.

$$U_o = \left[(U_R)^2 + (U_s)^2\right]^{1/2}$$ **Equation 2.11**

where U_O is the overall uncertainty, U_R is the random uncertainty and U_S the overall systematic uncertainty. Inhomogeneity of the PVA C samples due to cross linking led to an estimated uncertainty in repeat measurements of ± 5 m s^{-1}. This uncertainty dominated the overall error associated with the measurement of speed of sound. The accuracy of attenuation measurements using the SAM system was previously estimated to be ± 0.03 dB cm^{-1} due to a random error of ± 0.02 dB cm^{-1} and a systematic error of ± 5% (Browne et al., 2003). The systematic error was due to reflection, diffraction, alignment of the transducer, and uncertainty in the measurement of the sample thickness. The repeatability of the backscatter measurements was found to be ± 1 dB from three repeat measurements.

2.2.2 Mechanical characterisation

Sample preparation

For the characterisation of the mechanical properties of PVA C only one batch of the material was tested (PVA C+ 0.75% Bc). This was the batch was chosen as it had the most suitable acoustic properties as a vessel mimicking material and therefore further mechanical testing was perform to fully characterise the material. Using a plastic syringe, 15 ml of liquefied PVA was slowly injected into the 6 wells of a rectangular aluminium mould (100 × 10 × 3 mm) as shown in Figure 2.4. The aluminium lid was firmly closed and the mould was left to stand for 24 hours to allow any bubbles to rise and settle. The aluminium mould then underwent 1 freeze-thaw cycle and the samples were removed and stored in distilled water at 5°C. This procedure was repeated until 6 samples were prepared for each freeze-thaw cycle, for cycles 1 through to 6.

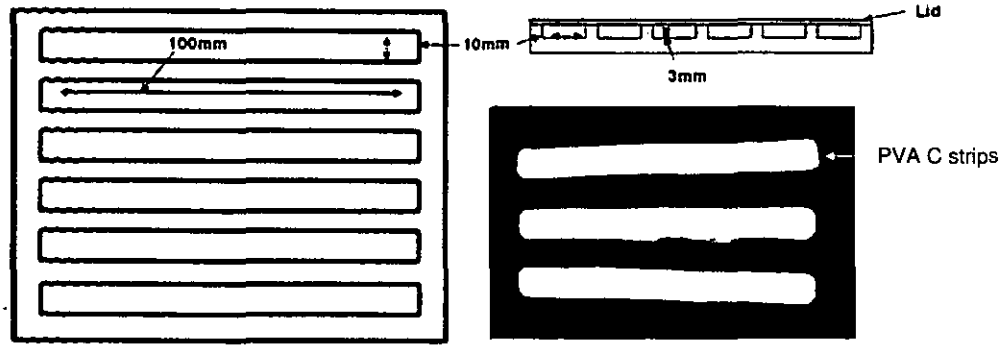

Figure 2.4 Aluminium mould for preparation of PVA C tensile testing strips

Mechanical testing

Uniaxial tensile testing was performed using the Lloyd Instrument LR30K (Lloyd Instruments Ltd., Hampshire, UK) fitted with a 500 N load cell (Figure 2.5(a)). All mechanical tests on the samples were carried out at room temperature. Due to the non-linear and visco-elastic properties of the material, preliminary tests were carried out to investigate if the PVA C Young's modulus depends on the extension rate of the samples. Three different extension rates (5 mm min^{-1}, 10 mm min^{-1} and 50 mm min^{-1}) were used on samples which had undergone 6 freeze-thaw cycles. The samples were loaded at the various extension rates to a maximum displacement of 80% of the gauge length. No significant difference in the behaviour of the PVA C samples was evident, indicating that the modulus of the material was not rate dependant, as shown later in Figure 2.17 in section 2.3.2. Had this not been the case the slopes of the force displacement graphs would have differed significantly. This allowed the higher feed rate of 50 mm min^{-1} to be used for the remainder of the mechanical tests which minimised the time required per test.

The PVA C test strips were fixed between tensile grips as shown in Figure 2.5(b). The distance between the grips was 60 mm. Samples were subjected to 5 stress-strain cycles to a maximum strain of 80%. A minimum load of 0.1 N was maintained on the specimen in order to prevent buckling of the PVA C samples. To prevent dehydration of the samples during testing, distilled water was sprayed on to the samples while they were secured in the test rig as it underwent cyclic deformation.

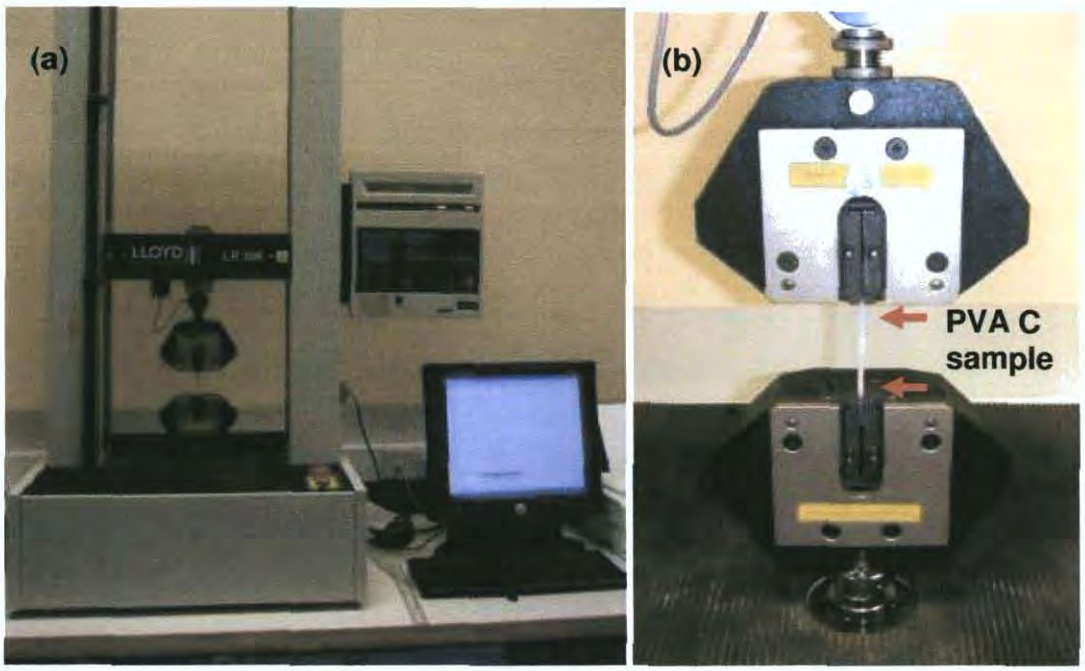

Figure 2.5 (a) Lloyd instrument for stress-strain testing (b) PVA C sample secured in grips at a gauge length of 60 mm

Raw data in the form of load-extension curves were converted into engineering stress and engineering strain plots using the initial gauge length and sample dimensions. Engineering stress and strain is based on the original dimensions of the specimen. The Young's moduli were calculated for the upward loading portion of the 5^{th} stress strain cycle. The modulus was evaluated as the mean gradient of the best fit line fitted to the

data from 0-30% strain where the behaviour was found to be linear and also corresponds to typical *in-vivo* strain values (Nichols and O'Rourke, 1990).

2.2.3 Variation in dimensions

During the preparation of the PVA C test samples for the acoustic measurements, the diameters of the samples were measured to investigate if changes occurred in the sample dimensions with increasing numbers of freeze-thaw cycles. The percentage difference in diameter from the original 50 mm diameter (mould diameter) was calculated for each freeze-thaw cycle. A sample PVA C renal artery vessel (wall thickness 2 mm) was also created using the silicone moulds of the renal artery, which is described in section 3.2.1. The wall thickness of the vessel was measured after each freeze-thaw cycle. Measurements were made at five locations along the length for each sample, using vernier callipers.

2.3 RESULTS

2.3.1 Acoustic measurements

The measured acoustic properties of the three TMM batches are presented in Table 2.7. The results obtained for the speed of sound and attenuation coefficient were found to be within the recommended values for the IEC TMM.

Table 2.7 Acoustic properties of the TMM used in this study at 3.5 MHz

Property	**TMM (a)**	**TMM (b)**	**TMM (c)**
Speed (± 5) m s^{-1}	1551	1552	1549
Attenuation coefficient (± 0.03) dB cm^{-1} MHz^{-1}	0.52	0.52	0.53
Relative backscatter (± 1) dB	64	62	63

Speed of sound

Presented in Figure 2.6 are the speed of sound results for the PVA C samples and PVA C +Bc+SiC (concentration 1) for the 7 MHz. Plotted on the same graph are the speed of sound results from previous published studies, Dineley et al., (2006) and Surry et al., (2004). Note that Dineley et al., (2006) used 15% PVA C with 0.75% SiC at 7MHz and Surry et al., (2004) used 10% PVA C at 3 - 8 MHz.

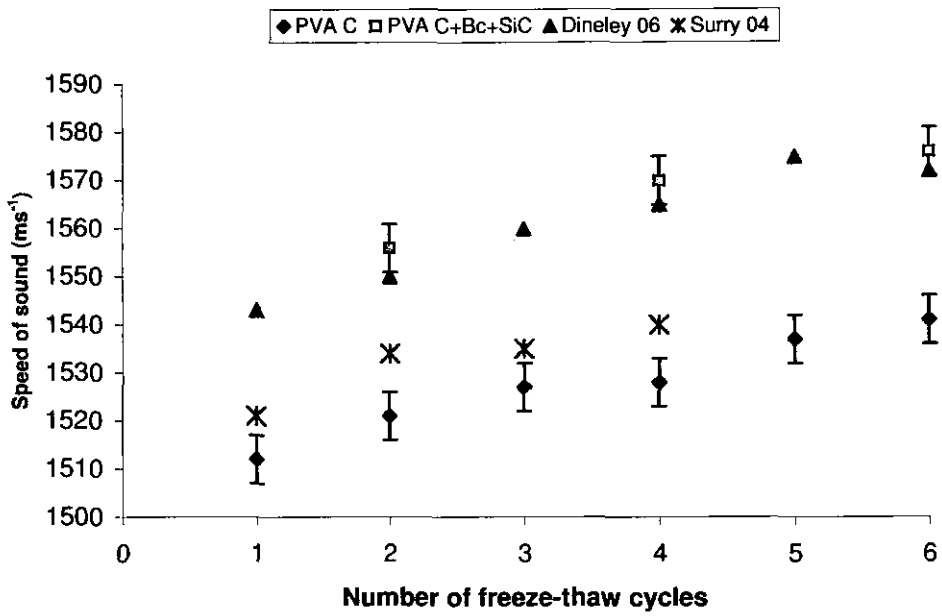

Figure 2.6 Effect of increasing number of freeze-thaw cycles on the speed of sound for 10% PVA C at 7MHz, compared with data by Dineley et al., (2006) and Surry et al., (2004)

The effects of the increasing number of freeze-thaw cycles on the speed of sound for the four batches are presented in Figures 2.7 – 2.11 for the 3.5 MHz transducer. The results for the 3.5 MHz transducer are presented here as these are the frequencies most commonly used for abdominal imaging. Similar trends were also observed for the 7 MHz transducer, the results of which are given in Appendix A.

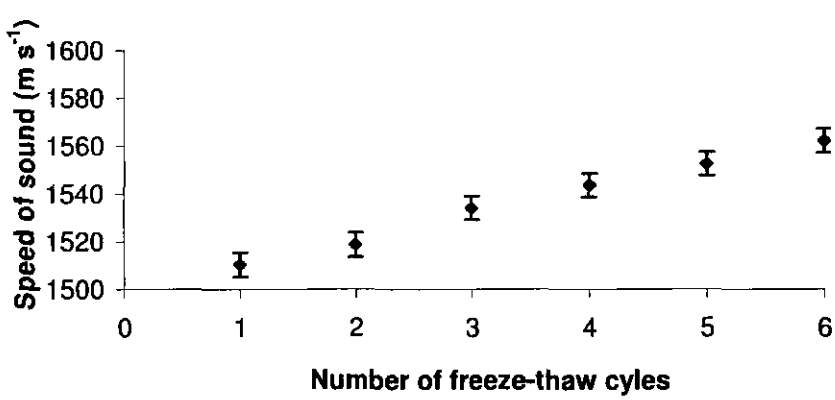

Figure 2.7 Effect of increasing number of freeze-thaw cycles on the speed of sound of 10% PVA C at 3.5 MHz

For PVA C only samples, the speed of sound increased linearly (R^2 = 0.99) with increasing number of freeze-thaw cycles (1 - 6) as shown in Figure 2.7. The speed of sound after one freeze-thaw cycle was 1510 m s^{-1}. This increased approximately by 10 m s^{-1} with each freeze-thaw cycle and reached 1562 m s^{-1} after 6 freeze-thaw cycles.

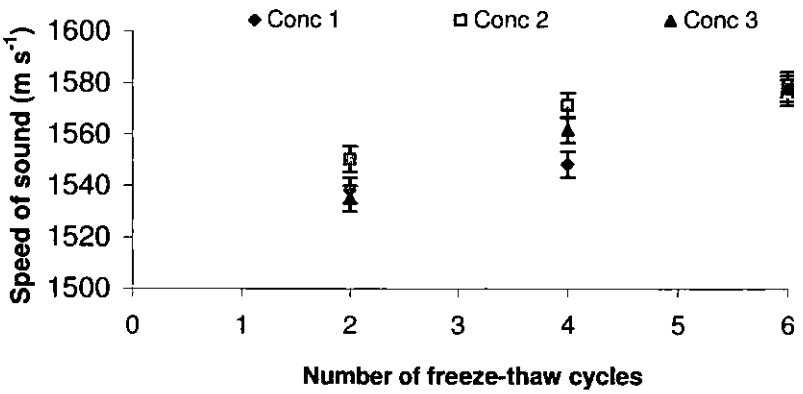

Figure 2.8 Effect of increasing number of freeze-thaw cycles on the speed of sound of 10% PVA C with three different concentrations of Bc at 3.5 MHz

The PVA C + Bc samples were observed to follow a similar trend as the PVA C samples (Figure 2.8). The speed of sound increased linearly for the three concentrations of Bc with increasing number of freeze-thaw cycles, the R^2 correlation values for the three concentrations were Bc concentration 1= 0.92, Bc concentration 2 = 0.89 and Bc concentration 3 = 0.98 ($p < 0.05$). No significant difference was found in the speed of sound of the different PVA C samples with varying concentration of Bc. The speed of sound for the PVA C + Bc samples were found to be in general higher than those for the PVA C only samples.

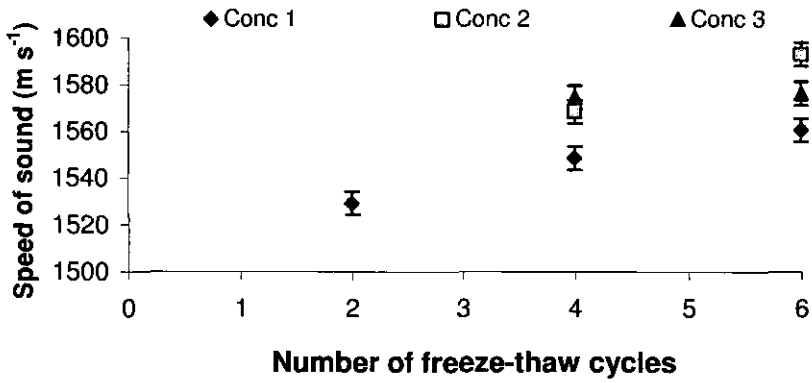

Figure 2.9 Effect of increasing numbers of freeze-thaw cycles on the speed of sound of 10% PVA C with antibacterial agent (Bc) and scatterers (SiC), at 3.5 MHz

A similar trend was observed in Figure 2.9 with the PVA C + Bc + SiC samples, with correlation values for SiC + Bc concentration 1 = 0.98, SiC + Bc concentration 2 = 1 and SiC + Bc concentration 3 = 1 ($p < 0.05$). PVA C samples with SiC and Bc concentrations 2 and 3 had higher speed of sound than samples containing SiC and Bc concentration 1.

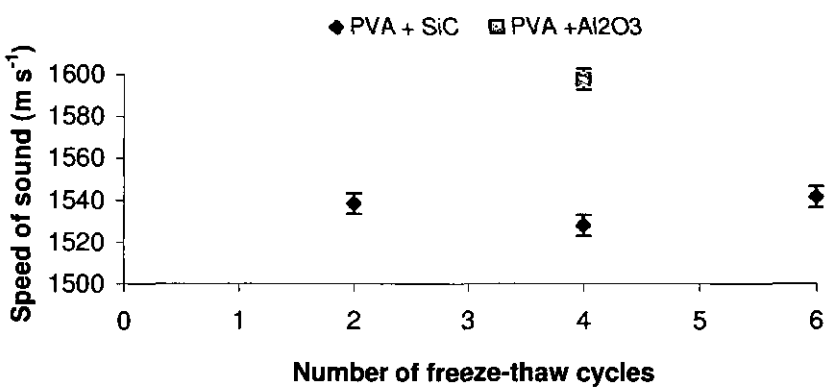

Figure 2.10 Effect of increasing number of freeze-thaw cycles on the speed of sound of 10% PVA C with the addition of scatterers SiC and Al_2O_3 at 3.5 MHz

As shown in Figure 2.10, it was found that the PVA C + SiC samples did not follow the trend of increasing speed of sound with increasing numbers of freeze-thaw cycles, a non linear relationship was found between addition of scatterers and speed of sound (R^2 = 0.5, $p < 0.05$). The values obtained after 2, 4 and 6 freeze-thaw cycles were 1538 ± 5 m s^{-1}, 1528 ± 5 m s^{-1} and 1541 ± 5 m s^{-1}, respectively.

Presented in Figure 2.11 is a 2D map of the speed of sound at 3.5 MHz plotted using the MATLAB analysis program with the colour map scaled in m s^{-1} for the PVA C+ SiC sample after 2 freeze-thaw cycles. From this map it can be seen that the speed of sound was not uniform and ranged from 1532 m s^{-1} to 1550 m s^{-1} throughout the scan area of the sample. Although this shows that the sample is inhomogeneous it can be calculated from the map that the mean speed of sound of the sample is approximately 1541 ± 10 m s^{-1}.

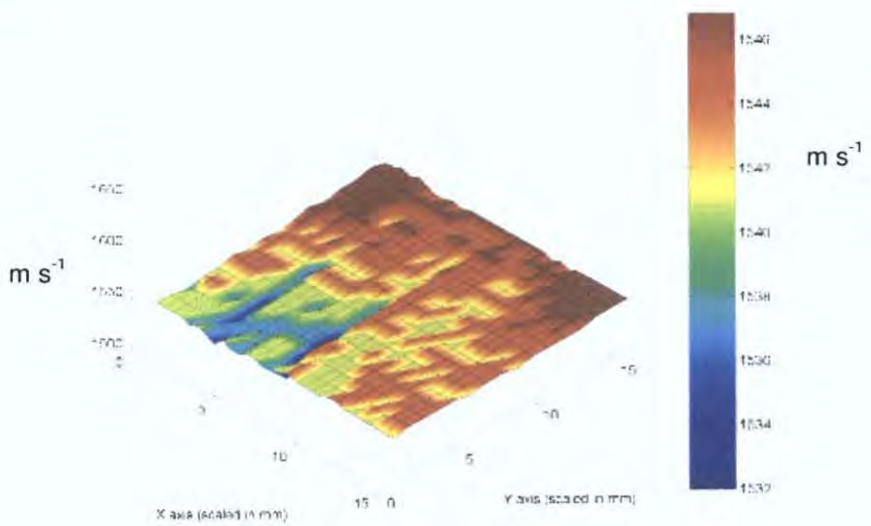

Figure 2.11 2D map of speed of sound at 3.5 MHz with colour map scaled in m s^{-1} of PVA C + SiC sample after 2 freeze-thaw cycles

Attenuation coefficient

Presented in Figure 2.12 are the attenuation coefficient results for the PVA C samples and PVA C +Bc+SiC (concentration 1) for the 7 MHz. Plotted on the same graph are the attenuation coefficient results from previous published studies, Dineley et al., (2006) and Surry et al., (2004). Note that Dineley et al., (2006) used 15% PVA C with 0.75% SiC at 7MHz and Surry et al., (2004) used 10% PVA C at 7 MHz.

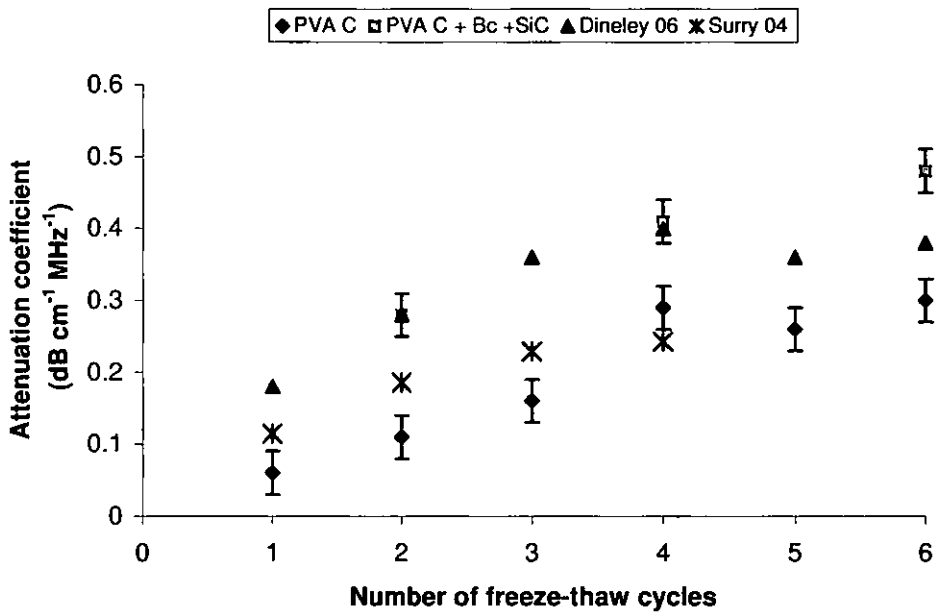

Figure 2.12 Effect of increasing freeze-thaw cycles on attenuation coefficient for 10% PVA C at 7 MHz compared with data by Dineley et al., (2006) and Surry et al., (2004)

Presented in the following plots (Figures 2.13 – 2.16) is the attenuation coefficient for the 3.5 MHz transducer for batches 1 - 4. For the PVA C only samples, the attenuation coefficient increased from 0.02 – 0.06 ± 0.03 dB cm^{-1} MHz^{-1} although this was not found to be significant with increasing number of freeze-thaw cycles (1 - 6). All data points were within experimental variation (Figure 2.13).

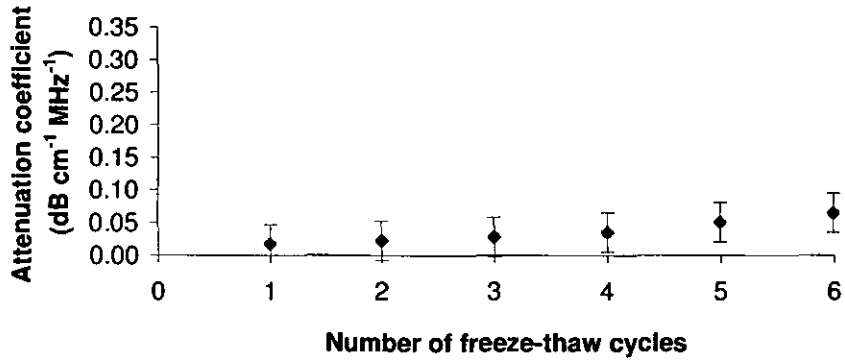

Figure 2.13 Effect of increasing freeze-thaw cycles on attenuation coefficient (at 3.5 MHz) for 10% PVA C

The addition of the antibacterial agent Bc resulted in an increase in the attenuation in the PVA C samples, as shown in Figure 2.14. The attenuation coefficient increased linearly with increasing number of freeze-thaw cycles, demonstrating excellent correlation: Bc concentration 1 = 1.0, Bc concentration 2 = 0.95 and Bc concentration 3 = 1.0 ($p < 0.05$).

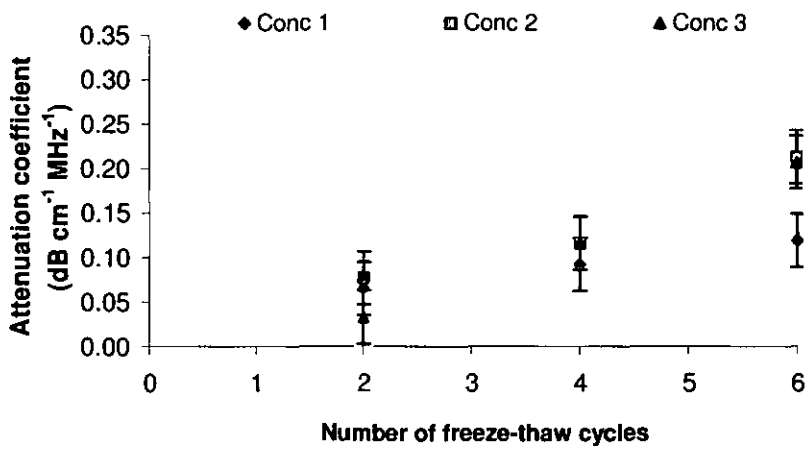

Figure 2.14 Effect of increasing number of freeze-thaw cycles on attenuation coefficient (at 3.5 MHz) for 10% PVA C with 3 different concentrations of Bc

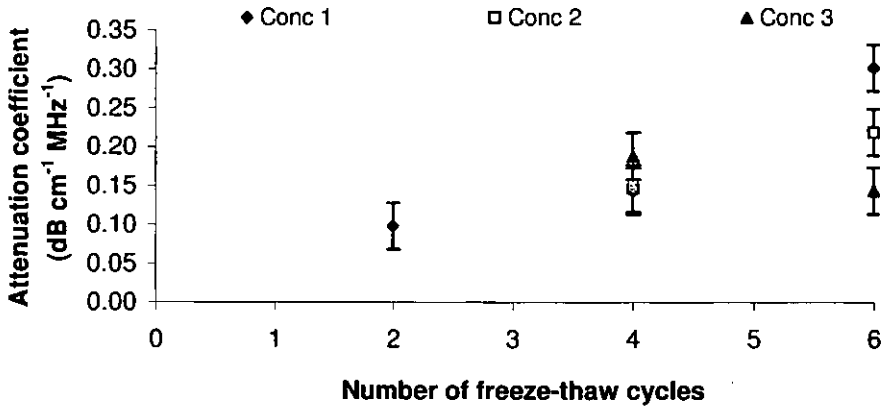

Figure 2.15 Effect of increasing number of freeze-thaw cycles on attenuation coefficient (at 3.5 MHz) for 10% PVA C with antibacterial agent and scatterers (SiC)

The PVA C samples with SiC and Bc also resulted in an increase in the attenuation coefficient with increasing number of freeze-thaw cycles with the exception of the samples containing Bc concentration 3 which decreased from 0.19 dB cm^{-1} MHz^{-1} (freeze-thaw cycle 4) to 0.14 dB cm^{-1} MHz^{-1} (freeze-thaw cycle 6) as shown in Figure 2.15.

For the PVA C samples containing SiC, the attenuation coefficient increased from 0.09 – 0.35 ± 0.03 dB cm^{-1} MHz^{-1} with increasing freeze-thaw cycles (2 - 6) as shown in Figure 2.16.

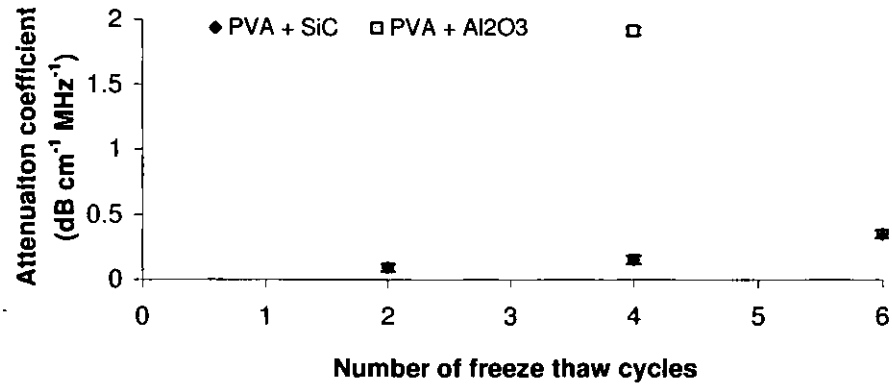

Figure 2.16 Effect of increasing number of freeze-thaw cycles on attenuation coefficient (at 3.5 MHz) for 10% PVA C with scatterers SiC and Al_2O_3. Note a larger scale was used here to accommodate the higher attenuation of the PVA C with Al_2O_3 sample compared to the other PVA C samples.

Relative backscatter

The effect of increasing number of freeze-thaw cycles on relative backscatter for a range of PVA C samples using the 3.5 MHz transducer is presented in Table 2.8. Relative backscatter was found to decrease with increasing number of freeze-thaw cycles. Comparison between 2, 4 and 6 freeze-thaw cycles for PVA C and PVA C + Bc samples showed similar results. Also, with the addition of SiC, there was a decrease in the relative backscatter.

Table 2.8 Relative backscatter using the 3.5MHz transducer (± 1 dB)

F/T cycle	PVA C (dB)	PVA C+ Bc (1) (dB)	PVA C +Bc (1) + SiC (dB)	PVA C + SiC (dB)	PVA C + Al_2O_3 (dB)
1	393				
2	386	380	328	338	
3	386				
4	374	368	329	311	346
5	364				
6	350	347	282	311	

2.3.2 Mechanical characterisation

Presented in this section are the results for the mechanical characterisation of PVA C. Figure 2.17 illustrates the results of the preliminary rate dependence investigation for the PVA C samples after 6 freeze-thaw cycles. The lack of any major difference in the behaviour of the samples at the different extension rates led to the selection of the higher feed rate for subsequent tests.

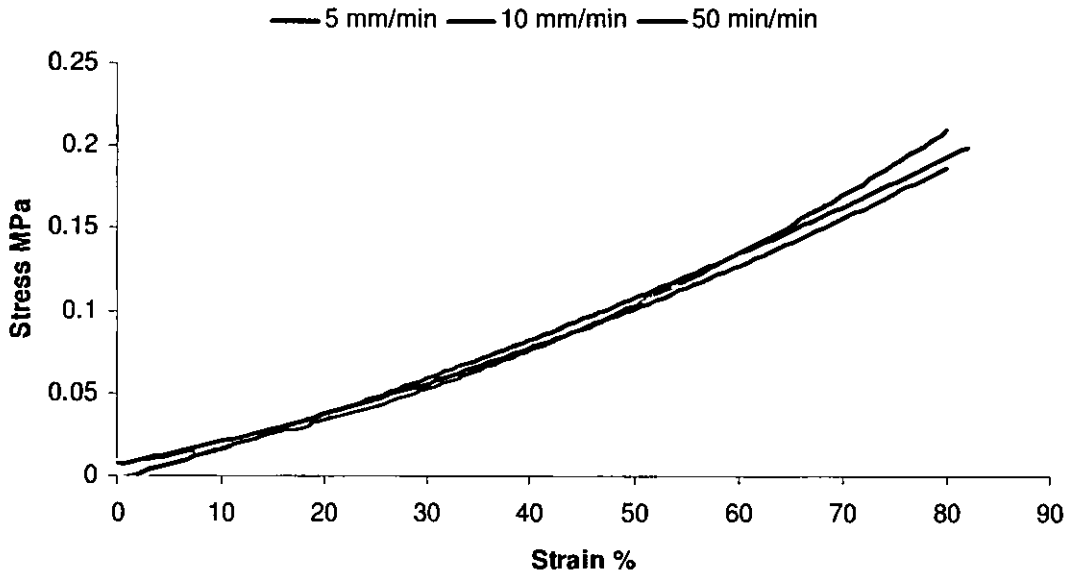

Figure 2.17 Rate dependence stress-strain curve for 3 different extension rates, 5 mm min^{-1}, 10 mm min^{-1} and 50 mm min^{-1}

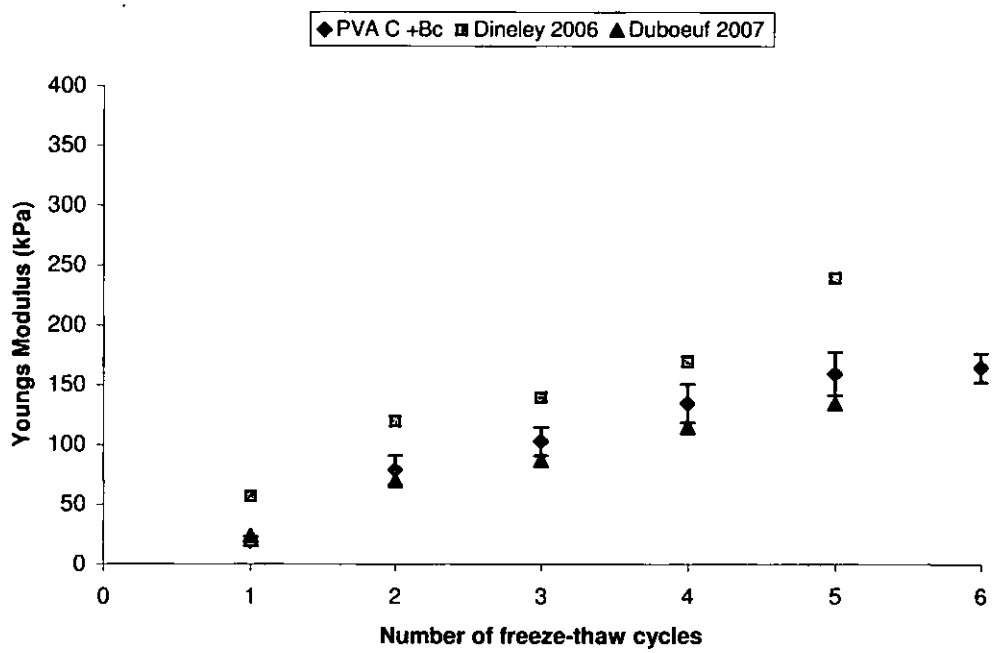

Figure 2.18 Young's modulus for 10% PVA C with increasing number of freeze-thaw cycles compare with data by Dineley et al. (2006), Duboeuf et al., (2007)

The relationship between the number of freeze-thaw cycles and the reported Young's modulus (in kPa) is presented in Figure 2.18. An increase in Young's Modulus was observed for increasing number of freeze-thaw cycles. Also in Figure 2.18 are the Young's Modulus obtained by Dineley et al., (2006), Duboeuf et al., (2007) and Fromageau et al., (2007). Note Dineley et al., (2006) used 15% PVA C with 0.75% SiC, while both Duboeuf at el., (2007) used 10% PVA C.

2.3.3 Variation in sample dimensions

The variations in PVA C dimensions with increasing number of freeze-thaw cycles (1 - 6) are presented in Figures 2.19 and 2.20. The error bars represent a combination of the measurement error associated with using vernier callipers on soft material and is the standard deviation of 5 measurements. The dimensions of the PVA C samples decreased with increasing number of freeze-thaw cycles. In Figure 2.19 the percentage difference in sample diameter and renal artery PVA C vessel wall thickness is shown for increasing number of freeze-thaw cycles,

$$\text{Percentage difference in sample diameter (\%)} = \Delta d/d \times 100 \quad \textbf{Equation 2.12}$$

where Δd is the change in PVA C diameter from original mould diameter and d is the original mould diameter.

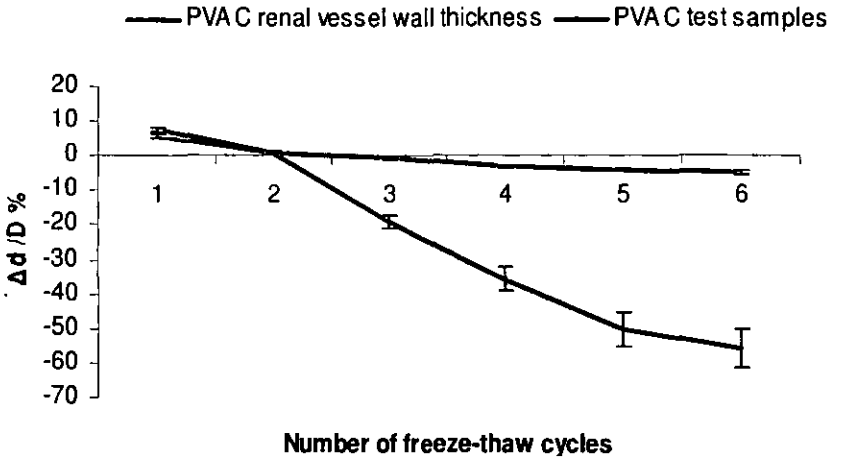

Figure 2.19 Variation in PVA C sample dimensions from 2 different moulds as a function of freeze-thaw cycles

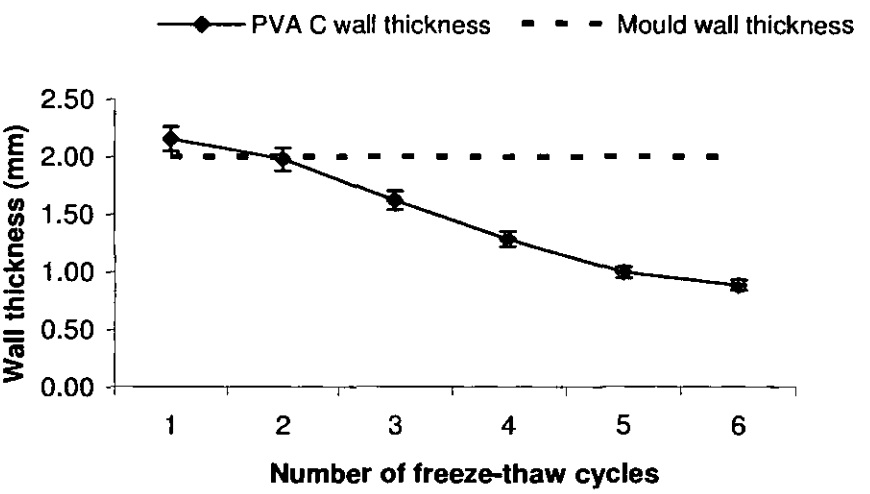

Figure 2.20 PVA C vessel wall thickness measured as a function of freeze-thaw cycles, the renal artery mould wall thickness was 2 mm

2.4 DISCUSSION

In this chapter the acoustic properties of the TMM were determined and both the acoustic and mechanical properties of the VMM for the anatomically realistic renal artery flow phantom were measured. As described in the introduction, to obtain a physiologically realistic phantom it is important to choose materials whose speed and attenuation coefficient match that of tissue and blood. The TMM chosen for the anatomically realistic renal artery flow phantom was the IEC recommended TMM. This agar-based TMM was developed as part of an EC project (IEC, 2001; Ramnarine et al., 2001; Teirlinck et al., 1998). The fundamental acoustic properties of this TMM at a range of frequencies 2 - 23 MHz have been characterised in 2 comprehensive studies (Brewin et al., 2008; Browne et al., 2003). For this reason the acoustic measurements performed on the TMM were simply to ensure the reliability of the TMM production and not an evaluation of its acoustical properties. The acoustic properties of the three TMM batches were presented in Table 2.7. The results from the three batches agreed well with existing data, speed of sound 1546 m s^{-1} and attenuation coefficient 0.57 dB cm^{-1} MHz^{-1} (Browne et al., 2003). The results obtained for the speed of sound and attenuation coefficient were within the recommended values for the IEC TMM (Table 2.1).

The IEC recommended BMF was also chosen for the renal artery flow phantom experiments (Ramnarine et al., 1998). The acoustic properties of this material were not evaluated in this study as its production is straight-forward and has been shown to be very reliable (Ramnarine et al., 1998; Ramnarine et al., 1999). Furthermore the experimental set-up to measure the acoustic properties of BMF is complex as the fluid is required to be flowing during testing to obtain the correct distribution of scatterers.

This chapter focused on the acoustic and mechanical characterisation of the VMM, PVA C. Within the acoustic characterisation study, the effect of increasing number of freeze-thaw cycles was evaluated for a range of PVA C samples. The overall aim of this study was to determine the required number of freeze-thaw cycles to achieve acoustic and mechanical properties similar to those of the renal artery *in-vivo*. With increasing numbers of freeze-thaw cycles, the dimensions of the samples changed, and therefore it was important to characterise the expansion and shrinkage of the PVA C to determine the required dimensions of moulds.

The speed of sound, c, in soft tissue depends on its bulk modulus (B) and density (ρ) ($c = \sqrt{B/\rho}$). In general the less compressible the material, the higher the speed of sound in that material (Evans and McDicken, 2000). In PVA C, each freeze-thaw cycle induces intermolecular cross linking and the formation of crystallites. It is the number and nature of these freeze-thaw cycles which determine the mechanical properties of the material. Therefore, it is expected that increasing mechanical stiffness, which causes an increase in the bulk modulus, results in an increase in the speed of sound. The both the speed of sound and attenuation coefficient results for PVA C and PVA C+Bc+SiC obtained in this study (at 7 MHz) are comparable to those of published data (Dineley et al., 2006; Surry et al., 2004). It is important to note in each study the length and rate of the freeze-thaw cycles differed and this determines the acoustic properties of the material.

This study shows that the speed of sound of all samples increased with increasing number of freeze-thaw cycles (at least up to 6), with the exception of the PVA C + SiC

batch where clumping of the SiC particles may have occurred, this will be further discussed in the next section. The PVA C + Bc samples were found to follow a similar trend as the PVA C only samples. In general, the speed of sound values of these samples were approximately 2% higher than in the PVA C only samples. No consistent pattern of change in the speed of sound was observed with increasing concentrations of Bc. This may due to the low concentrations of Bc used (0.46%, 0.92%, 1.40%), if higher concentrations have been used in this study a further increase in speed of sound with increasing Bc concentration may have been observed. The reason for choosing low concetrations was to prevent bacterial growth without altering the speed of sound of the PVA C. A similar trend was observed with the PVA C+ Bc + SiC samples.

It was found that the PVA C + SiC samples did not follow the overall trend of the speed of sound increasing with increasing number of freeze-thaw cycles. It was noted that the sample with 2 freeze-thaw cycles may have had inhomogeneous mixing of the SiC particles, causing the sample to have a higher speed of sound due to clumping of the particles. It was observed during the preparation of the samples, that the SiC particles did not remain evenly suspended in the sample during the freeze-thaw process. Various methods were attempted to overcome this problem, including cooling the gel to 60°C before introducing the particles, stirring the mixture for an additional hour before pouring into moulds, and using different percentage weights. Although the above methods improved the natural suspension of the scatterers in the gel, the sinking and separation of particles within the sample was still a problem with increasing number of freeze-thaw cycles. With increasing number of cycles, the SiC particles drifted to the bottom of the sample. This resulted in samples having two very different layers, the top containing very few or no SiC particles and the bottom where the majority of the

scatterers were located. When performing speed of sound measurements a sample scan of the top and bottom of the sample were obtained. The final value for each sample was the mean speed of sound of these two measurements. This is not an ideal method; although the introduction of scatterers enhanced the backscatter signal only on one side of the sample, it also introduced inhomogeneity into the sample. The acoustic measurements obtained from the samples containing SiC particles are not reliable. The effect of the particles settling out prevented accurate speed of sound, attenuation and backscatter measurements as the material was not suspend homogenously throughout the sample. Further refinement is required in the preparation stages to ensure homogenous mixing of the SiC particles throughout the PVA gel and the acoustic measurements repeated.

The highest speed of sound obtained from all samples was 1598 m s^{-1} from the sample containing PVA C + Al_2O_3 (Figure 2.10). The metallic content present in the sample, increased the overall density of the material which would contribute to a greater speed of sound. Although this powder remained suspended in the PVA gel through freeze-thaw cycles 1 - 6, areas of clumping were observed. This also occasionally occurred when using the powder in the production of TMM.

Attenuation is due to scattering, reflection, refraction, non-linear propagation and divergence of the US beam (Evans and McDicken, 2000). Therefore, increasing the number of freeze-thaw cycles, and so increasing the number of areas of cross-linking in the PVA C, should result in an increase in the attenuation coefficient due to scattering and reflection from the areas of increased cross-linking. An increase in attenuation coefficient was observed for PVA C only and PVA C + Bc with increasing number of

freeze-thaw cycles. A further increase in attenuation was expected by the addition of scatterers such as SiC and Al_2O_3. As expected the samples containing the additional scatterers had a significantly higher attenuation coefficient in comparison to the samples containing PVA C only and the antibacterial agent. At 3.5 MHz, the attenuation coefficient obtained for PVA C + SiC samples ranged from 0.09 – 0.35 ± 0.03 dB cm^{-1} MHz^{-1}. This significant increase in magnitude of the attenuation coefficient is likely due to the scattering and absorption of the ultrasound beam.

There are no published studies on the backscatter properties of PVA C. *In-vivo* arterial vessels backscatter sound 100 times (corresponding to 20 - 30 dB) more strongly than blood for frequencies in the range of 2 to 10 MHz (Shung, 1985). At higher frequencies, the wavelength approaches the dimensions of red cell aggregates, leading to strong backscatter which may be comparable or even higher than the surrounding tissue (Hoskins, 2008). Chu, (1997) reported that scattering will appear in PVA C with no additives after several freeze-thaw cycles. Here relative backscatter measurements were found to decrease with increasing number of freeze-thaw cycles. An increase in backscatter was expected with the addition of the SiC particles since these particles have been used to modify the backscatter of the TMM (Teirlinck et al., 1998). Although no relative backscatter measurements were performed Dineley et al., (2006) visually observed an increase in backscatter after the addition of SiC particles (0.75% by mass). In biological tissues refraction, reflection, scattering and absorption all contribute to the total loss (attenuation) of sound energy due to the tissue. Therefore, attenuation and backscatter are related. A relationship between the attenuation coefficient and relative backscatter measurements was not observed here. Further work is required to investigate the analysis of the software used to determine the relative

backscatter, as the results obtained from this study were inconclusive. Furthermore the current method for evaluating TMM or VMM backscatter using a plane reflector surface as a reference lacks clinical relevance; a better estimate of relative backscatter would be a comparison of the measured backscatter from a standard TMM with well characterised acoustic properties similar to *in-vivo* soft tissue.

Speed of sound results for PVA C only samples obtained from freeze-thaw cycles (1 - 3) correspond to values found *in-vivo* for a human artery (1501 - 1534 m s^{-1}) (Greenleaf et al., 1974). Attenuation in human tissue varies widely, with ranges reported as low as 0.3 – 0.6 dB $cm^{-1}MHz^{-1}$ (Duck, 1990). These values are considerably higher than those achieved with PVA C at 3.5 MHz. For PVA C only samples, the attenuation coefficients for freeze-thaw cycles 1 - 6 were less than 0.06 dB cm^{-1} MHz^{-1}.

Currently the PVA C samples chosen to mimic the renal artery do not match the higher speed of sound reported for healthy arteries of 1616 ± 23 m s^{-1}. The speed of sound of the sample corresponds to previous values found *in-vivo* for a human artery (1501 - 1534 m s^{-1}) and is very close to that of the TMM therefore within the recommended IEC specifications. As a result focusing and defocusing of the ultrasound beam will not occur due to the mismatch found *in-vivo* between the tissue, vessel and blood will not be replicated. It has been reported that the effects of this mismatch of speed of sounds are negligible for normal health arteries (Hoskins, 1994). Therefore the Doppler measurements obtained from the anatomically realistic phantoms are valid and the lower speed of sound of the VMM will not result in unrealistic results. As an improvement for future phantoms a comprehensive study of the acoustic properties of PVA-C, varying different factors such as the concentration of PVA powder used, rate of

freeze-thaw cycles and variation of scatterers may allow for higher speeds of sound and attenuation coefficients to be obtained.

It was desirable to have an antibacterial agent present in the PVA C samples to prevent bacterial growth. Bacterial growth appeared on a number of PVA C only samples after several days. The sample containing 0.75% Bc solution resulted in a speed of sound and attenuation coefficient of 1538 m s^{-1} and 0.07 dB cm^{-1} MHz^{-1}, respectively after 2 freeze-thaw cycles. Once again the attenuation coefficient is considerably lower than the values reported for soft tissue. The sample which had speed of sound and attenuation coefficient values closest to the desired values was the PVA + SiC (c and α, 1538 m s^{-1} and 0.35 dB cm^{-1} MHz^{-1}, respectively). Unfortunately due to the SiC particles separating and sinking to the bottom of the sample during preparation and hence variability in measurements, this sample was not suitable for the VMM. Until a solution is found to aid the suspension of the SiC particles in the samples, the PVA + Bc sample with 2 freeze-thaw cycles was chosen for this study. The attenuation coefficient of this sample is significantly lower than that found *in-vivo* (0.3 – 0.6 dB cm^{-1} MHz^{-1}). The IEC 61685 standard specifies that the vessel wall in an ultrasound flow test object should reduce the signal by an amount less than the signal reduction caused by a layer of TMM having a thickness equal to the vessel diameter (IEC, 2001). The PVA C samples described here, with an attenuation of 0.07 dB cm^{-1} MHz^{-1} (0.18 dB cm^{-1} at 2.5 MHz), results in a 0.035 dB loss through a 2 mm wall compared to a 0.925 dB loss through a 7.4 mm (~ equivalent to the i.d. of the lumen in the renal artery flow phantom) of TMM. Therefore, the PVA C vessel complies with this IEC standard.

In this study the Young's modulus of PVA C samples with 0.75% Bc as a function of the number of freeze-thaw cycles 1 - 6 were determined using a tensile testing instrument. The Young's modulus of the PVA C samples increased with increasing number of freeze-thaw cycles. After the 5th freeze-thaw cycle the Young's modulus did not increase significantly. This may suggest that the PVA C was approaching saturation point of the cryogel in terms of intermolecular cross-linking. This effect has been observed elsewhere (Chu and Rutt, 1997) and places an upper limit on elastic moduli available for a given concentration of cryogel. The measured Young's modulus ranged from 19 ± 4 kPa to 165 ± 11 kPa. These results follow a similar trend to previous published data. These results are comparable to those obtained by Duboeuf et al., (2007), 24 ± 1 kPa to 135 ± 10 kPa over five freeze-thaw cycles for 10% PVA concentration. These results were lower than those obtained by Dineley et al., (2006), 57 ± 6 kPa to 330 ± 21 kPa over seven freeze-thaw cycles. It is important to note that a 15% PVA concentration was used and since the materials stiffness varies directly with stiffness, higher Young's modulus can be expected (Chu, 1997). For healthy arteries a Young's Modulus ranging from 70 - 100 kPa has been reported (Kawasaki et al., 1987). By undergoing 2 or 3 freeze-thaw cycles it is possible to produce PVA C samples with mechanical properties similar, in respect of Young's modulus, to that found *in-vivo* for healthy arteries.

During the preparation of the test samples for the acoustic measurements, variations in the PVA C sample dimensions were observed with additional freeze-thaw cycles. The test sample diameter decreased by a total of 5% after 6 freeze-thaw cycles (Figure 2.18). Further tests were carried out to investigate if the variation in PVA C dimensions was a

function of freeze-thaw cycles and was dependant on the mould size. A sample PVA C renal artery vessel (wall thickness 2 mm) was created using the silicone moulds of the renal artery and this is described in section 3.2.1. The wall thickness of the vessel was measured after each freeze-thaw cycles. From Figure 2.19 it can be seen that variation in sample dimensions is dependant on mould diameter. There is a greater change in the dimensions of the PVA C renal artery vessel then the PVA C test samples. This variation in sample dimensions was attributed to an increase in the PVA C density after each freeze-thaw cycle due to free water being expelled from the gel as the crystallite formation increases (Chu, 1997). Although the overall dimensions of the PVA C samples decreased after 6 freeze-thaw cycles, expansion occurred after the first freeze-thaw cycle. The aqueous PVA solution expands during freezing since it contains water. After the first freeze-thaw cycle the amount of crystallites present is low, thus, the quantity of water which expands when frozen is probably greater than the volume of free water expelled from the sample. As the number of freeze-thaw cycles increases, the free water is predominantly expelled, resulting in continuous shrinkage of the sample. Using Figure 2.20, it is possible to calculate the wall thickness which will be achieved after each freeze-thaw cycle (1 - 6) using the renal artery mould. In addition, care must be taken to ensure the manufacturing conditions remain constant for each batch produced.

2.5 CONCLUSIONS

This study shows that the IEC TMM can be reliably reproduced within the recommended specification for its acoustic properties. The sample containing PVA C + Bc (concentration 1) was chosen as the optimal PVA C mixture to form anatomically realistic renal vessel mimic. The acoustic and mechanical characterisation of PVA C showed that it exhibited properties similar to that of arteries *in-vivo* is a suitable VMM for the anatomically realistic renal flow phantoms and after 2 freeze-thaw cycles had a speed of sound, attenuation coefficient and Young's modulus of 1538 ± 5 m s^{-1}, 0.07 ± 0.03 dB cm^{-1} MHz^{-1}, 79 ± 11 kPa, respectively.

CHAPTER 3 DEVELOPMENT OF ANATOMICALLY REALISTIC RENAL ARTERY FLOW PHANTOMS

3.1 INTRODUCTION

This chapter describes the steps involved in the development of a range of anatomically realistic renal artery flow phantoms with normal and diseased lumens. Developments in computer-aided design (CAD) and rapid prototyping (RP) have allowed three dimensional (3D) anatomical reconstruction using data from clinical 3D data sets obtained from imaging techniques such as MRI and CT. Currently, there are no anatomically realistic renal artery Doppler flow or kidney perfusion phantoms available commercially. The novel renal phantoms developed as part of this project will provide a means of evaluating current and emerging ultrasound technologies as well as developing methods to observe and quantify hemodynamic features within the renal artery. These phantoms offer the potential of being useful training tools for practitioners engaged in the detection of RAS. Two types of Doppler flow phantoms with varying degrees of stenosis were developed, a wall-less flow phantom where there is no tubing material and a walled flow phantom with a VMM. In the former BMF is in direct contact with the TMM and in the latter a vessel wall is between the BMF and the TMM.

Additionally, a range of multi-modality wall-less phantoms with varying degrees of stenosis were designed to allow a comparative study between four of the imaging techniques currently used to detect renal artery stenosis (US, DSA, MRI and CT).

These phantoms were primarily designed as ultrasound flow phantoms, but using materials which are also compatible with DSA, MRI, and CT. They also contain fiducial markers as a means of aligning images acquired by the different imaging systems. Using the multi-modality phantom it was possible to make direct quantitative comparisons between the different imaging modalities with the phantoms as a reference standard of known dimensions and features. In this chapter, the development of a wall-less and walled anatomically realistic renal artery flow phantom as well as a wall-less multi-modality renal phantom are described.

3.2 METHODOLOGY

3.2.1 Phantom fabrication

Data acquisition and image processing

A 3D model of the renal artery was developed using a 64-slice CT scan of the abdominal region acquired from a healthy volunteer with normal renal vasculature, one slice of which is shown in Figure 3.1. The data were obtained using a Siemens SOMATOM Sensation Cardiac 64 (64 images/slices per rotation at 0.7 mm resolution).

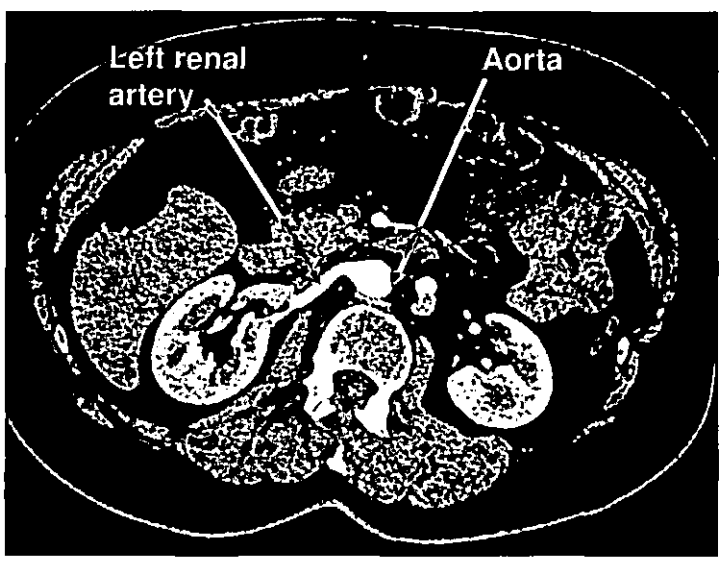

Figure 3.1 A CT slice (Siemens SOMATOM Sensation Cardiac 64) of the abdominal region from a healthy volunteer with the aorta and left renal artery highlighted

The CT images were imported into a commercial software package (MIMICS 6.3, Materialise, Leuven, Belgium) which provided an interface for the visualisation and segmentation of CT images and the 3D rendering of a region of interest (ROI). Using MIMICS the 2D scan slices were viewed, and from the 319 images, images 157 – 302 were identified as containing the left kidney and left renal artery. The area including the left renal artery and aorta was selected in each slice. The left renal artery was chosen as

it was clearly identifiable in the CT images having a more horizontal and straight course.

A mask was created to select the portions of the scan that were relevant to the studies, a threshold was applied to the grey-scale images ensuring that only the pixels corresponding to the tissues of the correct density were highlighted (renal artery and aorta). Each slice was inspected and edited by the author if extra surrounding soft tissue with a similar density had also been highlighted. From the defined ROI a 3D model was rendered. Additional modification of the lumen contours was accomplished manually at pixel level in all three views to attain a more refined model of the renal artery and aorta lumen.

Generation of computer model

The resulting model was exported as a STL file into the 3D CAD design software program SolidWorks® (Dassault Systèmes SolidWorks Corp., MA, USA) for further manipulation. The model was further refined to produce a generic model of the renal artery. A spline curve was created which followed the axis of the vessel lumen reconstruction in one plane. The spline curve was adjusted in the other two orientations to account for out-of-plane curvature of the vessel lumen. The solid sweep command was used to construct the renal artery with a 6.8 mm diameter along the whole length of the model that followed the path of the spline. To aid centring of the metal replica during vessel prototype fabrication, an extrusion was constructed at each end of the model. This was to ensure that the model remained in the centre of the mould when preparing the vessel wall. These extrusions were 10 mm (in length) 4-sided projections

on each end of the renal artery model. Figure 3.2 shows the computer generated model of a normal renal artery with no blockages present.

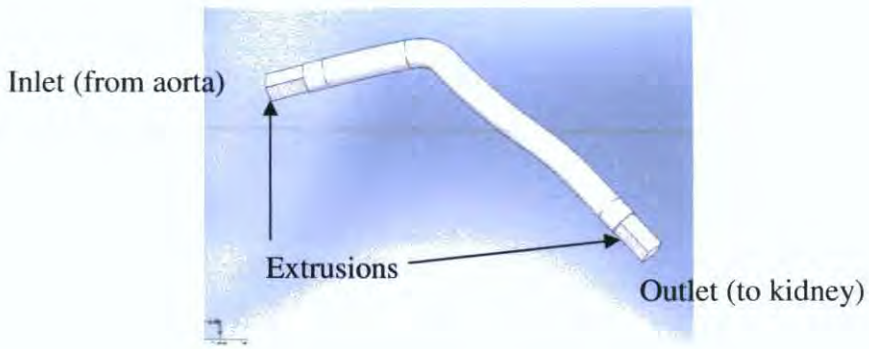

Figure 3.2 Computer model of normal renal artery

To develop diseased renal artery models an experienced vascular technician was consulted and a series of hand drawings highlighting the position and extent of RAS with various degrees of blockages were prepared. The position of the blockage was chosen as approximately 10 mm along the renal artery from the aorta as it has been stated that up to 66% of RAS is due to atherosclerosis, which typically involves the ostium and proximal 20 mm of the renal artery (Beattie et al., 1997). This was reiterated in discussions with a number of experienced vascular technicians.

A series of symmetrical stenoses (30%, 50%, 70% and 85%), each 10 mm in length were chosen. Each stenosis inset was modelled so that its surfaces were tangential to the surfaces of the renal artery at the edges of the stenosis. This procedure was repeated to generate a series of geometrically similar inserts that differed only in the reduction in diameter, the stenosis itself having been scaled in cross-section throughout. The following insert models were generated; normal healthy renal artery (0% stenosis) and four diseased models with smooth symmetrical stenoses of 30%, 50%, 70% and 85%.

The computer models of the inserts were split into halves to allow easy removal of the rapid prototyped inserts from the metal replicas as shown in Figure 3.3.

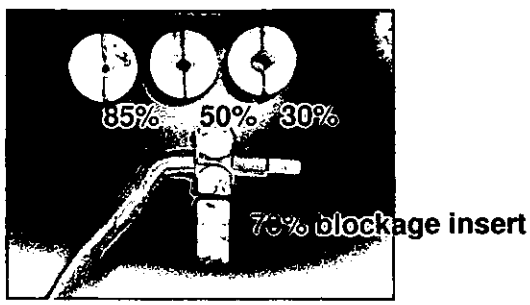

Figure 3.3 The stenosis inserts used to fabricate the diseased metal models of the renal artery

Instead of producing a whole model for each diseased renal artery an insert with the desired blockage was developed. The computer model of the normal renal artery was altered to accommodate these inserts. At the desired location of the blockage the diameter was increased from 6.8 mm to 20 mm as shown in Figure 3.4(a). This model would be used to create a silicone mould into which the blockages could be placed. To aid this process the model was split in two to facilitate the fitting of split lines; this will be discussed in a later section. For the development of the vessel in the walled phantom, a second computer model of the original renal artery was required. This model would create the outer wall of the renal artery and was constructed by offsetting the first model by the artery wall thickness (2 mm), as shown in Figure 3.4(b).

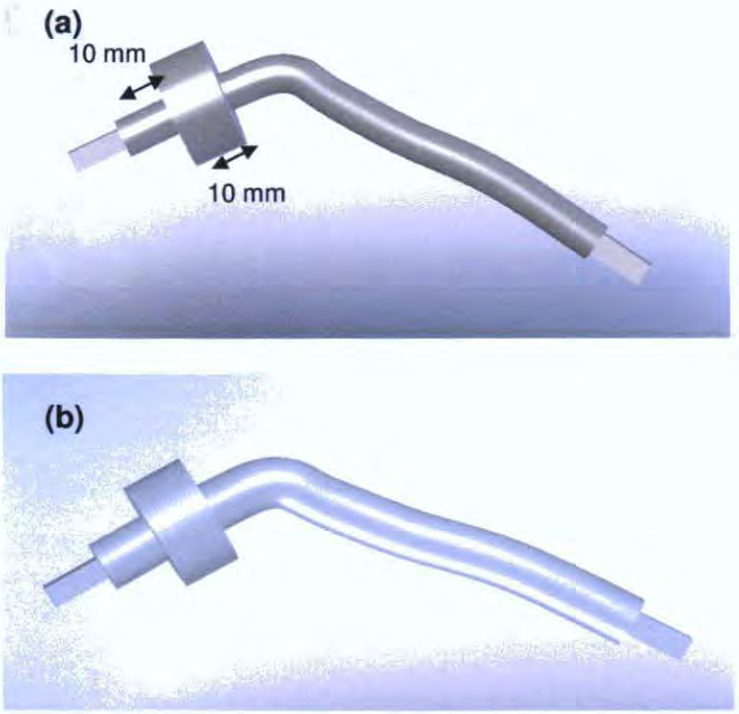

Figure 3.4 (a) Modified normal renal artery model for the stenosis insert soft tool, (b) outer wall computer model with diameter increased to 8.8 mm to allow creation of vessel with wall thickness of 2mm

Rapid prototyping

Rapid prototyping (RP) is a type of computer aided manufacturing. Both models and inserts were exported from SOLID WORKS into the RP machine in the form of STL files. The RP machine used was a Zprint 3D printer (Zcorporation, MA, USA). This used data from the STL file to produce a physical model of the renal artery and blockages. The models were constructed using a powder (similar to polyfil or plaster) and a water-based resin. The slice thickness was 0.1 mm. It was important to choose a small slice thickness to minimise stepping effects and reduce the amount of manual finishing required. After the models were printed they were left to dry for one hour. When the models were removed from the printer they were very fragile. Each model was carefully sanded to remove any ridges and the excess powder was vacuumed off. Super glue was painted on all surfaces of each model; this strengthened and sealed the

model. Since the superglue was absorbed into the powder resin, it did not alter the dimensions of the rapid prototyped model. This was verified by measuring the diameter of the model in three locations along its length before and after the super glue was applied.

Soft tool

A soft tool was made with silicone rubber around the master model of the lumen using a vacuum casting process. For the normal renal artery model, the split lines were selected where the two halves joined. Sellotape® was attached along the line and hooks were attached to the model using Araldite™ adhesive. The models were placed in a box (14 cm x 7 cm x 4 cm) and hooked onto supports and silicone was poured in. When set the soft tool was split along the predefined parting plane and the lumen model removed as shown in Figure 3.5. The above procedure was repeated to produce a soft tool of the renal artery outer wall.

Figure 3.5 Development of soft tool for renal artery lumen

Metal renal model development

A low melting point alloy with a melting point of 47°C (MCP 47 Mining and Chemical Products Ltd., Northamptonshire, UK) was used to construct the vessel lumen. The

desired inserts were selected and slotted into the soft tool. The soft tool was clamped together and sealed. The alloy was melted by heating it above 47°C in a Pyrex beaker. The liquid MCP 47 was slowly poured into the fill port of the soft tool and allowed to solidify. When the alloy was set, it was removed from the soft tool, the inserts were removed and the metal lumen was hand polished. Suitable protective clothing (face mask, safety glass, gloves, and laboratory coat) were worn during polishing and filing because the alloy contains heavy metals. The renal artery metal models produced are presented in Figure 3.6.

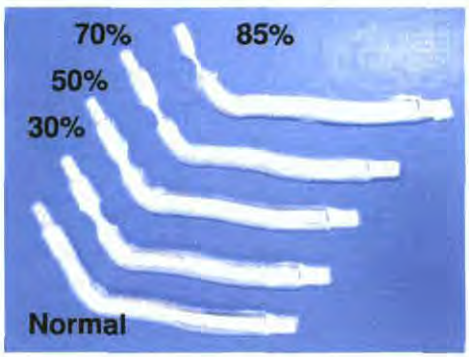

Figure 3.6 Metal models of the renal artery with varying degrees of stenosis (normal healthy artery, 30%, 50%, 70% and 85%)

3.2.2 Phantom construction

Three versions of the anatomically realistic renal phantom were developed, a multi-modality wall-less phantom and 2 flow simulation phantoms (wall-less and walled) all with varying degrees of stenosis.

Multi-modality phantom (wall-less)

There are 2 main differences between the flow simulation phantoms and the multi-modality phantoms, (1) size of the phantom container and (2) presence of fiducial markers. The phantoms for the flow measurements had dimensions of 230.0 mm x 135.4 mm x 103.7 mm (L x W x H) with a wall thickness of 2.6 mm. A large container was used for the flow measurements to allow more space for scanning the entire length of the renal artery at the required angle and also to allow for extra tubing on either end of the vessel lumen to alleviate problems with BMF leakage. The dimensions of the phantoms for the multi-modality study were 115.1 mm x 78.9 mm x 91.7 mm (L x W x H) with a wall thickness of 1.4 mm. This size was chosen to facilitate the transportation of the set of phantoms to each imaging facility and set-up in each of the imaging systems.

Fiducial markers were used in the multi-modality phantom as a means of aligning images acquired by the different imaging systems (US, DSA, MRI, and CT). Glass beads (Crown Jewels, Dublin, Ireland) with a diameter of 4 mm were chosen as suitable fiducial markers for this phantom. Using sewing thread (0.8 mm) 4 rows of 4 beads were threaded through the phantom, with 2 rows of beads located on either side of the renal artery lumen. On each row the beads were secured with adhesive 2.8 mm apart. The bottom row was secured 57 mm from the top of the container and 20 mm from the edges of the container. The second row of each pair was placed 8 mm above the first and 10 mm from the edge of the container. The inclination of the top row was to minimise any obstruction of the lower row that might cause shadowing in the US images. The glass bead marker system is presented in Figure 3.7.

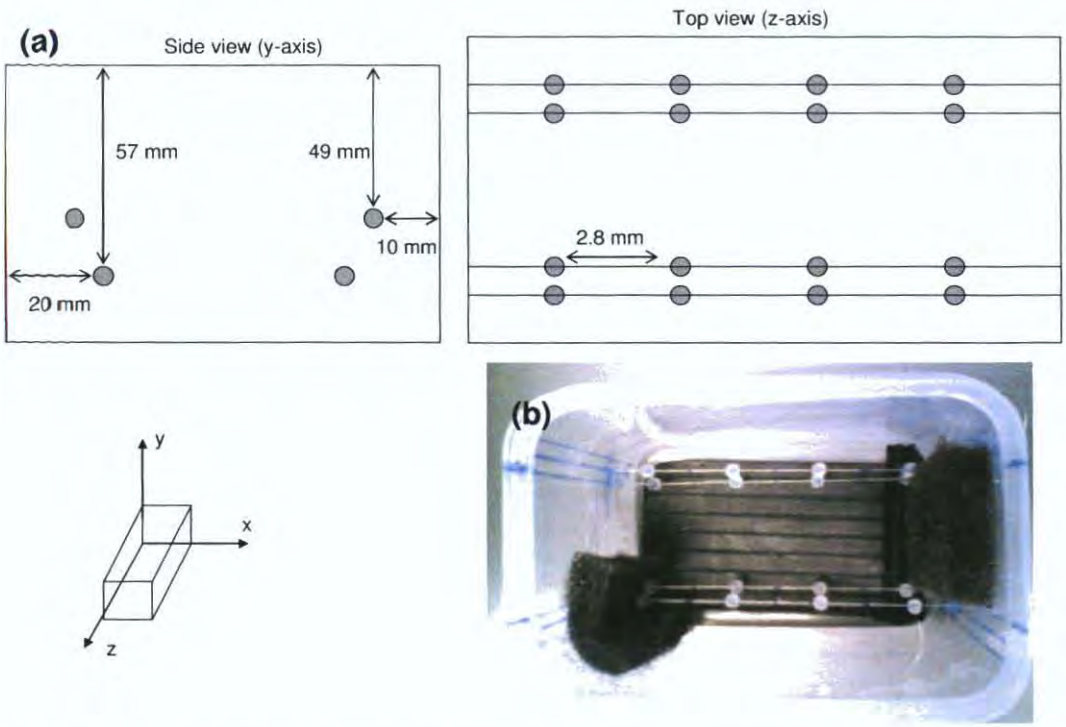

Figure 3.7 (a) Cross-sectional schematic diagram of the fiducial markers in phantom, (b) photograph of multi-modality phantom with glass bead markers before the placement of the metal model

Wall-less flow phantom

For the wall-less phantom, 2 plastic barbed connecters 7.5 mm i.d. (Cole-Parmer, Walden, UK) were secured to the container to act as inlet and outlet ports. Nalgene PVC plastic tubing 7.9 mm i.d. (Thermo Fisher Scientific, NY, USA) was attached to the connectors to allow the metal model to be secured between them. Reticulated foam (30 pore per inch (PPI), Foam Techniques, Northamptonshire, UK) (50 x 50x 10 mm) was fixed using Araldrite^{TM} adhesive around the sides of the phantom container, the connectors and tubing to help seal the phantom (Ramnarine et al., 2001). A rubber mat (Cannon Mats, London, UK) was placed on the bottom of the container to minimise reflections. Before securing the metal model in place, a single layer of clingfilm

(thickness 0.1 mm) was carefully wrapped around it. Using a vernier callipers the diameter of the metal models with and without the single layer of clingfilm were recorded along the length of the models. It was verified that the presence of the clingfilm did not significantly alter the dimensions of the models. At each end of the model an extra length of clingfilm was passed out through the connectors (Figure 3.8). The metal model of the renal artery was secured between the two plastic tubes. The IEC TMM was then poured into the container. When the TMM was set, the phantom was placed in a temperature controlled water bath ($50^{\circ}C \leq T \leq 60^{\circ}C$) for approximately 4 hours to allow the renal artery metal models (melting point 47°C) to melt. The clingfilm containing the molten metal was carefully removed; resulting in a realistic renal artery lumen with no residual metal remaining.

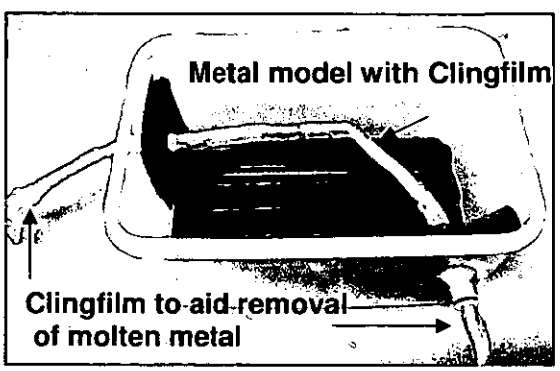

Figure 3.8 Wall-less phantom prior to TMM pouring with a single layer of clingfilm wrapped around the metal model and extended out the plastic tubing

Walled flow phantom

For the walled phantom both the renal artery lumen and outer wall soft tools were required. The renal artery metal model was constructed using the same procedure as described above. After it was hand polished, the metal lumen was positioned into the soft tool of the renal artery wall. The lumen was centred in the soft tool by the 10 mm

extrusions which were added to both models. When clamped together this produced a complete mould assembly. The area which was offset around the original length of the renal artery enabled fabrication of a thin walled hollow vessel (2 mm wall thickness). The preparation of PVA gel was described in section 2.2.1, Chapter 2. The PVA gel was injected into the void between the metal replica and the outer mould. The complete mould assembly was then put through 2 freeze-thaw cycles. The PVA C vessel was then carefully removed from outer mould. The walled phantoms were housed in the same rectangular containers as used for the wall-less phantom flow simulations (230.0 mm x 135.4 mm x 103.7 mm (L x W x H)). The PVA C vessels were carefully attached to tubing using cable ties as shown in Figure 3.9. Water was pumped through the vessel to prevent it from collapsing while the TMM was poured into the container and allowed to set.

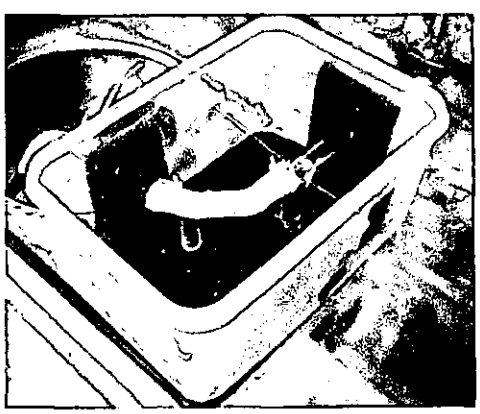

Figure 3.9 Walled phantom with PVA C vessel attached to the inlet and outlet tubing

To ensure long term stability of the phantoms, when not in use they were stored in air tight containers at room temperature with the scanning wells of the phantoms filled with the following solution of 87.7% water, 11.8% glycerol, and 0.5% Bc similar to the water, glycerol, and Bc concentration in the TMM. The vessel lumens were also filled

with this solution for the wall-less phantoms and with distilled water for the walled phantoms. This was to prevent the phantoms from drying out and also to prevent bacterial growth.

3.2.3 Geometric accuracy

To ensure the fabrication method for the renal artery model was reproducible the geometric accuracy of the metal models and phantom lumens was determined. The diameter of 5 metal models was measured in 3 locations along the length of the model to establish the statistical significance of any differences within and between each metal models. The three locations measured were 10 mm from inlet (A), 10 mm from bend (B) and 10 mm from outlet (C) (Figure 3.10). All measurements were made in triplicate using a vernier calliper.

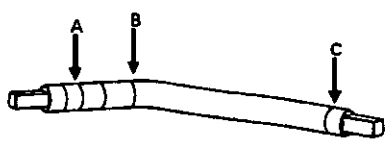

Figure 3.10 Validation measurement locations on renal model

A one-way repeated measure of ANOVA statistical test was carried out to compare diameters from the individual metal models. Each of the 5 metal cores were used to produce a wall-less phantom. Once the metal alloy was melted from the phantom, the diameters of the vessel lumen were measured from B-mode images acquired during test flow experimentation with the vessels filled with a speed of sound corrected solution (water 90.5%: glycerol 9.5%) (Goldstein and Langrill, 1979). Accurate relative positioning of the transducer was accomplished with a micromanipulator. Longitudinal

images were taken with the transducer position adjusted until the vessel lumen was brightest, corresponding to specular reflection. The transducer was positioned at three acoustic markers in each phantom which corresponded to the three measurement locations A, B ad C on the metal models. Prior to pouring in the TMM three rows of thread (0.8mm) which were inserted across the width of the phantom container at right angles to the vessel and in the horizontal plane at a depth of 60 mm from the surface of the TMM. These produced bright focal areas of reflected ultrasound therefore acting as acoustic markers.

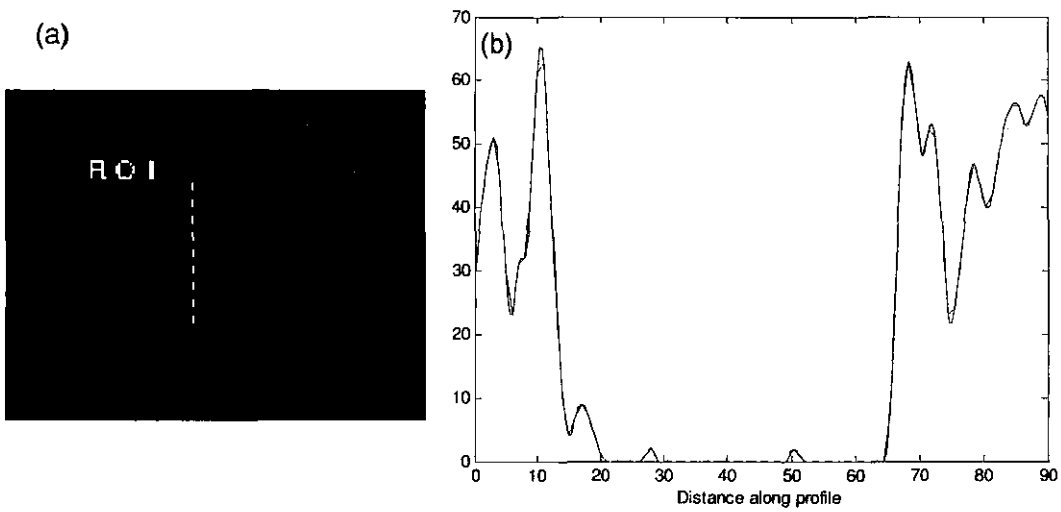

Figure 3.11 Calculation of the vessel diameter from B-mode ultrasound image, (a) profile line marked across lumen, (b) plot of image intensity vs. distance along line of interest

The vessel lumen diameter was determined by plotting the image intensity vs. distance across each region, as shown in Figure 3.11. Using MATLAB a graphical interface displayed the intensity profile along a line of interest, allowing the user to specify the beginning and end of the vessel. The peaks corresponding to the edges of the near and far walls were located. The distance in mm was calculated by measuring the known dimensions of the phantom and converting the pixel distance in mm. Li et al., (1993)

showed that B-mode diameter estimation is typically in error by half the ultrasound pulse length. Three distributions of intensity vs. distance were obtained for each region for the three phantoms. A one-way repeated measure of ANOVA statistical test was carried out to compare lumen diameters from the individual phantoms. The diameters from each metal model and the corresponding phantom were compared using a paired t-test. Finally the difference in diameters between the original computer model, rapid prototype model, metal models and vessel lumens were investigated using a repeated measure of ANOVA statistical test. The null hypothesis being tested was that there was no difference in the dimensions of the models. If $p < 0.05$, the null hypothesis was rejected and there was a statistical difference in the dimensions of the models. All statistical tests were carried out using Minitab® Statistical Software (version 15).

3.2.4 Basic flow simulations

All finished phantoms were tested for leakage and examined for residual metal remaining in the lumen, since this could lead to imaging or flow artefacts. A HDI 3000 (ATL/Philips, Amsterdam, The Netherlands) with a linear broadband transducer, L12-5 was used to obtain B-mode images of each phantom. The phantoms were connected to a simple flow system which provided *in-vitro* flow. The flow system consisted of a magnetically driven gear pump head (Cole Parmer, Walden, UK) coupled to a direct current servo motor (McLennan Servo Suppliers Ltd., Surrey, UK). The motor was driven by a servo amplifier (Aerotech Ltd., Berkshire, UK). A computer controller program developed in Labview (National Instruments, TX, USA) was programmed to send a variety of different flow patterns, such as steady, pulsatile, or arbitrary shaped flow. BMF which had been degassed using a sonicator was pumped through the phantoms using the gear pump for 1 hour prior to measurements to ensure air bubbles

remained. Each phantom was tested at three set mean velocities 12 cm s^{-1}, 25 cm s^{-1} and 40 cm s^{-1} (calibrated using timed weight collection) and BMF was continually pumped through each phantom for at least 1 hour to ensure there was no leakage or ruptures within the vessel lumen.

3.3 RESULTS

3.3.1 Geometric accuracy

Validation of metal core and phantom lumen diameters

Table 3.1 shows the mean of the three repeated diameter measurements made on each of the metal cores at each region. Using a one-way repeated measure of ANOVA statistical test, no significant difference was found between the 3 regions on each model and between the 5 models (p=0.336). The mean of the three repeated diameter measurements made of the lumen at each region for the 5 phantoms is shown in Table 3.2. Again no significant difference was found between the 3 regions on each model and between the 5 models (p=0.152).

Table 3.1 Mean diameters (in mm) of the 3 locations measured for each of the 5 metal cores

Location	Core 1	Core 2	Core 3	Core 4	Core 5
A	7.62	7.63	7.63	7.59	7.70
B	7.68	7.59	7.68	7.68	7.66
C	7.57	7.62	7.71	7.64	7.64

Table 3.2 Mean diameters (in mm) of the 3 locations measured for each of the 5 phantom lumens

Location	Lumen 1	Lumen 2	Lumen 3	Lumen 4	Lumen 5
A	7.70	7.70	7.70	7.70	7.80
B	7.70	7.60	7.70	7.60	7.70
C	7.60	7.60	7.70	7.60	7.70

Using a paired t-test, corresponding metal core and phantoms lumens were compared. The p values are presented in Table 3.3 for the 5 sets; they show no significant

differences in the diameters between the corresponding metal cores and lumens of the phantoms ($p > 0.05$).

Table 3.3 The p values calculated from paired t-tests for each corresponding metal core and phantom lumen

Core & lumen	P Value
1	0.145
2	0.529
3	0.371
4	0.959
5	0.064

Table 3.4 *Mean diameter* (in mm) of the 3 locations of the original CAD geometry, RP model, metal core and phantom lumen

Set	CAD	RP	Metal Core	Lumen
1	6.8*	7.68	7.62	7.67
2	6.8*	7.68	7.61	7.63
3	6.8*	7.68	7.67	7.70
4	6.8*	7.68	7.64	7.63
5	6.8*	7.68	7.67	7.73

The mean diameters of the 3 locations for each of the models (original CAD, RP, metal core and phantom lumen) are shown in Table 3.4. Statistically significant differences were found between the original computer model, RP model, metal cores and phantom lumens ($p < 0.05$), in Table 3.4 the asterisk (*) denotes that the CAD model diameter was significantly to the other three models. Although statistically significant differences were found between the original CAD model, RP model, metal cores and phantom lumens, these differences are due to the rapid prototyping process which

resulted in the model diameter increasing by 1 mm. As the other tests showed there are no statistical differences between the metal cores and phantom lumens showing that the fabrication methods are valid and reproducible.

3.3.2 Basic flow simulations

All phantoms developed underwent basic flow measurements for a minimum of 1 hour to ensure there were no ruptures or leakages. Of the wall-less phantoms there was no leakage of BMF through the normal healthy vessel, 30%, and 50% stenosis lumens at a mean velocity of 40 cm s^{-1}. The 70% phantom leaked 2 hours after flow started at a velocity of 40 cm s^{-1}. The 85% phantom leaked within 1 hour of starting flow. All other phantoms did not leak even after 5 hours continuous flow. No leakage of BMF occurred with the walled phantoms except for the 85% phantom which leaked when the velocity was set 12 cm s^{-1}. After removing the TMM and inspecting the PVA C vessel, the site of BMF leakage was identified at the inlet where the vessel had come away from the rigid tubing. An in-depth study of the flow measurements obtained using both the wall-less and walled phantoms is presented in Chapter 4. The lumens of the wall-less phantoms were also examined to ensure no residual metal remained. Residual metal was not an issue for the walled flow phantoms as the metal was removed before the PVA C vessels were placed in the phantoms. Initially it was found that metal remained in the wall-less phantom lumens even after 4 hours in a water bath. Figure 3.12 shows an example of the amount of metal found remaining in the lumen. To overcome the problem of residual metal, clingfilm was used as described in section 3.2.2. Figure 3.13 shows that by using the clingfilm it was possible to obtain lumens that had no residual metal for all wall-less phantoms with the varying degrees of stenosis.

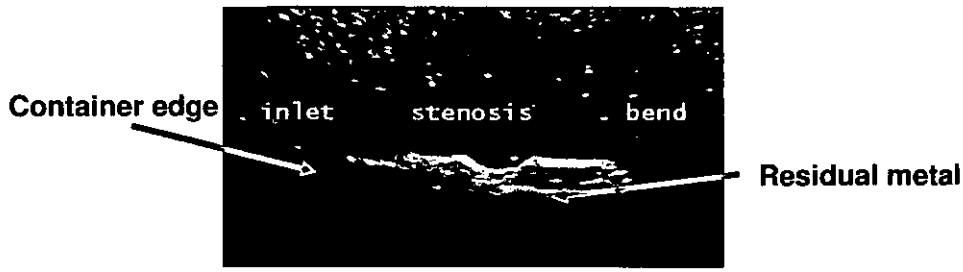

Figure 3.12 B-mode image of 50% stenosis lumen with residual metal present

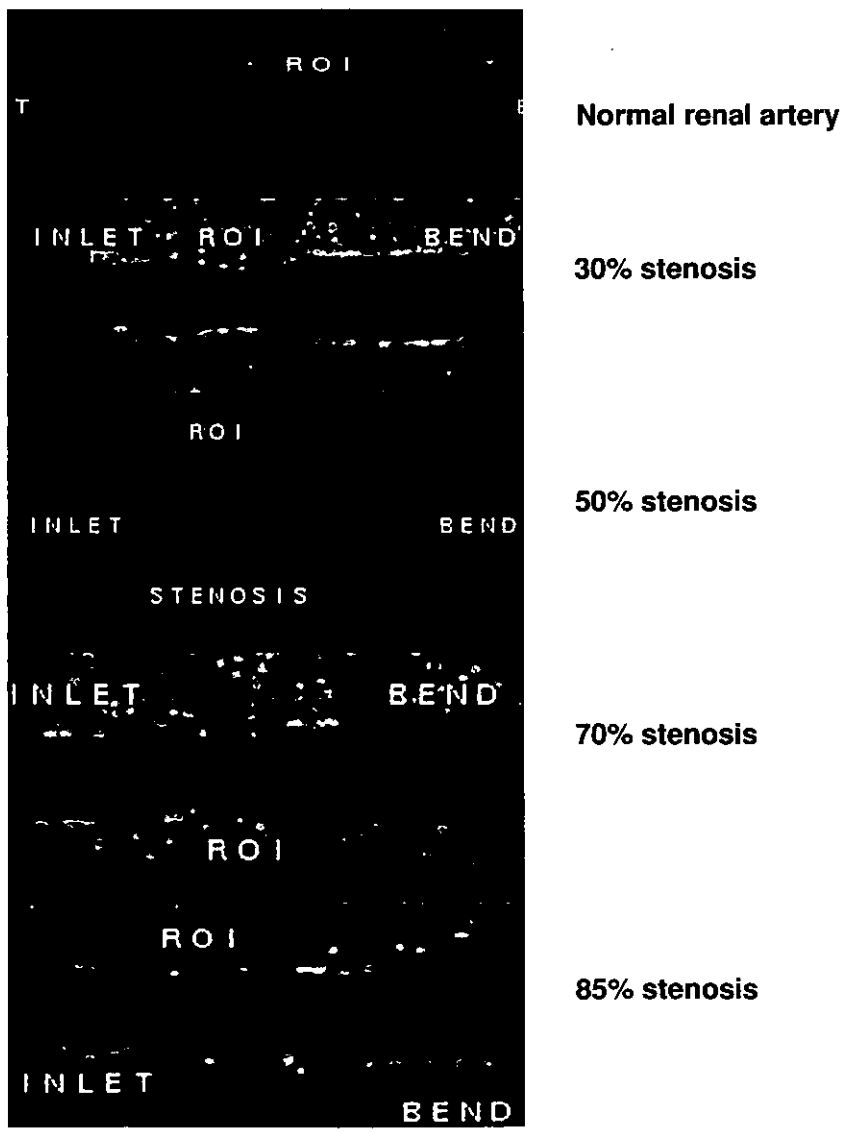

Figure 3.13 B-mode images showing inlet of renal artery flow phantom with varying degrees of stenosis (normal healthy artery, 30%, 50%, 70% and 85%)

3.4 DISCUSSION

In this chapter the development of a range of anatomically realistic renal artery flow phantoms with varying degrees of stenosis was described. Three versions of this novel anatomically realistic renal phantom were developed, 2 flow experimental phantoms (wall-less and walled) and a multi-modality wall-less phantom. The phantoms developed had to meet 3 requirements, (1) to be anatomically realistic, the geometry of vessels should mimic the complexity of real human vessels, (2) be compatible with all imaging modalities evaluated and (3) contain markers visible in all modalities to allow image calibration.

With the advancement of CAD and RP techniques, it is possible to fabricate anatomically realistic complex models of arteries as found *in-vivo*. A 3D model of the renal artery was developed using a 64-slice CT scan of the abdominal region of a healthy volunteer with normal renal vasculature. From this data set a generic 3D model of the renal artery was rendered. During the development of the renal artery model (normal and diseased models) slight changes to the computer model were implemented to aid the lost core casting technique. The changes did not alter the geometry of the renal artery which remained anatomically realistic. In the original computer models there were 6-sided polygon extrusions on each side of the model. It was observed that the 6-sided polygon extrusions lost their definition in the metal lumen model. This resulted in problems centring the metal lumen in the silicone moulds. The computer model was altered and a better defined 4-sided polygon extrusion was used on each side to aid the centring of the metal model.

Originally in the computer model of the diseased renal arteries, the chosen area for the blockage was scaled about its centroid by an amount that corresponded to the desired degree of stenosis. While designing the 70% and 85% diseased models it was felt that this method would produce models so fragile that they would break while being rapid prototyped. To overcome this problem a type of 'goalpost support' was used. These supports were built on the top and bottom of the stenosis to frame the area and provide extra support while the model was being machined. Unfortunately, even with the presence of the supports, the stenosis area was still too weak and fragile.

Finally, a method was developed that allowed for the whole range of stenosis to be machined successfully. Instead of producing a whole new renal artery for each blockage an insert with the desired blockage was developed as discussed in section 3.2.1. This allowed for the insert to be placed into an adapted silicone mould of the normal renal artery lumen 10 mm from the inlet. The advantage of this method was that the outside walls of the insets were thickened to increase the stability of the model even for the most stenosed models (85%). Also, it reduced the number of rapid prototyped models and silicone moulds required. With the advancements in the production techniques, accurate and reproducible renal artery models were possible at reduced cost and time. In particular the development of the novel stenosis inserts does not appear to have been used before. Previous studies created a separate mould for each of the required blockages (Poepping et al., 2002; Watts et al., 2007).

Although statistically significant differences were found between the original CAD model, and the final vessel lumen these differences were due to the rapid prototyping process which resulted in the model diameter increasing by 1 mm. As the other tests

showed there were no statistical differences between the metal cores and phantom lumens showing that the fabrication methods were valid and reproducible. Similar results were observed by Meagher et al., (2007). This allows for the fabrication and development of many exact duplicates of the renal flow phantom to enable the study of disease progression in the renal artery with increasing stenosis.

Initially during the removal of the low melting alloy from the phantom, a large amount of residual metal was found remaining in the lumen. A number of studies have used similar low melting alloys to create realistic vessels (Meagher et al., 2007; Poepping et al., 2002; Poepping et al., 2004; Smith et al., 1999) and did not disclose any major problems with residual metal in phantoms. Smith et al., (1999) pumped nitric acid solution (7% NHO_3 by volume) through the phantom lumen for 4 hours to ensure no residual metal was left. This was repeated in this study and after 6 hours there was still a significant amount of low melting alloy remaining in the lumen particularly at the bend and at the site of stenosis (Figure 3.11). This method was very time consuming and there was concern about the effect of the acid on the acoustic properties of the TMM as it was in constant contact within the TMM lumen. To overcome this problem a thin layer of clingfilm was wrapped around each of the metal models before they were placed in the phantoms. Care was taken not to change the dimensions or geometry of the models. This method was successful in removing all the low melting alloys as can be seen in Figure 3.13.

Wall-less flow phantoms have no tubing material and the BMF is in direct contact with the TMM. Therefore, it is important to have a good seal between the inlet and outlet tubes and the TMM vessel lumen to prevent BMF leakage. A number of methods have

been described to seal the vessel adequately and overcome TMM rupture (Poepping et al., 2002; Ramnarine et al., 2001; Rickey et al., 1995). In the phantoms described here reticulated foam was placed around the connectors and tubing to help seal the phantom by aiding the adhesion between the TMM and wall of the container as described by Ramnarine et al., (2001). In early phantoms BMF leakage occurred at the inlet. It was felt that the pressures within the lumen were too great for the TMM and that it was splitting causing the BMF to leak. The problem was finally overcome by using the layer of clingfilm wrapped around the metal model. The addition of the clingfilm helped seal the interface between the tubing and the TMM channel. The presence of the clingfilm allowed the TMM set with a smooth continuous surface once the metal had melted out. Previous a ridge was presence between the metal models and the tubing providing a weak point where the TMM would split and rupture. No leaking of BMF occurred in the wall-less flow phantoms except for 70% and 85% stenosis. For the walled phantoms, BMF leakage did not occur except in the 85% stenosis which burst when a velocity of 12 cm s^{-1} was reached. Flow measurements obtained using the wall-less and walled renal artery flow phantoms are described in detail in Chapter 4.

Fiducial markers are very useful in the identification and orientation of plane views in DSA, CTA, MRA and US (Cloutier et al., 2004). To date very few vascular phantoms have provided fiducial markers (Cloutier et al., 2004; Dabrowski et al., 1997; Frayne et al., 1993). Careful consideration was required when choosing the type of fiducial marker as it needed to be visible in the images of all four modalities. For US and MRI, the markers need to be small and have high contrast in tissue. For imaging techniques based on x-rays (DSA and CT) the markers need to have high x-ray attenuation. For these reasons glass beads (4mm) were chosen. These multi-modality phantoms were

used to carry out a comparative study between US, DSA, CT and MRI and the images and data obtained will be presented in Chapter 6.

3.5 CONCLUSIONS

Computer-aided modelling techniques were used to generate a range of anatomically realistic phantoms of the renal artery from medical images of a 64-slice CT scan of the abdominal region which was acquired from a healthy volunteer with normal renal vasculature. From this data a computer model of a normal healthy renal artery was generated. Using a 3D printer a physical model of the renal artery was produced. A range of diseased renal artery models were also constructed (with 30%, 50%, 70% and 85% stenoses). An investment casting technique was employed to fabricate the phantoms. Using the above techniques a range of anatomically realistic renal flow phantoms with varying degrees of stenosis were developed for Doppler ultrasound flow measurements and for a comparative multi-modality study of the 4 imaging techniques used to detect renal artery stenosis (US, DSA, MRI and CT). Currently, there are no anatomically realistic renal artery and kidney flow phantoms available commercially. These novel renal phantoms can provide a means of evaluation of current and emerging ultrasound technology as well as being able to observe the hemodynamic features within the renal artery. They may also become useful training tools for practitioners engaged in the detection of renal artery stenosis.

CHAPTER 4 EXPERIMENTATION USING ANATOMICALLY REALISTIC RENAL ARTERY FLOW PHANTOMS

4.1 INTRODUCTION

This chapter describes the flow experiments carried out with the (wall-less and walled) anatomically realistic renal artery flow phantoms developed as part of this project using steady state velocities. Maximum velocity measurements were obtained to determine if it is possible to detect lower grade stenosis (30%) by interrogating the entire vessel of the phantoms in a systematic manner and looking for changes related to known diameter reductions. Here current ultrasound technology was evaluated to determine if it can distinguish changes in maximum velocity measurements due to the presence of a range of stenosis in the *in-vitro* anatomically realistic renal arteries.

4.1.1 Maximum Doppler velocity measurements

Doppler ultrasound measurements of the peak blood flow velocity are the most common method for determining the severity of a stenosis in the carotid, renal and peripheral arteries and for detecting stenosis in bypass grafts (Steinman et al., 2001). In arteries, increased velocities occur in a region of a stenosis and an indication of the degree of stenosis may be derived directly from the maximum velocity measurement as discussed in section 1.4.3. The % stenosis and corresponding PSV according to the guidelines set out in the Institute of Physics and Engineering in Medicine (IPEM), Vascular Laboratory practise manual 2004 are given in Figure 4.1 and Table 4.1 (IPEM, 2004).

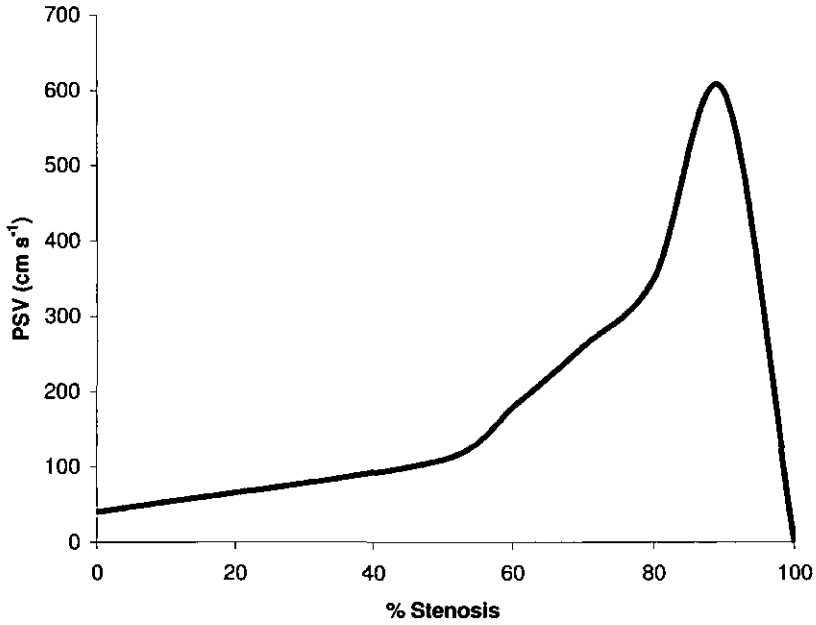

Figure 4.1 Quantification of RAS (IPEM Vascular Laboratory Practice Manual 2004)

Table 4.1 Summary of the classification of renal artery stenosis, criteria developed by D.E. Strandness, (2002)

Normal (0% diameter reduction)
PSV < 180 cm s^{-1}
No focal renal artery velocity increase
No post-stenotic disturbance
RAR < 3.5
Low Grade (<60% diameter reduction
PSV > 180 cm s^{-1}
Focal renal artery velocity increase
No post stenotic flow disturbance
RAR < 3.5
High Grade (60-90% diameter reduction)
PSV > 180 cm s^{-1}
Focal renal velocity increase
Post-stenotic turbulence
RAR > 3.5
Total Occlusion (100% stenosis)
No renal artery flow
RAR not measurable
Parenchymal velocity < 10 cm s^{-1}
Kidney length < 9 cm

4.1.2 Blood flow

Blood is a viscous, non-Newtonian fluid and blood flow is a complex pulsatile flow of a non-homogenous fluid in elastic tubes. When one layer of fluid moves with respect to another the frictional force that arises between them is due to viscosity. In a non-Newtonian fluid the viscosity is dependant on shear rate and the velocity. It is possible to treat blood as a Newtonian fluid for vessels whose diameter is greater than 0.1 mm as this effect of viscosity dependence is not significant in vessels of this size. A Newtonian fluid has a constant viscosity coefficient which is independent of shear rate at a particular temperature. Blood flow in normal non-diseased arteries usually has a flattened parabolic profile due to the pulsatile flow in the majority of major vessels. Here the blood moves in layers with each layer remaining a fixed distance from the tube wall as shown in Figure 4.2. The velocity of the blood in the layer becomes greater as the distance of the layer from the wall increase, in a parabolic function. At the vessel wall, the blood moves the slowest and may even be stationary due to the viscous drag exerted by the wall.

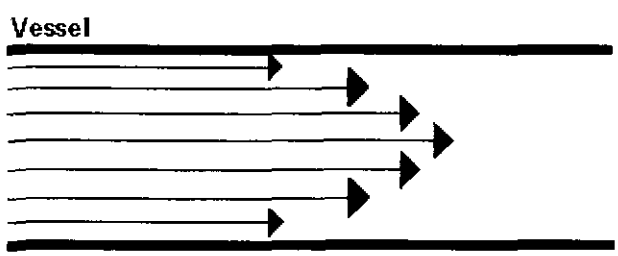

Figure 4.2 Velocity profile of a fluid exhibiting laminar flow in a vessel

To gain an understanding of the complexity of blood flow, it is important to carry out flow experimentation using simple basic models that initially consist of steady flow in straight rigid tubes or anatomically realistic vessels with curves and blockages. Steady

laminar flow occurs where all conditions at any point in a stream remain constant with respect to time. Laminar flow (also referred to as Poiseuille flow) of Newtonian fluids in rigid tubes is well understood. Poiseuille's law states that the pressure drop along a section of tube (Δp), is proportional to the volumetric flow (Q), the fluid viscosity (η) and the length of the tube (L), and inversely proportional to the fourth power of the radius (r),

$$\Delta p = 8\eta QL/\pi r^4 \qquad \textbf{Equation 4.1}$$

RAS due to atherosclerosis is an obstruction in the arterial lumen due to the formation of plaque. Plaques are associated with degenerative changes in the arterial wall by lipid and calcium deposits. When a stenosis is present, the flow is disturbed, resulting in an increase in the flow velocity across the narrowed lumen as shown in Figure 4.3. In order for the blood to pass through the stenosis, the flow streamlines must converge, possibly changing the Doppler angle leading to potential misinterpretation of velocity and velocity changes. For this study only concentric stenoses were used and since these have radial symmetry, the maximum velocity will be exhibited centrally within the vessel. However, for higher stenosis the highest velocity will be at the site of turbulence downstream from the stenosis.

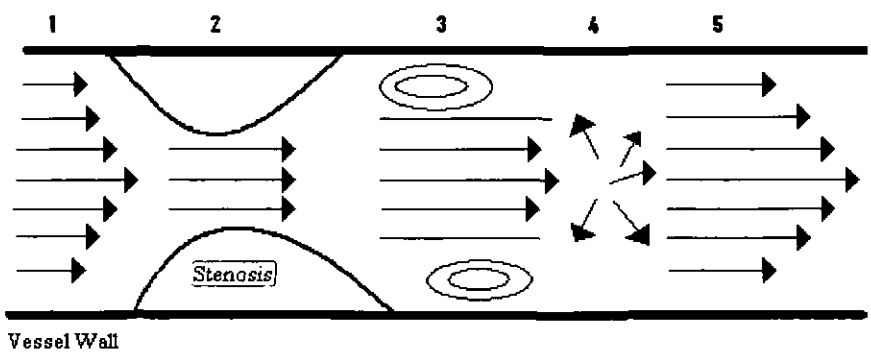

Figure 4.3 Velocity profile at stenosis (1-proximal to stenosis, 2-concident, 3- immediately distal of stenosis, 4- distal, and 5 –more distal of site of stenosis)

The high velocity jet at the site of the stenosis has a flat velocity profile. As the jet exits the stenotic region, the lumen widens to its original diameter. The expanded area causes the high velocity jet to slow and areas of flow reversal may be found immediately beyond the stenosis and distal to the stenosis. Here turbulent flow may occur before laminar flow is re-established. Turbulent flow occurs when laminar flow becomes unstable at high velocities and breaks down. The stage at which laminar flow breaks down into turbulent flow can be predicted by the Reynolds' number, Re, which is defined as:

$$(Re=\rho dv/\eta) \qquad \textbf{Equation 4.2}$$

where ρ is the density, d (cm) is the inner diameter of the tube, v (cm/s) is the highest mean velocity, and η is the fluid viscosity. The critical Reynolds' number, Re_{crit}, is the Re at which the flow becomes turbulent. The Re_{crit}, for the renal artery is 700 (Milnor, 1982).

When flow enters a tube it must travel a certain distance before laminar flow is established. To establish laminar flow, the required inlet length can be determined by the Equation 4.3 below (Nichols and O'Rourke, 1990).

$$L=0.04dRe \qquad \textbf{Equation 4.3}$$

where L (cm) is the inlet length of tubing required to achieve laminar flow conditions, d (cm) is the inner diameter of the tube and Re is the Reynolds' number ($Re = \rho dv/\eta$, where ρ is the density of the BMF (1.037 g cm^{-3}), v is the mean velocity used (cm s^{-1}), and η is the fluid viscosity (0.041 g cm^{-1} s^{-1}). *In-vivo* for the renal arteries the inlet

length is 13 cm and due to the entrance effects from the aorta a steady state mean profile can never be established (Evans and McDicken, 2000).

In the human body vessels are rarely straight, and curves and branching of vessels will modify both the velocity profile and the local pressure gradient. When flow enters a curved section of a tube it experiences a centrifugal force. This force is proportional to the velocity squared and inversely proportional to the radius of the curvature. The resulting change in the flow pattern depends on the velocity profile existing before entering the curve. The renal artery lumen in the phantoms has a bend in the vessel and therefore the resulting flow pattern exiting the bend will depend on the presence and size of a stenosis before the bend.

4.2 METHODOLOGY

An ATL HDI 3000 ultrasound scanner with a broadband curvilinear transducer C4-2 (nominal frequency 2.5 MHz) set to a user-defined clinical preset, and optimised for renal imaging was used to carry out the velocity measurements in the anatomically realistic renal flow phantoms.

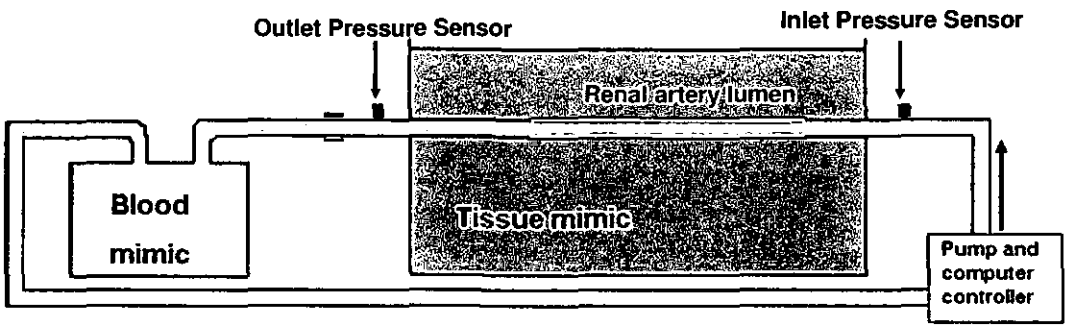

Figure 4.4 Schematic of flow circuit used for the renal artery flow phantom experiments

The experimental set-up is shown in Figure 4.4. Two gauge pressure sensors (Honeywell S&C, MN, USA) were positioned 40 mm from the inlet and outlet ports of the phantom. The pressure sensors were connected to a data logger computer program developed in LabVIEW (National Instruments, TX, USA). The pressure gradient across the stenosis was measured using these two pressure sensors located at the inlet and outlet ports.

BMF was pumped through the flow circuit using a high flow suction shoe head pump (Cole-Parmer, Walden, UK). The temperature of the flow phantom and BMF was maintained at 22°C ± 1°C. Three steady state velocities of 12, 25 and 40 cm s^{-1} were used in this study. It was important to ensure that the flow was laminar; therefore, the

inlet tube was straightened to the required inlet length of 26 cm as determined by Equation 4.3. Maximum velocity measurements were recorded using PW Spectral Doppler at 9 locations along the length of the renal artery (Table 4.2 and Figure 4.5).

Table 4.2 Spectral Doppler measurement locations along the length of renal artery vessel

Measurement	Location	Distance (mm)
A	10 mm before ROI	10
B	ROI (stenosis)	15
C	5 mm after ROI	20
D	5 mm before bend	25
E	Inlet bend	30
F	Outlet bend	35
G	10 mm from bend	45
H	20 mm from bend	55
I	30 mm from bend	65

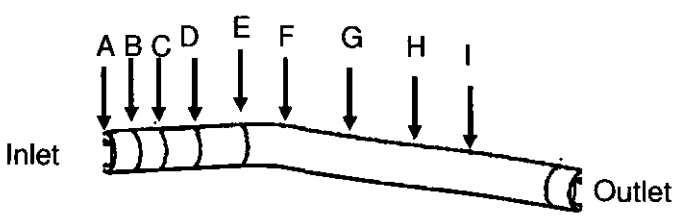

Figure 4.5 Spectral Doppler measurement locations along the length of renal artery vessel

The transducer was positioned longitudinally over the vessel at the each location, and held in place using a clamp attached to a micrometer manipulator on a translation stage. The focal zone was positioned in the centre of the vessel and the time gain compensation (TGC) control was adjusted to produce a uniform image. Spectral Doppler was turned on and Doppler velocity measurements were recorded with a SV of

1 mm positioned in the centre of the vessel. The depth of the SV was approximately 4.5 cm for each phantom. The following settings were used throughout the study. The PRF was adjusted so that the maximum flow velocity was no greater than 75% of the maximum spectral display to minimise the effect of Doppler aliasing. The wall filter was set to the lowest setting. The transducer was manually positioned to give a Doppler angle of 60°, as typically used clinically. The mechanical index was set to maximum (MI 1.3). The Doppler gain was adjusted to 57% in order to obtain a strong Doppler waveform which was free from extraneous noise. A cine-loop of the Doppler waveform was obtained and the maximum velocity was manually determined by positioning the cursor at the maximum position in the spectra, an average of five measurements was taken. This was repeated for the range of renal artery flow phantoms (wall-less and walled).

Doppler spectra post stenosis showed considerable noise. Figure 4.6 shows the placement of the callipers to record the maximum velocity. For such Doppler spectra 10 maximum velocity readings were recorded to overcome variability.

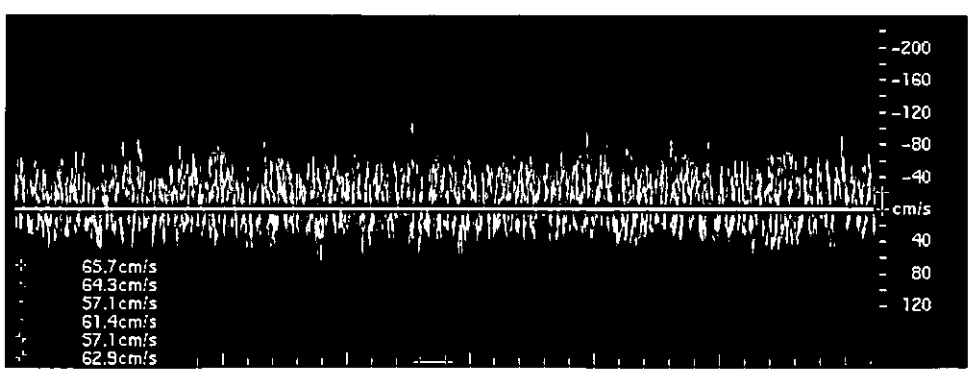

Figure 4.6 Maximum velocity measurements of turbulent flow

4.3 RESULTS

The pressure gradient across the stenosis was measured using two pressure sensors located at the inlet and outlet ports of the phantom as shown in Figure 4.4. The results are shown in Table 4.3 as the mean of 10 measurements ± 1 standard deviation.

Table 4.3 Measured pressure gradients from pressure sensors

Stenosis (%)	**Δ pressure (mm Hg)**	
	Wall-less	*Walled*
Normal	1.8 ± 0.5	0.2 ± 0.4
30	7.7 ± 1.3	6.4 ± 1.1
50	2.7 ± 0.4	2.2 ± 0.9
70	-	3.2 ± 0.9
85	-	5.0 ± 1.8

Presented in Figure 4.7 are images of the inlet region of the 30% and 70% wall-less phantoms at a set velocity of 12 cm s^{-1}. The Colour Doppler image is of the inlet region of the renal artery with stenosis, turbulent and reverse flow is evident in the post stenosis region (Figure 4.7(b)). Also shown in Figure 4.7(c) is a Spectral Doppler image obtained at the inlet bend of the renal artery with 70% stenosis present.

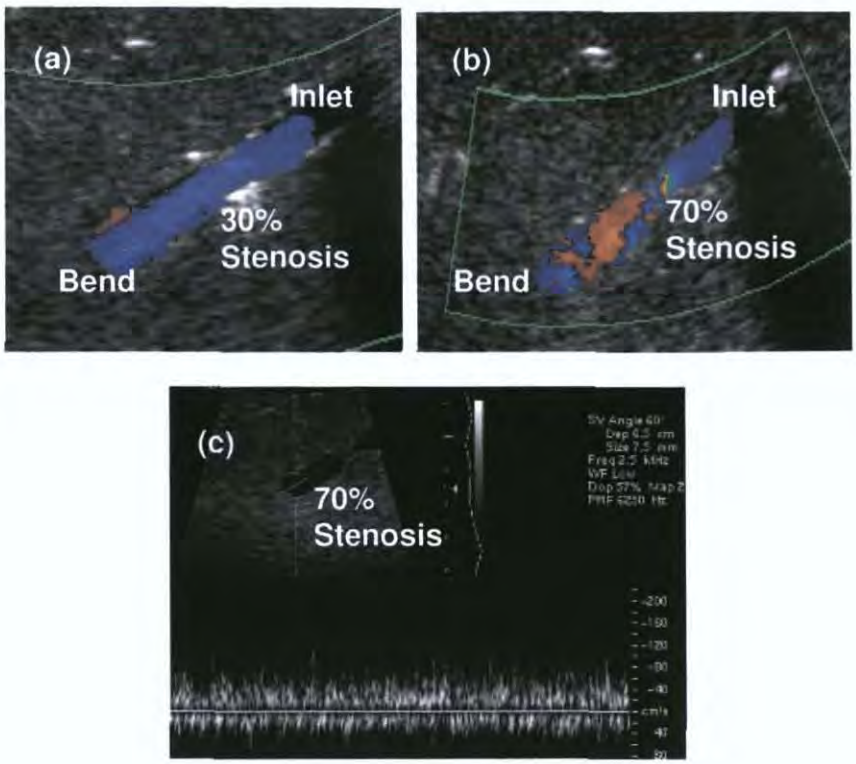

Figure 4.7 Doppler ultrasound images of wall-less phantoms (a) Colour Doppler image showing the inlet region of the renal artery with 30% stenosis, a small area of reverse flow is present at the bend, (b) Colour Doppler image showing the inlet region of the renal artery with 70% stenosis, turbulent and reverse flow are evident in the post stenosis region, and (c) Spectral Doppler image showing the spectral trace obtained at the inlet bend (measurement location E) of the 70% phantom

4.3.1 Maximum velocity measurements along renal artery vessel in wall-less phantoms

Maximum velocity measurements were obtained at 9 locations along the renal artery for the wall-less phantoms. Three steady state velocities were used; 12 cm s^{-1}, 25 cm s^{-1} and 40 cm s^{-1}. Maximum velocity measurements were obtained for the normal healthy vessel, 30% and 50% stenosed vessels at all three velocities as shown in Figures 4.8 - 4.10. For the 70% wall-less phantom only measurements at 12 cm s^{-1} were obtained as the phantom ruptured before measurement with the higher velocities could be recorded. The 85% wall-less phantom ruptured before any Doppler measurements could be recorded.

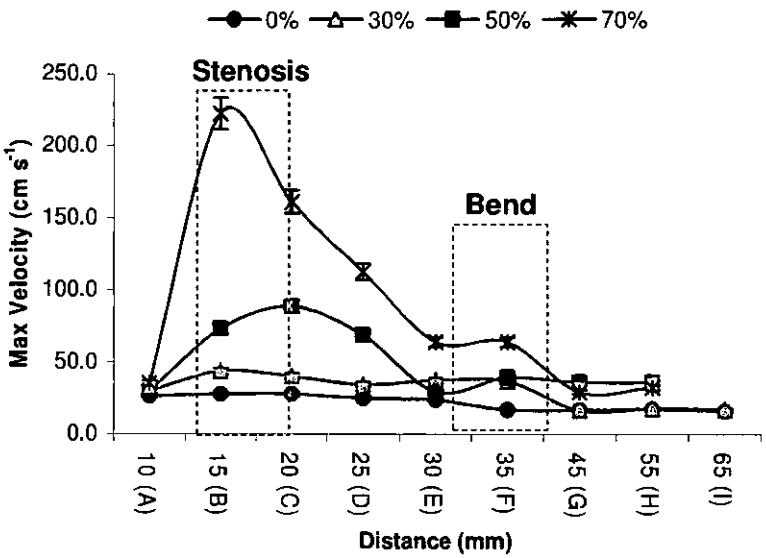

Figure 4.8 Maximum velocity measurements along the length of the renal artery vessel for the wall-less phantoms at a steady state velocity of 12 cm s^{-1}

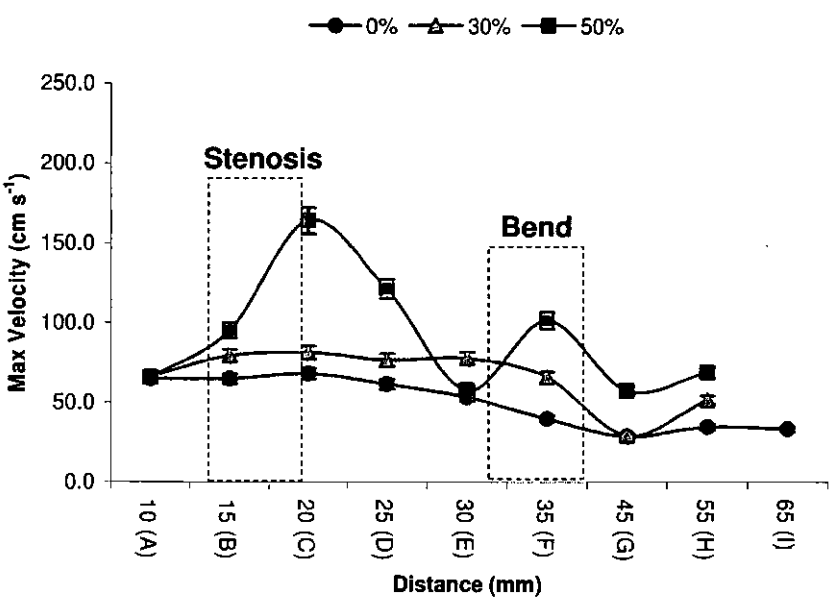

Figure 4.9 Maximum velocity measurements along the length of the renal artery vessel for the wall-less phantoms at a steady state velocity of 25 cm s^{-1}

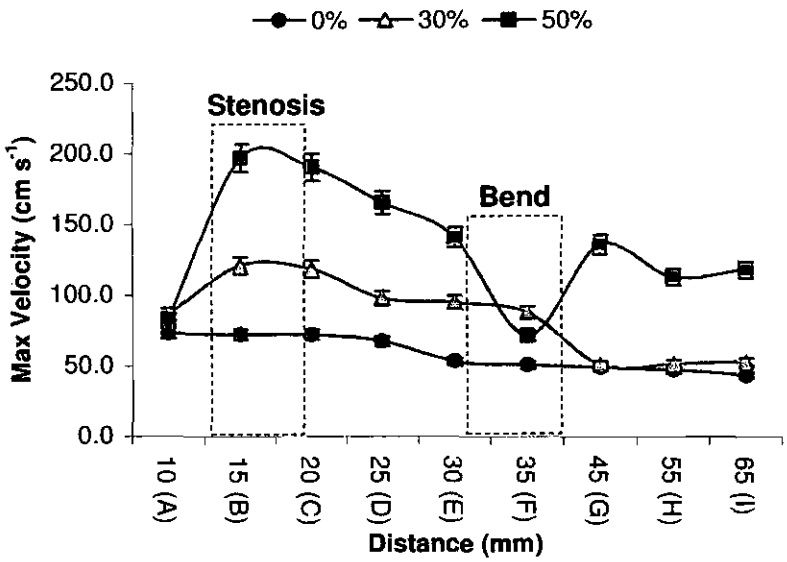

Figure 4.10 Maximum velocity measurements along the length of the renal artery vessel for the wall-less phantoms at a steady state velocity of 40 cm s^{-1}

Over the three velocity ranges used (12 cm s^{-1}, 25 cm s^{-1} and 40 cm s^{-1}), a significant difference between the maximum velocities at the site of the normal healthy artery and 30% stenosis was observed (Figures 4.8 - 4.10); this difference was most clearly identifiable when the higher velocity of 40 cm s^{-1} was used. This increase in maximum velocity at the site of stenosis was maintained until it passed through the bend and returned to its original velocity. In the normal vessel the velocity was only disturbed as it passed through the bend, a decrease in the maximum velocity was noted. The effect of the 50% and 70% stenosis were clearly observed with a significant increase in the maximum velocity at the site of stenosis. However, the 70% could only be studied at the lower velocity. For the 50% stenosis, an increase in maximum velocity was recorded after the bend.

4.3.2 Maximum velocity measurements along renal artery vessel in walled phantoms

Using the walled flow phantoms, maximum velocity measurements were obtained at 9 locations along the renal artery for the normal healthy a vessel, 30%, 50% and 70% at all three velocities (12 cm s^{-1}, 25 cm s^{-1} and 40 cm s^{-1}). For the 85% walled phantom it was only possible to obtain measurements at 12 cm s^{-1} before the PVA C vessel burst. In Figures 4.11 – 4.13, the maximum velocity measurements recorded along the length of the renal artery for the walled phantoms are presented.

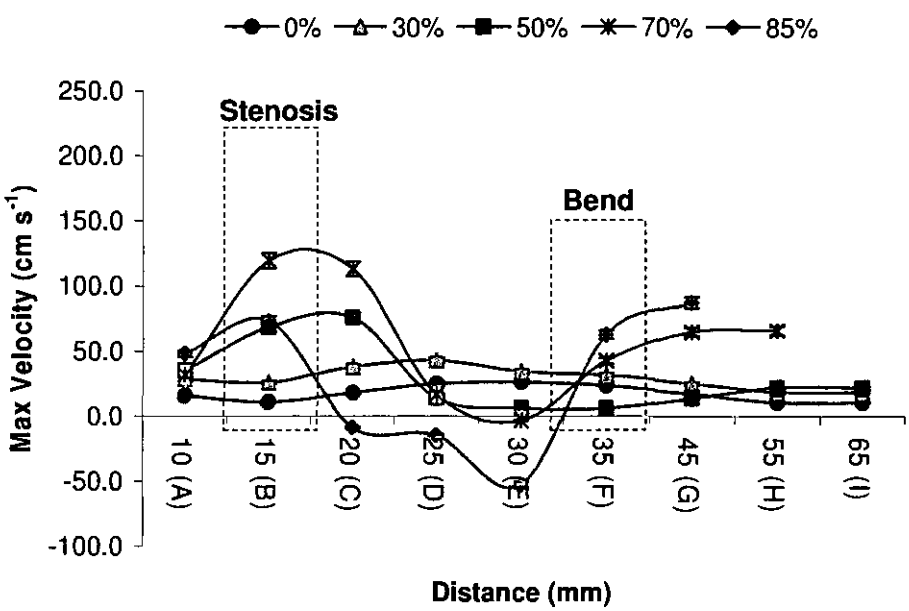

Figure 4.11 Maximum velocity measurements along the length of the renal artery vessel for the walled phantoms at a steady state velocity of 12 cm s^{-1} (note the scale is different to the wall-less phantoms due to the presence of reverse flow in the 70% and 85% phantoms)

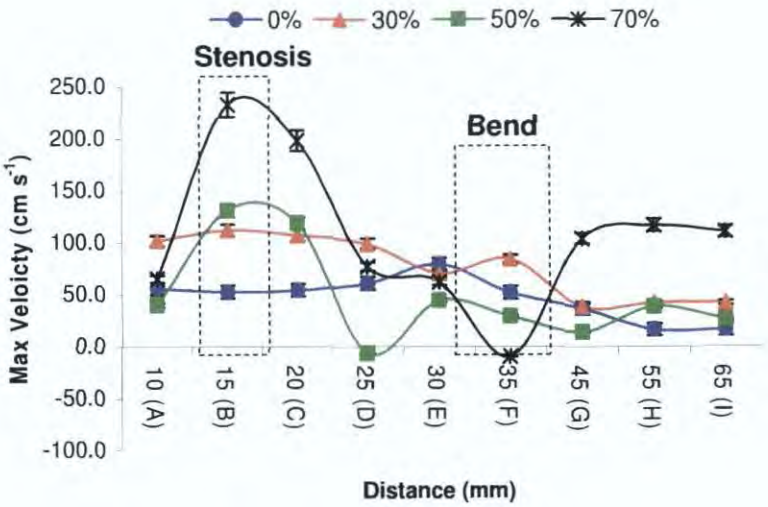

Figure 4.12 Maximum velocity measurements along the length of the renal artery vessel for the walled phantoms at a steady state velocity of 25 cm s^{-1} (note the scale is different to the wall-less phantoms due to the presence of reverse flow in the 50% and 70% phantoms)

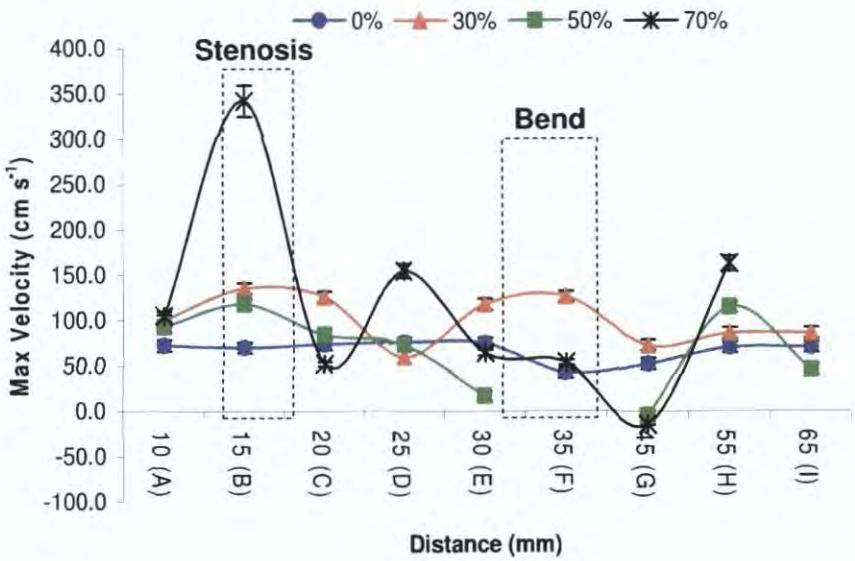

Figure 4.13 Maximum velocity measurements along the length of the renal artery vessel for the walled phantoms at a steady state velocity of 40 cm s^{-1} (note the scale is different to the wall-less phantoms due to the presence of reverse flow in the 50% and 70% phantoms and the high *maximum velocity* obtained at the site of stenosis for the 70% phantom)

For the walled phantoms with the normal healthy vessel and 30% stenosis, the maximum velocity remained relatively constant at a velocity of 12 cm s^{-1} (Figure 4.11). At this velocity, the 50%, 70%, and 85% stenosis resulted in a sudden increase in the maximum velocity at the site of the stenosis. At velocities of 25 cm $s^{-1}$and 40 cm s^{-1}, the 30% stenosis resulted in an increase in the maximum velocity, although this rise was not in a pronounced peak at it was for the higher stenosis, as shown in Figures 4.12 and 4.13. It was a gradual rise which remained elevated until it reached the inlet of the bend. It should be noted that for the 70% and 85% stenosis the maximum velocity still does not return to laminar flow 30 mm after the bend.

4.3.3 Comparison of maximum velocity measurements at site of stenosis for the wall-less and walled phantoms

The maximum velocity measurements recorded at the site of stenosis (15 mm from inlet of renal artery) for the wall-less and walled phantoms were compared. Using a paired t-test, the maximum velocities recorded from wall-less and walled phantoms were compared for the normal healthy vessel and for each stenosis 30% and 50%. The mean maximum velocity ± 1.96 (standard error (SE)), with corresponding 95% confidence intervals and p values recorded for each stenosis are presented in Table 4.4. The results show that there is a significant difference between the wall-less and walled phantom measurements ($p< 0.05$) for all stenoses.

Table 4.4 Comparison of the maximum velocity (V_{max} ± 1.96 (SE)) measured at the site of stenosis for the wall-less and walled phantoms at 40 cm s^{-1}, with the corresponding 95% confidence intervals and p value

Stenosis	**Phantom**	V_{max} (cm s^{-1})	**95% Confidence Intervals**		**P value**
			Lower	*Upper*	
Normal	Wall-less	79 ± 1	77	80	<0.0001
	Walled	70 ± 1	68	72	
30%	Wall-less	120 ± 2	117	125	<0.0001
	Walled	136 ± 1	133	139	
50%	Wall-less	197 ± 1	195	200	<0.0001
	Walled	118 ± 2	114	123	

4.4 DISCUSSION

The aim of the work was to develop a realistic *in-vitro* system for controlled flow experimentation that would have the potential to improve the assessment of *in-vivo* RAS and to detect low grade stenoses. To gain an understanding of the complex behaviour of the blood flow profile in the renal artery, it is important to begin with flow experimentation using anatomically realistic geometries which consist of steady flow in wall-less flow phantoms and walled phantoms with vessels which have visco-elastic properties.

For the wall-less phantoms it was possible to achieve 40 cm s^{-1} for normal vessel, 30% and 50% stenosis without rupturing of the vessel. The walled phantoms proved to be more mechanically robust achieving velocities similar to that found *in-vivo*, a maximum velocity 40 cm s^{-1} was achieved without rupturing in all the phantoms except the 85% stenosis. Previous studies using anatomically realistic carotid arteries have also had rupturing of vessels with high stenosis present and high flow rate. Walled vessels allow the development of a robust flow phantom which can withstand physiological flow stress (Poepping et al., 2002; Poepping et al., 2004).

During the initial set-up of the experiments the pressure gradient between the inlet and outlet ports of the phantoms were measured as shown in Table 4.2. As expected for the normal healthy vessel phantoms the pressure gradient was very small as there was no blockage present in the vessel. For phantoms with a stenosis present, the 30% stenosis for both the wall-less and walled phantom had the greatest pressure gradient of 7.7 mm Hg and 6.4 mm Hg, respectively. The pressure gradients observed in the renal

artery flow phantoms with stenosis > 50% were significantly lower than those observed *in-vivo*. As discussed in section 1.6, a stenosis of 50% is considered to be hemodynamically significant as it is at this level the pressure gradient increases significantly (> 20 mm Hg). Since there was a large distance between to two pressure sensors, the flow may have returned to laminar flow and the energy dissipated by the time it reached the second sensor, resulting in a low pressure gradient.

In clinical practice, Colour Doppler is often used to guide the sonographer to the area of the stenosis and then Spectral Doppler is used to measure the local maximum velocity. Colour Doppler was used to visualise turbulent and reverse flow which occurred after tight stenosis (70%). Figure 4.7 shows the Colour Doppler images obtained from wall-less phantoms with 30% and 70% stenoses at a set velocity of 12 cm s^{-1}. For the 30% stenosis, the flow does not appear to be disturbed after the stenosis. An area of reverse flow can be seen at the upper wall of the bend. With an increase in the stenosis (70%) one can observe disturbed and reverse flow immediately distal to the stenosis. This is similar to that found *in-vivo*. Care was taken when measuring the post stenosis maximum velocities as considerable noise was presence with the higher blockages. A sample image of how the measurements were performed is shown in Figure 4.6. The manual method is time consuming and prone to high operator variability in turbulent areas. Although the development of an automated method was outside the remit of this project, it may eliminate the operator variability and reduce the time taken to record the measurements

As the geometry of the renal artery vessel in the phantoms was based on clinical data, the presence of the bend 10 mm after the stenosis, introduced an additional effect on the

velocity profile, for this reason maximum velocity measurements were recorded over distance to observe how the velocity profile changed. It is important to note that clinically the maximum velocity is measured at the point of the minimum lumen. From Figures 4.8 - 4.13, a number of trends were observed regarding the maximum velocity measurements. At all three velocities, there was a significant increase in the maximum velocity with the presence of a 30% stenosis in both the wall-less and walled flow phantoms. At 40 cm s^{-1} the presence of this low grade stenosis was clearly identifiably due to the increase of the maximum velocity at the site of stenosis and approaching the bend. The presence of the bend in the vessel resulted in a decrease in the maximum velocity at 30 - 35 mm along the renal artery. Regions of reverse flow were observed for the 70% and 85% stenosed vessels at the location of the bend in the walled phantoms. The higher degrees of stenosis caused greater flow disturbance which was further disrupted by the presence of the bend, taking longer for the flow to return to its laminar profile. At approximately 45 mm from the inlet the maximum velocity measurements plateau for all phantoms except the walled 70% stenosis phantom at 40 cm s^{-1}.

These basic flow experiments have shown the potential for these anatomically realistic renal artery flow phantoms allowing interrogation along the entire vessel in a systematic manner and looking for changes in the maximum velocity related to known diameter reductions. Here current ultrasound technology was evaluated to determine if it can distinguish changes in maximum velocity measurements due to the presence of a range of stenosis in the anatomically realistic renal arteries. In the Chapter 5, the presence of fat layers which are a major limitation of renal imaging will be discussed. By adding a

fat mimicking material to the anatomically realistic renal artery phantoms the effect of an overlying oil layer on velocity measurements will be evaluated.

As discussed in the section 1.4.3, the most generally accepted criteria for the identification of a significant RAS (generally 50% or 60% stenosis) is a PSV greater than 180 cm s^{-1}. Both the 30% stenosis (wall-less and walled phantoms) would have been classified as low grade stenosis with maximum velocities less than 180 cm s^{-1}. For the 50% stenosed wall-less vessel the maximum velocity measured was 197 cm s^{-1} and this vessel would be classified as a high grade stenosis (> 180 cm s^{-1}). The 50% stenosed walled phantom had a measured maximum velocity of 118 cm s^{-1} at site of stenosis. This would be incorrectly classified as a low grade stenosis. The 70% stenosed walled vessel would be correctly recorded as a high grade stenosis with a maximum velocity of 342 cm s^{-1}.

Two types of renal artery flow phantoms were developed, wall-less and walled phantoms. Although wall-less phantoms avoid mismatch problems in acoustic properties they lack the presence of a realistic vessel wall. This was overcome by developing a PVA C vessel (2 mm wall thickness) mimicking the shape of the renal artery. In this study the presence of the PVA C vessel wall showed a significant effect on the maximum velocity measurements at the region of the stenosis (where the PVA C wall is at its thickest). In the normal vessel and 50% stenosis walled phantoms, a lower maximum velocity was recorded, whereas for the 30% stenosis a higher maximum velocity was measured. This may be due to the vessel wall distending under pressure as occurs at high flow rates (Hein and O'Brien, 1992). This causes an increase in the vessel diameter in the presence of slow flow, leading to overestimation. It would have

been expected that for the 50% stenosis an overestimation of the velocity would be recorded, if the PVA C vessel wall had distended. A possible reason for the reduction in velocity in the walled vessels is the presence of friction creating a drag force on the velocity profile. The PVA C vessel will have a significant effect on the maximum velocity measurements using pulsatile flow. The pump will produce pressure waves which travel down the vessel at a speed determined by the elastic properties of the vessel wall. Since the PVA C vessel is a visco-elastic material, reflections of the pressure waves will occur at the stenosis and bending of the vessel. If the material is very elastic a second peak on the flow waveform could occur (IPEM, 2004). These false secondary waves could be removed by the use of a high out-flow impedance (Hoskins et al., 1989). In this study only maximum velocity measurements were performed in the flow experimentations. A recent meta-analysis found maximum velocity measurements to be the most accurate test parameter, as discussed in section 1.4.3 (Williams et al., 2007). In future studies using the anatomically realistic renal artery phantoms and pulsatile flow, the investigation of other indices such as spectral broadening, renal-aorta ratio, pulsatile index, resistive index and acceleration index would be important to determine if lower stenosis can be accurately detected (Beattie et al., 1997; Williams et al., 2007).

4.5 CONCLUSIONS

In summary, basic flow experimentation using the novel anatomically realistic renal flow phantoms has demonstrated the potential of this *in-vitro* system to mimic the velocities observed in the renal arteries *in-vivo*. These studies have shown potential indicators of early stenosis, with changes in the maximum velocity at the site of stenosis and distal to the stenosis. Since steady state velocities were used it is important to carry out pulsatile flow experimentation and to obtain a full 3D flow profile of the range of vessels with increasing stenosis.

CHAPTER 5 THE EFFECT OF A FAT MIMICKING LAYER ON MAXIMUM VELOCITY MEASUREMENTS

5.1. INTRODUCTION

This chapter investigates the effect of an overlying fat mimicking (oil) layer on maximum velocity measurements. Doppler ultrasound has a number of limitations that have hampered its development as a tool for examining the renal system, where vessel diameters range from 5 μm – 8 mm. These limitations include the presence of overlying subcutaneous fat layers in many patients giving rise to signal distortion and excessive attenuation of the ultrasound beam. This causes increased difficulty in detecting areas of small blood flow such as kidney perfusion and regions of stenosis. Olive oil was chosen to replicate a very simple fat mimicking layer. In order to evaluate fully how this basic fat mimicking layer alone affected the velocity information, string phantom experiments were performed first. The string phantom was used to observe and quantify the maximum velocity error in absence of an attenuating medium and to observe any misregistration effects due to the superficial oil layer. Then a simple straight vessel flow phantom was used, here the ultrasound beam will be affected differently since an attenuating medium (TMM) is present. The simple fat mimicking layer and the presence of a tissue mimicking material should replicate roughly what can occur *in-vivo.* Finally maximum velocity measurements were performed with out and with the oil layer using the anatomically realistic renal artery flow phantoms. By studying the effect of the fat mimicking layer using these Doppler phantoms, a useful approximation to the errors in maximum velocity measurements can be determined and their implications for measurements in patients with RAS evaluated.

5.1.1 Maximum velocity measurements

The classification of RAS is based on the maximum velocity obtained in the region of stenosis as discussed in section 4.1.1. Therefore, errors in the maximum velocity measurements in the renal artery can lead to over- or under-estimation in the degree of stenosis measured. Many studies have assessed the accuracy of Doppler velocity measurements, in particular for maximum velocity measurements (Christopher et al., 1995; Daigle et al., 1990; Eicke et al., 1995; Goldstein, 1991a; Hoskins, 1996; Steinman et al., 2001; Steinman et al., 2005). There are a number of possible reasons for either over- or under-estimation of the maximum velocity. A complete description of the main factors contributing to these errors is provided by Christopher et al., (1995). Some of these factors include; Doppler angle mis-measurement, frequency-dependant attenuation of ultrasound by tissue, single calibrated speed of sound value, and Doppler angle measurements error due to refraction. It is expected that the presence of a fat layer will result in these factors and contribute to errors in the maximum velocity measurements.

Although there are many studies on the accuracy of Doppler velocity measurements, only a limited number have investigated the effect of incorrect speed of sound on these measurements (Christopher et al., 1995; Daigle et al., 1990; Goldstein, 1991a). Among these only Christopher and colleagues used a modified string phantom with 2 layers of media with different speeds of sound which permitted refraction to occur, thus mimicking what may occur with the superficial fat layers of tissue as found in many situations within the body.

Other secondary sources of error include intrinsic spectral broadening, intra-transducer and intra-machine variations and the effects of beam steering (Hoskins et al., 1999;

Steinman et al., 2001). Intrinsic spectral broadening (ISB) is the broadening of the Doppler spectrum due to the actual mechanism of delivering and receiving acoustic energy (the finite dimensions of the transducers) (Evans and McDicken, 2000). ISB results in a measured maximum velocity which is greater than the actual maximum velocity in the SV (Daigle et al., 1990; Hoskins et al., 1999). ISB in Doppler ultrasound is a combination of local geometric spectral broadening and transit time broadening (Fish, 1986; Guidi et al., 2000). In commercial ultrasound systems ISB is dominated by geometric spectral broadening. Geometric spectral broadening is due to the spread in frequency range due to the range of angles that the velocity vector subtends at the transducer (Newhouse et al., 1980).

Errors in maximum velocity may be measured by comparing the Doppler maximum velocity with the known maximum velocity using a Doppler test object. String phantoms have been widely used in determining these error measurements as it is possible to accurately calculate errors in the maximum velocity because the filament is set at one constant velocity. The true string velocity may be calculated from the speed of the rotation of the wheel attached to the motor. This is not the case for a flow phantom, where the true maximum velocity is obtained indirectly from the measured flow rate and the known cross-sectional area, and assuming laminar flow and a parabolic flow profile. Only a small number of maximum velocity studies have used a flow phantom (Boote and Zagzebski, 1988; Winkler and Wu, 1995).

A common problematic feature in renal imaging is the presence of abdominal subcutaneous fat layers. Such fat layers constitute substantial tissue path inhomogeneity because of the difference in the speed of sound and non uniform physical nature (fat

globules) in the fat layers relative to the deeper tissues. This gives rise to enhanced refraction of the outgoing beam and of the returning echoes. The presence of a fat layer also causes beam distortion, phase aberrations and attenuation of beam signals. Beam distortion is where the ultrasound beam is altered from its original cross-sectional contour and/or temporal waveform during propagation between two media with different speeds of sound. Phase aberration due to different delays from structures equidistant from the transducer causes defective focussing as well as blurring and degradation of the image (Ng et al., 1997). Many techniques have been suggested for measuring and correcting aberrations due to near field velocity inhomogenities such as cross correlation, adaptive processing and time-reversal point target focusing (Fink and Dorme, 1994; Krishnan et al., 1998; Ries and Smith, 1997). A new ultrasound scanner has been introduced which carries out a correction for different speeds of sound within the tissue. A focus-quality factor is used to estimate the optimum speed of sound required to achieve the sharpest image. It operates by focusing on one point of speckle in the image and sharpening the speckle by modifying the speed of sound utilised (McLaughlin, 2007). However, this changes the entire speed of sound of the image to one new speed of sound.

5.1.2 Theory

In its image reconstruction algorithm, the ultrasound scanner uses an assumed speed of sound of 1540 m s^{-1}. As a result potential artefacts due to the different speeds of sound of overlying tissue layers are neglected. In the clinical setting, the ultrasound wave originates from outside the body and usually passes through several tissue layers before reaching the blood flowing in the vessel. Figure 5.1 shows a simple example of the path

of an ultrasound beam path after it leaves the transducer (a) in the actual *in-vivo* situation, (b) in the ultrasound system's interpretation.

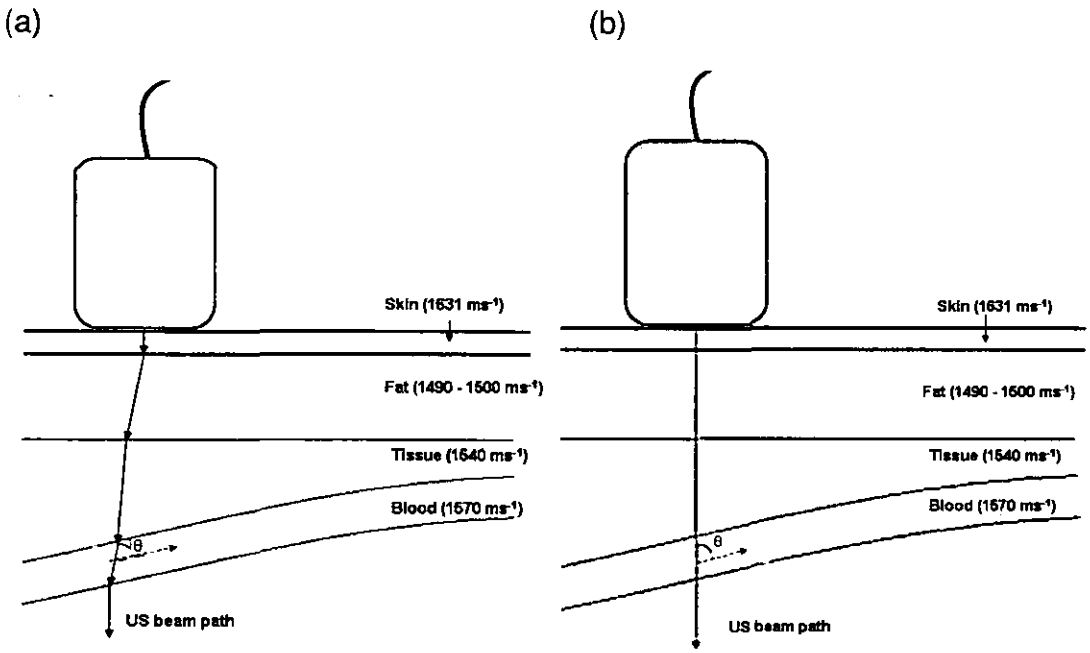

Figure 5.1 Ultrasound beam path through the tissue in the (a) actual *in-vivo* situation, and (b) ultrasound system's interpretation

The speed of sound for subcutaneous fat was reported to be between 1430 m s^{-1} and 1500 m s^{-1} (Duck, 1990). The difference in speed of sound from the calibrated machine value causes distortions in the final image, such as incorrect distance measurements, axial and lateral artefacts in image and refraction in transmitting and receiving ultrasound beams. Since the ultrasound machine uses 1540 m s^{-1} as the speed of sound to calculate distances (from the equation $d = ct$, where d is distance, t is time and c is assumed speed of sound 1540 m s^{-1}), differences in the speed of sound in the tissue will lead to inaccurate distances displayed on the B-mode image. An artefact can be defined

as false or misleading information in the image introduced by the ultrasound system due to assumptions made by the ultrasound scanner in forming the image.

Figure 5.2 (a) illustrates two rays emerging perpendicularly from the transducer, parallel to each other, and a perpendicular distance (D) apart. As the rays travel through the different layers and encounter tissue boundaries, ray B will have a longer time-of-flight than ray A. This time-of-flight difference occurs because of the unequal paths of the rays in the skin layer, a consequence of the tilted transducer relative to the boundary between the skin and fat layers. Refraction occurs when the ultrasound beam strikes a boundary at an angle of incidence, θ_i, (> 0), to the normal of the interface between two tissues with different speed of sound values. The diagram in Figure 5.2 (b) shows the two refractions of a ray travelling in the outgoing direction when a parallel-sided fat mimicking layer is present, to produce a lateral deflection or displacement of the beam.

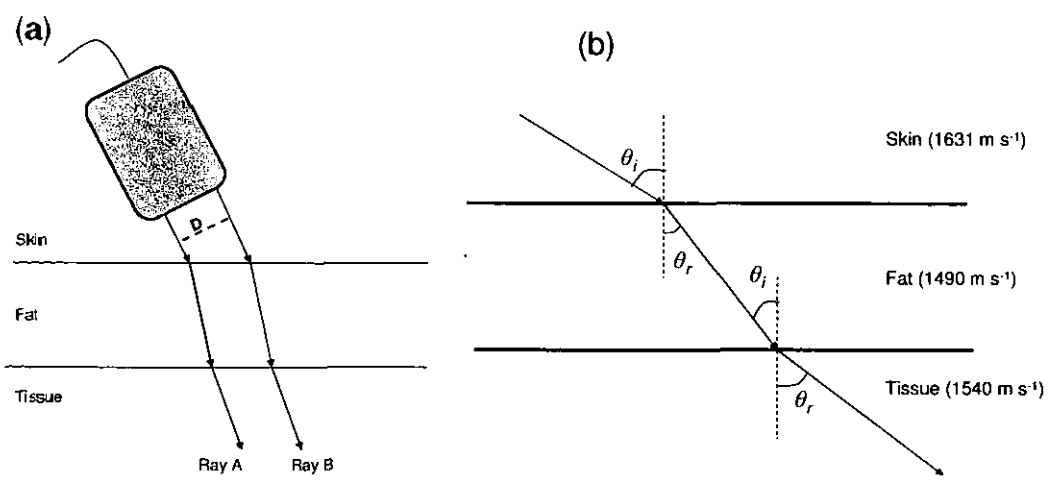

Figure 5.2 (a) Simplistic diagram showing time of flight difference due to unequal paths of the rays in the skin layer, (b) ray refraction by a fat mimicking layer

The refractive bending of the beam at a boundary occurs because part of the wave front in one medium travels more slowly than it does in the other. The resultant angle of propagation is determined by Snell's law,

$$\frac{\sin \vartheta_i}{\sin \vartheta_r} = \frac{c_1}{c_2} = n \qquad \textbf{Equation 5.1}$$

Where θ_i is the angle between the original beam and the normal to the vessel, θ_r the angle between the refracted beam and the normal to the vessel, c_1 speed of sound of the first medium, c_2 speed of sound of the second medium, and n is termed the acoustic refractive index. Therefore as a result of layers with different speeds of sound and the multiple refraction of the outgoing and returning waves, distances and angles in the displayed B-mode images will be likely to be distorted. In the Doppler application, the Doppler angle may be in error because the operator measures the Doppler angle directly from the images using an on-screen graphical calliper. Errors in the Doppler angle will give rise to errors in the maximum velocity measured (Christopher et al., 1995).

Table 5.1 Deviations in beam direction due to refraction at some tissue interfaces for an angle of incidence of 30°

Tissue Interfaces	Ratios of Speeds of Sound ($m\ s^{-1}$)	Deviation
Muscle/fat	1580/1450	2°24'
Muscle/blood	1580/1570	0°47'

As an example, Table 5.1 shows the changes in beam direction expected due to refraction at single tissue interfaces for an angle of incidence of 30° (Evans and McDicken, 2000). The small deviations which occur at muscle/fluid interfaces are

usually not highly significant. Greater deviations are to be expected when a wall is more rigid due to the presence of plaque. Using Snell's law (Equation 5.1), it is possible to calculate the expected deviations for the angle of incidence at the fat/water interface. This deviation of the ultrasound beam may result in an incorrect Doppler angle which will result in an erroneous Doppler shift being calculated and therefore the velocity measurement as given previously in Equation 1.1.

Attenuation of the beam results in the gradual loss in intensity as the beam travels through a medium. Accounting for the attenuation effects is important because reduced signal amplitude affects the quality of the image produced. The transducer has been designed to focus the beam in a medium with a speed of sound of 1540 m s^{-1}. In the case of a heterogeneous medium, such as human tissues with subcutaneous fat layers and the analogous system used in this study with the simple fat mimicking layer present, focusing can be strongly degraded due to degraded focusing of the transmitted beam and of the received echoes due to phase delays. This results in a broadening of the lateral beam profile at the tissue of interest (Chen and Zagzebski, 2004), resulting in deterioration in lateral resolution and blurring of the image and reduction in cross-sectional intensity in beam attenuation. There is also an increase in the slice thickness resulting in partial volume effects and deterioration in resolution of the scan plane (Browne et al., 2005). This in turn may increase the intrinsic spectral broadening, and also increase the error in the maximum velocity measurements.

5.2 METHODOLOGY

The ultrasound scanner used was the ATL HDI 3000 with broadband curvilinear transducer C4-2 (nominal frequency 2.5 MHz) set to a user-defined clinical preset, and optimised for renal imaging.

String phantom

The string phantom was designed in-house based on the BBS string phantom, with an O-ring rubber filament (diameter 1 mm) (BBS) as shown in Figure 5.3. The Perspex tank (25 × 12 × 29 cm) contained water which had been adjusted to a speed of sound of 1540 m s^{-1} by the addition of 9.5% propanol (Martin and Spinks, 2001). A rubber mat (Cannon Mats, London, UK) was placed at the bottom of the tank to absorb reflections from the Perspex bottom.

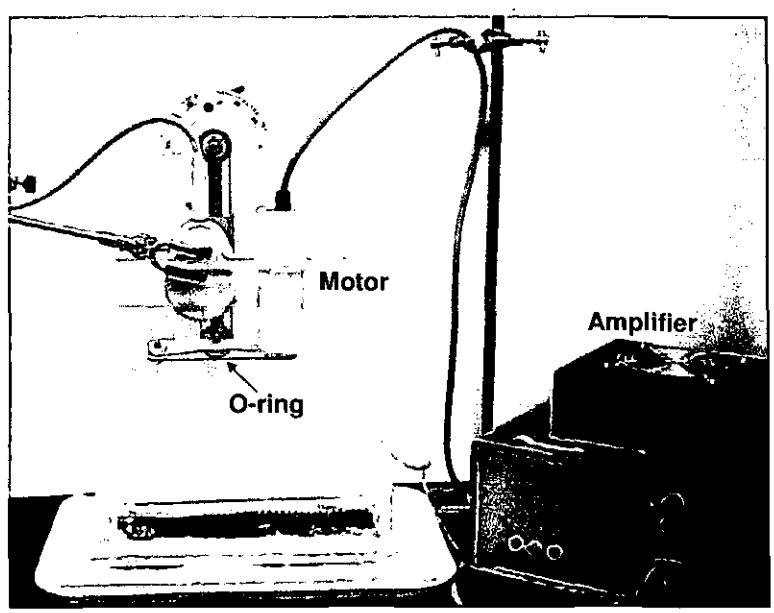

Figure 5.3 String phantom used in the fat layer study

Simple flow phantom

The simple Doppler flow phantom consisted of IEC TMM surrounding a tube through which blood mimicking fluid (BMF) was pumped by a computer controlled pump and motor as shown in Figure 5.4. The vessel used was C-Flex® tubing with an i.d. of 4.8 mm; see section 2.1.1 for acoustic properties. The tube was orientated at 60° to the US beam with the deepest point of the vessel at a depth of 16 cm from the transducer face (as measured with the scanners on screen callipers). The temperature of the flow phantom and BMF was recorded over the period of the experiments using a digital thermometer and were maintained at 22°C ± 1°C.

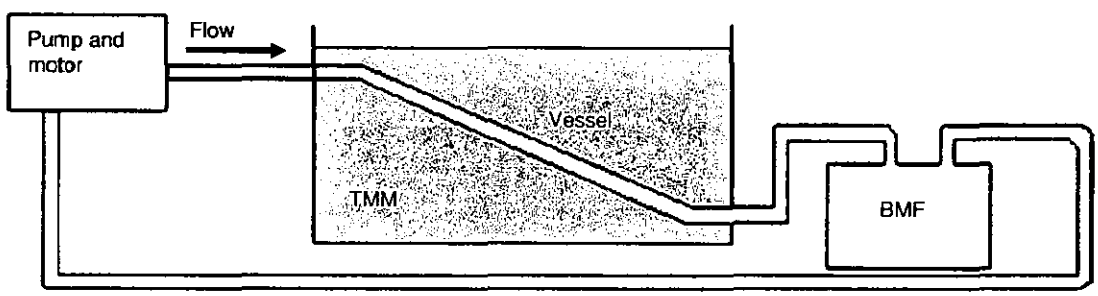

Figure 5.4 Doppler simple flow phantom with angled C-flex® tubing vessel

It was important to ensure the flow was laminar, the inlet tube was straightened to the required inlet length as determined by Equation 4.3. The maximum inlet lengths required to achieve laminar flow for the range of velocities used are listed in Table 5.2. The inlet tube in the flow circuit was straightened to 50 cm which ensured laminar flow was established before reaching the flow phantom.

Table 5.2 Flow phantom inlet lengths to ensure laminarity for a range of velocities

V_{mean} (cm s^{-1})	Re	L (cm)
15	182	4
30	364	7
40	486	9
50	607	12
60	728	14
100	1214	23

5.2.1 The effect of a fat mimicking layer on maximum velocity measurements using string phantom and simple flow phantom

The string phantom was used to evaluate the change in the frequency (velocity) components in the ultrasound pulse resulting from a fat mimicking layer in a non-attenuating medium. It was possible to calculate both the error in the maximum velocity measurements and the ISB. The simple flow phantom was used, because it is a more realistic representation of the *in-vivo* situation due to the presence of an overlying attenuating tissue mimicking material and a blood mimicking fluid. In this case only the error in maximum velocity measurements was studied as it was not possible to investigate the effect of the fat mimicking layer on ISB in the simple flow phantom due the velocity gradient present which gives rise to severe geometric spectral broadening.

Olive oil was chosen as the fat mimicking material for this study as it has acoustic properties similar in value to those of human subcutaneous fat which have been reported to be 1430 - 1500 m s^{-1} and 0.2 dB cm^{-1} MHz^{-1} at 3 MHz (Evans and McDicken, 2000; Turnbull et al., 1989). The speed of sound and attenuation of the olive oil has been reported to be 1490 m s^{-1} and 0.29 dB cm^{-1} MHz^{-1} respectively at 3 MHz (Browne et

al., 2005). For the measurements with the fat mimicking layer, the transducer was positioned 20 mm above the water and alcohol solution, and then a depth of 20 mm of degassed oil was carefully poured on top of the water and alcohol solution so as not to introduce any air bubbles or disturb the fat, water and alcohol interfaces. The same volume of water and alcohol as the volume of oil introduced (616 cm^3) was extracted to ensure the depth between the transducer and filament or vessel remained constant. Care was taken when pouring in the oil and extracting the water solution not to disturb the experimental set-up and transducer position.

Experimental set-up

A number of factors were varied to establish the effect of the fat mimicking layer on the measurement of the Doppler shift obtained from the simulated blood flow.

Doppler angle of insonation

Measurements were performed at a Doppler angle of $60^\circ \pm 1^\circ$ which is routinely used clinically in renal imaging. For the string phantom and simple flow phantom, the angle between the ultrasound beam and the vessel was set to $60^\circ \pm 1^\circ$.

Transducer alignment

Two transducer set-ups were used. The first investigated the effect of refraction and defocusing (set-up 1 in Figure 5.5), the transducer was placed at $60^\circ \pm 1^\circ$ to the fluid interface and the string or vessel remained parallel to the fluid interface. In this situation the ultrasound beam was not incident to the normal (90°) to the interface, allowing both refraction and defocusing effects to be studied. The second set-up looked at the effect of beam defocusing (set-up 2 in Figure 5.5). The transducer was aligned so

that the ultrasound beam was incident normally to the fluid interface while the string or vessel was orientated at $60^{\circ} \pm 1^{\circ}$ to the ultrasound beam.

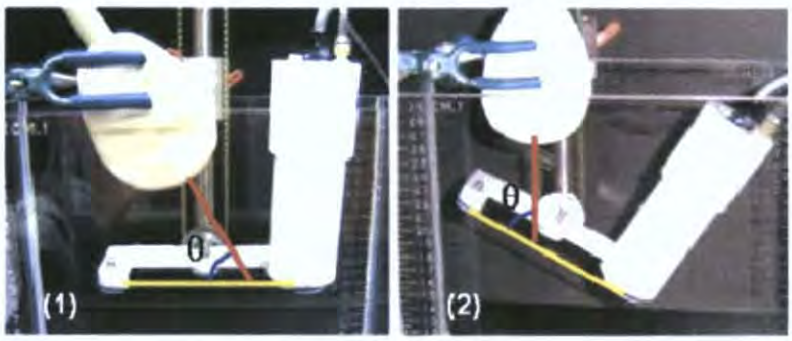

Figure 5.5 Experimental set-up shown here for the string phantom (1) transducer placed at $60^{\circ} \pm 1^{\circ}$ to the interface and the string/vessel remained parallel to the fluid interface (2) transducer aligned so that the ultrasound beam was incident to the normal to the interface while the string/vessel was orientated at $60^{\circ} \pm 1^{\circ}$ to the ultrasound beam

Test protocol

Distortion of B-mode and Doppler clinical parameters by the fat mimicking layer

For both the string and simple flow phantom a B-mode image was captured before and after the introduction of the fat mimicking layer so as to compare the images and determine any distortion due to the oil. Using Snell's law (Equation 5.1), it was possible to calculate the expected deviations at the fat and water interface for any given angle of incidence. Using the scanner's angle correction software, the actual angle was measured on the B-mode images using the ultrasound's own angle calliper and compared to the expected angle, as calculated by Snell's law.

Doppler examinations require acquisition of the Doppler frequency shift information from the correct spatial locations. The acquired Doppler information is critically

determined by the positioning of the SV in the blood flow field. The following test assessed the effect that the fat mimicking layer had on the accuracy of the range gate registration (indicating that the Doppler spectrum display only presents Doppler-shifted frequencies by reflectors located at the spatial position of the range gate) (Goldstein, 1991b), the sample volume and the sample volume dimensions. The transducer was positioned directly over the string phantom filament or vessel. Spectral Doppler was turned on and the angle correction was set to 60°. The acoustic power was set to the maximum setting (MI 1.3). The Doppler gain was adjusted to obtain a strong waveform free from saturation and noise. The gate length was set to its minimum (1 mm) and the velocity set to 100 cm s^{-1}. The range gate position was adjusted around the vessel axially until the strongest Doppler spectrum was registered. To determine the SV dimensions, the range gate position was adjusted around the vessel axially and the range gate depths over which the Doppler signal was present were noted. Both the maximum and minimum gate positions were recorded and the SV dimensions were then calculated.

Maximum velocity measurements

Maximum velocity measurements were recorded using PW Spectral Doppler before and after a 20 mm oil layer was introduced. The transducer was positioned directly over the string or vessel so that it appeared in the centre of the screen image. The range gate size was set to 2.5 mm for the string phantom measurements and to 5 mm for the simple flow phantom measurements at a depth of 94 mm. A cine-loop of the Doppler waveform was obtained and the maximum velocity was manually measured by positioning the cursor at the maximum position in the spectra at five different positions. This was repeated for a range of steady state velocities, 15, 30, 40, 50, 60 and

100 cm s^{-1}. From these measurements the measured maximum velocity error for each set velocity was calculated using Equation 5.2 (Steinman et al., 2001),

$$v_{error}(\%) = \frac{v_{max} - v_{set}}{v_{set}} \times 100 \qquad \textbf{Equation 5.2}$$

where v_{error} is the maximum velocity error expressed as a percentage, v_{max} the measured maximum velocity and v_{set} the set maximum velocity set by the computer controlled motor. A positive v_{error} is an overestimation error and a negative value is an underestimation error.

Intrinsic spectral broadening

The effect of a fat mimicking layer on ISB was investigated using the string phantom only, and using the same experimental procedure as the maximum velocity measurements. From the cine-loop of the Doppler waveform both the maximum velocity and minimum velocity were manually measured by positioning the cursor at the maximum and minimum position in the spectra, and an average of five measurements were taken. The degree of broadening was calculated as a percentage using Equation 5.3 (IPEM, 1994),

$$ISB(\%) = \frac{v_{max} - v_{min}}{v_{max} + v_{min}} \times 100 \qquad \textbf{Equation 5.3}$$

where v_{max} is the measured maximum velocity and v_{min} the measured minimum velocity. Uncertainties in the accuracy of the velocity measurements were determined for both the string phantom and simple flow phantom from inherent errors in the respective measurement tools coupled with an analysis of 5 repeated measurements.

5.2.2 The effect of a fat mimicking layer on maximum velocity measurements using anatomically realistic renal flow phantoms

Maximum velocity measurements were measured before and after a 20 mm layer of oil was introduced on top of the phantom at 4 locations along the renal artery vessel (locations, A, B, D and H from Table 4.1 and Figure 4.5). Here only one transducer set-up was used, the transducer was placed at $60^{\circ} \pm 1^{\circ}$ to the fluid interface and the vessel remained parallel to the fluid interface. Using a paired t-test, the maximum velocities recorded before and after the fat mimicking layer was introduced were compared for each stenosis (normal healthy artery, 30% and 50% stenosis) for the wall-less and walled phantoms.

5.3 RESULTS

5.3.1 The effect of a fat mimicking layer on maximum velocity measurements using string phantom and simple flow phantom

The effect of an overlying fat mimicking layer on the measurement of the Doppler shift obtained using two Doppler test devices; a string phantom and a simple flow phantom were investigated.

String phantom results

Distortion of B-mode and Doppler clinical parameters

With the introduction of the fat mimicking layer, a misplacement artefact was observed in the B-mode image. When the fat mimicking layer was introduced into the water tank of the string phantom, the filament appeared 3 ± 1 mm deeper than its true position (Figure 5.6). This misregistration was present when the transducers were both in set-up 1 and set-up 2.

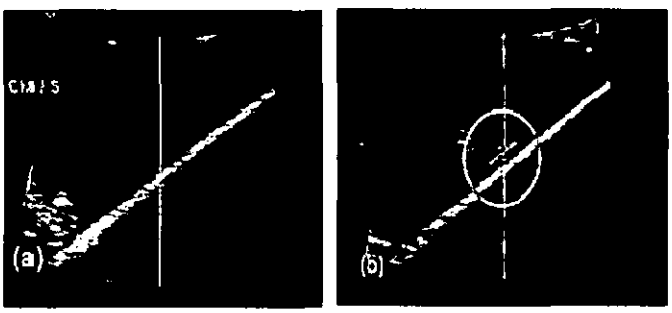

Figure 5.6 Distortion of the B-mode image (a) without fat layer present, (b) with fat layer, filament appears deeper than its true position

Using Snell's law the expected angular deviations due to the oil/water boundary for each beam/vessel to angle were calculated. The actual angle was measured using the angle measurement system of the scanner (± 2°). The results for the string phantom are presented in Table 5.3 with the expected Doppler frequency shift for each set-up with angle deviation present as calculated using Equations 1.1 and 5.1. The measurement accuracy was comparable with the expected deviation. For these results it is not possible to determine if an actual deviation of occurred. Using a range of Doppler angles it would be possible to observe the angle deviation with increased certainty.

Table 5.3 Theoretical and experimental deviations for the 2 experimental set-ups of the string phantom

Set-up	Theoretical Deviation	Actual Deviation (± 2°)	Calculated Doppler Shift (f_t = 2.5 MHz)
1	3°25'	2°	762. 2 Hz
2	0°	0°	881.7 Hz

Other than the initial misregistration of the filament due to the addition of the oil layer no further changes in the range gate registration were observed using the two set-ups. The measured SV dimensions also remained unchanged with the introduction of the fat mimicking layer. The results for both the range gate registration and SV dimensions are given in appendix B.

Maximum velocity measurements

In Table 5.4, mean maximum velocity error, with the corresponding 95% confidence intervals and p value obtained with no oil layer present and with an overlying 20 mm oil layer for the two transducers set-ups using the string phantom are presented. The full

set of maximum velocity measurements are given in appendix B. Overall, there was a mean overestimation of 20% with no fat mimicking layer present for each transducer. In both set-up 1 and 2 the presence of an oil layer caused a significant overestimation in the maximum velocity measurements ($p < 0.05$).

Table 5.4 Maximum velocity error (% error ± 1.96 (SE)) measured using string phantom without and with the presence of an oil layer, with the corresponding 95% confidence intervals and p value

Stenosis	Oil layer Present	Velocity Error (%)	95% Confidence Intervals		P value
			Lower	*Upper*	
Set-up 1	No	14 ± 1	10	18	<0.0001
	Yes	31 ± 2	27	36	
Set-up 2	No	32 ± 2	20	32	0.0127
	Yes	37 ± 1	30	37	

Effect of refraction and defocusing (transducer set-up 1)

Here the effects of the presence of an overlying fat mimicking layer and the resultant refractions and defocusing of the ultrasound beam were evaluated (Figure 5.7).

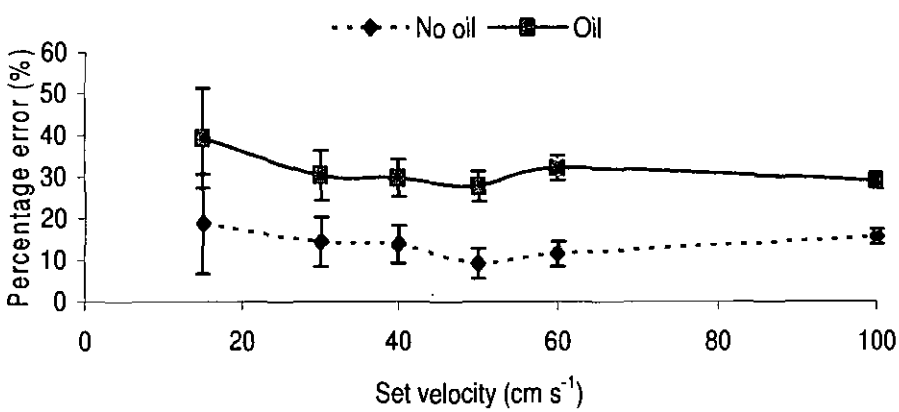

Figure 5.7 Effect of refraction and defocusing on string phantom maximum velocity accuracy using transducer set-up 1

With a beam and string angle of 60° the presence of the fat mimicking layer resulted in a significant overestimation ($p < 0.05$) in the maximum velocity being measured for velocities greater than 15 cm s^{-1} (Figure 5.7).

Effect of defocusing

To investigate solely the effect of defocusing, the transducer being investigated was aligned so that the ultrasound beam was incident normally to the fluid interface while the string was orientated at an angle, so that no refraction would occur due to the oil layer.

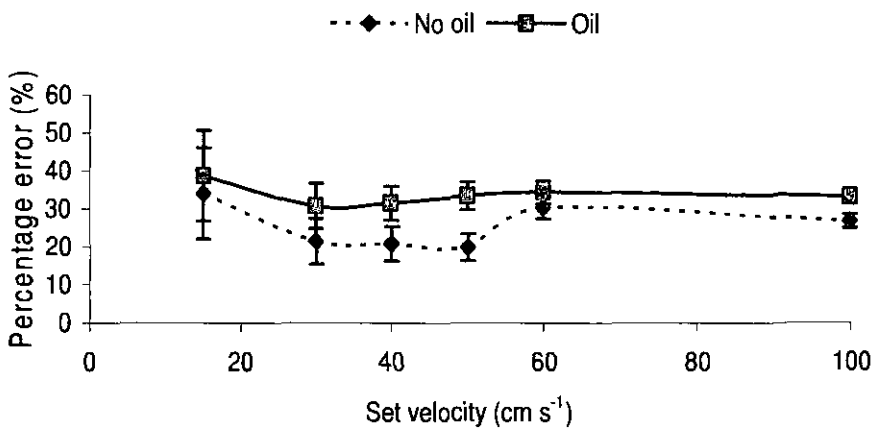

Figure 5.8 Effect of defocusing on string phantom maximum velocity accuracy using transducer set-up 2

Figure 5.8 illustrates that in transducer set-up 2 the fat mimicking layer did cause an overestimation in the maximum velocity for velocities greater than 30 cm s^{-1}.

The effect of fat layer on intrinsic spectral broadening

The ISB was found to be larger at velocities less than 15 cm s^{-1} but reducing to approximately 20% once the velocity was over 30 cm s^{-1} as shown for set-ups 1 and 2 in Figures 5.9 and 5.10.

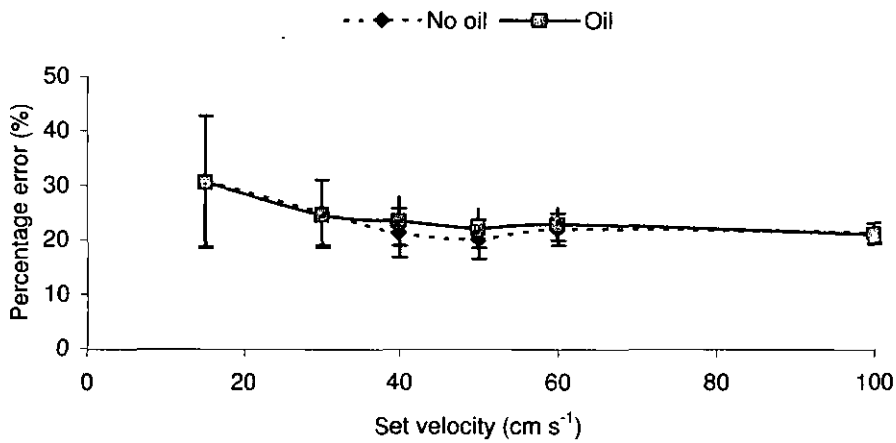

Figure 5.9 Effect of refraction and defocusing on intrinsic spectral broadening using transducer set-up 1 using a string phantom

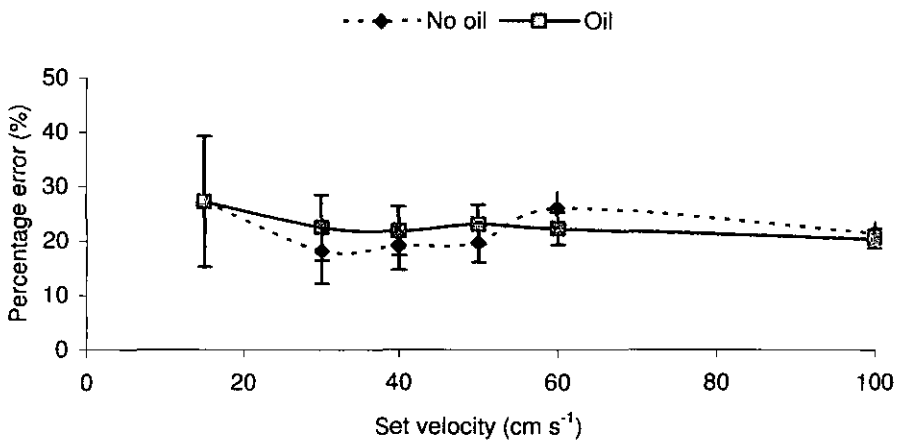

Figure 5.10 Effect of defocusing on intrinsic spectral broadening using transducer set-up 2 using a string phantom

The mean ISB (obtained for steady state velocities between 30 and 100 cm s^{-1}) values for both experimental set-ups are presented in Table 5.5. It was found for all cases, that the presence of an oil layer did not have a significant effect on ISB of the transducers tested ($p > 0.05$). Furthermore, there was no observed difference between the results for the two experimental set-ups, 1 and 2.

Table 5.5 ISB (ISB ± 1.96 (SE)) measured using string phantom without and with the presence of an oil layer, with the corresponding 95% confidence intervals and p value

Stenosis	**Oil layer**	**ISB**	**95% Confidence Intervals**		**P value**
	Present	*(%)*	*Lower*	*Upper*	
Set-up 1	No	24 ± 2	19	28	0.7124
	Yes	24 ± 1	20	28	
Set-up 2	No	22 ± 2	18	26	0.6527
	Yes	23 ± 1	20	25	

Simple flow phantom results

Distortion of B-mode and Doppler clinical parameters

Similar to the string phantom a misregistration error in the SV (5 ± 1 mm) was observed when the fat mimicking layer was introduced into the scanning well of the flow phantom for the C4-2 transducer. The misplacement artefact remained consistent when the transducer was in experimental set-ups, 1 and 2.

Maximum velocity measurements

Maximum velocity measurements were performed for a range of steady state maximum velocities; 15, 30, 40, 50, 60 and 100 cm s^{-1} and the results for the two experimental set-ups are presented in Figures 5.11 and 5.12.

The effect of refraction and defocusing

The maximum velocity was underestimated by the simple flow phantom. When the layer of oil was introduced, a decrease in the underestimation was found.

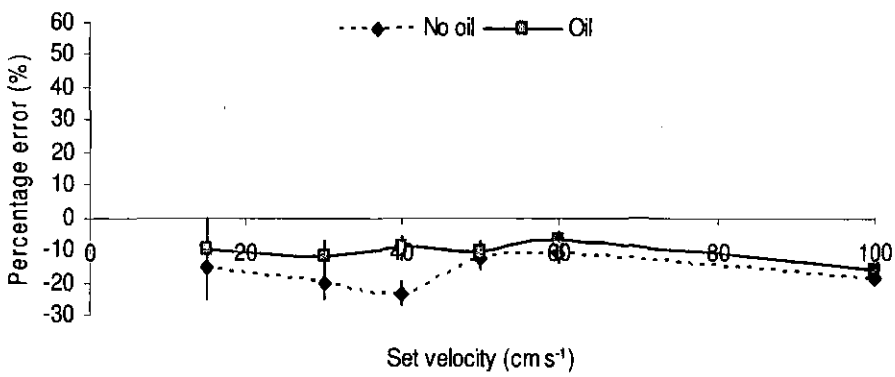

Figure 5.11 Effect of refraction and defocusing on maximum velocity accuracy using transducer set-up 1 using a simple flow phantom

The effect of defocusing

In the second set-up, without the fat mimicking layer, overestimation of the maximum velocity was observed for all velocities except 100 cm s^{-1} where underestimation was found (Figure 5.12). When the fat mimicking layer was added a lower overestimation in the maximum velocity measurements were obtained. A decrease in the maximum velocity overestimation was found with increasing set velocities.

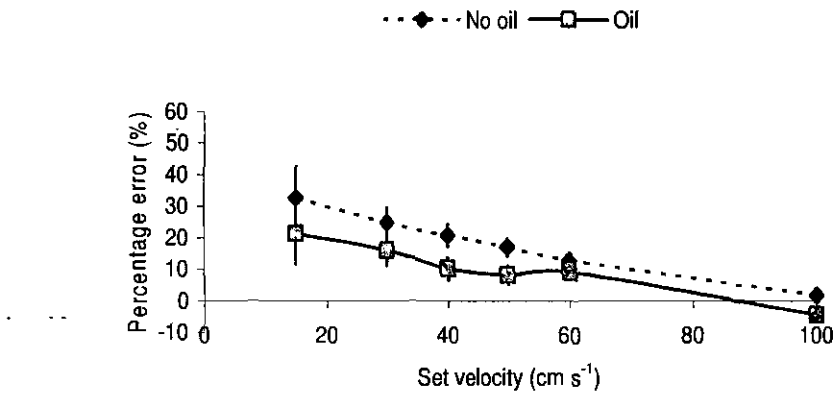

Figure 5.12 Effect of defocusing on maximum velocity accuracy using transducer set-up 2 using a simple flow phantom

Table 5.6 shows the averaged percentage error in the maximum velocity measurements for set-up 1 using the simple flow phantom. The presence of an oil layer resulted in a significant underestimation in the maximum velocity measurement ($p < 0.05$). In set-up 2 the percentage error showed dependence on true velocity therefore it was no possible to average data.

Table 5.6 Velocity error (% error ± 1.96 (SE)) measured using flow phantom without and with the presence of an oil layer, with the corresponding 95% confidence intervals and p value

Stenosis	**Oil layer Present**	**Velcoity error (%)**	**95% Confidence Intervals**		**P value**
			Lower	*Upper*	
Set-up 1	No	-17 ± 2	-12	-22	0.0183
	Yes	-11 ± 1	-8	-14	

5.3.2 The effect of a fat mimicking layer on maximum velocity measurements using anatomically realistic renal flow phantoms

Maximum velocity measurements were recorded at the site of stenosis (15 mm for inlet of renal artery) for the wall-less and walled phantoms before and after a 20 mm layer of oil was added above the phantom compared. The mean maximum velocity ± 1.96 (standard error (SE)), with corresponding 95% confidence intervals and p values are presented for the wall-less and walled phantoms in Tables 5.7 and 5.8, respectively. The presence of the fat mimicking layer resulted in a significant increase ($p< 0.05$) in the maximum velocity measurement obtained from the both the wall-less and walled phantom for all stenoses.

Table 5.7 Effect of fat mimicking layer on the maximum velocity (V_{max}) measured at the site of stenosis for the wall-less phantoms at 40 cm s^{-1}

Stenosis	Fat layer	V_{max} (cm s^{-1})	95% Confidence Intervals		P value
			Lower	*Upper*	
Normal	No	79 ± 1	77	80	<0.0001
	Present	97 ± 2	92	103	
30%	No	121 ± 2	117	125	0.0007
	Present	140 ± 3	131	148	
50%	No	142 ± 1	136	145	<0.0001
	Present	168 ± 1	165	171	

Table 5.8 Effect of a fat mimicking layer on the maximum velocity (V_{max}) measured at the site of stenosis for the walled phantoms at 40 cm s^{-1}

Stenosis	Fat layer	V_{max} (cm s^{-1})	95% Confidence Intervals		P value
			Lower	*Upper*	
Normal	No	70 ± 1	68	72	<0.0001
	Present	86 ± 1	84	88	
30%	No	135 ± 1	133	139	0.0001
	Present	144 ± 1	143	146	
50%	No	118 ± 2	114	123	0.0012
	Present	127 ± 1	125	129	

5.4 DISCUSSION

The effects of an overlying fat mimicking layer on maximum velocity measurements by the ATL HDI 3000 ultrasound scanner using a string phantom, a simple flow phantom and a range of anatomically realistic renal artery flow phantoms were investigated. Two experimental set-ups were used to investigate the effect of the overlying fat mimicking layer on the calculation of the Doppler angle (Figure 5.5). Depending on the orientation of the transducer, and hence of the beam to the interface, refraction and/or defocusing of the ultrasound beam may occur. Both of these effects may lead to errors in the calculation of the Doppler angle and consequently to inaccurate estimation of the maximum velocity.

The first observation was the distortion of both the B-mode image and the Doppler angle as produced by the angle correction software in the scanner. The difference in the speed of sound between the 2 layers (the water and alcohol and the oil layer for the string phantom, the TMM and the oil layer for the flow phantom) caused inaccurate distance representations and a misplacement artefact was observed in the B-mode image. The SV appeared 3 mm nearer to the face of the transducer than its true position. The error was found to be not as significant in the case of the simple flow phantom (misregistration of 1 mm when a larger SV = 5 mm was used). Since a curvilinear transducer was used there would be repositioning of the image date but there would be no mis-registration between the B-mode and Doppler beams as the beams are unsteered. In this case clinically the operator will place the sample volume accurately within the vessel. Goldstein, (2000) examined the effect of differences in the speed of

sound from the assumed speed of sound 1540 m s^{-1} on distance measurements and also found the difference in speed of sound caused small misregistrations of image location.

In the case of the string phantom, as the ultrasound beam passes through the fat mimicking layer into the water and alcohol solution a number of factors need to be considered. One is whether or not the beam is at an angle of incidence greater than 0 or is incident normally. If it strikes at an angle of incidence greater than 0 to the normal, then refraction will occur and the Doppler angle will be deviated (as produced by experimental set-up 1, as shown in Figure 5.5). Here the ultrasound beam wave front does not travel at equal times of flight through the phantom as shown in Figure 5.2(a). If the ultrasound beam is incident normally then no refraction will occur (produced by experimental set-up 2 as shown in Figure 5.5). In experimental set-up 1 (investigating the effect of refraction and defocusing), when the fat mimicking layer was introduced deviations of the displayed angle occurred. There was no angular deviation with the transducers in set-up 2 as expected since no refraction occurred in this case.

It is known that in general for Doppler ultrasound systems, there tends to be an overestimation of the maximum velocity (Daigle et al., 1990; Hoskins, 1996; Winkler and Wu, 1995). In this work it was found for the string phantom that all the maximum velocity measurements were overestimated between 19 – 29% (Table 5.4) without a fat mimicking layer present. This overestimation is as a result of geometric spectral broadening, which is purely a geometric effect with no dependence on the true velocity (Christopher et al., 1995; Hoskins, 2008; Li et al., 1993). The aim of this study was to use both a string and a simple flow phantom to investigate if the magnitude of the overestimation would be significant with the addition of a fat mimicking layer. It was

found for experimental set-up 1 that for the C4-2 transducer set at a Doppler angle of 60° the presence of the fat mimicking layer caused a significant increase in the maximum velocity measurements. Interestingly for experimental set-up 2, where refraction did not occur, a significant increase in the maximum velocity measurements was found for the C4-2 transducer.

The effect of the fat mimicking layer on ISB was determined using the string phantom. It was found for all cases, that the presence of the fat mimicking layer did not have a significant effect on ISB as shown in Table 5.5, and also, that there was no observed difference between the results for the two experimental set-ups. The transducer used has a wide aperture which results in a narrow beam width. Although this improves lateral resolution at the narrowest beam width at the focus and increases Doppler sensitivity, it also increases the ISB, thereby increasing the velocity overestimation. In this study the SV depth was set at 94 mm. Abdominal imaging is usually performed at deeper depths, where the ISB is much less than would be experienced in peripheral vascular ultrasound. The importance of ISB depends on the use made of the spectral information. Even large degrees of ISB will not influence the measurement of mean velocity, since the broadening is more or less symmetrical, but the maximum velocity may be overestimated (by the blurring of the spectrum) and can potentially lead to misdiagnosis if the effect is not corrected or at least appreciated (Daigle et al., 1990; Hoskins, 1996; Winkler and Wu, 1995).

The string phantom does not represent the *in-vivo* situation well as the water and alcohol solution used is effectively a non-attenuating medium. For most biological tissue the ultrasound attenuation is nearly proportional to frequency (Bamber, 1997). As a result

of this property, when an ultrasound pulse propagates through tissue, high frequency components of the pulse are preferentially attenuated, reducing the effective bandwidth with increasing depth. The magnitude of the frequency shift will be proportional to the actual attenuation value at the centre frequency and the square of the pulse bandwidth (Evans and McDicken, 2000). The ultrasound scanner uses the original transmitted frequency in the calculation of the Doppler shift, so there appears to be a decrease in the maximum velocity estimation; also the mean velocity appears higher. For this reason a simple flow phantom was chosen which stimulates more closely some of the properties of soft tissue, blood vessels and blood. Although the effect of frequency dependant attenuation on measured maximum velocity estimations was not specifically investigated when a fat mimicking layer and tissue mimicking medium are present. This is one possible explanation for the decrease in velocity observed in the flow phantom experiments. Further specific experiments are needed to verify this possible explanation.

With the transducer positioned at an angle to investigate the effect of refraction and defocusing, and with no oil layer present, the effect of frequency dependant attenuation on the ultrasound beam resulted in an underestimation of the maximum velocity, most likely due to the downshift of the centre frequency. When the layer of oil was introduced, a decrease in the underestimation was found. In the second set-up where no refraction occurred, and without the fat mimicking layer, overestimation of the maximum velocity was observed for all velocities, except 100 cm s^{-1} where underestimation was found. When the oil layer was added lower overestimations of the maximum velocity were found. A decrease in the maximum velocity overestimation was found with increasing set velocities. The significant underestimation which was

found using the straight vessel flow phantom could have serious implications for patients with RAS as it could cause a patient to be recorded as having a smaller stenosis than is actually present. This might lead to poor patient management as patients might receive drug treatment rather then surgical intervention and so increase their risk of hypertension and kidney failure. The underestimation of velocity may be as a result of the highly attenuating C-flex® tubing which was used as the vessel in this phantom. As reported in Section 2.1.1, this material has a reported attenuation coefficient of 5.6 dB cm^{-1} MHz^{-1} which results in an attenuation of 14 dB cm^{-1} at 2.5 MHz. Maximum velocity measurements were also recorded, before and after a layer of oil was introduced using the anatomically realistic renal artery flow phantoms. For both the wall-less and walled phantoms, the presence of the fat mimicking layer resulted in a significant increase in the maximum velocity measurements.

The IPEM clinical classification of RAS and corresponding PSV are presented in Table 5.9 along with the effects on the PSV due to the average overestimation observed for the string phantom (30%) and the underestimation of some 10% for the flow phantom when a fat mimicking layer is present. As shown in Table 5.9, with 30% overestimation in PSV, an artery with no blockages may be misinterpreted as having a low grade stenosis present, as a PSV of 234 cm s^{-1} would be measured. However as discussed above in the case of the simple flow phantom, where significant underestimation occurred with the presence of a fat layer, a low grade stenosis may be recorded as 0% stenosis. RAS is the most common cause of potentially curable secondary hypertension and therefore early detection is important. If left untreated it may result in permanent kidney damage and the loss of renal function. A more serious possibility would be the clinicians assume the system is overestimating by 30% but is

actually underestimating by 10%. In this case the PSV is 234 cm s^{-1} the stenosis may be recorded as 0% stenosis when in fact a high grade blockage may be present. This would lead to very serious patient mismanagement.

Table 5.9 Comparison of maximum velocity to percentage diameter stenosis with presence of fat layer using the classification guidelines provided by the Institute of Physics and Engineering in Medicine, Vascular Laboratory practise manual 2004

Classification	Diameter Stenosis (%)	PSV (cm s^{-1})	String phantom PSV (cm s^{-1}) +30%	Flow phantom PSV (cm s^{-1}) -10%
Normal	0%	<180	<234	<162
Low grade	0-60	>180	>234	>162
High grade	60-99	>260	>338	>234
Total occlusion	100	0	0	0

A limitation of this study was the use of olive oil as the fat mimicking layer. Olive oil has quite a high speed of sound for a fat mimicking material. The use of an oil with a lower speed of sound such as paraffin oil (1440 m s^{-1}) would have resulted in higher overestimation in the maximum velocities. Also olive oil does not have the inhomogeneous structure of subcutaneous fat. The subcutaneous layer refers to the fat tissue below the skin. It consists of spongy connective tissue interspersed with adipocytes (fat cells) as shown in Figure 5.13. These fat cells are grouped together in large cushion-like clusters held in place by collagen fibres called connective tissue septa or sheaths. Browne et al., (2005) used subcutaneous pig fat in a study to investigate its effect on the image quality and whether these effects could be reduced with new imaging modalities. The speed of sound and attenuation of pig fat *"in-vivo"* and *"in-*

vitro" at 37°C have been previously reported in the literature to be 1426 m s^{-1} and 3 dB cm^{-1} respectively at 2 MHz (Gammell et al, 1979; Lewin and Busk, 1982).

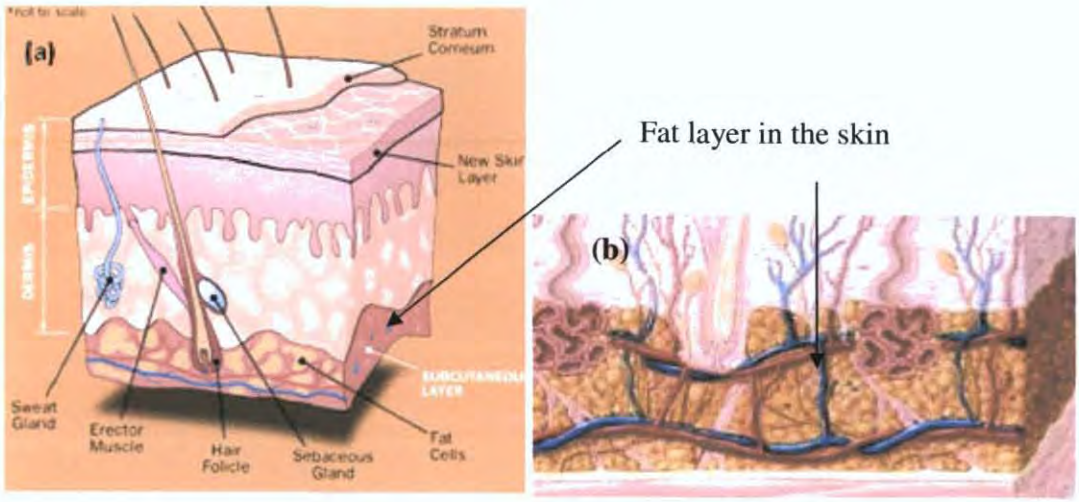

Figure 5.13 (a) Location of subcutaneous layer in the skin and (b) the presence of fat cells.

(Images adapted from (a) http://health.howstuffworks.com/sunscreen.htm and (b) (http://www.nlm.nih.gov/medlineplus/ency/imagepages/19490.htm)

The use of a layer of subcutaneous pig fat in this study instead of olive oil would mimic very closely what happens to the ultrasound beam *in-vivo*. The uneven surface and multiple layers in the subcutaneous pig fat would cause phase aberrations due to spatial and phase inhomogeneities. It would cause higher attenuation due to diffuse scattering. Globules of fat within it might be likely to act as lenses, defocusing and focusing the ultrasound beam. Such an extension to the present work might be likely to produce still more clinically relevant results.

5.5 CONCLUSIONS

This chapter describes the investigations on the effect of a fat mimicking layer on maximum velocity measurements. It was found that the fat mimicking layer caused significant overestimation of maximum velocity in the non-attenuating medium (string phantom) and the anatomically realistic renal artery flow phantoms; this would indicate that such a patient would to be recorded as having a more severe stenosis than might actually be present. However, for the simple flow phantom, significant underestimation of maximum velocity occurred, and this would indicate that such a patient might be recorded as having a less severe stenosis than is present. This latter situation could have serious implications for patient management as the patients might receive a more conservative treatment than required - drug treatment rather than surgical intervention possibly increasing their risk of hypertension and kidney failure.

CHAPTER 6 A COMPARATIVE IMAGING STUDY USING A MULTI-MODALITY RENAL ARTERY PHANTOM

6.1 INTRODUCTION

In this chapter the range of multi-modality renal artery phantoms developed in Chapter 2 were used to evaluate and compare current imaging techniques used to detect RAS (US, MRI, CT and DSA). This range of phantoms consisted of vessels with varying degrees of stenosis (normal healthy renal artery, 30%, 50%, 70% and 85%). To date there has been little quantitative work to compare the imaging capabilities of all four imaging modalities used to detect RAS as discussed in Chapter 1. Valid comparative studies require a single standardised vascular phantom to be imaged with each of the different modalities. Three multi-modality vascular phantoms have previously been described (Cloutier et al., 2004; Dabrowski et al., 1997; Frayne et al., 1993). These phantoms contained fiducial markers to aid image registration. Frayne et al., (1993) developed a carotid vascular phantom for comparative studies of projection radiography, x-ray, US and MRI. In this phantom lead core fishing line (0.8 mm outer diameter with 0.2 mm diameter lead core) was used as the fiducial marking system; however, it was only clearly detectable in the x-ray images. Dabrowski et al., (1997) used a phantom containing a formaldehyde fixed section of a real human iliac artery cannulated onto two acrylic tubes. The imaging modalities (x-ray angiography, CT, and 3-D B-mode US) were evaluated by comparing images of the phantom. The stainless steel ball bearings (diameter 1.19 mm) used as fiducial markers introduced artefacts in both US and CT images. The multi-modality phantom developed by Cloutier et al., (2004) contained a straight lumen with double stenosis (70% and 85%). The markers

used were glass balls (diameter 3 mm) and were clearly visible without artefacts in the ultrasound, the MRI, the CT and the DSA images.

In this study a range of novel standardised anatomically realistic renal artery phantoms were imaged using US, MRI, CT, and DSA. The primary aims of this study were to evaluate current imaging technology by assessing the visualisation of the phantoms and by determining the geometric accuracy of each technique. These phantoms were primarily designed as ultrasound flow phantoms, using materials which were also compatible with DSA, MRI and CT. They contained fiducial markers as a means of aligning the images acquired using the different imaging systems. Using these multi-modality phantoms it should be possible to make direct quantitative comparisons of the phantoms' dimensions between the different imaging modalities using the standardised phantoms as a reference.

6.2 METHODOLOGY

6.2.1 Reference measurements

To determine the spatial accuracy of each imaging modality, the diameter of the vessel lumen was measured at three locations. These measurements were compared with the reference measurements (the diameter of the metal model used to produce the lumen in each phantom). For each phantom produced (normal, 30%, 50%, 70% and 85% stenosis) three locations along the inlet of the metal model at (A) 10 mm from inlet, (B) 15 mm from inlet and (C) 10 mm from bend as shown in Figure 6.1. At each location the diameter was measured 5 times using vernier callipers.

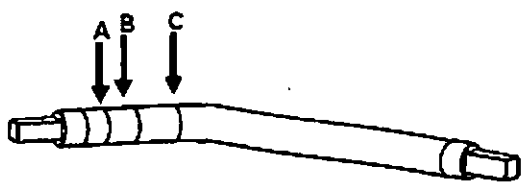

Figure 6.1 Location of reference measurements on the metal model at (A) 10 mm from inlet, (B) 15 mm from inlet and (C) 10 mm from bend

6.2.2 Image acquisition of phantoms

The multi-modality renal artery phantoms (with normal healthy artery, 30%, 50%, 70% and 85% stenosis) were imaged with standard clinical devices. Only basic imaging protocols were followed and not specific clinical protocols or flow measurements as the study was to asses the geometry of the phantoms with each imaging modality and determine the geometric accuracy of each technique. For US imaging the phantoms were imaged with the vessels filled with a water/glycerol solution which was corrected

for speed of sound 1540 m s^{-1}. For CT and MRI the phantoms were imaged with no liquid in the vessels. The vessels of the phantoms were filled with water and contrast for DSA.

US

The HDI 3000 with linear array transducer (L12-5) at a nominal frequency of 6 MHz was used to image the multi-modality phantoms. The B-mode images were optimised with the output power set at maximum, focal position at centre of the vessel and a field of view of 8 cm. A translational stage was used to allow accurate and precise positioning of the transducer along the length of the vessel. Longitudinal and transverse images of the phantoms were acquired using the L12-5 linear array transducer. All images were saved for off-line analysis which is described in section 6.3.

MRI

Magnetic resonance imaging was performed with a 3T Philips Achieva MRI System (Philips, Amsterdam, Netherlands) using a 3D T_2-weighted turbo spin echo (TSE) technique. The phantoms were placed inside an 8 channel phased array detector coil (Philips Head SENSE 8). Images were obtained using the following parameters: resolution = 0.8 x 0.8 x 0.8 mm, field of view =15 x 141 x 130 mm, time to echo (TE) = 380 ms, time to repetition (TR) = 2500 ms, Turbo factor =120, Number of signals averaged = 2.

CT

The phantoms were scanned with a GE Discovery STE system (GE Healthcare, Buckinghamshire, UK) which included a full GE light speed helical 16-Slice CT using a

slice thickness of 0.6 mm and a scan range of 120 mm, matrix size was 1024. The current density was 250 mA and peak voltage was 120 kV. The computed tomography dose index (CTDI) was 35.52 mGy and dose length product (DLP) was 572.20 mGy cm.

DSA

DSA projections were acquired on a Philips Integris Allura System, (Philips, Amsterdam, Netherlands). Each vascular phantom was filled initially with water and then with a contrast solution of Ultravist at 240 mg ml^{-1}. The concentration of the contrast agent was carefully selected to mimic the image intensity enhancement obtained clinically. Projections were obtained parallel to the vessel using the following parameters; source-to-detector distance = 67 cm, field-of-view = 23 cm, table height 99 cm, current density = 400 mA and peak voltage = 50 kV. Each image sequence was captured at a frame rate of 6 frames per second with 4 ms of exposure with a matrix size of 1024.

6.2.3 Image analysis

Transverse B-mode images were used to determine the diameter of the vessels. For MRI and CT images the fiducial markers were used to identify and orientate the plane views and the coronal slices containing the mid point of the vessel for each phantom were selected. For DSA images the diameter was calculated from the projection radiograph for each phantom. All images acquired were analysed using a MATLAB program developed in-house. Three locations were measured in each image, 10 mm from the inlet, centre of the site of stenosis (15 mm from inlet) and 20 mm from inlet. A profile line was drawn across the lumen extending over the vessel-lumen boundaries

at each position. The vessel lumen diameter was determined by plotting the image pixel intensity vs. distance across each region. The distance in mm was calculated by measuring the known dimensions of the phantom and converting the pixel distance in mm. The diameter of the vessel at each position was determined from the full width of the plot. This was repeated 5 times at each of the three positions for the 5 metal models. A one way ANOVA statistical test was carried out to compare the vessel lumen diameters determined from each imaging modality.

6.3 RESULTS

6.3.1. Visualisation of fiducial markers

Images of the fiducial markers obtained from the four imaging modalities are presented in Figure 6.2. For all the imaging modalities the fiducial markers were clearly identifiable and did not introduce artefacts in the images. For US (Figure 6.2 (a)) the glass beads appeared as bright spots in the B-mode images, as the glass had a much greater acoustic impedance ($z = 12.1 \times 10^6$ rayl) (Selfridge, 1985) than the surrounding TMM ($z = 1.6$ rayl) (calculated acoustic impedance (z) = ρc where ρ density = 1049 kg m^{-3} and c = 1540 m s^{-1} (Teirlinck et al., 1998). For MRI, contrast is essentially based on the difference in relaxation times (longitudinal relaxation time T_1 and transverse relaxation time T_2). The signal from the TMM was much higher than that from the glass beads and so they appeared as black spheres as shown in Figure 6.2(b). For imaging techniques based on x-rays (DSA and x-ray) contrast images results from a difference in x-ray absorption of different materials. Glass beads have a significantly higher absorption coefficient than that of the TMM and therefore, they appeared clearly both in DSA and CT images (Figure 6.2(c) and (d)).

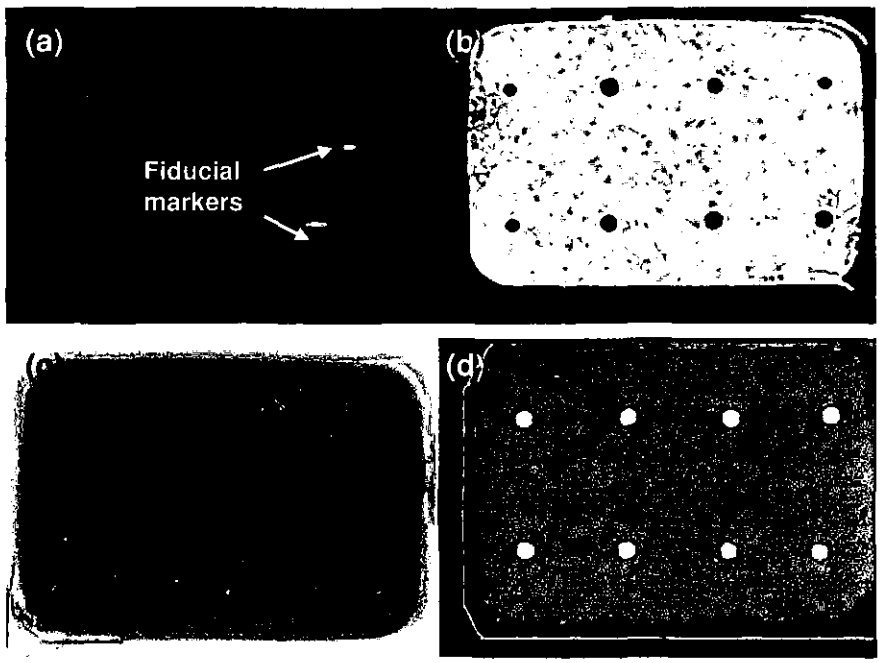

Figure 6.2 Fiducial markers are clearly identifiable in all the imaging modalities (a) ultrasound, transverse image showing cross section of the lumen and 2 beads at depth 49 mm and 57 mm on the right side of the phantom, (b) MRI showing a slice at with 2 rows of beads, (c) DSA and (d) CT showing a slice at with 2 rows of beads

6.3.2. Visualisation of phantoms

The images obtained using each imaging modality for the set of multi-modality renal artery phantoms are presented in Figures 6.3 – 6.5. Figure 6.3 shows the 2D B-mode longitudinal images of the inlet of each phantom. An example of the 2D transverse B-mode images captured at the 3 regions of interest for the 50% stenosis is shown in Figure 6.4. These images were used to asses the geometric accuracy of US compared to the other imaging modalities and the results are presented in section 6.3.3.

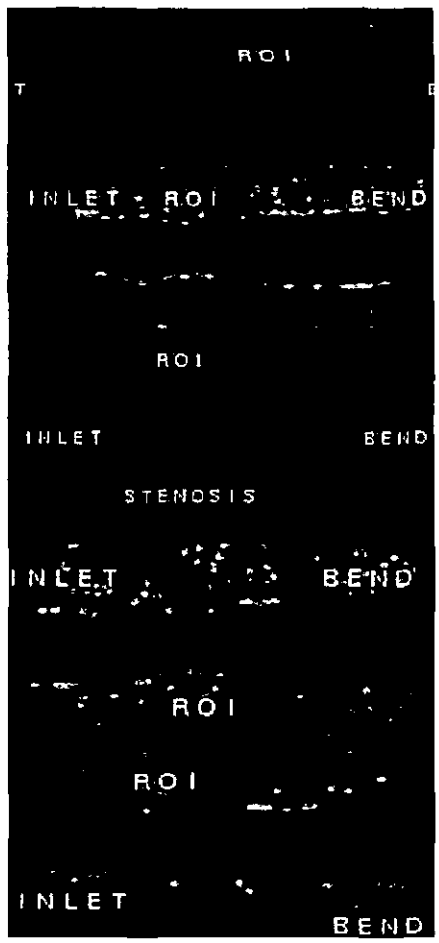

Figure 6.3 B-mode images showing inlet of renal artery flow phantom with varying degrees of stenosis (normal, 30%, 50%, 70% and 85%)

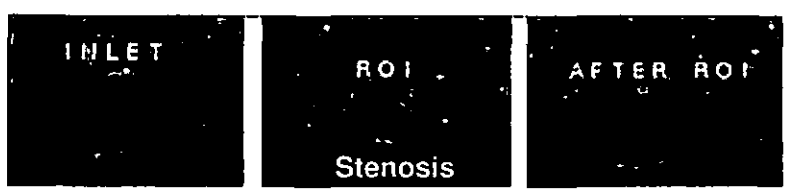

Figure 6.4 Transverse view of 50% stenosis for the inlet, ROI at the stenosis and 1 cm before bend

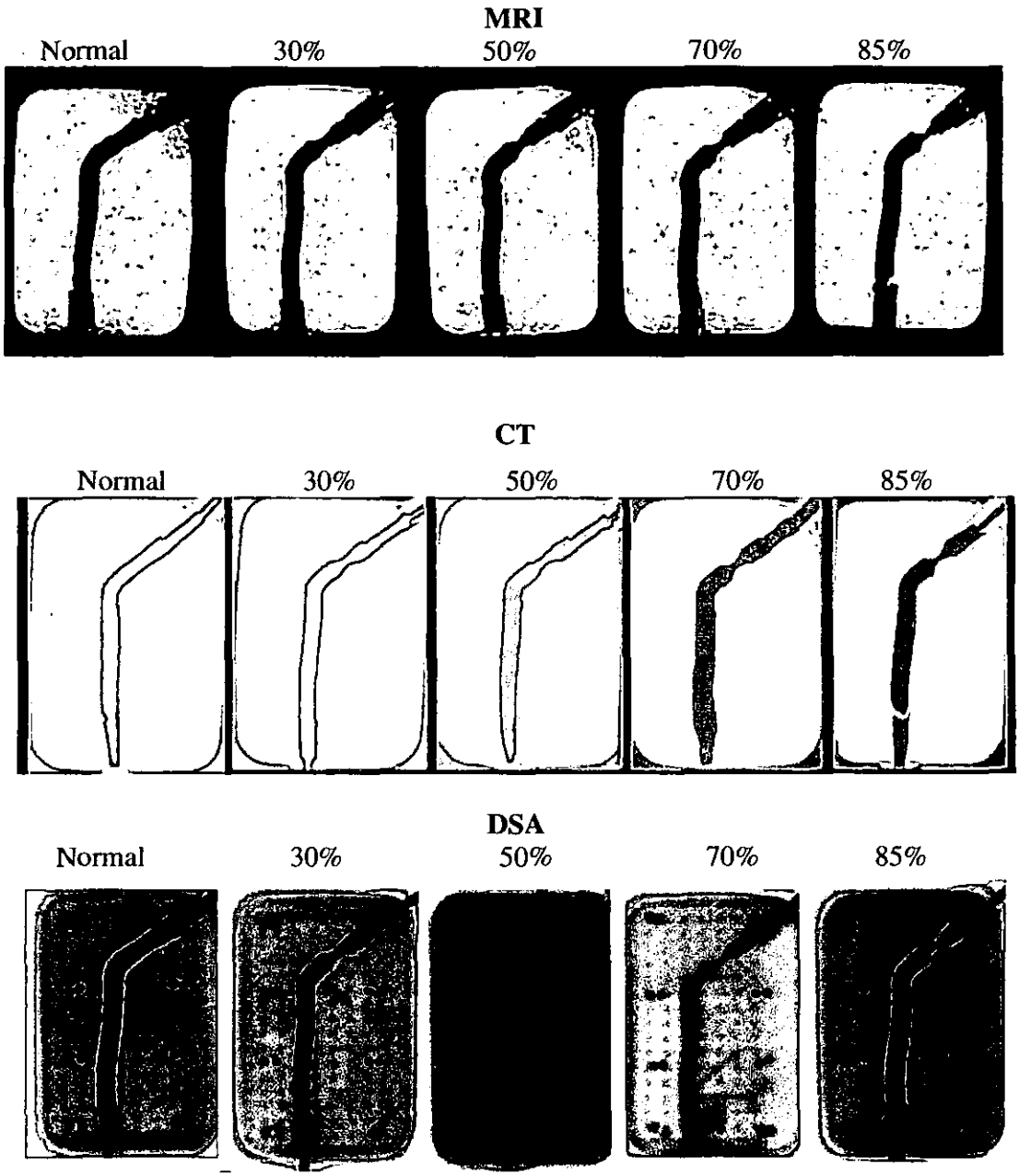

Figure 6.5 MRI, CT and DSA images of the range of multi-modality phantoms

Presented in Figure 6.3 and 6.5 are the images of the 5 multi-modality phantoms with varying degrees of stenosis acquired from US, MRI, CT and DSA. As can be seen from these images, the vessel of each phantom is clearly visualised and identifiable.

6.3.3. Measurements of the vessel diameter

The measurements of the diameters of the metal models used to create the lumens in the multi-modality renal artery phantoms were used as the reference measurements for this study. As shown in Chapter 3 these models were accurately reproduced without significant differences in their diameters. The diameter of the vessel in each phantom was calculated from images acquired from each of the imaging modalities. For ultrasound, the diameter was calculated from the 2D transverse images, an example image being shown for 50% stenosis in Figure 6.4. For both MRI and CT the diameter was calculated from single slices extracted from their acquired volumes at the mid-point of the vessel as shown in Figure 6.5. For DSA images the diameter was calculated from the projection radiograph for each phantom, also shown in Figure 6.5.

The values obtained for the diameter measurements are summarised for each stenosis in Tables 6.1 – 6.5. The reference measurements are also presented to classify the studied modalities according to their spatial accuracy. In accordance with clinical practice, based on the dimensions taken from the 2D projection, the degree of stenosis in an artery is defined as;

$$(1 - L/R) \times 100 \qquad \textbf{Equation 6.1}$$

where L is the diameter of the lumen at the site of the stenosis and R the reference site diameter, representing the diameter of the lumen pre-stenosis. Using this formula the % stenosis was calculated for the reference and for each imaging technique, where L was taken to be the diameter at location B and R the average diameter from locations A and C. The calculated % stenoses are presented also in Tables 6.1 - 6.5.

Table 6.1 Measured diameters and calculated stenosis for normal phantom

0% stenosis	Diameter measurements (mm)			Calculated stenosis
	A	B	C	
Reference	7.40	7.38	7.40	0%
Ultrasound	7.12 ± 0.14	7.07 ± 0.12	7.04 ± 0.07	0%
MRI	7.66 ± 0.11	7.62 ± 0.04	7.94 ± 0.17	2%
CT	7.30 ± 0.36	7.30 ± 0.21	7.82 ± 0.13	3%
DSA	7.87 ± 0.10	7.12 ± 0.13	7.67 ± 0.30	8%

Table 6.2 Measured diameters and calculated stenosis for 30% stenosis phantom

30% stenosis	Diameter measurements (mm)			Calculated stenosis
	A	B	C	
Reference	7.60	5.40	7.80	30%
Ultrasound	7.37 ± 0.38	5.59 ± 0.11	7.12 ± 0.14	23%
MRI	7.68 ± 0.15	5.74 ± 0.05	7.98 ± 0.08	27%
CT	7.80 ± 0.11	5.80 ± 0.02	7.40 ± 0.10	24%
DSA	7.84 ± 0.17	5.21 ± 0.16	7.85 ± 0.07	34%

Table 6.3 Measured diameters and calculated stenosis for 50% stenosis phantom

50% stenosis	Diameter measurements (mm)			Calculated stenosis
	A	B	C	
Reference	7.87	4.02	8.10	50%
Ultrasound	7.34 ± 0.08	3.97 ± 0.17	8.05 ± 0.45	48%
MRI	7.74 ± 0.05	4.20 ± 0.10	8.16 ± 0.11	47%
CT	8.06 ± 0.16	4.14 ± 0.13	7.76 ± 0.16	48%
DSA	7.72 ± 0.44	4.43 ± 0.32	7.95 ± 0.22	43%

Table 6.4 Measured diameters and calculated stenosis for 70% stenosis phantom

70% stenosis	Diameter measurements (mm)			Calculated stenosis
	A	B	C	
Reference	7.90	2.42	8.10	70%
Ultrasound	7.86 ± 0.21	3.10 ± 0.23	7.83 ± 0.18	60%
MRI	7.74 ± 0.05	2.78 ± 0.08	8.34 ± 0.05	65%
CT	7.30 ± 0.35	3.01 ± 0.42	7.76 ± 0.16	60%
DSA	7.64 ± 0.26	3.15 ± 0.23	7.39 ± 0.33	58%

Table 6.5 Measured diameters and calculated stenosis for 85% stenosis phantom

85% stenosis Location	Diameter measurements (mm)			Calculated stenosis
	A	B	C	
Reference	7.80	1.20	8.20	85%
Ultrasound	7.51 ± 0.11	2.03 ± 0.06	7.78 ± 0.11	73%
MRI	7.82 ± 0.11	1.96 ± 0.03	8.10 ± 0.10	75%
CT	7.98 ± 0.44	2.28 ± 0.29	8.16 ± 0.44	72%
DSA	7.49 ± 0.29	2.28 ± 0.35	8.26 ± 0.31	71%

Figure 6.5 and Table 6.6 give a summary of over/under estimation of stenosis (%) with US, MRI, CT and DSA. Using a one-way ANOVA statistical test, significant differences (< 0.05) from the reference measurement where found for some of the imaging modalities at each stenosis. In Table 6.6 the imaging modality which is significantly different is denoted by an asterisk (*).

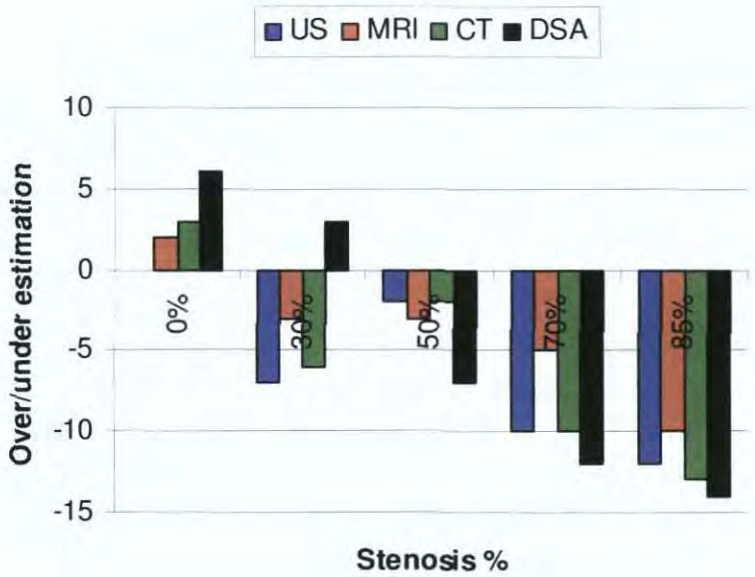

Figure 6.6 Summary of over/under estimation of stenosis (%) with US, MRI, CT and DSA

Table 6.6 Summary of over/under estimation of stenosis (%) with US, MRI, CT and DSA, where * denotes significant (95% confidence interval)

	0%	**30%**	**50%**	**70%**	**85%**	**Overall Mean error**
US	0	-7*	-2	-10*	-12*	-6
MRI	2	-3	-3	-5*	-10*	-4
CT	3	-6*	-2	-10*	-13*	-6
DSA	6*	3	-7*	-12*	-14*	-5
P value	0.0045	<0.0001	0.0110	<0.0001	<0.0001	

6.4 DISCUSSION

In this chapter the range of multi-modality renal artery phantoms developed in Chapter 3 were used for a comparative study between four of the imaging techniques currently used to detect RAS (US, MRI, CT and DSA). The primary aims of the study were to asses the visualisation of the phantoms with each imaging modality and determine the geometric accuracy of the technique.

All renal artery phantoms were successfully imaged with the four imaging modalities. Glass beads (4 mm) were chosen to be used as fiducial markers for the multi-modality phantoms. As shown in Figure 6.2 the fiducial markers were clearly identifiable and did not introduce artefacts into the images of the four different modalities. It was found that for the normal and 50% phantoms the measured diameters were most accurately determined by US, CT and MRI. However, DSA overestimated the normal stenosis by 8% while it underestimated the 50% stenosis by 7%. The 30% stenosis was underestimated by US, CT and MRI, most significantly by ultrasound and CT. For stenosis < 50% MRI was the most consistent modality. For the higher stenosed phantoms (70% and 85%) all four imaging modalities significantly underestimated the stenosis, with DSA having the greatest underestimation. It has been shown previously that DSA tends to underestimate diameters (Boussion et al., 2004). This study has shown that the non-invasive imaging techniques used to detect renal artery stenosis result in underestimation of the stenosis in particular for blockages > 50%. The accuracy of ultrasound for stenosis < 50% with errors of 2 - 6% was comparable to results reported in the literature (Beux et al., 2001; Boussion et al., 2004).

This study shows the potential for these novel anatomically realistic renal artery phantoms to be used as standard vascular phantoms for comparative studies of US, MRI, CT and DSA. MRI was the most accurate imaging modality with a mean error of 4%, while both US and CT had comparable results. The primary aims of the study were to asses the geometry of the phantoms with each imaging modality and determine the geometric accuracy of each technique. For this reason only basic imaging protocols were followed and not specific clinical protocols. In ultrasound, velocity measurements using Spectral Doppler are the most common method of calculating the degree of renal artery stenosis. MRA and CTA are more commonly used for imaging renal artery stenosis. This study has shown the potential of these novel phantoms and further studies following standardised clinical protocols for the detection of renal artery stenosis would be necessary to develop this potential. It has also demonstrated that the range of novel anatomically realistic renal artery phantoms can be used as standardised vascular phantoms for comparative studies of ultrasound, MRI, CT, and DSA.

6.5 CONCLUSIONS

The range of multi-modality renal artery phantoms developed in Chapter 3 were used for a comparative study between four of the imaging techniques currently used to detect renal artery stenosis (US, MRI, CT and DSA). This study has shown the potential of these novel phantoms to be used as a standard vascular phantom to allow comparative studies of the different imaging modalities. They provide a means of evaluating current and emerging US, MRI, CT, and DSA technology as well as being able to observe the hemodynamic features within the renal artery as discussed in Chapters 4 and 5.

CHAPTER 7 KIDNEY PERFUSION PHANTOM DEVELOPMENT

7.1 INTRODUCTION

In this chapter the development of a kidney perfusion phantom for CEUS is described. Due to the microcirculation of the kidney conventional ultrasound is limited in its application. The intracortical capillaries (dimensions < 200 μm) and deep vessels result in very weak Doppler signals. Furthermore, the slow capillary flow (< 3 mm s^{-1}) can be beyond the velocity detection of Doppler ultrasound systems. Advancements in new applications in renal blood flow imaging such as the use of ultrasound contrast agents with contrast specific imaging, offers promising improvements in the detection of abnormal microvascular and macrovascular disorders (Correas et al., 2006). The existing ultrasound perfusion phantoms reviewed in section 1.7.4 all lack some of the characteristics essential to mimic perfusion of the kidney. Currently there is no commercially available phantom suitable for verification of ultrasound perfusion measurements in the kidney. Comprehensive *in-vitro* experimentation is required to optimise the performance of UCAs for renal imaging. Four different types of phantoms were developed, beginning with basic phantoms consisting of bundles of tubes and progressing to capillary phantoms and foam phantoms. The phantom which matched the design criteria the best to mimic perfusion in the kidney will be used in the contrast enhanced perfusion studies described in Chapter 8. This perfusion phantom is intended to be a significant tool for testing and validating ultrasound techniques which assess perfusion within organs such as the kidney.

7.1.1 Kidney vasculature

In the kidney the anatomic distribution of vessels related to macro- and microvasculature is well defined. This organ receives its blood supply from the renal artery, and the blood exits through the renal vein. The renal artery divides into segmental arteries with further division into the interlobular arteries in the medulla, then into the arcuate arteries and then into the microvasculature in the renal cortex as displayed in Figure 7.1. In Table 7.1 the typical diameters of the vessels in the kidney and their corresponding velocities are presented.

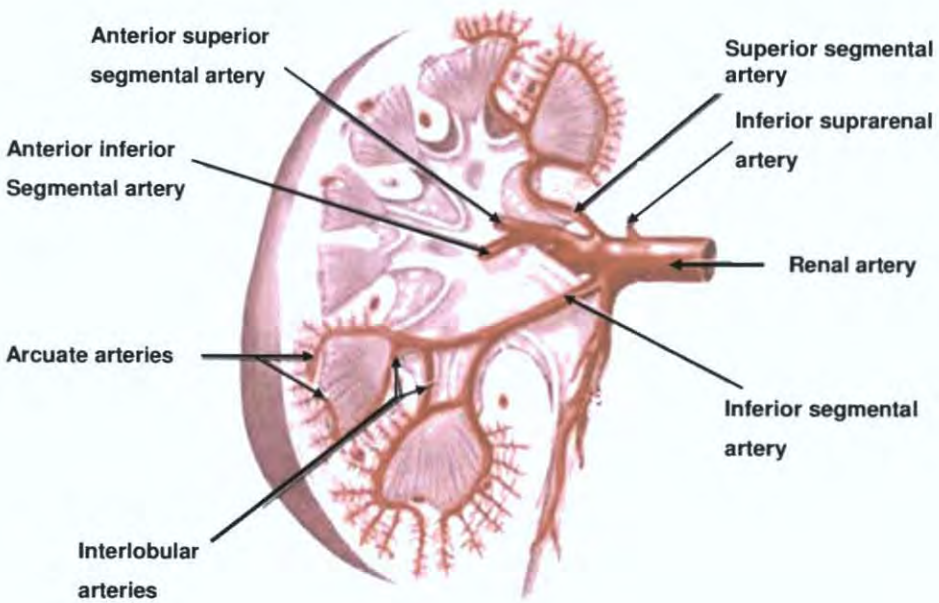

Figure 7.1 The complex vasculature of the kidney (adapted from A.D.A.M.Medical Encylcopedia, http://www.nlm.nih.gov/medlineplus/ency/imagepages/8817.htm)

Table 7.1 Typical diameters and corresponding velocities of vessels in the kidney

	Diameter (mm)	Velocity (cm s^{-1})
Renal artery	5 – 8	60 – 80
Segmental arteries	1 - 2	30 - 50
Interlobular arteries	< 2	10 -30
Arcuate arteries	< 1	10 -30
Capillaries	< 200 μm	< 0.3

7.1.2 Kidney perfusion phantom design criteria

Although there are no standard specifications for perfusion phantoms, the IEC specifications for standard flow phantoms can be used as a starting point in the design of a phantom to mimic perfusion in the kidney. The phantom should consist of a TMM and BMF which match the acoustic properties IEC specifications as presented previously in Table 2.1. The phantom should consist of a number of small vessels which have diameters and velocities similar to those presented in Table 7.1. The vessels of interest should be located at a depth of 3 - 6 cm similar to that in the kidney. The most important vessels to mimic are the capillaries as this is where the Doppler signal is the weakest. The presence of the larger sized vessels will enhance the physiological relevance of the phantom but may not be required for all contrast studies. The capillary sized vessels should be distributed in a spatially random manner with isotropic flow direction. Other desirable features which would enhance the kidney phantom would be the presence an inlet and outlet vessel similar to the renal artery and renal vein. Also, the presence of an overlying fat mimicking layer would be advantageous. These two features would be important when carrying out contrast enhanced investigations of the kidney perfusion phantoms to show how microbubbles can help overcome some of the limitations when imaging the renal system.

7.2 METHODOLOGY

7.2.1 Phantom construction

Phantom 1 - basic microcirculation phantom

This phantom was designed to mimic the randomly distributed vessels with isotropic flow. This simple phantom consisted of a bundle of C-flex® tubing (i.d. 1.6 mm) held together with cable ties. The bundle was placed in a small plastic container (0.5 litre) with four holes drilled in the sides. The vessels were fed through the holes so that there was flow going in both directions. A rubber mat was placed on the bottom of the container to reduce reverberation artefacts. A modified agar TMM with no scattering medium (evaporated milk) and no scatterers was poured into the container (Madsen et al., 1998).

Phantom 2 - second microcirculation phantom

This phantom was designed to mimic the randomly distributed vessels found in the kidney and the branching of the vessels into smaller vessels. This phantom consisted of a 3.2 mm (i.d.) vessel branching into two smaller vessels (i.d.1.6 mm) by means of a Y-connector, both of which in turn branched into a further two vessels with a inner diameter of 0.8 mm again by means of a Y-connector. Each of the four 0.8 mm vessels were clustered together to form a nest. The outlets of these vessels were branched back into two vessels, and then back to one vessel again using Y-connectors. A rubber mat was placed on the bottom of the container to reduce reverberation artefacts. A modified agar TMM with no scattering medium (evaporated milk) and no scatterers as described above was poured into the container Madsen et al., (1998).

Phantom 3 - kidney capillary phantom

This phantom was designed to mimic the capillaries in the kidney using vessels which have similar dimensions and velocities to that found *in vivo*. A dialysis filter FX 80 (Fresenius Medical Care AG & Co. KGaA, Bad Homburg, Germany) was used to replicate the microcirculation of the kidney. An external polypropylene plastic casing housed the capillaries. This filter consisted of approximately 10,000 capillaries with a wall thickness of 35 μm and inner diameter of 185 μm. The total capillary volume of the phantom was 95 ml. A degassed liquid tissue-mimicking material was pumped into the spaces between the capillaries (micro-vessels) and the outlet ports were sealed. A uniform distribution was assumed from visual inspection. The composition of this liquid TMM is presented in Table 7.2. This TMM has a reported speed of sound 1540 m s^{-1} and attenuation coefficient of 0.5 dB cm^{-1} MHz^{-1} (Madsen et al., 1998).

Table 7.2 Recipe for production of 1 L of liquid TMM

Component	**Composition**
Distilled water	644 ml
N-propanol	56 ml
Agar	28 g
Benzalkoniumchloride (10%)	1 ml
Evaporated milk	500 ml

The filter was submerged in a water bath consisting of liquid TMM at room temperature. C-flex® tubing (i.d. 4.8 mm) was connected to the inlet and outlet ports of the filter. The tubing was arranged so that the inlet, outlet and filter could be scanned simultaneously (Figure 7.2).

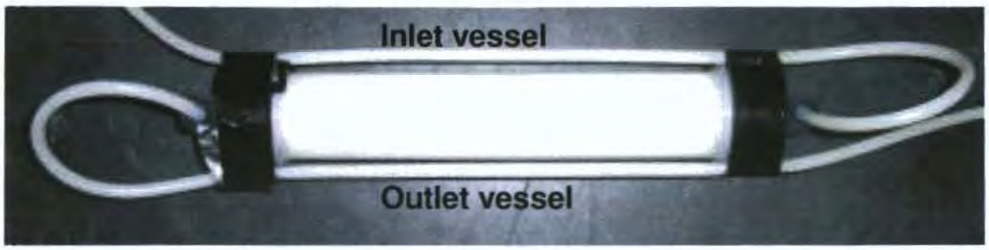

Figure 7.2 Dialysis filter with the inlet and outlet vessels aligned

Phantom 4 - kidney foam phantom

This phantom attempted to replicate the fractal nature of the vessels in the kidney by starting with one 3.2 mm vessel which branched in smaller vessels and ultimately into the reticulated foam. C-flex® tubing was chosen as the vessel material. One vessel (3.2 mm i.d.) was connected to two vessels of smaller diameter (1.6 mm i.d.) by means of a Y-connector. Each of the vessels (1.6 mm i.d.) were then connected to two vessels with 0.8 mm i.d. by means of a Y–connector. The outlet of each 0.8 mm i.d. vessel was embedded in the (30 PPI) polyester foam. The side of the phantom where the C-flex® tubing was attached to the foam was sealed with Araldite™. The network of inlet vessels is shown in Figure 7.3(b).

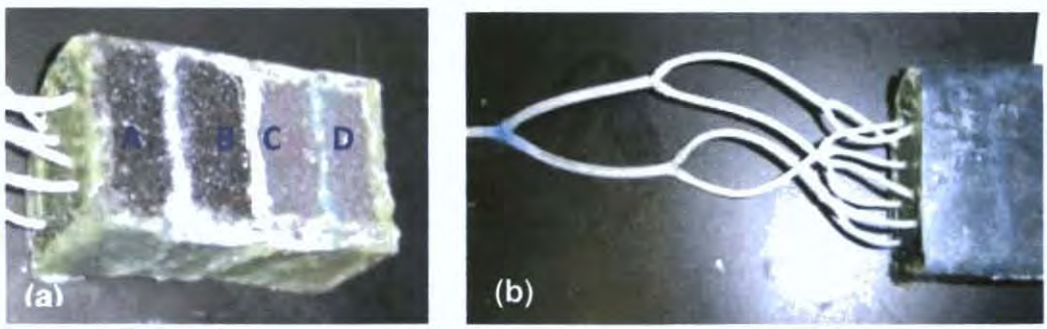

Figure 7.3 Kidney foam phantom showing (a) the different foam sections A, B, C and D, (b) the network of inlet tubing with decreasing diameters

The reticulated foam progressed from coarse (30 PPI) polyester foam, sections A and B to fine (80 PPI) polyester foam, sections C and D polyester foam as shown in Figure 7.3. The pieces of polyester foam with 80 PPI were glued around the edges using the adhesive Araldite^{TM} to the polyester foam pieces with (30 PPI). The dimensions of each piece of foam were (65 x 65 x 30 mm). Three sides of the completed microvasculature block were sealed using Araldrite^{TM}. The top side remained unsealed to act as the acoustic window for scanning access. A piece of electrostatic plastic was affixed to the surface to act as a membrane. The other end of the phantom remained unsealed to allow outflow of the BMF from the phantom. Before use the phantom was submerged in a water tank of degassed water and left overnight to absorb the water and facilitate removal of any remaining air bubbles from the foam.

7.2.2 Simple perfusion studies

Basic contrast studies were performed to determine which phantom was the most suitable to replicate perfusion in the kidney. The ultrasound scanner used for these investigations was the HDI 3000 with curvilinear broadband transducer C4-2. A computer controlled system was used to send steady state signals to a 24 V dc servo feedback motor which drove the pump as previously described in section 2.2.4. The IEC recommended BMF was used in all flow investigations (Ramnarine et al., 1998). The phantoms were assessed using flow rates, 30 ml min^{-1} and 100 ml min^{-1}.

Luminity® preparation

Before agent activation of the contrast agent, a vial of Luminity® was removed from the refrigerator and allowed to equilibrate to room temperature. The contrast agent was prepared by shaking the vial in a Vial-Mix^{TM} (Bristol Myers Squibb, NY, USA) for

45 s, according to the manufacturer's recommendations. The vial initially contains a clear, colourless, sterile, non-pyrogenic, hypertonic liquid, which upon activation becomes a homogeneous, opaque, milky white, injectable suspension of lipid microspheres. After agitation the agent was gently extracted from the vial while it was inverted, using a 20 gauge needle inserted with the base of its bevelled tip just inside the rubber stopper. A second 20 gauge needle was also fully inserted for venting purposes. The contrast agent Luminity®, 0.1 ml diluted in 5 ml of saline, was injected as a bolus into the flow circuit by means of a three-way tap. Images were captured on the hard drive of the ultrasound scanner. A full description of the analysis of contrast enhanced images is provided in section 8.5.3. To prevent recirculation of the contrast agent in the phantom, the BMF in the flow circuit was passed through the model once only.

7.3 RESULTS

Phantom 1

Since the TMM used in this phantom was a modified version of the recipe as described by Madsen et al., (1998), it was not possible to assume the acoustic properties reported for the original version. The IEC BMF was used in all flow experimentation. C-flex tubing was used, which as discussed in sections 1.7 and 5.4 has a very high attenuation coefficient and is not a suitable material to mimic human vessels. The vessel diameter in this phantom was 1.6 mm which is only suitable to mimic the larger vessels in the kidney and not the capillaries. As a result it does not obtain the low velocities found in the capillaries. A positive feature of this phantom is the random distribution of the vessels but it is important to note that they are of only of one vessel diameter. A MRI 3D volume set of the phantom was obtained with a 7 Tesla Bruker MRI scanner (Bruker Corporation, MA, USA) using the 3D Flash Gradient Echo technique to visualise the random arrangement of tubing, two slices from the MRI data set are presented in Figure 7.4.

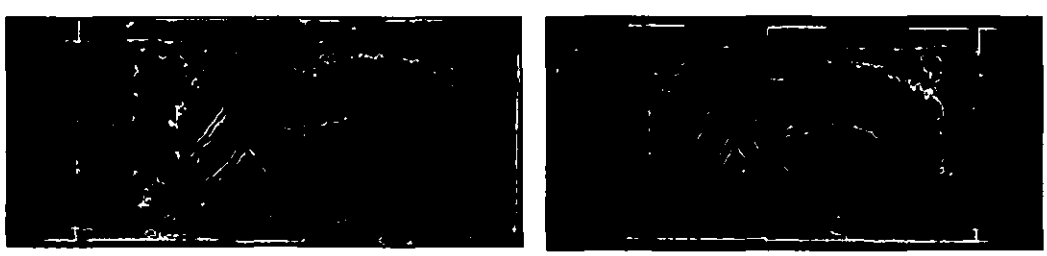

Figure 7.4 3D MRI images of phantom 1, the basic microcirculation phantom

Presented in Figure 7.5 are images captured for the first basic microcirculation phantoms at a flow rate of 30 ml min^{-1}. The flow of the BMF was easily visualised

using Colour Doppler and Power Doppler. This phantom is not suitable for contrast studies as the flow can be visualised without the use of UCAs.

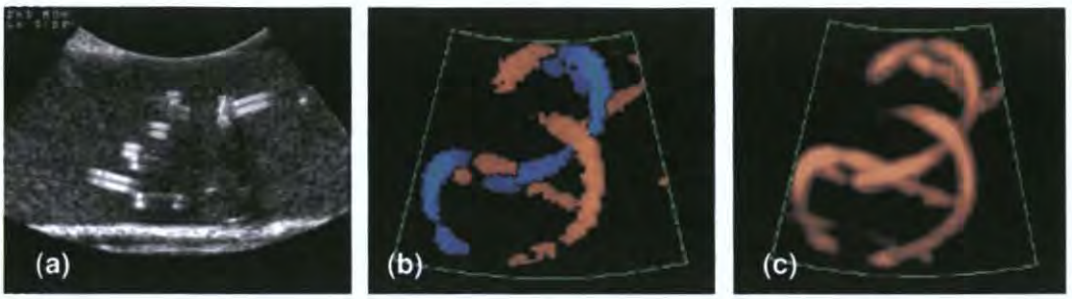

Figure 7.5 Example of the images obtained from phantom 1, (a) B mode image, (b) Colour Doppler and (c) Power Doppler image of the same area

Phantom 2

This phantom had the same drawbacks as phantom 1 in relation to the TMM and VMM. The phantom did have three different sized vessels distributed randomly but once again they were too large to mimic the capillaries. This phantom consisted of four bundles of vessels held together with cable ties. The vessels used in the bundles were half the size in diameter of those used in the first design. Another feature of this phantom was the branching of the vessels. Samples of the images obtained from this phantom are presented in Figure 7.6. With a steady flow rate of 30 ml min^{-1}, when the flow reached the bundle of vessels, the vessels branched from one vessel to four vessels resulting in a reduction of the flow rate to 7.5 ml min^{-1}, calculated by dividing the original flow rate by four. This resulted in a maximum velocity of approximately 21 cm s^{-1} (measured V_{max} was 28 cm s^{-1}) in the 0.8 mm i.d. vessels which can be observed in the images in Figure 7.6. Once again the flow was easily visualised with out the use of UCAs.

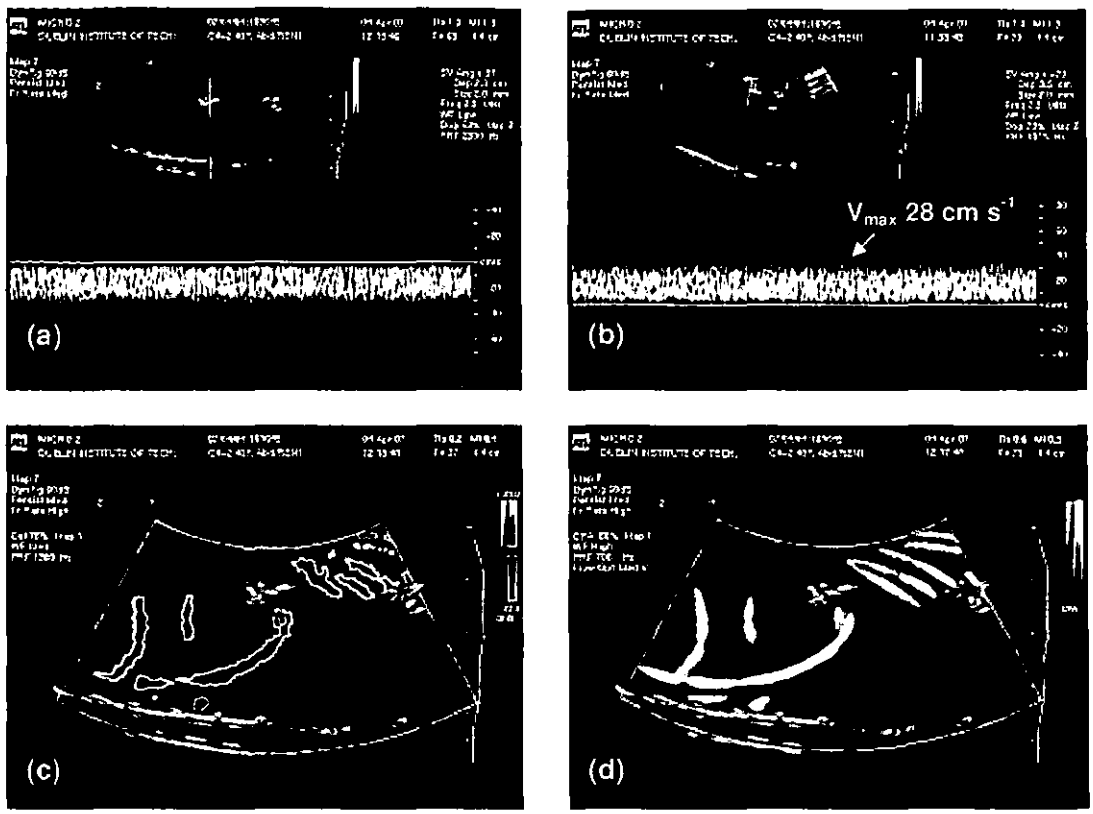

Figure 7.6 Example of the images captured using phantom 2, (a) & (b) Spectral Doppler, (c) Colour Doppler, and (d) Power Doppler

Phantom 3

In phantom 3, the kidney capillary phantom a liquid TMM described by Madsen et al., 1998 was used. This TMM had acoustic properties similar to that specified by the IEC. The IEC BMF was pump through the capillaries. The vessels were thin walled and had dimensions similar to that of capillaries found *in vivo*. Assuming a uniform flow distributed through all the capillaries (approximately 10,000) this resulted in a flow of approximately 0.01 ml min^{-1} per capillary and an approximate speed of 0.6 cm s^{-1} in each capillary. The mean velocity in the inlet and outlet tubes was 11 cm s^{-1} which was calculated from timed collection using a measuring cylinder and stopwatch.

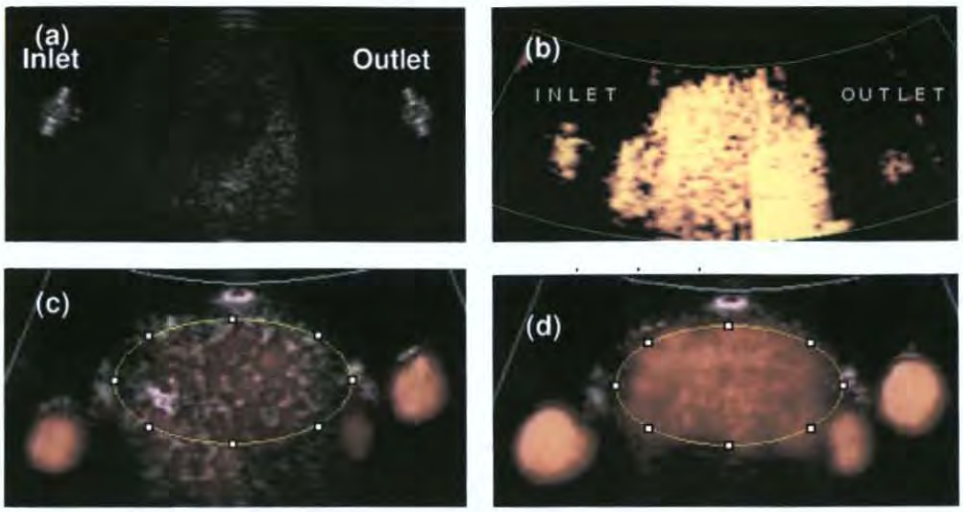

Figure 7.7 Phantom 3, kidney capillary phantom (a) 2D Harmonic image with UCA visible in inlet and outlet vessels, (b) conventional Power Doppler of phantom with UCA present, (c) Harmonic Power Doppler imaging with no UCA present, (d) Harmonic Power Doppler imaging with UCA present

Figure 7.7 presents a range of images captured of the kidney capillary phantom. Without the presence of the UCA, only limited perfusion is visualised in the filter (Figure 7.7(c)). This is increased significantly after a bolus injection of Luminity® contrast agent, within the ellipse ROI (119 (w) x 64 (h) pixels), the perfusion increased 64% after a bolus injection of Luminity® (Figure 7.7(d)). Note the flow is clearly visualised in the inlet and outlet vessels with no UCA present (Figure 7.7(c)) due to the large dimensions on the tubing (4.8 mm), however very little perfusion in the phantom can be observed. With the introduction of the UCA flow can be clearly observed in the larger vessels and in the perfusion phantom, Figure 7.7(d).

Phantom 4

The fourth phantom consisted of degassed reticulated foam in a water bath. The acoustic properties for similar foam has been reported to have a speed of sound and attenuation

of 1487 m s^{-1} and 0.8 dB cm^{-1} MHz^{-1} at 5 MHz, respectively (Hoskins, 1994). This material is not within the IEC specifications of a speed of sound, 1540 ± 15 m s^{-1} and attenuation coefficient of 0.5 ± 0.05 dB cm^{-1} MHz^{-1}. This phantom comprised of a network of c-flex tubing branching into smaller vessels before entering the reticulated foam. Therefore this phantom had a range of different vessel sizes with the flow being pefused through a section of reticulated foam. For the flow experiments, it was possible to visualize some flow in the foam sections at a flow rate of 30 ml min^{-1} using conventional Power Doppler. At a steady flow rate of 100 ml min^{-1}, a more consistent flow pattern was observed as shown in Figure 7.8. Using the CSI mode Harmonic Power Doppler imaging, a bolus injection of Luminity® was injected and a series of images were captured. No enhancement was observed, due to severe acoustic shadowing as shown in Figure 7.9.

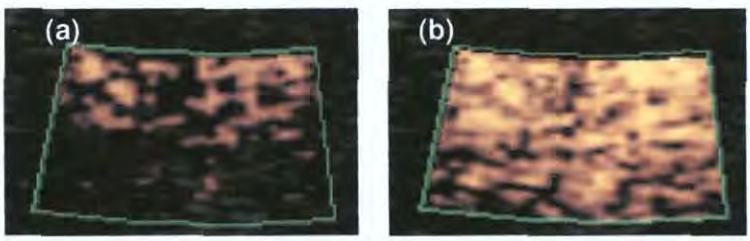

Figure 7.8 Phantom 4, kidney foam phantom conventional Power Doppler at a flow rate (a) 30 ml min^{-1} and (b) 100 ml min^{-1}

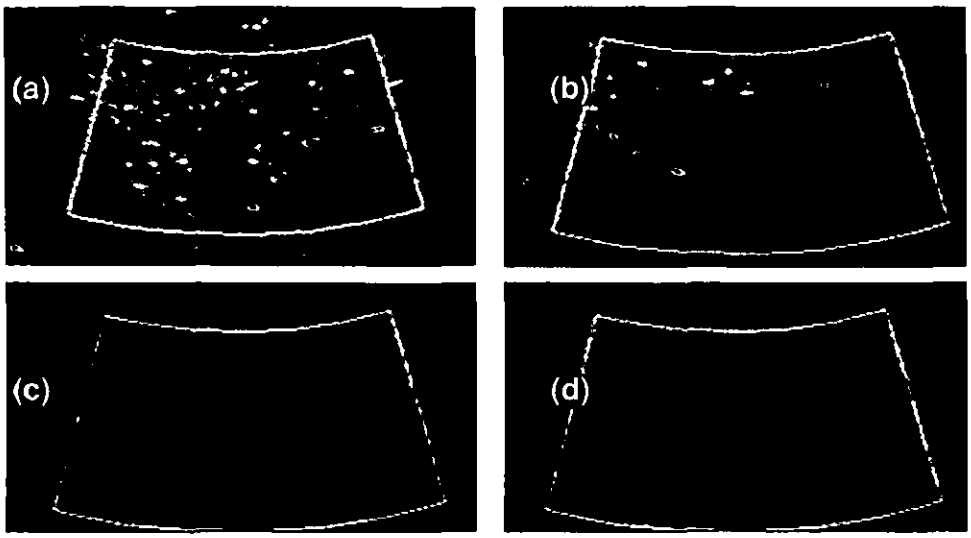

Figure 7.9 Acoustic shadowing due to 0.1ml Luminity® bolus injection-foam phantom, (a) before injection, (b) 15 sec after injection, (c) 35 sec after injection, (d) 40 sec after injection

Summary

Each phantom was evaluated in terms of how it meet each design criteria specified in section 7.1.2. Also images obtained from the flow experimentation were visually assessed to determine the phantoms suitability for contrast studies. Table 7.3 provides a summary of how well each phantom met the design criteria and its suitability for contrast enhanced studies. From this table, phantom 3 matched the design criteria the best and was also the most suitable for contrast studies.

Table 7.3 Summary of the design features of the four phantoms developed

Phantom	TMM	BMF	VMM	Vessel diameter	Velocity	Vessel distribution	Suitability for contrast studies
1	*	***	*	*	*	**	*
2	*	***	*	*	*	***	*
3	***	***	**	***	***	*	***
4	*	***	**	**	**	***	*

* does not adequately match design criteria, ** has some features of the design criteria, *** matches design criteria

7.4 DISCUSSION

This chapter describes the development and assessment of a series of perfusion phantoms attempting to replicate perfusion in the kidney. Four different types of phantoms are described, beginning with basic phantoms consisting of bundles of tubes and progressing on to a capillary phantom and a foam phantom.

The first basic microcirculation phantom developed consisted of vessels (i.d. 1.6 mm) bundled together to simulate several spatially distributed small vessels with various flow directions. The vessels in this phantom were too large to mimic those of the microcirculation in the kidney and UCAs were not required to improve the Doppler signal during blood flow measurements. This phantom would not therefore be suitable for contrast studies. It may although be used to simulate larger vessels in the kidney such as the segmental arteries. A similar phantom was described by Erickson et al., (1995) using a bundle of polyethylene tubes with an inner diameter of 0.28 mm.

From the experience obtained in developing the first phantom, a second microcirculation phantom was designed to overcome the limitations encountered in the first phantom. This phantom was designed using vessels with a range of inner diameter sizes (3.2 mm, 1.6 mm and 0.8 mm). Also, Y-connectors were used to allow the vessels to branch, thereby mimicking the fractal nature of the kidney. This phantom also had its limitations, although the vessels used in the nest were half the size of the vessels used in the first phantom, they are still much larger than those found in the microcirculation (5 μm to 100 μm). One again this phantom would not be suitable for perfusion studies but may be used to mimic the random distributed vessels found in the

kidney and the branching of the vessels into smaller vessels such as the segmental arteries in the interlobular arteries.

Both phantoms 1 and 2 used much larger vessels than those used in Erickson et al., (1995). It was important to use tubing which has it acoustic properties well characterised, therefore C-flex tubing was used. For smaller C-flex tubing the wall-thickness is larger than the inner diameter. This is highly undesirable as the material has a very high attenuation as discussed in section 7.3. Is that it is very difficult to find tubing materials with the correct dimensions and acoustic properties. As discussed in Chapter 2, this has been a problem encountered by many investigators in the development of flow phantoms and has ultimately resulted in the use of wall-less phantoms. It is currently not possible to make such phantoms for microcirculation studies, as the dimensions of the vessels are so small the TMM would be damaged when removing the metal moulds or the vessels would collapse.

Another approach is to use dialysis filters as perfusion phantoms, this is advantageous because the capillary size is well defined and has the correct dimensions to simulate capillaries in the kidney (< 200 μm). Also they offer a relatively simple, cost effective method of investigating perfusion. A similar approach has been taken in previous perfusion studies (Hindle and Perkins, 1994; Ugolini et al., 2000; Veltmann et al., 2002; Yeh et al., 2003). In some of these capillary phantoms a portion of the plastic casing had to be removed, as the plastic caused severe reverberation and attenuation artefacts (Hindle and Perkins, 1994; Veltmann et al., 2002). It is very difficult to measure the flow in a single capillary due to the small size and the low velocity. Therefore, the total flow (perfusion) in a volume of tissue is how the microcirculation is measured. Cutting

away the shell can damage the fragile capillaries leading to loss of the perfusion medium and the effective flow in the phantom volume cannot be calculated precisely.

The previous phantoms have been designed to mimic microcirculation but not the microcirculation of a specific organ. Here in phantom 3, the kidney capillary phantom was designed with tubing entering and exiting the filter arranged to replicate the renal vein and artery. The tubing was arranged so that the inlet, outlet and filter could be scanned simultaneously. This arrangement was similar to that described by Yeh et al., (2003), the position of the inlet and outlet vessels allowed time intensity curves to be obtained for the inlet, perfusion phantom and outlet and subsequently a comparison to be made of the different compartments of the phantom. The particular filter used here had a polypropylene plastic housing which did not introduce strong attenuation artefacts in the scan plane. Therefore it was not required to cut the plastic housing away, this ensured the capillaries were not damages and there was no loss of BMF.

This phantom used a liquid TMM was used to attenuate the US beam and a BMF. A BMF with scatterers has only been used once previously in perfusion studies using dialysis filters (Li and Yang, 2003); otherwise either water (degassed and non degassed) or simple blood analogues based on modified Krebs-Henseleit solutions have been used (Claassen et al., 2001; Lohmaier et al., 2004; Veltmann et al., 2002; Yeh et al., 2003). The BMF was successfully perfused through the phantom, it should be noted that it was important to flush the phantom with water after each use in order to prevent the Orgasol® particles from settling in the capillaries and causing blockages and aneurysms to form in the C-flex® tubing. For this reason liquid TMM was chosen over solid TMM as the TMM could be removed easily to allow the replacement of damaged tubing

without the need to produce an entire new phantom. As can be seen from Table 7.3, this phantom matched the majority of the design criteria. It mimics the *in-vivo* situation by using a suitable TMM which was within the IEC specifications of the IEC. BMF was perfused through capillaries with dimensions (capillary i.d. 185 μm) similar to that found *in-vivo.* The only drawback of this phantom was all of the capillaries were parallel, with flow in all in the same direction.

The final phantom , the kidney foam phantom comprised of a tubing network branching into smaller vessels, dividing before entering the layers of polyester foams with different pore sizes. The phantom was designed to replicate the renal artery dividing into two segmental arteries with further division into the interlobular arteries then into the arcuate arteries and microvasculature or tissue perfusion. Using conventional Power Doppler the perfusion with the foam phantom was observed. Unfortunately, after a bolus injection of Luminity® contrast medium enhancement of the perfusion within the foam was not observed. This was due to acoustic shadowing in the top section of the phantom. Acoustic shadowing is attenuation due to the strong absorption and scattering of the ultrasound beam by the microbubbles close to the transducer. This limits the penetration of the ultrasound beam into deeper layers. Acoustic shadowing in this instance depends on the concentration of the contrast agent. The measurements were repeated with the concentration of the UCA decreased but acoustic shadowing still occurred. Due to the design of the foam phantom there was no resistance for the UCAs when they travelled through the foam layers. They appear to float to the top of the phantom. Although this phantom incorporated branching vessels with decreasing diameters and reticulated foam to mimic the microcirculation, the current design

requires further improvement to accommodate perfusion studies. The phantom may need to be in a vertical position to prevent microbubble flotation.

7.5 CONCLUSIONS

The application of UCAs to the kidneys is still in its infancy but there are several areas of great potential (Correas et al., 2006; Correas et al., 2009; Robbin et al., 2003). One such area is the detection of RAS using CEUS either by direct or indirect techniques. Comprehensive *in-vitro* experimentation is required to optimise the performance of ultrasound contrast agents for renal imaging. In this chapter four types of phantoms were developed and evaluated in an attempt to develop a kidney perfusion phantom for contrast enhanced ultrasound. They range from very simple microcirculation phantoms with bundles of C-flex® tubing to complex capillary and foam perfusion phantoms. From the four phantoms developed phantom 3 the kidney capillary phantom was chosen to be used for the contrast enhanced kidney perfusion studies in Chapter 8, as it matched the most design criteria and perform the most satisfactory in the contrast studies. Using this novel kidney capillary phantom it was possible to achieve estimated flow speeds comparable with those in the blood vessels of the macrocirculation (renal artery and renal vein) and also that of the microcirculation of the kidney (0.1 – 3.2 cm s^{-1}) (Milnor, 1982). Significant improvements have been made to the physiological relevance of perfusion phantoms with the addition of a blood mimicking fluid with scatterers and an attenuating tissue mimicking material.

CHAPTER 8 CONTRAST ENHANCED RENAL PHANTOM STUDIES

8.1 INTRODUCTION

This chapter describes an evaluation of an emerging technology in the area of RAS, namely CEUS using the newly developed anatomically realistic renal artery flow phantoms and kidney capillary perfusion phantom (Correas et al., 2003; Correas et al., 2006; Correas et al., 2009; Robbin et al., 2003). Four main studies are described here; the first evaluates the Doppler dynamic range of the US system used for the majority of the renal phantom studies. This is the only study which does not use the realistic renal artery or kidney perfusion phantom. In this study a straight vessel flow phantom was used. The second uses the UCA Luminity® in the anatomically realistic renal artery flow phantoms, to investigate the contrast agent's effect on Spectral Doppler velocity measurements. The third compares the TICs obtained from the kidney capillary phantom using 2 different carrier fluids, to determine if they affect the resultant TIC parameters. Finally, using the kidney perfusion phantom, flow experiments were performed to attempt to obtain TICs similar to that found *in-vivo* in the kidney. The TICs for 2 CSI modes were compared to determine which was more suitable for detecting perfusion similar to that found in the kidney.

8.2 DETERMINATION OF DOPPLER DYNAMIC RANGE

8.2.1 Introduction

In the visualisation of areas with slow flow in small vessels such as the kidney, including regions with some stenosis the Doppler signal is very weak. Furthermore, the signals from the red blood cells in these vessels produce very weak echoes relative to the echoes from the surrounding stationary structures. Therefore, the Doppler ultrasound system used for examining the renal system needs to have a large dynamic range for imaging purposes and Doppler examination. As this thesis is primarily concerned with Doppler US, only Doppler dynamic range (DR) will be dealt with here. Doppler DR is a measure of the range of the linear operation of the Doppler US system (AIUM, 2002) and is defined as the ratio of the largest signal that can be detected without saturation to the smallest signal that can be detected above the electronic noise of the system. If a system has a limited Doppler DR several problems could arise. For example, moving tissue or structures could cause an increase in the noise and mirror, or harmonically related images of flow patterns, could be produced (AIUM 2002). Using a novel protocol the Doppler DR of the HDI 3000 ultrasound scanner was evaluated.

By measuring the signal amplitude from BMF with varying concentrations of particles it is possible to reproduce signal from areas of slow flow (low scatterer volume, RBCs) which may be beyond the detection limits of the Doppler system (corresponding to the low particle concentrations) and also areas of high flow in larger arteries and veins (corresponding to the particle concentration greater than 1.82%). The currently IEC recommended BMF has a concentration of 1.82% per volume of Orgasol® scatterers (diameter 5 μm) for blood-equivalent backscatter (Ramnarine et al., 1998). Limited

work has been carried out in the area of the evaluation of Doppler DR (Ramnarine et al., 2002). It is particularly important for the application of UCAs as a limited Doppler DR will affect the information obtained from these contrast agents (AIUM 2002). Forsberg et al., (1994) showed in-vitro an artificial increase frequency shifts with the used of contrast agents and described this change as arising from the limited dynamic range of the spectral display. For contrast enhanced measurements that are based on the amplitude of the Spectral or Power Doppler signal it is essential to characterise and know the limitations of the processing of the Doppler system used. Artefacts associated with UCAs are colour blooming as discussed in Section 1.5.6 and spectral bubble noise which causes a loud crackling noise in the audio output and may manifest itself as very large excursions in the spectral display (Forsberg et al., 1994). Another possible approach proposed by the AIUM is the use of an acoustic injection device although this has not been implemented to date for the measurement of Doppler DR.

8.2.2 Methodology

The Spectral and Power Doppler DR of the HDI 3000 ultrasound scanner were evaluated. Nine batches of BMF were prepared with varying concentrations of Orgasol® particles (Atofina, PA, USA) to determine the Doppler DR of the system. The following were the Orgasol® particle concentrations (% weight) used: 0.02%, 0.25%, 0.50%, 1.00%, 1.50%, 1.82%, 2.50%, 3.00% and 3.50%. The straight vessel Doppler flow phantom used in this study was previously described in section 5.2. The scanning-well of the flow phantom was filled with speed of sound corrected water (water 90.5%: glycerol 9.5%) (Goldstein and Langrill, 1979). The transducer was positioned to image the 4.8 mm tube in a longitudinal direction, and held in place using a retort stand and clamp. Flow experiments were carried out at a mean velocity of

50 cm s^{-1} for each concentration of the scatterers. Care was taken when changing the BMF concentrations to ensure that the experimental set-up and instrument controls remained constant. The recommended IEC backscatter concentration of 1.82% was used initially to optimise the baseline settings of the study.

Table 8.1 gives the control settings used to optimise the scanner and these were maintained throughout the study, unless otherwise stated. Once the B-mode image was optimised the Spectral Doppler mode was enabled. The Doppler gain was adjusted subjectively in order to obtain a well defined waveform free from saturation and noise. The Doppler gain was optimised for the baseline backscatter concentration of 1.82%, this gain setting was used for subsequent Spectral Doppler investigations which used the other BMF concentrations. A cine-loop was captured and 5 Spectral Doppler images were saved for off-line analysis.

The Power Doppler mode was enabled and the resulting image of the vessel was optimised by adjusting the size of the Power Doppler box and the gain, to give the optimum image of the appropriate section of the vessel. The Power Doppler gain was assessed subjectively and was increased as far as possible without introducing noise. Again the gain was optimised for the baseline concentration of 1.82% and was used for subsequent Power Doppler concentrations of the other BMF concentrations. A cine-loop was captured and 5 Power Doppler images were saved for off-line analysis.

Table 8.1 US scanner settings for Doppler dynamic range study

B-mode	**HDI**
Image depth	13.7 cm
Focal zone	6.5 cm
Gain	Optimised
Spectral Doppler	
Sample volume depth	6.3 cm
Sample volume size	0.5 cm
Doppler angle	60°
Doppler gain	63%
Wall filter	Low
Output power (MI)	0.7
Power Doppler	
Gain	76%
Output power (MI)	0.9
Wall filter	Low
PD Colour box	30 x 26 mm

For the studies on the effect of instrument controls and penetration depth, only 6 concentrations of BMF were used (0.02%, 0.25%, 0.50%, 1.00%, 1.82% and 3.50%). The effects of the following instrument settings on the Spectral and Power Doppler DR were investigated; output power (MI settings 0.3, 0.5, 0.7 and 0.9) and Doppler gain (baseline concentration gain and optimised gain for each concentration).

The Doppler DR was determined by measuring the amplitude of the Doppler signal for each concentration of BMF. From each cine-loop 5 images were captured for off-line analysis. The images acquired were analysed using the software package HDILab

(Philips Medical Systems, Bothell, WA, USA). Using this software it was possible to acquire not only the ultrasound data but also the system parameters such as scaling and compression curves. This allowed the signal amplitude to be expressed in dB. For Spectral Doppler a profile line was placed over the maximum velocity position in the spectrum. The position of this line was noted on the velocity scale, and this is where the profile line was placed for all subsequent images at each different concentration as shown in Figure 8.1(a).

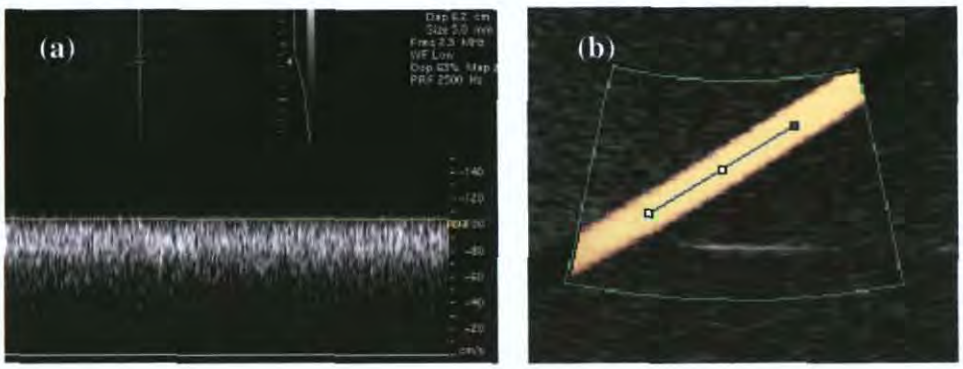

Figure 8.1 Doppler DR image analysis (a) Spectral Doppler and (b) Power Doppler

For Power Doppler a profile line was drawn in the centre of the vessel as shown in Figure 8.1(b). The ROI was measured and its position recorded to ensure the analysis was consistently of the same region in each image. The mean signal amplitude expressed in dB from the five images of each cine-loop corresponding to each BMF concentration was determined for Spectral and Power Doppler.

8.2.3 Results

Figures 8.2 and 8.3 show the signal amplitude for each particle concentration for Spectral and Power Doppler.

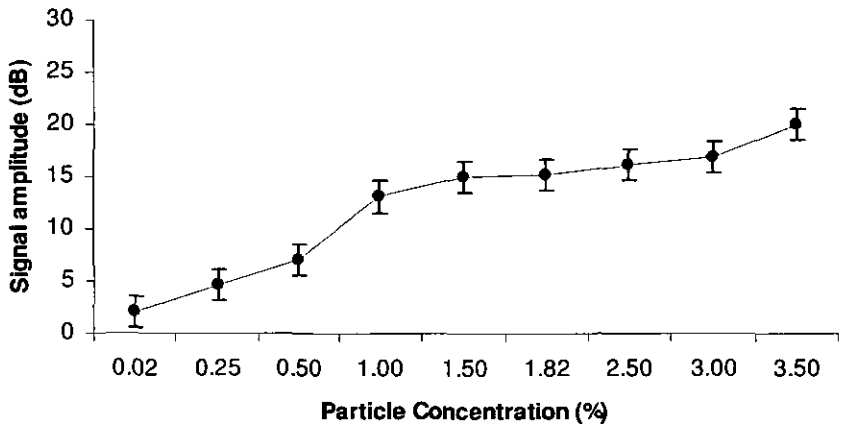

Figure 8.2 The effect of increasing particle concentration on Spectral Doppler dynamic range

The Spectral Doppler DR was calculated to be 18 ± 2 dB. This was calculated by subtracting the lowest signal amplitude (2 ± 2 dB) from the highest signal amplitude (20.0 ± 2 dB). The Power Doppler DR was calculated to be 18 ± 2 dB. Again this was calculated by subtracting the lowest signal amplitude (11 ± 2 dB) from the highest signal amplitude (29 ± 2 dB).

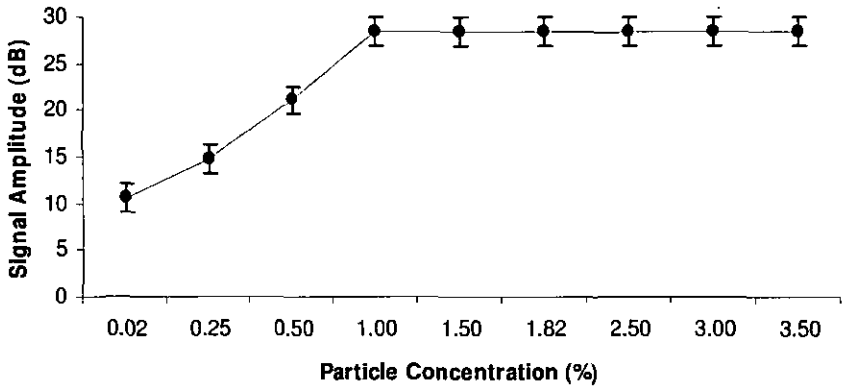

Figure 8.3 The effect of increasing particle concentration on Power Doppler DR for HDI 3000

Effect of system controls on Doppler dynamic range

The effect of system controls on Doppler DR was assessed for the HDI 3000. The following instrument settings were investigated for both Spectral and Power Doppler; output power (MI settings 0.3, 0.5, 0.7 and 0.9 and Doppler gain (baseline concentration gain and optimised gain for each concentration).

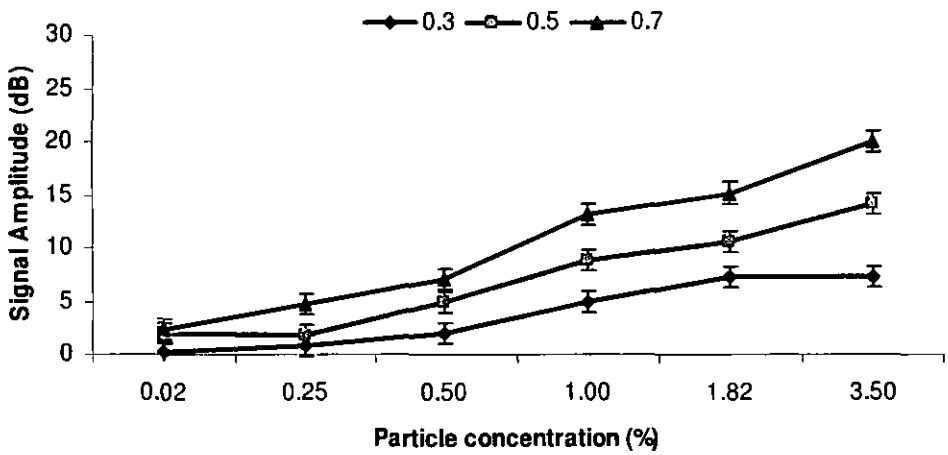

Figure 8.4 Effect of output power on Spectral Doppler signal amplitude for increasing particle concentrations, with the legend showing the output power (MI) values

The Spectral and Power Doppler signal amplitude increased with both increasing MI settings and particle concentrations as shown in Figures 8.4 and 8.5. For Spectral Doppler there was a significant increase in the gradient (MI 0.3 = 1.6, MI 0.5 = 2.6, MI 0.7 = 3.6) with particle concentration for increasing MI settings. For Power Doppler, the increase in gradient with increasing MI settings was small (MI 0.3 = 4.6, MI 0.5 = 4.1, MI 0.7 = 4.5, MI 0.9 = 3.2). The Power Doppler signal saturated faster at higher MI settings (0.7 and 0.9).

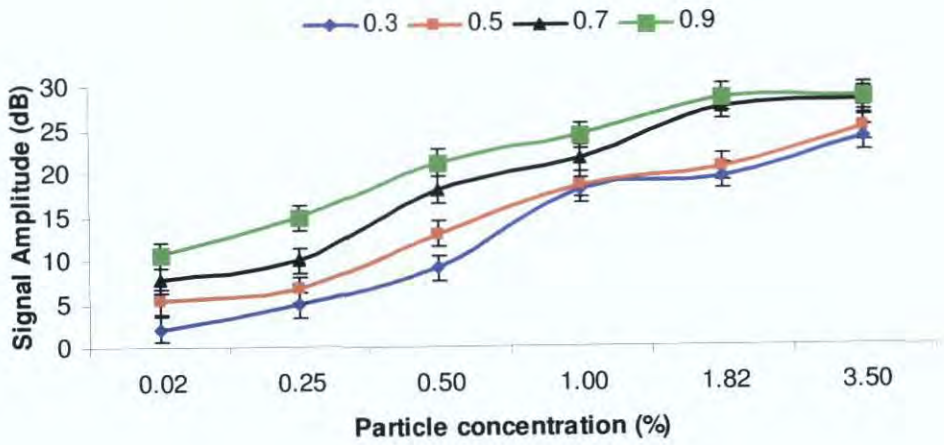

Figure 8.5 Effect of output power on Power Doppler signal amplitude for increasing particle concentrations

The effect of Doppler gain was investigated for Spectral and Power Doppler. At each particle concentration, two signal amplitude measurements for Doppler gain were taken. The first was at the baseline gain setting, which had been determined using the baseline concentration of 1.82%. The second setting was when the Doppler gain was adjusted in order to obtain a waveform free from saturation and noise at each particle concentration (using similar criteria as for the baseline setting). The effect of Doppler gain on the Doppler DR was investigated to verify if the level of increase in gain followed the same shape of the Doppler DR curve (baseline gain).

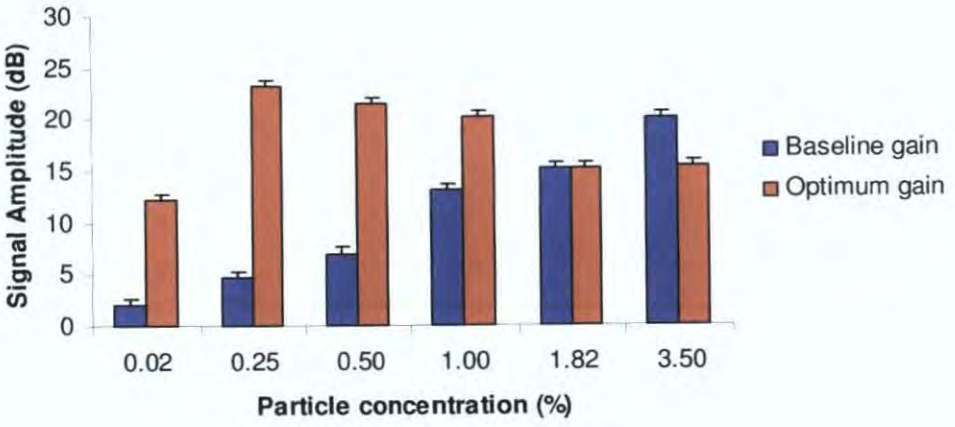

Figure 8.6 Effect of Doppler gain on Spectral Doppler signal amplitude for increasing particle concentrations

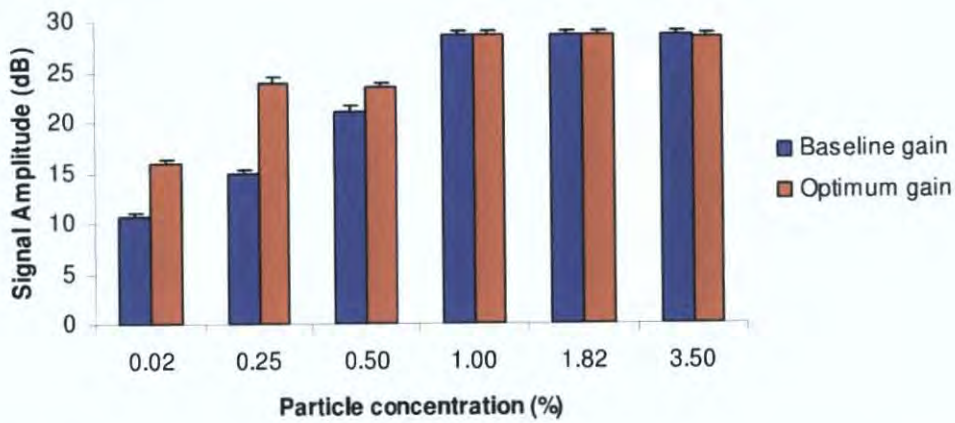

Figure 8.7 Effect of Doppler gain on Power Doppler signal amplitude for increasing particle concentrations

As Figure 8.6 illustrates, Doppler gain has a significant effect on Spectral Doppler signal amplitude measurements. The Power Doppler gain also has a significant effect on the signal amplitude measurements (Figure 8.7). For Power Doppler the gain reaches saturation faster than Spectral Doppler. For both gain settings, the maximum signal amplitude of 28.5 dB is reached at 1.0% particle concentration.

8.2.4 Discussion

A novel method for determining the dynamic range of Spectral and Power Doppler was devised. The effect of increasing particle concentration on Spectral Doppler was presented in Figure 8.6 and it was found that there was a linear relationship between peak-signal amplitude and particle concentrations up to a concentration of 1.00%. Since the data is still rising at both the beginning and end of the graph, this suggests that the minimum and maximum points have not been recorded. As a result a true calculation of the dynamic range has not been achieved. The results obtained for Spectral Doppler represent the minimum DR which was able to be measured which was found to be 18 ± 2 dB. For Power Doppler DR, the signal amplitude saturated for particle concentrations greater than 1.00%; again Doppler DR of 18 ± 2 dB was determined. In order to obtain a true measurement of the spectral Doppler DR the signal amplitude should be measured at 0% particle concentration and for concentrations higher than 3.50 % particle concentration until a plateau in the signal amplitude is observed, similar to that found for Power Doppler.

With increasing output power, the signal amplitude increases with increasing particle concentrations for both Spectral and Power Doppler. For Spectral Doppler, there was a significant difference between the three MI values 0.3, 0.5 and 0.7 for particle concentrations greater than 0.50%. As expected the highest MI value of 0.7 results in the highest signal amplitude at each concentration. A similar trend was observed for Power Doppler although for particle concentrations greater than 1.00% there was no significant difference in signal amplitudes for MI values 0.3 and 0.5 and also 0.7 and 0.9. Unlike Spectral Doppler, at particle concentration 3.50% the Power Doppler

appears to reach saturation at all the MI values. The effect of Doppler gain on the Doppler DR was investigated to verify if the level of increase in gain followed the same shape of the Doppler DR curve (baseline gain). A similar trend was observed for both Spectral and Power Doppler, with the Power Doppler reaching saturation faster than Spectral Doppler. For both Spectral and Power Doppler at the lowest particle concentration 0.02% the optimum gain was found to be significantly lower than the optimum gain settings found for the other particle concentrations. This was the maximum gain setting possible at this particle concentration without the signal being saturated with noise.

As discussed in the introduction, a Doppler ultrasound system used for imaging the renal system needs to have a high dynamic range. It needs to be able to clearly detect areas with slow flow in small vessels such as kidney perfusion and regions of stenosis where the dimensions of the vessels are very small as well as areas of high flow such as arteries and veins which supply blood to the kidney. The Doppler DR protocol was found to provide useful information regarding the performance of the C4-2 transducer of the HDI 3000. Using a clinical preset optimised for renal imaging, the dynamic range is sufficient to detect areas of slow flow (low scatterer volume, RBCs), (corresponding to the low particle concentrations) and also areas of high flow in larger arteries and veins (corresponding to the particle concentration greater than 1.82%). Although this is an effective method for determining the Doppler DR of systems, it is a time consuming procedure and would require BMF production facilities and an open circuit flow phantom. Therefore, this would not be an ideal Doppler DR test for routine use in hospitals. It would be better suited to ultrasound research laboratories or test laboratories which have the facilities to perform these tests.

8.3 *IN-VITRO* RENAL ARTERY PHANTOM CONTRAST ENHANCED FLOW MEASUREMENTS

8.3.1 Introduction

The diagnosis of RAS still relies on Spectral Doppler analysis as the main clinical tool in an US examination of the renal system as discussed in Chapter 1. It has been shown that the use of CEUS has the potential to improve the detection of RAS with CEUS Colour and Power Doppler (Correas et al., 2003; Correas et al., 2006; Drelich-Zbroja et al., 2004; Lencioni et al., 1999; Melany et al., 1999). However despite this demonstrated improvement to clinical diagnosis, many ultrasound scanners still do not have Spectral Doppler available with contrast specific imaging. In this study Spectral Doppler was used in conjunction with 2D harmonic imaging. The effect of contrast enhanced Spectral Doppler on the accurate determination of maximum velocity measurements using anatomically realistic renal artery flow phantoms with varying degrees of stenosis was investigated.

Several studies have examined the effect of UCAs on Spectral Doppler measurements both *in-vitro* and *in-vivo* but with conflicting results (Basseau et al., 2000; Forsberg et al., 1994; Gutberlet et al., 1998; Liepsch et al., 2004; Melany et al., 1999; Petrick et al., 1997; Yokoyama et al., 2003). There is still controversy about whether UCAs produce an increase in the detected velocity. Forsberg et al., (1994), Basseau et al., (2000) and Yokoyama et al., (2003) reported an increase in the maximum Doppler shift of 5 - 45%, with the Doppler gain not adjusted after the administration of the UCA. In studies by

Petrick et al., (1997), Gutberlet et al., (1998) and Melany et al., (1999) the UCA Levovist (Schering, Berlin, Germany) which was evaluated did not produce a statistically significant increase in the peak velocity when the Doppler gain was adjusted after the administration of the contrast agent. The main concern is that the increase in Doppler shift by the UCA may produce an overestimation of flow velocities in clinical practise and that this may lead to misdiagnosis of patient with stenosis and ultimately mismanagement of the patient.

8.3.2 Methodology

Contrast enhanced flow measurements were performed using the range of anatomically realistic renal artery flow phantoms with varying degrees of stenosis (both wall-less and walled) developed as part of this project and described in Chapter 3. The ultrasound scanner used for the following investigation was the HDI 3000 with a curvilinear broadband transducer C4-2 (nominal frequency 2.5 MHz). The IEC recommended BMF developed by Ramnarine et al., (1998) was used in all flow investigations. The computer controller described in Chapter 3 was set to output a steady velocity of 26 cm s^{-1}.

The transducer was positioned longitudinally over the vessel at the ROI (site of stenosis), and held in place using a retort stand and clamp. The contrast specific mode 2D Harmonic was enabled and the image was optimised by placing the focal zone at the depth of interest in the phantom and the TGC controls were optimised to produce a uniform image. Spectral Doppler was turned on and a sample volume of 1 mm was position in the centre of the stenosis (approx at a depth of 4.5 cm from the surface of phantom). The following settings were used throughout the study. The velocity scale

was adjusted so that the maximum flow velocity was no greater than 75% of the maximum Spectral display to minimise the effect of Doppler aliasing; the wall filter was set to the lowest setting. The Doppler angle was aligned with the vessel wall to 60°. The mechanical index was set to 0.2. The Doppler gain was adjusted in order to obtain a well-defined Doppler waveform which was free from extraneous noise.

One vial of Luminity® was prepared as described in section 7.2.2. The required amount of 0.1 ml was withdrawn from the vial using a needle and syringe and diluted in 5 ml of saline. The syringe containing the UCA and saline was attached to a three way tap in the flow circuit located 30 cm upstream from the site of insonation. Care was taken when introducing the contrast agent, to avoid introducing air into the BMF. The three way tap remained open until all the contrast agent had washed out and the measurements were completed. The BMF containing the contrast agent was not recirculated in the flow circuit.

Images were saved before the administration of the UCA and then at 2, 10, 30 and 60 s after the injection of the UCA. From these images, the maximum and minimum velocity was manually estimated by positioning the cursor at the maximum and minimum positions in the spectra, and an average of five measurements were taken.

8.3.3 Results

Enhancement of the Spectral Doppler waveform was observed after a bolus injection of 0.1ml Luminity® in 5ml of saline as shown in Figure 8.8 (b) for the walled renal artery flow phantom with 50% stenosis present. Figure 8.8(d) clearly shows a significant improvement in the visualisation of the renal artery lumen at the site of the 70%

stenosis. By using the CSI mode 2D harmonic imaging the exact shape of the stenosis could be visualised clearly and thus aid the positioning of the Spectral Doppler sample volume.

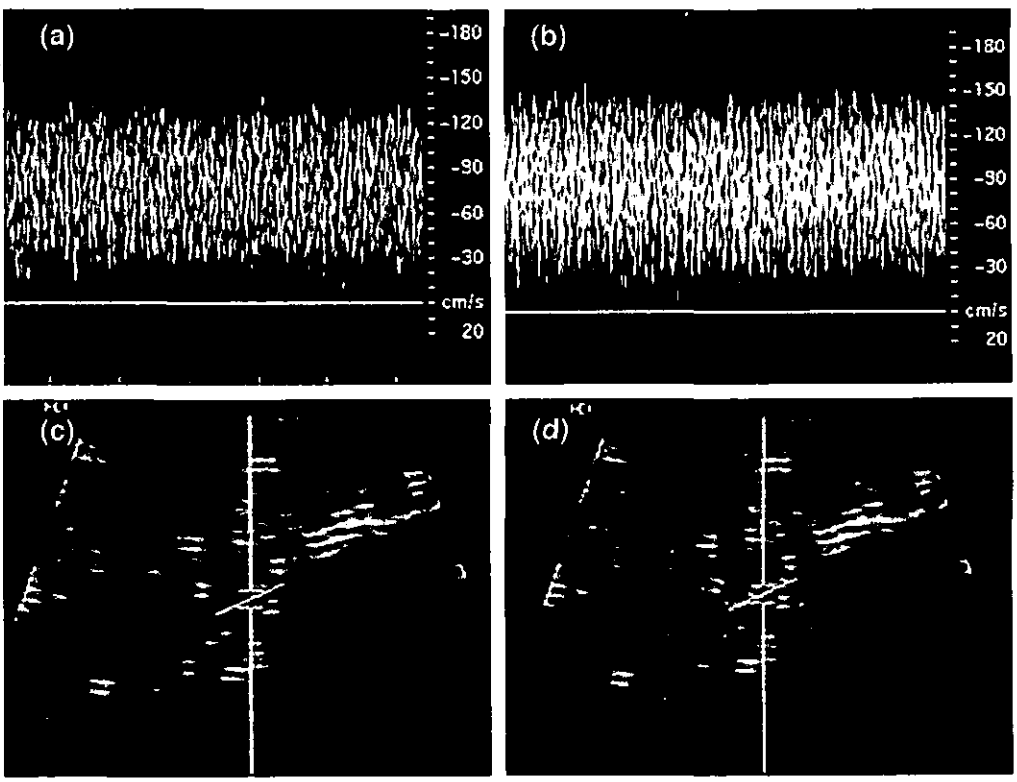

Figure 8.8 Walled renal artery stenosis with 50% stenosis, (a) Spectral Doppler waveform before UCA bolus injection, (b) Spectral Doppler waveform after UCA injection, (c) vessel lumen before UCA bolus injection, (d) vessel lumen after UCA bolus injection.

The maximum and minimum velocities were measured before the bolus injection of Luminity® and again at the following time intervals after the injection; 2, 10, 30 and 60 seconds. Presented in Table 8.2 are the velocity measurements at the site of stenosis for the walled (normal artery, 30%, 50%, 70% and 85% stenosis) renal artery phantoms pre-contrast and at the maximum enhancement after the contrast was introduced.

Table 8.2 Doppler measurements pre- and post UCA injection for 0% stenosis (walled) where ΔV ≈ post-contrast velocity – pre-contrast velocity and ΔV% = (post-contrast velocity – pre-contrast velocity)/ pre- contrast velocity x 100

0% stenosis	**Pre-contrast**	**Max enhancement**	**ΔV**	**ΔV %**
V_{Max} (cm s^{-1})	48 ± 1	92 ± 3	44 ± 2	91 ± 5.0
V_{Min} (cm s^{-1})	13 ± 1	3 ± 1	-9 ± 2	-74 ± 10.0
V_{Spread} (cm s^{-1})	36	89	53	149
30% stenosis				
V_{Max} (cm s^{-1})	78 ± 8	90 ± 1	12 ± 8	15 ± 14
V_{Min} (cm s^{-1})	7 ± 1	5 ± 1	-1 ± 2	-19 ± 36
V_{Spread} (cm s^{-1})	71	84	13	19
50% stenosis				
V_{Max} (cm s^{-1})	131 ± 3	170 ± 2	39 ± 8	30 ± 3
V_{Min} (cm s^{-1})	24 ± 4	6 ± 3	-18 ± 4	-75 ± 5
V_{Spread} (cm s^{-1})	108	164	56	52
70% stenosis				
V_{Max} (cm s^{-1})	235 ± 3	266 ± 3	31 ± 5	13 ± 2
V_{Min} (cm s^{-1})	135 ± 5	98 ± 7	-37 ± 15	-27 ± 10
V_{Spread} (cm s^{-1})	100	168	68	68
85% stenosis				
V_{Max} (cm s^{-1})	117 ± 5	195 ± 4	78 ± 7	67 ± 8
V_{Min} (cm s^{-1})	37 ± 9	50 ± 5	13 ± 9	36 ± 15
V_{Spread} (cm s^{-1})	81	145	64	80

The measured maximum velocity (V_{max}) and minimum velocity (V_{min}), and calculated spread of the velocity spectrum, ($V_{spread} = V_{max} - V_{min}$) are shown in each table. In addition, the following were calculated for each of the parameters: ΔV = post-contrast velocity – pre-contrast velocity and ΔV% = (post-contrast velocity – pre-contrast velocity)/ pre-contrast velocity x 100 were also calculated. The full sets of data are

given in Appendix C. These results show that the introduction of the UCA Luminity does have a significant effect on the velocities measured, with the maximum velocity increasing and the minimum velocity decreasing.

8.3.4.Discussion

From the *in-vitro* renal artery phantom contrast enhanced flow measurements, it was determined that the UCA resulted in significant changes in the measured Doppler velocity from pre-contrast to post-contrast. The signal amplitude of the Spectral trace was not measured as the focus was on the actual velocity measurements that are used to grade RAS. Here the gain remained unchanged for the duration of the contrast enhancement. These findings are similar to those of Basseau et al., (2000) and Yokoyama et al., (2003) where bolus injection of UCA produced significant increases in the Doppler velocity. The measured velocities from a Spectral Doppler waveform are highly dependent on the strength of the Doppler signal itself and on the setting of the Doppler gain of the system (Basseau et al., 2000). As in this study when the gain is not adjusted, the increase in the Doppler frequency shift is artificial, due to the increase in amplification of frequencies with low amplitude. In a clinical situation the gain would be altered throughout the study to obtain the optimum setting. The gain was not altered during the study to reduce the number of variables in the experiments and it allowed the pre-contrast measurements to be directly compared to the post-contrast measurements. In this study the Doppler Spectral waveform was clearly visible before the UCA was introduced. This did not replicate the *in-vivo* situation where the use of UCAs is required due to the poor visualisation of the vessels in the abdomen, where the Doppler signal is often weak and cannot be distinguished from noise. Therefore the peak

Doppler signal might be detectable only with the use of UCAs to enhance the echogenicity of the blood (Gutberlet et al., 1998). If a fat mimicking material which was similar in composition to subcutaneous fat was used, a result similar to Petrick et al., (1997) may be obtained where the UCA did not significantly increase in the peak velocity.

It was found that Spectral Doppler gate placement accuracy and angle correction were improved with better vessel delineation. The CSI mode allowed the visualisation of the microbubbles in the renal artery lumen and the exact shape of the stenosis could be identified clearly. The ability to improve the Spectral Doppler signal by better vessel visualisation is important clinically not only for the main renal arteries but also in the segmental intrarenal arteries as this decreases the number of inadequate Doppler studies (Claudon et al., 2000; Correas et al., 2006).

8.4 EFFECT OF CARRIER FLUIDS ON TIME INTENSITY CURVE PARAMETERS

8.4.1 Introduction

In order to develop new contrast specific imaging techniques and contrast agents, it is important to have an *in-vitro* setup to perform studies under controlled and stable conditions. To date the majority of these investigations involving the characterisation of UCAs have been performed using either water or saline as the carrier fluid (Claassen et al., 2001; Hindle and Perkins, 1994; Lohmaier et al., 2004; Meyer-Wiethee t al., 2005; Ugolini et al., 2000). However, clinically the UCA is injected into the blood stream which has different flow properties to water or saline. Blood is not a simple fluid; it is a non Newtonian, inhomogeneous fluid consisting of a suspension of red blood cells in plasma. In non Newtonian fluids, viscosity has strong dependence on shear rate. Blood is generally accepted to assume Newtonian behaviour in vessels larger than 100- 200μm (Nichols and O'Rourke, 1990).

Since the Doppler signal from blood arises from the moving red blood cells (RBC), the fluid used in perfusion experiments should contain scattering particles. The approximate diameter of a RBC is 5 μm and so the particles used in the BMF are chosen to be approximately the same size. Rayleigh scattering is a phenomenon which is associated with the scattering by particles which are much smaller than the wavelength of the ultrasound wave. In an attempt to reproduce the clinical situation, a BMF incorporating Orgasol® scatterers which replicates the red blood cells and dextran to reproduce the viscosity of blood, was used (Ramnarine et al., et al., 1998). The relevant

properties of blood, water, saline and BMF are shown in Table 8.3. The time intensity curve (TIC) parameters obtained using the two different carrier fluids; water and blood mimicking fluid (BMF) with the UCA Luminity® were compared.

Table 8.3 Properties of carrier fluids

Fluid Type	Density ($g\ cm^{-3}$)	Viscosity (mPas)	pH	Scatterers present
Blood	1.053	4.0	7.4	Yes
BMF	1.037	4.1	7.0	Yes
Water	1.000	1.0	7.0	No
Saline	1.068	~ 1.0	7.0	No

In this study three experimental set-ups were investigated. The first acted as a reference measurement, and is the set-up most commonly used for in *in-vitro* contrast agent studies (kidney capillary phantom filled with water, in a water tank and water as the carrier fluid). This is a non-physiological set-up and does not take in to account the acoustic properties of the carrier fluid used. In the second and third set-up BMF and TMM were used to increase the physiological relevance of the measurements. The TICs were compared from the three set-ups to determine the importance of the carrier fluid and presence of an attenuating medium.

8.4.2 Methodology

The kidney capillary phantom described in section 7.2.1 was used to compare TIC parameters obtained using the two different carrier fluids, water and BMF with the UCA Luminity®. Furthermore, the effect of the surrounding attenuating medium on the TIC parameters was also investigated. The experimental set-up was carried out in both a

non-attenuating medium (water) and an attenuating medium (liquid TMM) (Madsen et al., 1998).

A modified Sonos 5500 ultrasound scanner (Philips, Amsterdam, Netherlands) and phased array transducer (S3) were used to acquire the RF data from the region of interest in the filter following a bolus injection of Luminity® (0.1ml of Luminity® per 5ml of saline). The instrument settings used in these experiments are presented in Table 8.4. Measurements were performed at a flow rate of 200ml min^{-1} using degassed water and a BMF as the carrier fluids. The measurements were performed in a plastic tank (80 x 40 x 15 cm). A rubber mat was used to line the bottom of the tank in order to reduce reverberation artefacts from the bottom of the tank. Measurements were taken with and without an attenuating medium surrounding the kidney perfusion phantom.

Table 8.4 Settings used for the Sonos 5500 ultrasound system

Machine type	Modified Sonus 5500 with S3 phased array transducer
Frequency	1.5 MHz
Mechanical index	0.3
Frame rate	67 Hz
Gain	100%
Compression	100%
Depth	8 cm
Region of Interest	4-5 cm
Focus position	6 cm
Mode	2D Conventional

Figure 8.9 is a schematic diagram showing the location of the carrier fluid, filter medium and surrounding medium. The three experimental set-ups used are given in Table 8.5. The first acted as a reference measurement, and is the set-up most commonly used for in *in-vitro* contrast agent studies (kidney capillary phantom filled with water, in a water tank and water as the carrier fluid). In the second set-up the cavity space surrounding the capillaries in the phantom was filled with liquid TMM. For the third set-up, TMM was surrounding the capillaries in the phantom and submerged in liquid TMM.

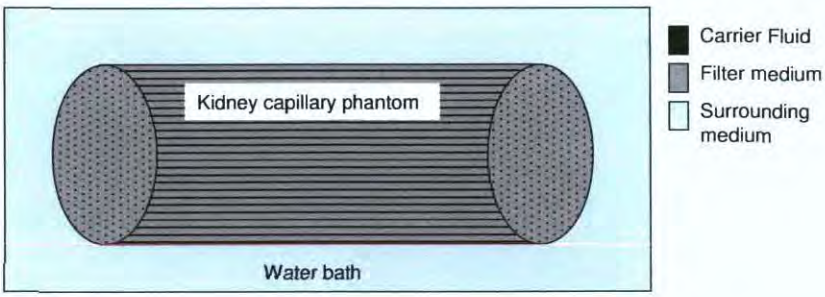

Figure 8.9 Schematic of the location of the carrier fluid, filter medium and surround medium

Table 8.5 Experimental set-ups used the carrier fluid, filter medium and surrounding medium

Set-up	Surrounding medium	Filter medium	Carrier fluid
1	Water	Water	Water
2	Water	TMM	(a) Water (b) BMF
3	TMM	TMM	(a) Water (b) BMF

The RF data were analysed using a MATLAB program developed in-house in Edinburgh. The data were converted and log compressed to yield images almost identical to those displayed on the scanner. This allowed accurate positioning of the 3 ROIs in the inlet, filter and outlet. The following parameters were determined from this region of interest; (a) delay, (b) time to peak, (c) peak signal amplitude, (d) AUC and (e) MTT.

8.4.3 Results

Presented in the following Figures 8.10 - 8.14 are the effect of different carrier fluids on the TIC parameters; (a) delay, (b) time to peak, (c) peak signal amplitude, (d) AUC and (e) MMT. In the Table 8.6 the different colour codes used to describe the carrier and filter mediums is shown.

Table 8.6 Colours codes used in results referring to the carrier fluid and filter medium used

Legend			
Carrier fluid	Water	Water	BMF
Filter medium	Water	TMM	TMM
Surrounding Medium	Water	Water or TMM	Water or TMM

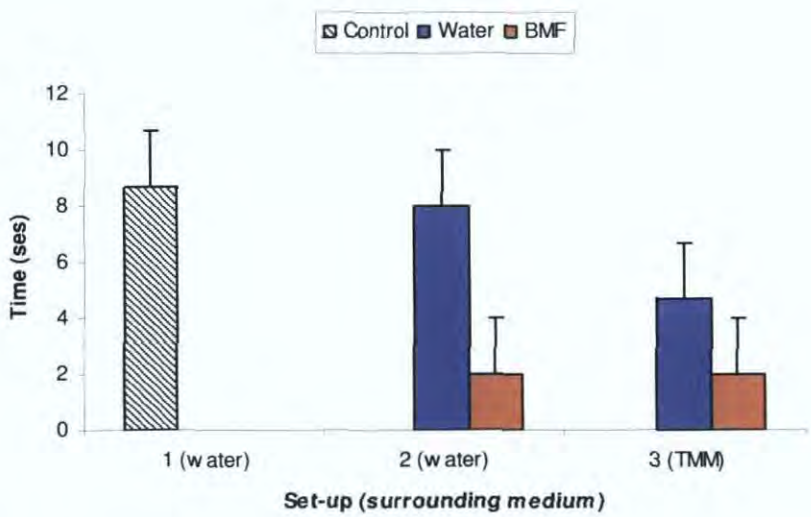

Figure 8.10 Delay time from injection to appearance of contrast in ROI, legend shows varying carrier fluid

Figure 8.10 shows that when BMF was used as a carrier fluid there was a significantly shorter delay time than when water was used for both set-ups 2 and 3. This may be due to the composition of the BMF which has a viscosity of 4.1 mPa s. This is closer to blood (4.0 mPa s), which is roughly four times greater than water. The first appearance of Luminity® occurred after 2 seconds using BMF compared to between 4 and 8 seconds when water was used as the carrier fluid. This longer time may be due to flotation of the bubbles in the water, which did not occur in the BMF. With BMF as the carrier fluid, its viscosity and the presence of the scatters may prevent floatation and aggregation of the UCA to the top of the vessel, therefore resulting in a lower delay time compared to water. Another possible reason may be due to the fact that the TMM is attenuating, such that the early part of the TIC cannot be visualised.

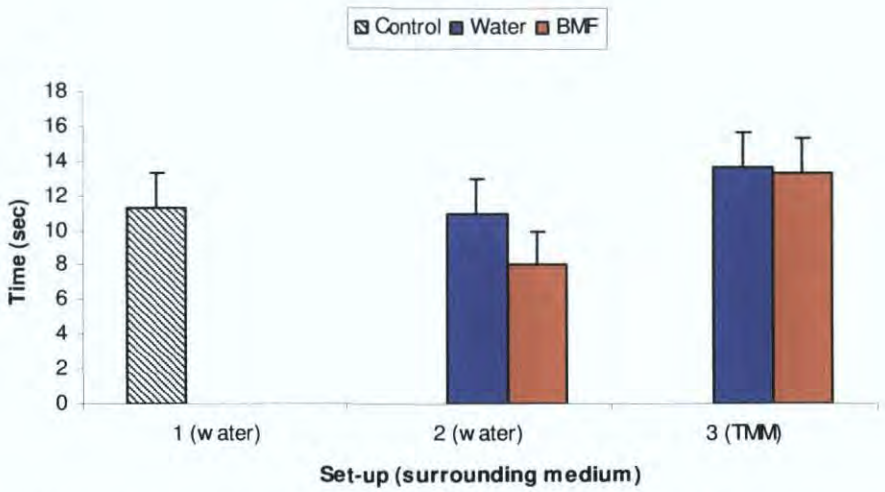

Figure 8.11 Time to peak, time from appearance of contrast in ROI to peak contrast effect, with legend showing varying carrier fluid

For the measurement conducted in the water bath for both carrier fluids the time for the contrast to peak was between 8 and 11 seconds (set-up 1 and 2). When the phantoms were submerged in TMM (set-up 3), this time increased to 14 seconds as shown in Figure 8.11. Again this may be due to the fact that the TMM is attenuating causing the

early part of the TIC not to be visualised as easily as compared to a non-attenuating medium like water.

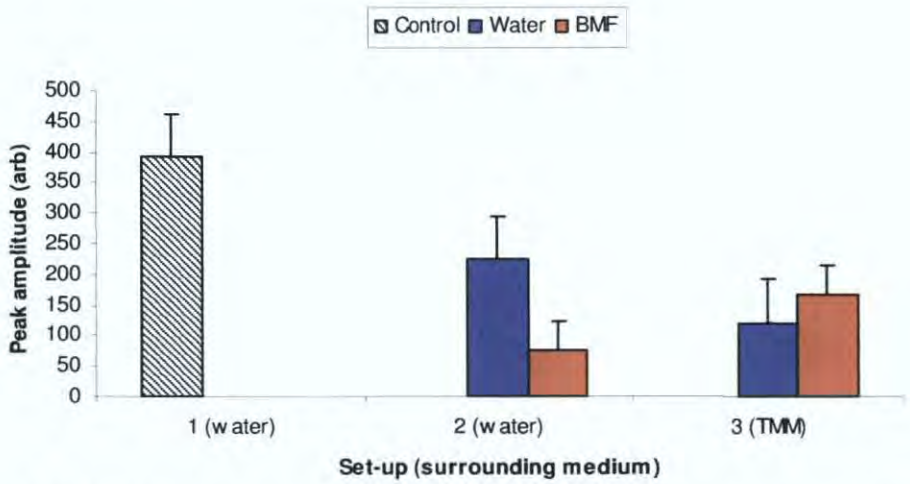

Figure 8.12 Peak amplitude of contrast effect in ROI, with legend showing varying carrier fluid

The peak amplitude for Luminity® with degassed water as a carrier fluid, in both set-ups 1 and 2 were significantly higher than when BMF was used in set-up 2, as shown in Figure 8.12. With set-up 3, there was no significant difference in the peak amplitude of the contrast agent between the two carrier fluids; this may be due to the attenuation from the TMM surrounding the filter leading to lower enhancement from the contrast agents.

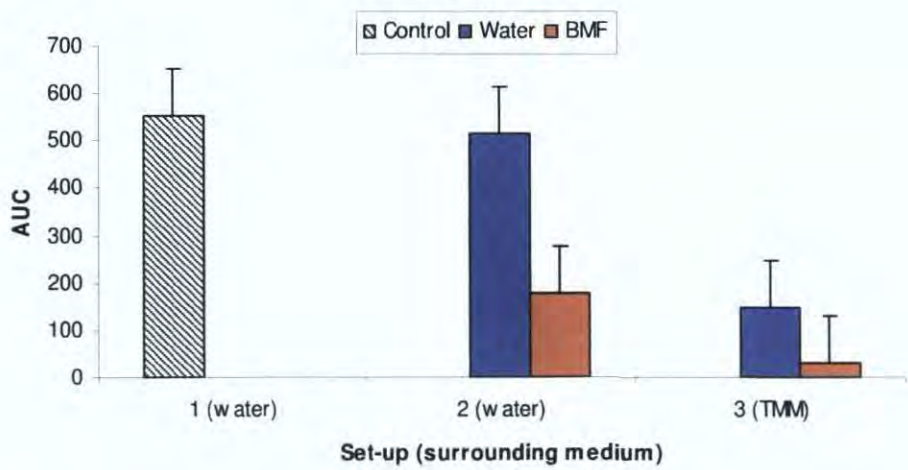

Figure 8.13 AUC, directly related to the carrier fluid volume, with legend showing varying carrier fluid

For measurements using water as the carrier fluid (set-ups 1 and 2), the AUC was significantly higher than with BMF used as the carrier fluid (set-up 2 and 3). With set-up 3, both carrier fluids had a significantly lower AUC than in set-ups 1 and 2 (Figure 8.13), once again this may be due to the attenuating effect of the TMM.

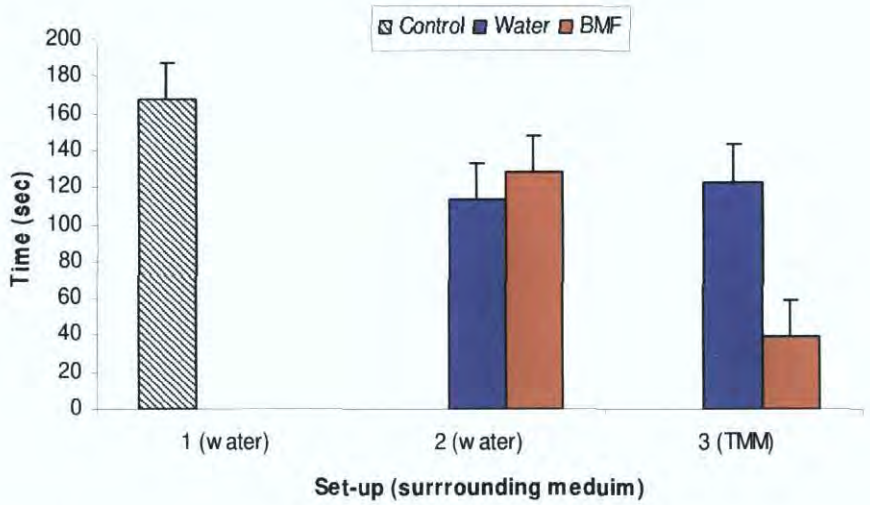

Figure 8.14 MTT, time for the entire carrier fluid volume to pass through the ROI, with legend showing varying carrier fluid

The MTT for Luminity® in BMF in set-up 3 had a significantly shorter MMT than the other measurements (Figure 8.14). This was the most attenuating set-up, with the TMM surrounding both the capillaries and the filter and BMF running though system and as the carrier fluid. Since the lowest AUC was obtained for this set-up therefore the MTT will also be shorter.

8.4.4 Discussion

As discussed in the section 8.4.1, previous studies characterising UCAs obtained using water may not be reflective of the clinical situation. The composition of the carrier fluid

influences the effect of the ultrasound contrast agent. When BMF was used as a carrier fluid there was a significantly shorter delay time than when water was used. This may be due to the composition of the BMF (viscosity and density), as shown in Figure 8.10. The first appearance of Luminity® occurred after 2 seconds using BMF compared to between 4 and 8 seconds when water was used as a carrier fluid. These results demonstrate that the carrier fluid has a significant effect on TIC parameters obtained in contrast enhanced perfusion measurements. The peak amplitude of Luminity® with degassed water as a carrier fluid, in both set-ups 1 and 2 was significantly higher than when BMF was used in set-up 2, as shown in Figure 8.11. A MI of 0.3 was used in these studies. Such a mechanical index may have caused the microbubbles to collapse releasing gas into the surrounding medium. With set-up 3, there was no significant difference in the peak amplitude of the contrast agent between the two carrier fluids; this may be due to the attenuation from the TMM (0.5 dB cm^{-1} MHz^{-1}) surrounding the filter leading to lower enhancement from the contrast agents.

A previous study by Lazewatsky et al., (1995) investigated the difference between *in-vitro* behaviour of Definity® (renamed Luminity®) under ultrasound exposure in a saline dilution and in blood. The study indicated that the effect of the UCA lasted significantly longer in blood than in saline under ultrasound exposure. The study was conducted under static conditions and the effect of flow and small vessels were not considered. Here a perfusion phantom was used to replicate contrast enhanced perfusion in the kidney. Furthermore, the presence of a tissue-mimicking material resulted in a decrease in the peak amplitude of the contrast agent which may be due to attenuation. This is an important feature in Doppler flow phantoms and should be considered for contrast enhanced perfusion measurements. Potential further work in

this area could involve a comparative study of the effect of blood and BMF on the TICs for Luminity® and the investigation of the effect of different carrier fluids on Harmonic Power Doppler. As evident from the results obtained, the effect of the carrier fluid is complex and is due to a combination of many factors, such as the properties of the carrier fluid, the UCA used and the acoustic properties of the phantom. Further in depth studies are required to fully understand this situation. BMF was chosen as the carrier fluid for the contrast enhanced perfusion studies using the kidney capillary phantom. Although this carrier fluid does not mimic non Newtonian behaviour it gives the best representation of the *in-vivo* situation.

8.5 *IN-VITRO* CONTRAST ENHANCED KIDNEY PERFUSION PHANTOM STUDY

8.5.1 Introduction

Ultrasound contrast agents offer the potential to detect perfusion within the kidney. Thereby, UCAs offer the potential to detect abnormal microvascular and macrovascular disorders of the kidney (Correas et al., 2006). To determine the accuracy of the UCAs in the detection of these disorders of the kidney an objective evaluation of the technique should be carried out either by a clinical trial or *in-vitro* experimentation. As discussed in Chapter 1 *in-vitro* experimentation can be used effectively to determine the potential of new techniques without the associated ethical issues and substantial cost. It is important that the *in-vitro* kidney perfusion phantoms replicate the *in-vivo* situation as closely as possible, in particular that they achieve blood flow similar to that found *in-vivo*. After a bolus injection of UCA into the blood, the concentration of the agent can be monitored as a function of time. TICs are often plotted for the uptake and clearance of a contrast agent. The signal enhancement effect of the contrast agent can be used to monitor concentration of the UCA and to make quantitative measurements. The typical parameters which can be used to assess perfusion are, (Claassen et al., 2001; Li et al., 2002; Li. et al., 2003; Yeh et al., 2003):

a) The delay, the time from the injection of the UCA to the first sign of its appearance at the site of interest
b) Time to peak, the time from the appearance of the UCA to the peak contrast
c) The peak signal amplitude, the maximum signal amplitude obtained from the injected dose (this is the maximum on the curve)

d) AUC is the area under the curve that indicates the perfused blood mimic volume

e) The MTT, mean transit time, represents the time it takes for the entire fluid volume to pass through the perfused area

Using these parameters it has been shown that the AUC is directly related to the perfusion blood volume (Claassen et al, 2001). Furthermore, with significant renal artery stenosis, the peak enhancement is delayed and reduced (Lencioni et al. 1999). Figure 8.15 shows the TICs from 3 regions of a human clinical kidney study over a period of 60s. From these TICs the following parameters were determined: delay, time to peak and peak signal amplitude and are tabulated in Table 8.7. The aim of this study is to achieve TICs similar to that found *in-vivo* to determine which contrast specific imaging mode (2D Harmonic or Harmonic Power Doppler imaging) is suitable to detect perfusion similar to that found in the kidney.

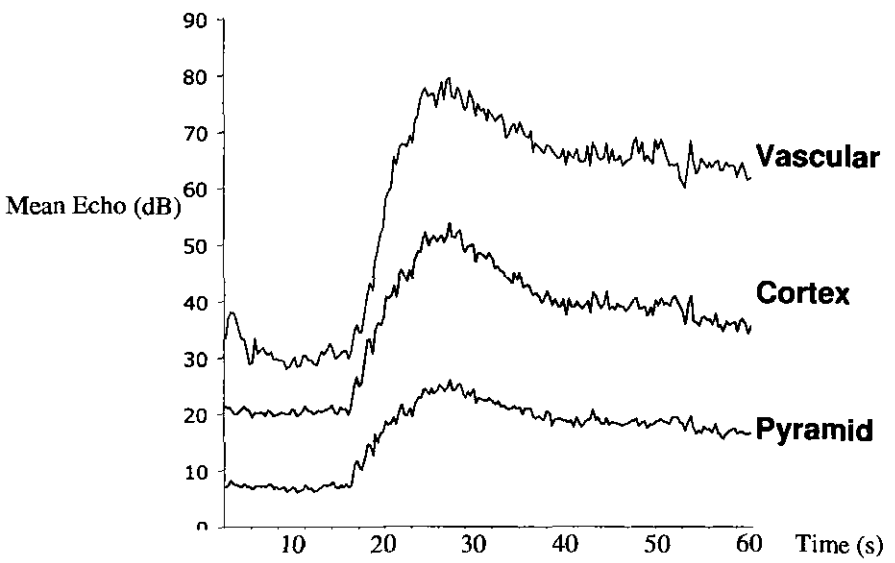

Figure 8.15 TICs from three regions of the kidney using the contrast agent SonoVue courtesy of Baxter G, BMUS Contrast Study Day 2007

Table 8.7 TIC parameters of a perfused kidney determine from Figure 8.1

TIC Parameters	Pyramid	Cortex	Vascular
Delay (s)	13.2	12.9	12.9
Time to peak (s)	10.2	12.6	11.7
Peak signal amplitude (dB)	25	54	80

8.5.2 Methodology

The kidney capillary perfusion phantom was used to determine which contrast specific imaging mode (2D Harmonic or Power Doppler Harmonic imaging) was most suitable for evaluating perfusion similar to that found in the kidney. The HDI 3000 US scanner was used with broadband curved array transducer (C4-2) at a nominal frequency of 2.5 MHz. The measurements were performed in a plastic tank (80 x 40 x 15 cm) filled with degassed water. A rubber mat was placed at the bottom of the tank in order to reduce reverberation artefacts. A schematic diagram of the experimental set-up is shown in Figure 8.16. The transducer was placed 2.5cm above the dialysis filter. A transverse view of the 3 regions of interest (ROI) was obtained for the 2 CSI modes: 2D Harmonic and Harmonic Power Doppler as shown previously in Figure 7.7.

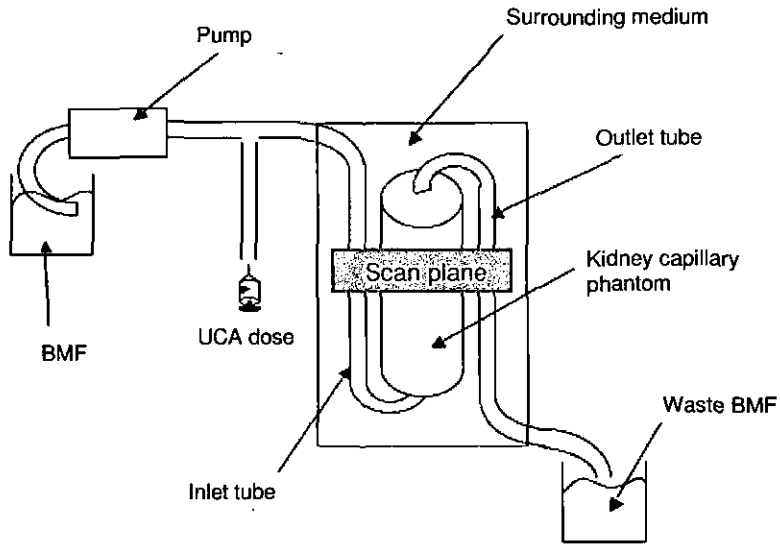

Figure 8.16 Experimental set-up for kidney perfusion study

The settings used in this study are shown in Table 8.8. For the Harmonic Power Doppler mode the size of the Power Doppler box was adjusted to encompass the 2 vessels and the dialysis filter. The flow rate was set to 750ml min^{-1}, a rate consistent with that in the renal artery and kidney. A series of 5 experiments were carried out in order to determine the repeatability of the measurements.

Table 8.8 US machine parameters for contrast enhanced perfusion studies

Control	Setting
MI	0.15
PRF	1000 Hz
Focus position	Below ROI
Frame rate	High
Wall filter	Low

An offline frame grabber (Picport Colour, Luetron Vision, Switzerland) was used to capture a video at a constant frame rate of 5 frames per second starting 5 seconds before a bolus of Luminity® (0.1ml in 5 ml of saline injected over 1 second) and continuing

recording for a further 3 minutes. All of the images captured were 768 x 576 [pixel]^2 with a 24-bit depth resolution (true colour). The resulting video was analysed in MATLAB. Before the TIC analysis was carried out on the series of images, a background subtraction was performed. The average of the first 5 frames without any UCA was subtracted from the mean signal amplitude of the subsequent frames with UCA. Three regions of interest were selected, (1) inlet vessel (circle ROI diameter 4 mm), (2) outlet vessel (circle ROI 4 mm diameter), (3) perfused area in dialysis filter (ellipse 24 x 12 mm) located near the top of the filter to exclude attenuation artefacts that occurred in deeper regions of the model. Figure 8.17 shows the placement of these three ROIs.

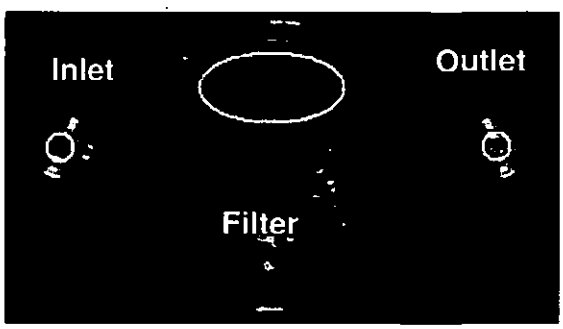

Figure 8.17 2D Harmonic image showing the placement of the 3 ROIs, inlet vessel, perfused area in dialysis filter and outlet vessel

The mean of the signal amplitude for each of the ROIs was computed and TICs were constructed for each sequence. From indicator-dilution theory the time variation of the UCA concentration in a ROI can be modelled as a gamma curve (Yeh et al., 2003). This allows the AUC and MTT to be calculated. The TICs were fitted to a gamma function defined as:

$$g(t) = \alpha(t - t_o)^{\gamma} e^{-\beta(t-t_0)} \qquad \textbf{Equation 8.1}$$

where γ, α, & β are parameters and t_o = the delay. The correlation coefficients between the original TICs and the fitted gamma function had to be higher than 0.9 to be accepted indicating that the gamma curve fits well with the experimental data. It also indicates that the flow model could be accurately described by indicator-dilution theory. For this study the following parameters were calculated from the gamma-corrected TICs; (a) delay, (b) time to peak, (c) peak signal amplitude, (d) AUC and (e) MTT.

The ratio of the inlet and outlet AUC should be approximately 1, indicating that all the injected UCA passed though the filter and was not absorbed by the phantom or made to collapse by the ultrasound. The AUC is defined as:

$$AUC = \int_0^\infty g(t)dt. \qquad \textbf{Equation 8.2}$$

where g(t) is defined in Equation 8.1. The mean transit time represents the time it takes for the entire fluid volume to pass through the perfused area. The MTT is defined as:

$$MTT = \int_0^\infty t.g(t)dt \Big/ \int_0^\infty g(t) \qquad \textbf{Equation 8.3}$$

According to the indicator-dilution theory there is an inverse relation between the flow rate and the MTT (Yeh et al., 2003) as shown here;

$$MTT = V/Q \qquad \textbf{Equation 8.4}$$

where V is volume and Q is the flow rate. TICs were plotted for each ROI using the data saved in the Excel file and the five parameters were calculated. The TIC parameters for each of the 2 CSI modes were then compared to determine which mode was more suitable in the detection of perfusion similar to that found in the kidney.

8.5.3 Results

Contrast enhanced perfusion studies were performed using the kidney capillary phantom at flow rates similar to that found in the kidney. Figure 8.18 shows a TIC obtained after a bolus injection of Luminity® was introduced. Three TICs are plotted for the inlet, filter and outlet vessel.

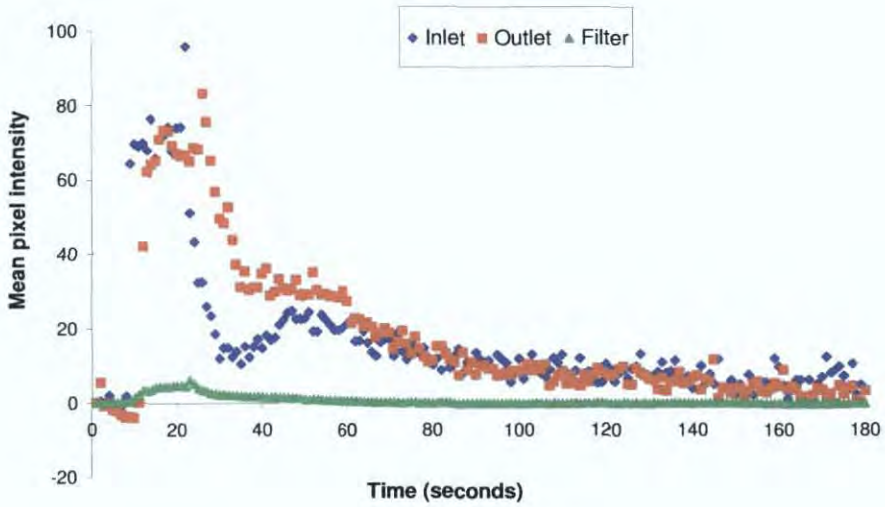

Figure 8.18 TIC of subtracted data using kidney perfusion phantom for flow rate 750ml min^{-1}

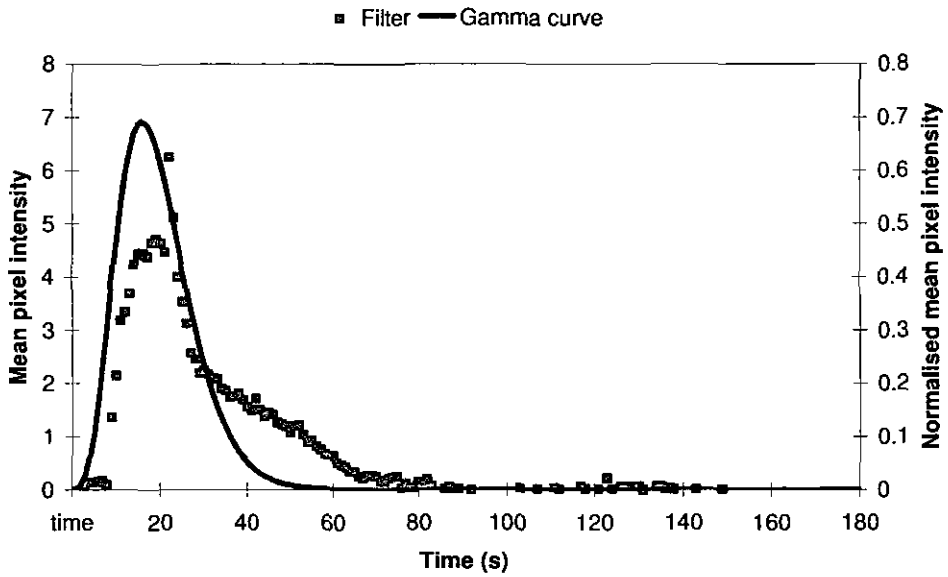

Figure 8.19 TIC and normalised TIC for filter from kidney perfusion phantom for flow rate of 750ml min^{-1}

Figure 8.19 the TIC and normalised gamma fitted function of the TIC for the filter. In Tables 8.9 and 8.10 the parameters calculated for the normalised gamma fitted functions for both the 2D harmonic imaging and Harmonic Power Doppler imaging are presented.

Table 8.9 2D Harmonic TIC parameters using kidney perfusion phantom

	Inlet	**Filter**	**Outlet**
Delay (s)	2.0 ± 0.3	2.5 ± 0.4	3.8 ± 1.5
Time to peak (s)	19.0 ± 2.5	21.0 ± 2.0	23.0 ± 2.8
Peak signal amplitude (arb units)	95.8 ± 0.4	6.2 ± 26.5	83.1 ± 0.1
AUC	150 .7± 17.9	105.9 ± 11.4	193.5 ± 17.9
MTT (s)	11.9 ± 2.0	20.8 ± 3.2	25.2 ± 0.7

Table 8.10 Harmonic Power Doppler TIC parameters using kidney perfusion phantom

	Inlet	*Filter*	*Outlet*
Delay (s)	2.5 ± 0.3	3.5 ± 0.4	4.8 ± 1.5
Time to peak (s)	7.6 ± 2.5	10.3 ± 2.0	11.2 ± 2.8
Peak signal amplitude (arb units)	254.8 ± 0.4	101.6 ± 26.5	255.0 ± 0.1
AUC	193.7 ± 19.6	-	240.2 ± 18.5
MTT (s)	69.8 ± 27.0	-	69.1 ± 48.7

As shown in section 8.5.2 there is an inverse relation between the flow rate and the MTT. Also the AUC has been shown to be directly related to the perfusion volume. The calculated values for the AUC and MTT for both imaging modes can be used to estimate the flow rate of the system. Comparing this to the actual flow rate can give an estimation of the errors associated with each imaging mode. Note that for the filter using Harmonic Power Doppler mode the gamma fitted functions had a correlation coefficient lower than 0.9 which indicated that the flow model cannot be accurately described by indicator-dilution theory. Therefore, the MTT and AUC could not be calculated from the filter in this case. Using the Equation 8.5 the flow rate Q was estimated from the 2D harmonic data and the Harmonic Power Doppler data, the calculated flow rates are presented in Table 8.11.

$$Q = AUC/MTT \qquad \textbf{Equation 8.5}$$

Table 8.11 Comparison of 2D harmonic greyscale and harmonic Power Doppler imaging

CSI Modes	**Calculated flow rate (ml min^{-1})**			**Actual flow rate**
	Inlet	**Filter**	**Outlet**	**(ml min^{-1})**
2D Harm	760	304	461	750
Power Harm	167	-	209	750

8.5.4 Discussion

The aim of this experiment was to determine which contrast specific imaging mode was most suitable for detecting kidney perfusion. Both the inlet and outlet TIC in Figure 8.18 show a second peak at approximately 50 s. This may be due to the adherence of some bubbles temporarily to the inner surface of the tubing. Therefore these bubbles arrived later to the insonifaction site than the initial bolus of UCA. There was no second peak observed for the filter TIC (Figure 8.19), as the microbubbles pass through the bundle of capillaries in a more uniform manner. For the analysis the gamma curve was fitted to the first peak only. Two CSI modes were evaluated; 2D Harmonic and Harmonic Power Doppler. From comparing the actual flow rate (flow rate from pump) to the calculated flow rate determined from the TIC parameters it was found that 2D Harmonic imaging (1.2% error) was more accurate although only for the inlet flow rate. Both CSI modes still had errors (of up to 80%) associated with the filter and outlet flow rates. In this study the novel perfusion capillary phantom containing liquid TMM and a BMF underwent flow rates similar to that found *in-vivo*. When compared to a simple TIC obtained from a kidney some of the parameters were similar (same order of magnitude). It should be noted that a different contrast agent SonoVue was used, which has different acoustic characteristics associated to it. However, the result indicates that this experimental set-up may be useful in the evaluation of new UCAs and contrast specific imaging techniques.

8.6 CONCLUSIONS

Contrast enhanced ultrasound is an emerging technology in the area of RAS. Contrast enhanced phantom studies evaluated the potential of UCA Luminity® in the renal imaging. Using *in-vitro* experimentation the contrast agent Luminity® was evaluated. It is particularly important for the application of UCAs that the US system used has a large dynamic range, as a limited Doppler DR will affect the information obtained. Using a novel protocol the Doppler DR of the HDI 3000 with C4-2 transducer was determined to be sufficient to detect areas of slow flow (low scatterer volume) (corresponding to the low particle concentrations) and high flow (corresponding to the particle concentrations greater than 1.82%). Using the anatomically realistic renal artery flow phantoms, it was found that the presence of the UCA caused a significant increase in the measured Doppler frequency which resulted in an overestimation of the actual velocity. The effect of the carrier fluids used on time intensity curve parameters was investigated. The results demonstrated that the carrier fluid had a significant effect on TIC parameters measured. Therefore, previous results obtained using water may not be reflective of the clinical situation and demonstrated that the composition of the fluid influences the TIC parameters obtained using the ultrasound contrast agent. This effect is complex and may be due to a combination of many factors that are still to be studied. It was outside the remit of this study to investigate these factors. Finally the use of the UCA Luminity® in the visualization of perfusion in the kidney capillary phantom was investigated. The perfusion within the phantom was assessed using TICs.

CHAPTER 9 CONCLUSIONS AND RECOMMENDATIONS FOR FUTURE

9.1 MAIN CONCLUSIONS

This thesis involved the development of anatomically realistic renal artery flow phantoms and kidney perfusion phantoms for the evaluation of current and emerging imaging technologies, in particular ultrasound imaging has been presented.

The acoustic and mechanical properties of a relatively new vessel mimicking material, PVA C, was characterised. It was found that PVA C exhibited similar acoustic and mechanical properties to human artery walls and after 2 freeze-thaw cycles had a speed of sound, attenuation coefficient and Young's modulus of 1538 ± 5 m s^{-1}, 0.07 ± 0.03 dB cm^{-1} MHz^{-1} and 79 ± 11 kPa, respectively. An antibacterial agent (Bc) was added to the PVA C to prevent bacterial growth. The effect of the addition of this agent was evaluated and resulted in an increase in the speed of sound of the PVA C, which has not been previously reported.

Using computer-aided modelling techniques 3 different types of renal artery flow phantoms were constructed; (1) a wall-less phantom, (2) a walled phantom with PVA C vessel and (3) a multi-modality phantom. The production and fabrication of the renal artery lumen were found to be accurate and reproducible. Currently, no anatomically realistic renal artery and kidney flow phantoms are available commercially.

Maximum velocity measurements were obtained using the novel anatomically realistic renal flow phantoms to determine if it is possible to detect lower grade stenosis (30%). For the wall-less phantoms, it was possible to achieve maximum velocities up to 40 cm s^{-1} for arteries without stenosis and 30% and 50% stenosis without rupture of the vessel. The walled phantoms proved to be more mechanically robust achieving velocities similar to that found *in-vivo*, a maximum velocity 40 cm s^{-1} was achieved without rupturing in all the phantoms except the 85% stenosis. These studies have shown it is possible to detect lower grade stenosis with changes in the maximum velocity at the site of stenosis and distal to the stenosis.

It was found that this fat mimicking layer caused significant overestimation of maximum velocity in the non-attenuating medium (string phantom) and also in the anatomically realistic renal artery flow phantoms. In a clinical situation this would correspond to a patient being recorded as having a more severe stenosis than might be present.

A comparative study was carried out between the four main imaging techniques currently used to detect renal artery stenosis (US, MRI, CT and DSA) to assess the visualisation of the phantoms with each imaging modality and determine the geometric accuracy of each technique. MRI was found to be the most accurate imaging modality particularly for stenosis < 50%, with US and CT having similar accuracies. All three non-invasive imaging modalities, US, MRI and CT were shown to be more accurate compared to DSA. This study demonstrated the potential for these novel anatomically realistic renal artery phantoms to be used as standard vascular phantoms for comparative studies of ultrasound, MRI, CT and DSA.

From the four phantoms developed the kidney capillary phantom was chosen to be used for the contrast enhanced kidney perfusion studies in Chapter 8, as it matched the most design criteria and perform the most satisfactory in the contrast studies. Using this novel kidney capillary phantom it was possible to achieve estimated flow speeds comparable with those in the blood vessels of the macrocirculation (renal artery and renal vein) and also that of the microcirculation of the kidney (0.1 – 3.2 cm s^{-1}) (Milnor, 1982). Significant improvements have been made to the physiological relevance of perfusion phantoms with the use of BMF and liquid TMM which should improve the clinical relevance of the contrast enhanced studies.

The Doppler dynamic range of the HDI 3000 with C4-2 transducer was determined to be sufficient to detect areas of slow flow (low scatterer volume, RBCs) which may be beyond the detection limits of the Doppler system (corresponding to the low particle concentrations) and high flow (corresponding to the particle concentrations greater than 1.82%).

Using anatomically realistic renal artery flow phantoms contrast enhanced Spectral Doppler was performed. The presence of the UCA causes significant increase in the measured Doppler frequency which results in an overestimation of the actual velocity. The presence of the UCA did aid in the visualisation of highly stenosed lumens > 70%.

The effect of the carrier fluids used on TIC parameters was investigated. The results demonstrated that the carrier fluid had a significant effect on TIC parameters measured. Therefore, previous results obtained using water may not be directly comparable to the

clinical situation and the composition of the fluid also influences the TIC parameters obtained using the ultrasound contrast agent.

Finally the use of the UCA Luminity in the visualization of perfusion in the kidney capillary phantom was investigated. The perfusion within the phantom was assessed using TICs. These *in-vitro* contrast studies have shown the potential of the low solubility UCA Luminity for low MI imaging of the renal vasculature.

The renal artery and more specifically the kidneys are technically challenging anatomical sites for imaging and obtaining reproducible diagnostically useful measurements. However, recent and ongoing technological developments in the area of medical imaging, in particular ultrasound imaging have the potential to provide improved diagnostic measurements. To this end, in this thesis, renal artery and kidney phantoms have been developed for *in-vitro* experimentation; to enhance the performance evaluation of current and emerging ultrasound technologies in kidney diagnosis, to improve the training of technologists using these phantoms and to facilitate improvement in the diagnosis of disease in the renal vasculature. This study has shown the importance of increasing the complexity of anatomically realistic phantoms with the addition of a fat mimicking layer. It has also shown their potential to act as standard reference phantoms in comparative studies between different imaging modalities.

9.2 RECOMMENDATIONS FOR FUTURE WORK

A number of avenues to extend the insights and conclusions of this work have emerged from the range of experiments carried out and from consideration of the clinical need to enhance the early detection of RAS. The following set of suggestions would enhance the work reported here on renal phantom development and contrast enhanced kidney phantom studies:

1. Development of different types of blockages (asymmetrical, eccentric, irregular surfaces) to mimic the complex heterogeneous composition and morphology of *in-vivo* renal artery plaques
2. Perform flow experiments using physiological waveforms to obtain 3D profiles of the flow distribution across the vessels for increasing degrees of stenosis
3. Incorporate a layer of subcutaneous pig fat or fat mimicking agar-like material to more closely mimic the passage of the ultrasound beam *in-vivo*, and the investigation of the effects of a such a fat layer on Doppler velocity measurements for a number of ultrasound scanners
4. Perform a comparative study using the current clinical protocols used to detect RAS for US, MRA, CTA and DSA using the multi-modality renal artery flow phantoms
5. Further *in-vitro* investigations into the effect of carrier fluids on TIC parameters comparing human blood and BMF

REFERENCES

AIUM, (2002) Performance Criteria and Measurements for Doppler Ultrasound Devices, American Institute of Ultrasound in Medicine Standards Committee.

Bale-Glickman, J, Selby, K, Saloner, D and Savas, O (2003) Experimental Flow Studies in Exact-Replica Phantoms of Atherosclerotic Carotid Bifurcations under Steady Input Conditions. J Biomech Eng, 125(1), 38-48.

Bamber, J C (1997). Attenuation and Aborption In Hill, C R, Bamber, J C and Ter Haar, G R (Eds) Physical Principles of Medical Ultrasonics 2nd ed, Wiley pp 93 - 166.

Basseau, F, Grenier, N, Trillaud, H, Douws, C and Saint-Amon, A (2000) Doppler Frequency Shift and Time-Domain Velocity Enhancement Induced by an Ultrasonographic Contrast Agent. J Ultrasound Med, 19(3), 171-6.

BBS, Medical Electronics, Hagersten, Sweden.

Beattie, D K, Golledge, J, Cuming, R, Greenhalgh, R M and Davies, A H (1997) Duplex Imaging and Renal Artery Stenosis. Journal of Vascular Investigation, 3(1), 9.

Beux, F, Carmassi, S, Salvetti, M V, Ghiadoni, L, Huang, Y, Taddei, S and Salvetti, A (2001) Automatic Evaluation of Arterial Diameter Variation from Vascular Echographic Images. Ultrasound Med Biol, 27(12), 1621-9.

Blomley, M, Claudon, M and Cosgrove, D (2007) Wfumb Safety Symposium on Ultrasound Contrast Agents: Clinical Applications and Safety Concerns. Ultrasound Med Biol, 33(2), 180-6.

Blum, U, Krumme, B, Flugel, P, Gabelmann, A, Lehnert, T, Buitrago-Tellez, C, Schollmeyer, P and Langer, M (1997) Treatment of Ostial Renal-Artery Stenoses with Vascular Endoprostheses after Unsuccessful Balloon Angioplasty. N Engl J Med, 336(7), 459-65.

Boote, E J and Zagzebski, J A (1988) Performance Tests of Doppler Ultrasound Equipment with a Tissue and Blood-Mimicking Phantom. J Ultrasound Med, 7(3), 137-47.

Boussion, N, Soulez, G, De Guise, J A, Daronat, M, Qin, Z and Cloutier, G (2004) Geometrical Accuracy and Fusion of Multimodal Vascular Images: A Phantom Study. Med Phys, 31(6), 1434-43.

Brewin, M P, Pike, L C, Rowland, D E and Birch, M J (2008) The Acoustic Properties, Centered on 20 Mhz, of an Iec Agar-Based Tissue-Mimicking Material and Its Temperature, Frequency and Age Dependence. Ultrasound Med Biol, 34(8), 1292-306.

Browne, J E, Ramnarine, K V, Watson, A J and Hoskins, P R (2003) Assessment of the Acoustic Properties of Common Tissue-Mimicking Test Phantoms. Ultrasound Med Biol, 29(7), 1053-60.

Browne, J E, Watson, A J, Hoskins, P R and Elliott, A T (2005) Investigation of the Effect of Subcutaneous Fat on Image Quality Performance of 2d Conventional Imaging and Tissue Harmonic Imaging. Ultrasound Med Biol, 31(7), 957-64.

Burlew, M M, Madsen, E L, Zagzebski, J A, Banjavic, R A and Sum, S W (1980) A New Ultrasound Tissue-Equivalent Material. Radiology, 134(2), 517-20.

Burns, P N, Hope Simpson, D and Averkiou, M A (2000) Nonlinear Imaging. Ultrasound Med Biol, 26 Suppl 1, S19-22.

Chen, Q and Zagzebski, J A (2004) Simulation Study of Effects of Speed of Sound and Attenuation on Ultrasound Lateral Resolution. Ultrasound Med Biol, 30(10), 1297-306.

Christopher, D A, Burns, P N, Hunt, J W and Foster, F S (1995) The Effect of Refraction and Assumed Speeds of Sound in Tissue and Blood on Doppler Ultrasound Blood Velocity Measurements. Ultrasound Med.Biol., 21(2), 187-201.

Chu, K C (1997) Chapter 5 Polyvinyl Alcohol Cryogel, University of Western Ontario, London.

Chu, K C and Rutt, B K (1997) Polyvinyl Alcohol Cryogel: An Ideal Phantom Material for Mr Studies of Arterial Flow and Elasticity. Magn Reson Med, 37(2), 314-9.

Claassen, L, Seidel, G and Algermissen, C (2001) Quantification of Flow Rates Using Harmonic Grey-Scale Imaging and an Ultrasound Contrast Agent: An *in-vitro* and *in-vivo* Study. Ultrasound Med Biol, 27(1), 83-8.

Claudon, M, Plouin, P F, Baxter, G M, Rohban, T and Devos, D M (2000) Renal Arteries in Patients at Risk of Renal Arterial Stenosis: Multicenter Evaluation of the

Echo-Enhancer Sh U 508a at Color and Spectral Doppler Us. Levovist Renal Artery Stenosis Study Group. Radiology, 214(3), 739-46.

Cloutier, G, Soulez, G, Qanadli, S D, Teppaz, P, Allard, L, Qin, Z, Cloutier, F and Durand, L G (2004) A Multimodality Vascular Imaging Phantom with Fiducial Markers Visible in Dsa, Cta, Mra, and Ultrasound. Med Phys, 31(6), 1424-33.

Correas, J M, Claudon, M, Tranquart, F and Helenon, A O (2006) The Kidney: Imaging with Microbubble Contrast Agents. Ultrasound Q, 22(1), 53-66.

Correas, J M, Claudon, M, Tranquart, F and Helenon, O (2003) Contrast-Enhanced Ultrasonography: Renal Applications. J Radiol, 84(12 Pt 2), 2041-54.

Correas, J M, Tranquart, F and Claudon, M (2009) Guidelines for Contrast Enhanced Ultrasound (Ceus)--Update 2008. J Radiol, 90(1 Pt 2), 123-38; quiz 39-40.

Dabrowski, W, Dunmore-Buyze, J, Cardinal, H N and Fenster, A (2001) A Real Vessel Phantom for Flow Imaging: 3-D Doppler Ultrasound of Steady Flow. Ultrasound Med Biol, 27(1), 135-41.

Dabrowski, W, Dunmore-Buyze, J, Rankin, R N, Holdsworth, D W and Fenster, A (1997) A Real Vessel Phantom for Imaging Experimentation. Med Phys, 24(5), 687-93.

Daigle, R J, Stravos, A T and Lee, R M (1990) Overestimation of Velocity and Frequency Values by Multielement Linear Array Dopplers. The Journal of Vascular Technology, 14(5), 7.

De Bruyne, B, Manoharan, G, Pijls, N H, Verhamme, K, Madaric, J, Bartunek, J, Vanderheyden, M and Heyndrickx, G R (2006) Assessment of Renal Artery Stenosis Severity by Pressure Gradient Measurements. J Am Coll Cardiol, 48(9), 1851-5.

De Cobelli, F, Venturini, M, Vanzulli, A, Sironi, S, Salvioni, M, Angeli, E, Scifo, P, Garancini, M P, Quartagno, R, Bianchi, G and Del Maschio, A (2000) Renal Arterial Stenosis: Prospective Comparison of Color Doppler Us and Breath-Hold, Three-Dimensional, Dynamic, Gadolinium-Enhanced Mr Angiography. Radiology, 214(2), 373-80.

de Jong, N, Bouakaz, A and Ten Cate, F J (2002) Contrast Harmonic Imaging. Ultrasonics, 40(1-8), 567-73.

Dineley, J, Meagher, S, Poepping, T L, McDicken, W N and Hoskins, P R (2006) Design and Characterisation of a Wall Motion Phantom. Ultrasound Med Biol, 32(9), 1349-57.

Douville, Y, Johnston, K W, Kassam, M, Zuech, P, Cobbold, R S and Jares, A (1983) An *in-Vitro* Model and Its Application for the Study of Carotid Doppler Spectral Broadening. Ultrasound Med Biol, 9(4), 347-56.

Drelich-Zbroja, A, Jargiello, T, Drelich, G, Lewandowska-Stanek, H and Szczerbo-Trojanowska, M (2004) Renal Artery Stenosis: Value of Contrast-Enhanced Ultrasonography. Abdom.Imaging, 29(4), 518-24.

Drieghe, B, Madaric, J, Sarno, G, Manoharan, G, Bartunek, J, Heyndrickx, G R, Pijls, N H and De Bruyne, B (2008) Assessment of Renal Artery Stenosis: Side-by-Side Comparison of Angiography and Duplex Ultrasound with Pressure Gradient Measurements. Eur Heart J, 29(4), 517-24.

Duboeuf, F, Liebgott, H, Basarab, A, Brusseau, E, Delachartre, P and Vray, D (2007) Static Mechanical Assessment of Elastic Young's Modulus of Tissue Mimicking Materials Used for Medical Imaging. Conf Proc IEEE Eng Med Biol Soc, 2007, 3450-3.

Duck, F A (1990) Physical Properties of Tissue: A Comprehensive Reference Book, Academic Press Inc, London.

Duck, F A (2002) Nonlinear Acoustics in Diagnostic Ultrasound. Ultrasound Med Biol, 28(1), 1-18.

Eicke, B M, Kremkau, F W, Hinson, H and Tegeler, C H (1995) Peak Velocity Overestimation and Linear-Array Spectral Doppler. J.Neuroimaging, 5(2), 115-21.

Eklöf, H, Ahlstrom, H, Magnusson, A, Andersson, L G, Andren, B, Hagg, A, Bergqvist, D and Nyman, R (2006) A Prospective Comparison of Duplex Ultrasonography, Captopril Renography, Mra, and Cta in Assessing Renal Artery Stenosis. Acta Radiol, 47(8), 764-74.

Eriksson, R, Persson, H W, Dymling, S O and Lindstrom, K (1995) A Micrcirculation Phantom for Performance Tesing of Blood Perfusion Measurement Equipment. European Journal of Ultrasound, 2, 65-75.

Evans, D H (2000) Doppler Signal Analysis. Ultrasound Med.Biol., 26 Suppl 1, S13-S5.

Evans, D H and McDicken, W N (2000) Doppler Ultrasound: Physics, Instrumental, and Clinical Applications, Wiley.

Fenchel, M, Nael, K, Herget-Rosenthal, S, Krishnam, M and Ruehm, S G (2006) Magnetic Resonance Imaging of Renal Disease: Recent Developments and Future Applications. Nephron Clin.Pract., 103(2), c37-c44.

Ferrara, K and DeAngelis, G (1997) Color Flow Mapping. Ultrasound Med.Biol., 23(3), 321-45.

Fink, M and Dorme, C (1994) Phase Aberrration Correction with Ultrasonic Time Reversal Mirrors. IEEE 1994 Ultrason Symp 9.

Fish, P J (1986). Doppler Methods In Hill, C R (Ed) Physical Principles of Medical Ultrasonics, Ellis Horwood Limited (Wiley), Chichester, UK.

Forsberg, F, Liu, J B, Burns, P N, Merton, D A and Goldberg, B B (1994) Artifacts in Ultrasonic Contrast Agent Studies. J Ultrasound Med, 13(5), 357-65.

Fraioli, F, Catalano, C, Bertoletti, L, Danti, M, Fanelli, F, Napoli, A, Cavacece, M and Passariello, R (2006) Multidetector-Row Ct Angiography of Renal Artery Stenosis in 50 Consecutive Patients: Prospective Interobserver Comparison with Dsa. Radiol Med, 111(3), 459-68.

Fraser, K H, Poepping, T L, McNeilly, A, Megson, I L and Hoskins, P R (2006) Acoustic Speed and Attenuation Coefficient in Sheep Aorta Measured at 5-9 Mhz. Ultrasound Med Biol, 32(6), 971-80.

Frayne, R, Gowman, L M, Rickey, D W, Holdsworth, D W, Picot, P A, Drangova, M, Chu, K C, Caldwell, C B, Fenster, A and Rutt, B K (1993) A Geometrically Accurate Vascular Phantom for Comparative Studies of X-Ray, Ultrasound, and Magnetic Resonance Vascular Imaging: Construction and Geometrical Verification. Med Phys, 20(2 Pt 1), 415-25.

Fromageau, J, Brusseau, E, Vray, D, Gimenez, G and Delachartre, P (2003) Characterization of Pva Cryogel for Intravascular Ultrasound Elasticity Imaging. IEEE Trans Ultrason Ferroelectr Freq Control, 50(10), 1318-24.

Fromageau, J, Gennisson, J L, Schmitt, C, Maurice, R L, Mongrain, R and Cloutier, G (2007) Estimation of Polyvinyl Alcohol Cryogel Mechanical Properties with Four Ultrasound Elastography Methods and Comparison with Gold Standard Testings. IEEE Trans Ultrason Ferroelectr Freq Control, 54(3), 498-509.

Gammell, P M, Le Croissette, D H and Heyser, R C (1979) Temperature and Frequency Dependence of Ultrasonic Attenuation in Selected Tissues. Ultrasound Med Biol, 5(3), 269-77.

Goldstein, A (2000) The Effect of Acoustic Velocity on Phantom Measurements. Ultrasound Med.Biol., 26(7), 1133-43.

Goldstein, A (1991a) Effect of Tank Liquid Acoustic Velocity on Doppler String Phantom Measurements. J.Ultrasound Med., 10(3), 141-8.

Goldstein, A (1991b) Performance Tests of Doppler Ultrasound Equipment with a String Phantom. J.Ultrasound Med., 10(3), 125-39.

Goldstein, A and Langrill, L N (1979) Ethylene Glycol-Water Mixture for Use in Ultrasound Test Objects. J Clin Ultrasound, 7(6), 465-70.

Grant, E G, Benson, C B, Moneta, G L, Alexandrov, A V, Baker, J D, Bluth, E I, Carroll, B A, Eliasziw, M, Gocke, J, Hertzberg, B S, Katarick, S, Needleman, L, Pellerito, J, Polak, J F, Rholl, K S, Wooster, D L and Zierler, E (2003) Carotid Artery Stenosis: Grayscale and Doppler Ultrasound Diagnosis--Society of Radiologists in Ultrasound Consensus Conference. Ultrasound Q, 19(4), 190-8.

Grenier, N, Hauger, O, Cimpean, A and Perot, V (2006) Update of Renal Imaging. Semin.Nucl.Med., 36(1), 3-15.

Guidi, G, Licciardello, C and Falteri, S (2000) Intrinsic Spectral Broadening (ISB) in Ultrasound Doppler as a Combination of Transit Time and Local Geometrical Broadening. Ultrasound Med Biol, 26(5), 853-62.

Gutberlet, M, Venz, S, Zendel, W, Hosten, N and Felix, R (1998) Do Ultrasonic Contrast Agents Artificially Increase Maximum Doppler Shift? *In-Vivo* Study of Human Common Carotid Arteries. J Ultrasound Med, 17(2), 97-102.

Hein, I A and O'Brien, W D, Jr. (1992) A Flexible Blood Flow Phantom Capable of Independently Producing Constant and Pulsatile Flow with a Predictable Spatial Flow Profile for Ultrasound Flow Measurement Validations. IEEE Trans.Biomed.Eng, 39(11), 1111-22.

Hindle, A J and Perkins, A C (1994) A Perfusion Phantom for the Evaluation of Ultrasound Contrast Agents. Ultrasound Med Biol, 20(3), 309-14.

Hirsch, A T, Haskal, Z J, Hertzer, N R, Bakal, C W, Creager, M A, Halperin, J L, Hiratzka, L F, Murphy, W R, Olin, J W, Puschett, J B, Rosenfield, K A, Sacks, D, Stanley, J C, Taylor, L M, Jr., White, C J, White, J, White, R A, Antman, E M, Smith, S C, Jr., Adams, C D, Anderson, J L, Faxon, D P, Fuster, V, Gibbons, R J, Hunt, S A, Jacobs, A K, Nishimura, R, Ornato, J P, Page, R L and Riegel, B (2006) Acc/Aha 2005 Practice Guidelines for the Management of Patients with Peripheral Arterial Disease (Lower Extremity, Renal, Mesenteric, and Abdominal Aortic): A Collaborative Report from the American Association for Vascular Surgery/Society for Vascular Surgery, Society for Cardiovascular Angiography and Interventions, Society for Vascular Medicine and Biology, Society of Interventional Radiology, and the Acc/Aha Task Force on Practice Guidelines (Writing Committee to Develop Guidelines for the Management of Patients with Peripheral Arterial Disease): Endorsed by the American Association of Cardiovascular and Pulmonary Rehabilitation; National Heart, Lung, and Blood Institute; Society for Vascular Nursing; Transatlantic Inter-Society Consensus; and Vascular Disease Foundation. Circulation, 113(11), e463-654.

Hoskins, P R (1994). Review of the Design and Use of Flow Phantoms In Hoskins, P R, Evans, J A and Sheriff, S (Eds) Testing of Doppler Ultrasound Equipment, IPEM, York, pp.12 - 29.

Hoskins, P R (1996) Accuracy of Maximum Velocity Estimates Made Using Doppler Ultrasound Systems. Br.J.Radiol., 69(818), 172-7.

Hoskins, P R (2007) Physical Properties of Tissues Relevant to Arterial Ultrasound Imaging and Blood Velocity Measurement. Ultrasound Med Biol, 33(10), 1527-39.

Hoskins, P R (2008) Simulation and Validation of Arterial Ultrasound Imaging and Blood Flow. Ultrasound Med Biol, 34(5), 693-717.

Hoskins, P R, Anderson, T and McDicken, W N (1989) A Computer Controlled Flow Phantom for Generation of Physiological Doppler Waveforms. Phys Med Biol, 34(11), 1709-17.

Hoskins, P R, Fish, P J, Pye, S D and Anderson, T (1999) Finite Beam-Width Ray Model for Geometric Spectral Broadening. Ultrasound Med.Biol., 25(3), 391-404.

Hoskins, P R and McDicken, W N (1997) Colour Ultrasound Imaging of Blood Flow and Tissue Motion. Br.J.Radiol., 70(837), 878-90.

IEC (2001) Ultrasonics - Flow Measurement Systems: Flow Test Object International Electrotechnical Commission, Geneva, Switzerland.

IPEM (1994) Report No. 70, P R, Evans, J A and Sheriff, S eds, Testing of Doppler Equipment. IPEM, York.

IPEM (2004) Vascular Laboratory Practise Manual IPEM, York.

Jaeger, K A (2007) Renovascular Hypertension--a Controversial Issue. Ultraschall Med., 28(1), 28-31.

Kaatee, R, Beek, F J, de Lange, E E, van Leeuwen, M S, Smits, H F, van, d V, Beutler, J J and Mali, W P (1997) Renal Artery Stenosis: Detection and Quantification with Spiral Ct Angiography Versus Optimized Digital Subtraction Angiography. Radiology, 205(1), 121-7.

Kawasaki, T, Sasayama, S, Yagi, S, Asakawa, T and Hirai, T (1987) Non-Invasive Assessment of the Age Related Changes in Stiffness of Major Branches of the Human Arteries. Cardiovasc Res, 21(9), 678-87.

Kaye, G W C and Laby, T H (1995) Tables of Physical and Chemical Constants (Kaye & Labys), 16 ed, Longman Sc & Tech.

Kollmann, C (2007) New Sonographic Techniques for Harmonic Imaging--Underlying Physical Principles. Eur J Radiol, 64(2), 164-72.

Krishnan, S, Rigby, K W and O'Donnell, M (1998) Efficient Parallel Adaptive Aberration Correction. IEEE Trans Ultrason Ferroelectr Freq Control, 45(3), 691-703.

Krumme, B, Blum, U, Schwertfeger, E, Flugel, P, Hollstin, F, Schollmeyer, P and Rump, L C (1996) Diagnosis of Renovascular Disease by Intra- and Extrarenal Doppler Scanning. Kidney Int, 50(4), 1288-92.

Law, Y F, Johnston, K W, Routh, H F and Cobbold, R S (1989) On the Design and Evaluation of a Steady Flow Model for Doppler Ultrasound Studies. Ultrasound Med Biol, 15(5), 505-16.

Lazewatsky, J, Kagan, M and Barrett, J A. (1995). The Effect of Dilution Medium on the Measurement of in-Vitro Properties of Ultrasound Contrast Agents, IEEE Ultrasonics Symposium (pp. 1737-42).

Leiner, T, de Haan, M W, Nelemans, P J, van Engelshoven, J M and Vasbinder, G B (2005) Contemporary Imaging Techniques for the Diagnosis of Renal Artery Stenosis. Eur.Radiol., 15(11), 2219-29.

Lencioni, R, Pinto, S, Cioni, D and Bartolozzi, C (1999) Contrast-Enhanced Doppler Ultrasound of Renal Artery Stenosis: Prologue to a Promising Future. Echocardiography., 16(7, Pt 2), 767-73.

Lewin, P A and Busk, H. (1982). *In-Vivo* Ultrasonic Measurements of Tissue Properties, Preceedingin of the IEEE Ultrasonics Symposium (pp. 3).

Li, J C, Wang, L, Jiang, Y X, Dai, Q, Cai, S, Lv, K and Qi, Z H (2006) Evaluation of Renal Artery Stenosis with Velocity Parameters of Doppler Sonography. J Ultrasound Med, 25(6), 735-42; quiz 43-4.

Li, P C and Yang, M J (2003) Transfer Function Analysis of Ultrasonic Time-Intensity Measurements. Ultrasound Med Biol, 29(10), 1493-500.

Li, P C, Yeh, C K and Wang, S W (2002) Time-Intensity-Based Volumetric Flow Measurements: An *in-Vitro* Study. Ultrasound Med Biol, 28(3), 349-58.

Li, S, McDicken, W N and Hoskins, P R (1993) Refraction in Doppler Ultrasound.Ultrasound Med Biol, 19(7), 593-4.

Liepsch, D, Schmid, T, McLean, J and Weigand, C (2004) Do Contrast Agents Affect Ultrasound Flow Measurements? Technol Health Care, 12(6), 411-23.

Lockwood GR, Ryan LK, Hunt JW, Foster FS. (1991) Measurement of the ultrasonic properties of vascular tissues and blood from 35–65 MHz. Ultrasound Med Biol, (17), 653– 666.

Lohmaier, S, Ghanem, A, Veltmann, C, Sommer, T, Bruce, M and Tiemann, K (2004) *In-Vitro* and *in-Vivo* Studies on Continuous Echo-Contrast Application Strategies Using Sonovue in a Newly Developed Rotating Pump Setup. Ultrasound Med Biol, 30(9), 1145-51.

Madsen, E L, Frank, G R and Dong, F (1998) Liquid or Solid Ultrasonically Tissue-Mimicking Materials with Very Low Scatter. Ultrasound Med Biol, 24(4), 535-42.

Madsen, E L, Zagzebski, J A and Frank, G R (1982) Oil-in-Gelatin Dispersions for Use as Ultrasonically Tissue-Mimicking Materials. Ultrasound Med Biol, 8(3), 277-87.

Marckmann, P, Skov, L, Rossen, K, Dupont, A, Damholt, M B, Heaf, J G and Thomsen, H S (2006) Nephrogenic Systemic Fibrosis: Suspected Causative Role of Gadodiamide

Used for Contrast-Enhanced Magnetic Resonance Imaging. J Am Soc Nephrol, 17(9), 2359-62.

Martin, K and Spinks, D (2001) Measurement of the Speed of Sound in Ethanol/Water Mixtures. Ultrasound Med Biol, 27(2), 289-91.

McDicken, W N (1986) A Versatile Test-Object for the Calibration of Ultrasonic Doppler Flow Instruments. Ultrasound Med Biol, 12(3), 245-9.

McLaughlin, G W (2007) Practical Aberration Correction Methods. Ultrasound, 15(2), 6.

Meagher, S, Poepping, T L, Ramnarine, K V, Black, R A and Hoskins, P R (2007) Anatomical Flow Phantoms of the Nonplanar Carotid Bifurcation, Part Ii: Experimental Validation with Doppler Ultrasound. Ultrasound Med Biol, 33(2), 303-10.

Melany, M L, Grant, E G, Farooki, S, McElroy, D and Kimme-Smith, C (1999) Effect of Us Contrast Agents on Spectral Velocities: *In-Vitro* Evaluation. Radiology, 211(2), 427-31.

Meyer-Wiethe, K, Cangur, H and Seidel, G U (2005) Comparison of Different Mathematical Models to Analyze Diminution Kinetics of Ultrasound Contrast Enhancement in a Flow Phantom. Ultrasound Med Biol, 31(1), 93-8.

Miller, A P and Nanda, N C (2004) Contrast Echocardiography: New Agents. Ultrasound Med Biol, 30(4), 425-34.

Milnor, W R (1982) Haemodynamics, Baltimore.

Nchimi, A, Biquet, J F, Brisbois, D, Reginster, P, Bouali, K, Saive, C and Magotteaux, P (2003) Duplex Ultrasound as First-Line Screening Test for Patients Suspected of Renal Artery Stenosis: Prospective Evaluation in High-Risk Group. Eur Radiol, 13(6), 1413-9.

Netuka, D, Benes, V, Mandys, V, Hlasenska, J, Burkert, J and Benes, V, Jr. (2006) Accuracy of Angiography and Doppler Ultrasonography in the Detection of Carotid Stenosis: A Histopathological Study of 123 Cases. Acta Neurochir (Wien), 148(5), 511-20; discussion 20.

Newhouse, V L, S., F E, Johnston, G F and Wolf, D A (1980) The Dependance of Ultrasound Doppler Bandwidth on Beam Geometery. IEEE Trans Sonics Ultrason 1980, 27, 9.

Ng, G C, Freiburger, P D, Walker, W F and Trahey, G E (1997) A Speckle Target Adaptive Imaging Technique in the Presence of Distributed Aberrations. IEEE Trans Ultrason Ferroelectr Freq Control, 44(1), 140-51.

Nichols, W W and O'Rourke, M F (1990) Mcdonald's Blood Flow in Arteries:Theoretical, Experimental and Clinical Principles, Edward Arnold, London.

Patel, S T, Mills, J L, Sr., Tynan-Cuisinier, G, Goshima, K R, Westerband, A and Hughes, J D (2005) The Limitations of Magnetic Resonance Angiography in the Diagnosis of Renal Artery Stenosis: Comparative Analysis with Conventional Arteriography. J Vasc Surg, 41(3), 462-8.

Paven, G, Waugh, R, Nicholson, J, Gillin, A and Hennessy, A (2006) Screening Tests for Renal Artery Stenosis: A Case-Series from an Australian Tertiary Referral Centre. Nephrology.(Carlton.), 11(1), 68-72.

Petrick, J, Zomack, M and Schlief, R (1997) An Investigation of the Relationship between Ultrasound Echo Enhancement and Doppler Frequency Shift Using a Pulsatile Arterial Flow Phantom. Invest Radiol, 32(4), 225-35.

Poepping, T L, Nikolov, H N, Rankin, R N, Lee, M and Holdsworth, D W (2002) An *in-Vitro* System for Doppler Ultrasound Flow Studies in the Stenosed Carotid Artery Bifurcation. *Ultrasound Med Biol*, *28*(4), 495-506.

Poepping, T L, Nikolov, H N, Thorne, M L and Holdsworth, D W (2004) A Thin-Walled Carotid Vessel Phantom for Doppler Ultrasound Flow Studies. Ultrasound Med Biol, 30(8), 1067-78.

Quaia, E (2005). Physical Basis and Principles of Action of Microbubble-Based Contrast Agents In Contast Media in Ultrasonography: Basic Principles and Clinical Applications, Springer, Berlin Heidelberg New York.

Ramnarine, K V, Anderson, T and Hoskins, P R (2001) Construction and Geometric Stability of Physiological Flow Rate Wall-Less Stenosis Phantoms. Ultrasound Med Biol, 27(2), 245-50.

Ramnarine, K V, Hoskins, P R, Routh, H F and Davidson, F (1999) Doppler Backscatter Properties of a Blood-Mimicking Fluid for Doppler Performance Assessment. Ultrasound Med Biol, 25(1), 105-10.

Ramnarine, K V, Leen, E, Oppo, K, Angerson, W J and McArdle, C S (2002) Contrast-Enhanced Doppler Perfusion Index: Clinical and Experimental Evaluation. J.Ultrasound Med., 21(10), 1121-9.

Ramnarine, K V, Nassiri, D K, Hoskins, P R and Lubbers, J (1998) Validation of a New Blood-Mimicking Fluid for Use in Doppler Flow Test Objects. Ultrasound Med Biol, 24(3), 451-9.

Rickey, D W, Picot, P A, Christopher, D A and Fenster, A (1995) A Wall-Less Vessel Phantom for Doppler Ultrasound Studies. Ultrasound Med Biol, 21(9), 1163-76.

Ries, L L and Smith, S W (1997) Phase Aberration Correction in Two Dimensions with an Intergrated Deformable Actuator/Transducer. IEEE Trans Ultrason Ferroelectr Freq Control, 44(6), 1366-1375.

Robbin, M L, Lockhart, M E and Barr, R G (2003) Renal Imaging with Ultrasound Contrast: Current Status. Radiol.Clin.North Am., 41(5), 963-78.

Rountas, C, Vlychou, M, Vassiou, K, Liakopoulos, V, Kapsalaki, E, Koukoulis, G, Fezoulidis, I V and Stefanidis, I (2007) Imaging Modalities for Renal Artery Stenosis in Suspected Renovascular Hypertension: Prospective Intraindividual Comparison of Color Doppler Us, Ct Angiography, Gd-Enhanced Mr Angiography, and Digital Substraction Angiography. Ren Fail, 29(3), 295-302.

Rubens, D J, Bhatt, S, Nedelka, S and Cullinan, J (2006) Doppler Artifacts and Pitfalls. Radiol.Clin.North Am., 44(6), 805-35.

Rubin, J M, Bude, R O, Carson, P L, Bree, R L and Adler, R S (1994) Power Doppler Us: A Potentially Useful Alternative to Mean Frequency-Based Color Doppler Us. Radiology, 190(3), 853-6.

Saijo, Y, Miyakawa, T, Sasaki, H, Tanaka, M and Nitta, S (2004) Acoustic Properties of Aortic Aneurysm Obtained with Scanning Acoustic Microscope. Ultrasonics, 42, 695-8.

Saijo, Y, Sasaki, H, Okawai, H, Nitta, S and Tanaka, M (1998) Acoustic Properties of Atherosclerosis of Human Aorta Obtained with High-Frequency Ultrasound. Ultrasound in Medicine & Biology, 24, 1061-4.

Schwan, H P and Carstensen, E L (1952) Ultrasonics Aids to Diathermy Experiments. Electronics, 4.

Selfridge, A R (1985) Approximate Material Properties in Isotropic Materials. IEEE Trans Sonics Ultrasound, SU-32, 13.

Shetty, A N, Bis, K G, Kirsch, M, Weintraub, J and Laub, G (2000) Contrast-Enhanced Breath-Hold Three-Dimensional Magnetic Resonance Angiography in the Evaluation of Renal Arteries: Optimization of Technique and Pitfalls. J Magn Reson Imaging, 12(6), 912-23.

Shung, K K (1985) Ultrasonic Characterization of Biological Tissues. J Biomech Eng, 107, 15.

Smith, R F, Rutt, B K, Fox, A J, Rankin, R N and Holdsworth, D W (1996) Geometric Characterization of Stenosed Human Carotid Arteries. Acad Radiol, 3(11), 898-911.

Smith, R F, Rutt, B K and Holdsworth, D W (1999) Anthropomorphic Carotid Bifurcation Phantom for Mri Applications. J Magn Reson Imaging, 10(4), 533-44.

Soares, G M, Murphy, T P, Singha, M S, Parada, A and Jaff, M (2006) Renal Artery Duplex Ultrasonography as a Screening and Surveillance Tool to Detect Renal Artery Stenosis: A Comparison with Current Reference Standard Imaging. J Ultrasound Med, 25(3), 293-8.

Souza, d O I, Widman, A, Molnar, L J, Fukushima, J T, Praxedes, J N and Cerri, G G (2000) Colour Doppler Ultrasound: A New Index Improves the Diagnosis of Renal Artery Stenosis. Ultrasound Med.Biol., 26(1), 41-7.

Stacul, F, Gava, S, Belgrano, M, Cernic, S, Pagnan, L, Pozzi Mucelli, F and Cova, M A (2008) Renal Artery Stenosis: Comparative Evaluation of Gadolinium-Enhanced Mra and Dsa. Radiol Med, 113(4), 529-46.

Strandness, D E, Jr. (2002) Duplex Scanning in Vascular Disorders, Third ed, Lippincott Williams & Wilkins.

Staub, D, Canevascini, R, Huegli, R W, Aschwanden, M, Thalhammer, C, Imfeld, S, Singer, E, Jacob, A L and Jaeger, K A (2007) Best Duplex-Sonographic Criteria for the Assessment of Renal Artery Stenosis--Correlation with Intra- Arterial Pressure Gradient. Ultraschall Med., 28(1), 45-51.

Steinman, A H, Tavakkoli, J, Myers, J G, Jr., Cobbold, R S and Johnston, K W (2001) Sources of Error in Maximum Velocity Estimation Using Linear Phased-Array Doppler Systems with Steady Flow. Ultrasound Med.Biol., 27(5), 655-64.

Steinman, A H, Yu, A C, Johnston, K W and Cobbold, R S (2005) Effects of Beam Steering in Pulsed-Wave Ultrasound Velocity Estimation. Ultrasound Med Biol, 31(8), 1073-82.

Sung, C K, Chung, J W, Kim, S H and Park, J H (2006) Urine Attenuation Ratio: A New Ct Indicator of Renal Artery Stenosis. AJR Am J Roentgenol, 187(2), 532-40.

Surry, K J, Austin, H J, Fenster, A and Peters, T M (2004) Poly(Vinyl Alcohol) Cryogel Phantoms for Use in Ultrasound and Mr Imaging. Phys Med Biol, 49(24), 5529-46.

Szabo, T, L. (2004) Diagnostic Ultrasound Imaging: Inside Out, First ed, Elsevier Academic Press, London.

Teirlinck, C J, Bezemer, R A, Kollmann, C, Lubbers, J, Hoskins, P R, Ramnarine, K V, Fish, P, Fredeldt, K E and Schaarschmidt, U G (1998) Development of an Example Flow Test Object and Comparison of Five of These Test Objects, Constructed in Various Laboratories. Ultrasonics, 36(1-5), 653-60.

Thornton, M J, Thornton, F, O'Callaghan, J, Varghese, J C, O'Brien, E, Walshe, J and Lee, M J (1999) Evaluation of Dynamic Gadolinium-Enhanced Breath-Hold Mr Angiography in the Diagnosis of Renal Artery Stenosis. AJR Am J Roentgenol, 173(5), 1279-83.

Turnbull, D H, Wilson, S R, Hine, A L and Foster, F S (1989) Ultrasonic Characterization of Selected Renal Tissues. Ultrasound Med.Biol., 15(3), 241-53.

Ugolini, P, Delouche, A, Herment, A and Diebold, B (2000) *In-Vitro* Flow Quantification with Contrast Power Doppler Imaging. Ultrasound Med Biol, 26(1), 113-20.

Utsunomiya, D, Miyazaki, M, Nomitsu, Y, Komeda, Y, Okigawa, T, Urata, J and Yamashita, Y (2008) Clinical Role of Non-Contrast Magnetic Resonance Angiography for Evaluation of Renal Artery Stenosis. Circ J, 72(10), 1627-30.

Vasbinder, G B, Nelemans, P J, Kessels, A G, Kroon, A A, de Leeuw, P W and van Engelshoven, J M (2001) Diagnostic Tests for Renal Artery Stenosis in Patients Suspected of Having Renovascular Hypertension: A Meta-Analysis. Ann Intern Med, 135(6), 401-11.

Vasbinder, G B, Nelemans, P J, Kessels, A G, Kroon, A A, Maki, J H, Leiner, T, Beek, F J, Korst, M B, Flobbe, K, de Haan, M W, van Zwam, W H, Postma, C T, Hunink, M G, de Leeuw, P W and van Engelshoven, J M (2004) Accuracy of Computed Tomographic Angiography and Magnetic Resonance Angiography for Diagnosing Renal Artery Stenosis. Ann.Intern.Med., 141(9), 674-82.

Veltmann, C, Lohmaier, S, Schlosser, T, Shai, S, Ehlgen, A, Pohl, C, Becher, H and Tiemann, K (2002) On the Design of a Capillary Flow Phantom for the Evaluation of

Ultrasound Contrast Agents at Very Low Flow Velocities. Ultrasound Med Biol, 28(5), 625-34.

Watts, D M, Sutcliffe, C J, Morgan, R H, Meagher, S, Wardlaw, J, Connell, M, Bastin, M E, Marshall, I, Ramnarine, K V, Hoskins, P R and Black, R A (2007) Anatomical Flow Phantoms of the Nonplanar Carotid Bifurcation, Part I: Computer-Aided Design and Fabrication. Ultrasound Med Biol, 33(2), 296-302.

Wilhjelm, J E, Vogt, K, Jespersen, S K and Sillesen, H (1997) Influence of Tissue Preservation Methods on Arterial Geometry and Echogenicity. Ultrasound Med Biol, 23(7), 1071-82.

Williams, G J, Macaskill, P, Chan, S F, Karplus, T E, Yung, W, Hodson, E M and Craig, J C (2007) Comparative Accuracy of Renal Duplex Sonographic Parameters in the Diagnosis of Renal Artery Stenosis: Paired and Unpaired Analysis. AJR Am J Roentgenol, 188(3), 798-811.

Willmann, J K, Wildermuth, S, Pfammatter, T, Roos, J E, Seifert, B, Hilfiker, P R, Marincek, B and Weishaupt, D (2003) Aortoiliac and Renal Arteries: Prospective Intraindividual Comparison of Contrast-Enhanced Three-Dimensional Mr Angiography and Multi-Detector Row Ct Angiography. Radiology, 226(3), 798-811.

Winkler, A J and Wu, J (1995) Correction of Intrinsic Spectral Broadening Errors in Doppler Peak Velocity Measurements Made with Phased Sector and Linear Array Transducers. Ultrasound Med.Biol., 21(8), 1029-35.

Wittenberg, G, Kenn, W, Tschammler, A, Sandstede, J and Hahn, D (1999) Spiral Ct Angiography of Renal Arteries: Comparison with Angiography. Eur Radiol, 9(3), 546-51.

Yeh, C K, Yang, M J and Li, P C (2003) Contrast-Specific Ultrasonic Flow Measurements Based on Both Input and Output Time Intensities. Ultrasound Med Biol, 29(5), 671-8.

Yim, P J, Cebral, J R, Weaver, A, Lutz, R J, Soto, O, Vasbinder, G B, Ho, V B and Choyke, P L (2004) Estimation of the Differential Pressure at Renal Artery Stenoses. Magn Reson Med, 51(5), 969-77.

Yokoyama, N, Schwarz, K Q, Chen, X, Steinmetz, S D, Becher, H, Schimpky, C and Schlief, R (2003) The Effect of Echo Contrast Agent on Doppler Velocity Measurements. Ultrasound Med Biol, 29(5), 765-70.

Zalunardo, N and Tuttle, K R (2004) Atherosclerotic Renal Artery Stenosis: Current Status and Future Directions. Curr Opin Nephrol Hypertens, 13(6), 613-21.

Zeqiri, B (1992) Errors in Attenuation Measurements Due to Nonlinear Propagation Effects. Journal of the Acoustical Society of America, 91, 8.

APPENDIX A

The acoustic properties for PVA C measured using the 7 MHz transducer

Table A.1 Effect of increasing freeze-thaw cycles on the speed of sound at 7 MHz

F/T #	Speed of Sound (± 5) m s^{-1}								
	PVA	Bc1	Bc2	Bc3	SiC+Bc1	SiC+Bc2	SiC+Bc3	SiC	Al_2O_3
1	1512								
2	1521	1525	1513	1507	1556			1542	
3	1527								
4	1528	1527	1525	1525	1570	1523	1525	1533	1560
5	1537								
6	1541	1530	1545	1528	1576	1573	1551	1550	

Table A.2 Effect of increasing freeze-thaw cycles on the attenuation coefficient at 7 MHz

F/T #	Attenuation coefficient (± 0.03) dB cm^{-1} MHz^{-1}								
	PVA	Bc1	Bc2	Bc3	SiC+Bc1	SiC+Bc2	SiC+Bc3	SiC	Al_2O_3
1	0.06								
2	0.11	0.25	0.20	0.19	0.28			0.37	
3	0.16								
4	0.29	0.31	0.30	0.30	0.41	0.42	0.50	0.36	0.62
5	0.26								
6	0.30	0.42	045	0.41	0.56	0.48	0.43	0.56	

Table A.3 Effect of increasing freeze-thaw cycles on the relative backscatter at 7 MHz

F/T #	Relative Backscatter (± 1) dB								
	PVA	Bc1	Bc2	Bc3	SiC+Bc1	SiC+Bc2	SiC+Bc3	SiC	Al_2O_3
1	302								
2	281	260	269	276	260			276	
3	264								
4	259	283	264	282	263	260	262	284	254
5	269								
6	262	268	279	250	252	278	277	254	

APPENDIX B

Table B.1 Misregistration of range gate

Set-up	Mis-reg (mm)	
	String Phantom	**Flow Phantom**
1	3	5
2	3	5

Table B.2 Sample volume dimensions without and with the presence of oil layer

Set-up	Spread (mm)			
	String phantom		**Flow phantom**	
	Water	*Oil*	*Water*	*Oil*
1	0.2	0.3	0.4	0.5
2	0.2	0.1	0.5	0.5

Table B.3 Doppler velocity measurements for string phantom

Set-up 1 (no oil layer present)					**Set-up 1 (oil layer present)**				
C4-2	Max	Min	**Error (%)**	**ISB (%)**	C4-2	Max	Min	**Error (%)**	**ISB (%)**
15	18	9	19	31	**15**	21	11	39	31
30	34	21	14	25	**30**	39	24	30	25
40	46	39	14	21	**40**	55	34	30	24
50	55	36	9	20	**50**	64	41	28	22
60	67	43	12	22	**60**	79	50	32	23
100	116	75	16	22	**100**	129	84	29	21
Set-up 2 (no oil layer present)					**Set-up 2 (oil layer present)**				
C4-2	Max	Min	**Error (%)**	**ISB (%)**	C4-2	Max	Min	**Error (%)**	**ISB (%)**
15	20	12	34	27	**15**	21	12	39	27
30	36	25	21	18	**30**	39	25	31	23
40	52	35	21	19	**40**	56	36	31	22
50	60	40	20	20	**50**	67	42	33	23
60	78	46	30	26	**60**	81	51	34	22
100	127	82	27		**100**	133	88	33	20

Table B.4 Doppler velocity measurements for simple flow phantom

Set-up 1 (no oil layer present)				**Set-up 1 (oil layer present)**			
C4-2	Max	Min	**Error (%)**	C4-2	Max	Min	**Error (%)**
15	13	4	-15	**15**	14	4	-10
30	24	9	-20	**30**	26	13	-12
40	31	12	-24	**40**	36	15	-10
50	44	22	-13	**50**	45	23	-10
60	53	26	-12	**60**	56	30	-7
100	81	48	-19	**100**	84	45	-16
Set-up 2 (no oil layer present)				**Set-up 2 (oil layer present)**			
C4-2	Max	Min	**Error (%)**	C4-2	Max	Min	**Error (%)**
15	19	9	33	**15**	18	7	21
30	37	19	25	**30**	35	16	16
40	48	25	21	**40**	44	24	10
50	59	32	17	**50**	54	28	8
60	68	38	13	**60**	66	35	9
100	102	55	2	**100**	96	61	-5

APPENDIX C

Complete set of data for contrast enhanced renal artery measurements.

Table C.1 Doppler measurements pre- and post UCA injection for 0% stenosis (wall-less) where ΔV = post-contrast velocity – pre-contrast velocity and ΔV% = (post-contrast velocity – pre-contrast velocity)/ pre- contrast velocity x 100

0% stenosis	*Pre-contrast*	*Max enhancement*	*Δ*	*Δ %*
V_{Max} (cm s^{-1})	67 ± 1	76 ± 1	9 ± 2	14 ± 3
V_{Min} (cm s^{-1})	7 ± 1	7 ± 2	1 ± 3	14 ± 9
V_{Spread} (cm s^{-1})	60	68	8	14
30% stenosis				
V_{Max} (cm s^{-1})	61 ± 1	84 ± 1	24 ± 3	39 ± 6
V_{Min} (cm s^{-1})	26 ± 1	2 ± 1	-24 ± 3	-92 ± 5
V_{Spread} (cm s^{-1})	34	82	48	139
50% stenosis				
V_{Max} (cm s^{-1})	120 ± 3	139 ± 3	19 ± 5	16 ± 5
V_{Min} (cm s^{-1})	67 ± 2	40 ± 1	-27 ± 3	-40 ± 3
V_{Spread} (cm s^{-1})	53	99	46	88

Table C.2 Doppler measurements before and at 2, 10, 30 & 60 s after contrast injection for wall-less renal artery phantoms

0% stenosis	*Pre-contrast*	*Post-contrast injection(s)*			
		2	*10*	*30*	*60*
V_{Max} (cm s^{-1})	67 ± 1	70 ± 1	69 ± 2	65 ± 1	76 ± 1
V_{Min} (cm s^{-1})	7 ± 1	3 ± 1	4 ± 1	5 ± 1	7 ± 2
V_{Spread} (cm s^{-1})	60	67	65	59	68
30% stenosis					
V_{Max} (cm s^{-1})	61 ± 1	84 ± 1	70 ± 3	57 ± 2	56 ± 2
V_{Min} (cm s^{-1})	26 ± 1	2 ± 1	5 ± 1	27 ± 1	27 ± 2
V_{Spread} (cm s^{-1})	34	82	65	30	29
50% stenosis					
V_{Max} (cm s^{-1})	120 ± 3	139 ± 3	133 ± 1	128 ± 3	122 ± 1
V_{Min} (cm s^{-1})	67 ± 2	40 ± 1	48 ± 1	52 ± 3	63 ± 2
V_{Spread} (cm s^{-1})	53	99	85	76	59

Table C.3 Doppler measurements before and at 2, 10, 30 & 60 s after contrast injection walled renal artery phantoms, where s represents saturated signal

0% stenosis	*Pre-contrast*	*Post-contrast injection(s)*			
		2	*10*	*30*	*60*
V_{Max} (cm s^{-1})	48 ± 1	92 ± 3	60 ± 3	57 ± 1	52 ± 3
V_{Min} (cm s^{-1})	13 ± 2	3 ± 1	4 ± 1	5 ± 1	6 ± 1
V_{Spread} (cm s^{-1})	36	89	56	52	46
30% stenosis					
V_{Max} (cm s^{-1})	78 ± 8	86 ± 3	90 ± 1	88 ± 1	84 ± 3
V_{Min} (cm s^{-1})	7 ± 1	5 ± 1	5 ± 1	6 ± 2	5 ± 3
V_{Spread} (cm s^{-1})	71	81	84	83	79
50% stenosis					
V_{Max} (cm s^{-1})	131 ± 3	164 ± 4	170 ± 2	146 ± 3	134 ± 3
V_{Min} (cm s^{-1})	24 ± 4	4 ± 2	6 ± 3	31 ± 6	39 ± 3
V_{Spread} (cm s^{-1})	107	160	164	115	95
70% stenosis					
V_{Max} (cm s^{-1})	235 ± 3	265 ± 1	264 ± 7	267 ± 3	241 ± 3
V_{Min} (cm s^{-1})	135 ± 5	98 ± 8	81 ± 7	98 ± 7	125 ± 3
V_{Spread} (cm s^{-1})	100	167	183	168	117
90% stenosis					
V_{Max} (cm s^{-1})	117 ± 5	s	s	s	195 ± 4
V_{Min} (cm s^{-1})	37 ± 9	s	s	s	50 ± 5
V_{Spread} (cm s^{-1})	81	s	s	s	145

PUBLICATIONS AND PRESENTATIONS

Publications in preparation

A number of publications are in preparation for submission to the following journals Ultrasound in Medicine and Biology, Physics in Medicine and Biology and Medical Physics.

- King DM, Moran CM & Browne JE, Development of a vessel mimicking material for use in Doppler ultrasound flow phantoms – part 1: acoustic characterization – **Physics in Medicine and Biology**
- McNamara J, King DM., Fagan AJ, Jerrams S & Browne JE Development of a vessel mimicking material for use in Doppler ultrasound flow phantoms – part 2 mechanical characterization – **Physics in Medicine and Biology**
- King DM, Ring M, Moran CM & Browne JE, Development of a range of anatomically realistic renal artery flow phantoms – **Ultrasound in Medicine and Biology**
- King DM, Fagan AJ, Moran CM & Browne JE, Comparative imaging study using a multi-modality renal artery phantom – **Medical Physics**

Conference publication

King DM, Moran CM, Hussey M, Browne JE. How Fat Layers Affect the Clinical Diagnosis from Doppler Data Ultrasonics Symposium 2007 IEEE, 28-31 Oct 2007:2457 - 2460.

Presentations

Characterization of disease within the renal artery using anatomically realistic flow phantoms with varying degrees of stenosis, Deirdre M King, Carmel M Moran, Matt Hussey, Jacinta E Browne. American Institute of Ultrasound in Medicine, Annual Convention. New York 2nd - 5th April 2009

The effect of instrument controls on Doppler dynamic range, Deirdre M King, Carmel M Moran, Matt Hussey, Jacinta E Browne. Institute of Physics and Engineering in Medicine Biennial Ultrasound, York, 3rd – 4th March 2009

The effect of fat layers on physiological spectral Doppler waveforms, Deirdre M King, Carmel M Moran, Matt Hussey, Jacinta E Browne. Institute of Physics and Engineering in Medicine Biennial Ultrasound, York, 3rd – 4th March 2009

Development of a perfusion flow phantom for use with Ultrasound Contrast Agents, Deirdre M King, Carmel M Moran, Matt Hussey, Jacinta E Browne, Association of Physical Scientists in Medicine, Annual Scientific meeting. Kilkenny, 27th February 2009

An anatomically realistic renal artery flow phantom with biomedical properties, Deirdre M King, Michael Ring, Carmel M Moran, Matt Hussey, Jacinta E Browne. British Medical Ultrasound Society, Annual Scientific meeting. Liverpool 9th - 11th December 2008

A new protocol for the evaluation of Doppler dynamic range, Deirdre M King, Carmel M Moran, Matt Hussey, Jacinta E Browne. British Medical Ultrasound Society, Annual Scientific meeting. Liverpool 9th - 11th December 2008 (poster), Runner up prize in poster competition

Study of time intensity curve parameters obtained using the ultrasound contrast agent Luminity with different carrier fluids, Deirdre M King, Thomas Cathcart, Carmel M Moran, Matt Hussey, Jacinta E Browne. British Medical Ultrasound Society, Annual Scientific meeting. Liverpool 9th - 11th December 2008 (poster)

Ultrasound, better with bubbles, Deirdre M King, Carmel M Moran, Matt Hussey, Jacinta E Browne. IOP in Ireland, Spring Weekend meeting. Monaghan 7th - 9th March 2008 (poster) 2nd Place in Rosse Medal Postgraduate poster competition

Characterization of polyvinyl alcohol cryogel (PVA C) for the use as a vessel mimicking material in a multi-modality flow phantom, Deirdre M King, Carmel M Moran, Matt Hussey, Jacinta E Browne. Association of Physical Scientists in Medicine, Annual Scientific meeting. Dublin 16th February 2008

How Fat Layers affect the Clinical Diagnosis obtained from Doppler Data? Deirdre M King, Carmel M Moran, Matt Hussey, Jacinta E Browne. IEEE Ultrasonics Symposium. New York, USA 28th - 31st October 2007 (poster)

Development of an anatomically realistic flow phantom, Deirdre M King, Michael Ring, Carmel M Moran, M Hussey and Jacinta E Browne. 19th Euroson Congress. Leipzig, Germany 24th - 27th October 2007

The Study of the Biomechanical Status of the Renal Artery through Experimentation, Deirdre M King, Michael Ring, Carmel M Moran, M Hussey and Jacinta E Browne. Faculty of Radiologists, Royal College of Surgeons in Ireland, Annual Scientific Meeting. Dublin 27th - 29th September 2007 (poster)

Development of an anatomically realistic flow phantom, Deirdre M King, Michael Ring, Carmel M Moran, M Hussey and Jacinta E Browne. Association of Physical Scientists in Medicine, Annual Scientific meeting. Dublin 10th -11th May 2007

The Effect of Fat Layer on Doppler Velocity Estimations, Deirdre M King, Carmel M Moran, Matt Hussey, Jacinta E Browne. Institute of Physics and Engineering in Medicine, Biennial Ultrasound meeting. Birmingham 28th - 29th March 2007

Colour Doppler Signal-to-Noise Ratio Performance for a Range of Scanners and Doppler Dynamic Range, Deirdre M King, Carmel M Moran, Matt Hussey, Jacinta E

Browne. British Medical Ultrasound Society, Annual Scientific meeting. Manchester 12^{th} - 14^{th} December 2006

AWARDS

Awarded runner up prize in scientific poster competition, British Medical Ultrasound Society Annual Scientific meeting, Liverpool 9th - 11th December 2008

Awarded 2nd place in the Rosse Medal poster competition for post graduate research in Physics, IOP in Ireland, Spring Weekend meeting. Monaghan 7th - 9th March 2008

Awarded the IOP Medical Physics Group Travel Bursary to attend the IEEE Ultrasonics Symposium, New York, October 2007

Awarded the IOP CR Barber Trust fund to attend the BMUS Annual Scientific meeting in Manchester UK December 2005